PFC/RR-91-15 MIT-GEM-DM-01

GEM Magnet Options: Preliminary Report

J.D. Sullivan, P.G. Marston, R.D. Pillsbury, Jr.
R.J. Thome, N. Diatchenko, H. Becker
M.I.T. Plasma Fusion Center

R.L. Myatt, P.H. Titus
Stone & Webster Engineering Corporation

November 25, 1991

Plasma Fusion Center
Massachusetts Institute of Technology
Cambridge, MA 02139

This work was supported in part by SSCL/DoE under contract P.O. #91-W-09962.

PFC/RR-91-15 MIT-GEM-DM-01

GEM Magnet Options: Preliminary Report

J.D. Sullivan, P.G. Marston, R.D. Pillsbury, Jr.
R.J. Thome, N. Diatchenko, H. Becker
M.I.T. Plasma Fusion Center

R.L. Myatt, P.H. Titus
Stone & Webster Engineering Corporation

November 25, 1991

Plasma Fusion Center
Massachusetts Institute of Technology
Cambridge, MA 02139

This work was supported in part by SSCL/DoE under contract P.O. #91-W-09962.

Contents

List of Figures

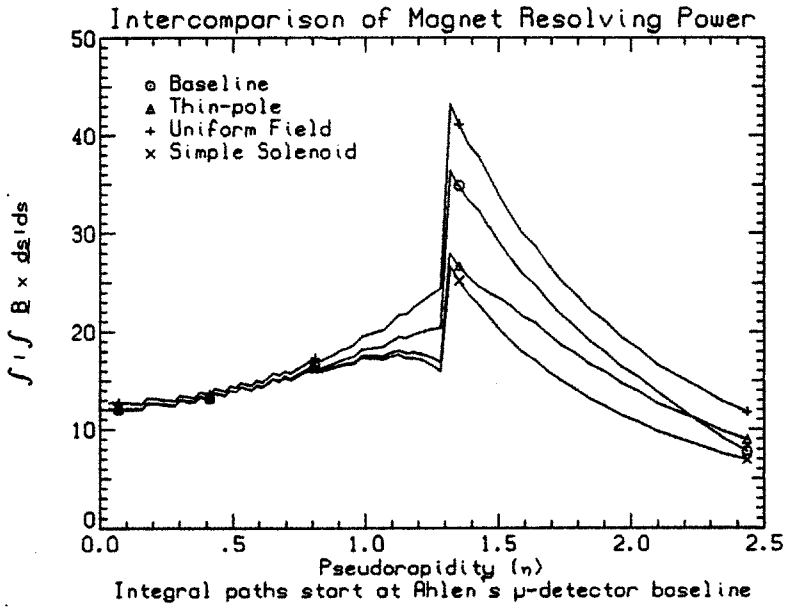

Figure 4: Comparison of various magnet designs: $\mathcal{BL}^2$ versus η. The curve for a uniform field is marked with a +, that for a simple solenoid with $\times$, for EoI baseline $\bigcirc$, and for the LoI baseline $\triangle$.

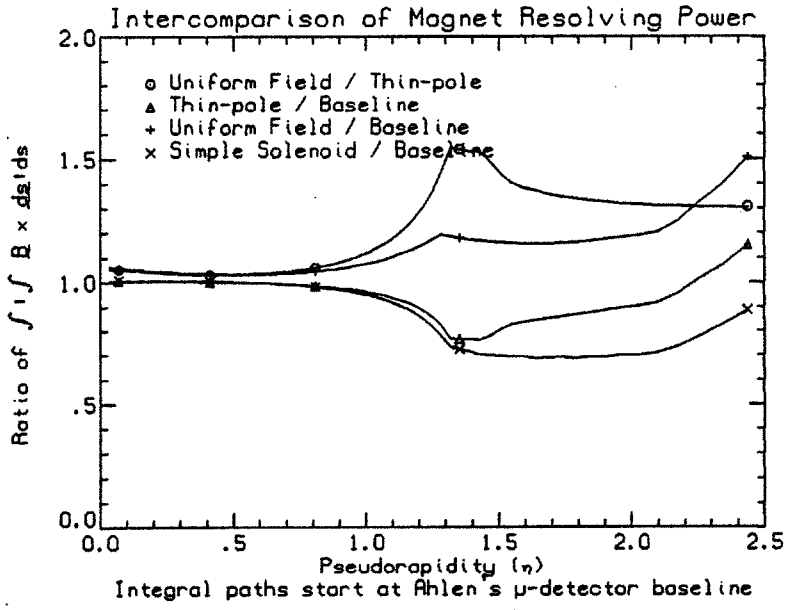

Figure 5: Comparison of various magnet designs: ratio of $\mathcal{BL}^2$ versus η. The curve for a uniform field/EoI baseline is marked with a +, that for a simple solenoid/EoI baseline with $\times$, for uniform field/LoI baseline $\bigcirc$, and for the LoI baseline/EoI baseline $\triangle$.

GEM Magnet Options: Preliminary Report

A strawman muon detector geometry is used in the evaluation of various designs for the GEM magnet. The muon track resolution for the EoI baseline magnet (superconducting solenoid with thick iron end poles) is compared with an option with modified end poles (the LoI baseline), and with a uniform field. Design magnet options to improve muon resolution at small angles ($1.5 \leq \eta \leq 2.5$) include the replacement of the iron poles with a superconducting "bottle" solenoid and/or the addition of conical shells (wedges) of iron for field shaping. Because of concern about the far (surface) field, shielded variants which use either a superconducting outer solenoid or an iron flux return are also presented.

1 Introduction

The designs for a GEM[1] magnet are based on satisfying the physics measurement requirements. The project goal is to develop designs for magnet systems which can be constructed within schedule and within budget, which have adequate safety margin, and which meet all environmental requirements. The possibility of staging of some magnet elements (e.g., small angle toroids) may be considered because of the tight construction schedule.

The initial conceptual approach (following L* [1, 2]) used a uniform field with the requirements of

- an 0.8 T uniform field in the central tracker (vertex detector),
- 5% momentum resolution for 500 GeV muon at 90° assuming 100 μm errors, and
- reasonable muon resolution (for constant P) out to $\eta = 2.5$.

The EoI[2] baseline design [3] sought to make a uniform field from a (superconducting) solenoid with (field shaping) thick iron pole pieces. However, the GEM collaboration was cognizant from the first of the lack of flux return and of the importance of muon resolution at fixed P_t as a function of η, e.g., the resolution at low angles needed to be improved. Consequently, in addition to cost and complexity, the magnet design options discussed below address the following two questions which were drawbacks inherent in the basic concept

1. How is the magnetic flux returned? and
2. What can be done about the rapid loss of resolution at forward angles?

[1] $\gamma e \mu$ detector

[2] EoI — Expression of Interest (in proposing an experiment)

To summarize the results of comparing these four options:

1. An ideal uniform field is better than either baseline.
2. At lower angles the LoI baseline is better than the EoI baseline because the iron pole extends further.
3. The surface field for the LoI baseline is slightly smaller than that for the EoI baseline because of less iron.
4. At intermediate angles the resolution for the LoI baseline is somewhat worse than that for the EoI baseline.

Although there is a loss of resolution at intermediate angles (where resolution is a maximum), the LoI baseline uses less iron (costs less) and gives better access than the EoI baseline design (which is why the change).

Finally, there has been some discussion of the possibility of adding muon detectors outside the superconducting windings (of the EoI baseline). For $\eta = 0$, a gain in achievable resolution seems feasible (depending on other errors); however, for $\eta >\sim 1$ the total $|\vec{\mathcal{I}}|$ decreases and no gain would appear to be possible. This is shown in Figures 8–11 where the dependence on angle is explicitly shown. The abscissa is the path (arc) length so that the turnover comes at different values depending on the angle of the path. Where the curves are straight, $\mathcal{BL}^2$ can be easily estimated as the product of the height difference and the length. The corresponding curves for the LoI baseline would be, for all practical purposes, identical.

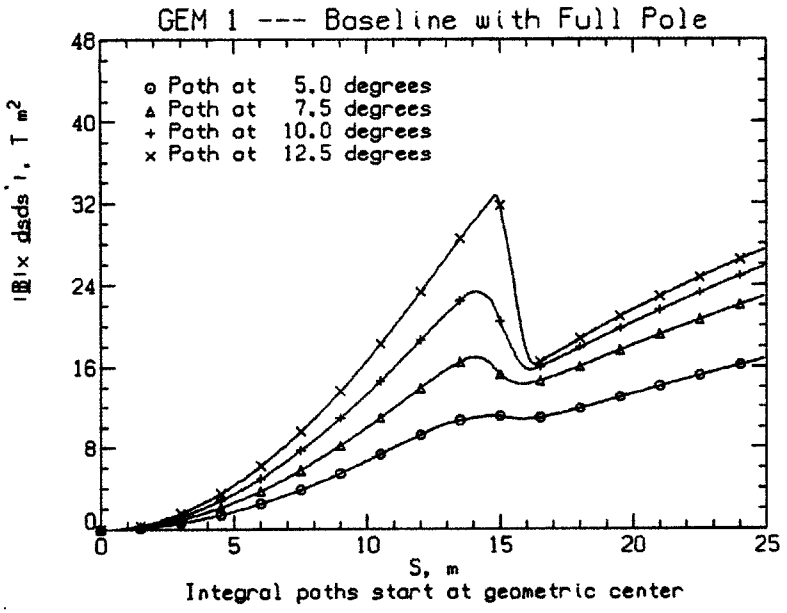

Figure 8: Plot of $|\vec{\mathcal{I}}|$ for the EoI baseline magnet versus path length from the interaction point for tracks at 5, 7.5, 10, and 12.5° (from the beam line).

For multiple scattering [5, 6, 7], the central superlayer is assumed to have $\frac{\overline{x}}{x_0} = 0.2$ at normal incidence, but $\frac{\overline{x}}{x_0} \sim \csc\theta$ or $\sec\theta$ for the barrel or endcap, so that

$$\sigma_{MS} = \frac{D}{2}\frac{1}{\sqrt{3}}\frac{14.1}{pc\beta}\left(1.0 + 0.1111\log\frac{\overline{x}}{x_0}\right), \tag{4}$$

where D is the distance between superlayers. Finally, the systematic error is assumed to be

$$\sigma_{sys} \equiv 25\ \mu\text{m}. \tag{5}$$

Occasionally, the outer edge of the central detectors and the inner edge of the magnet cryostat are used as the defining dimensions but graphs in which this is assumed are always so labeled.

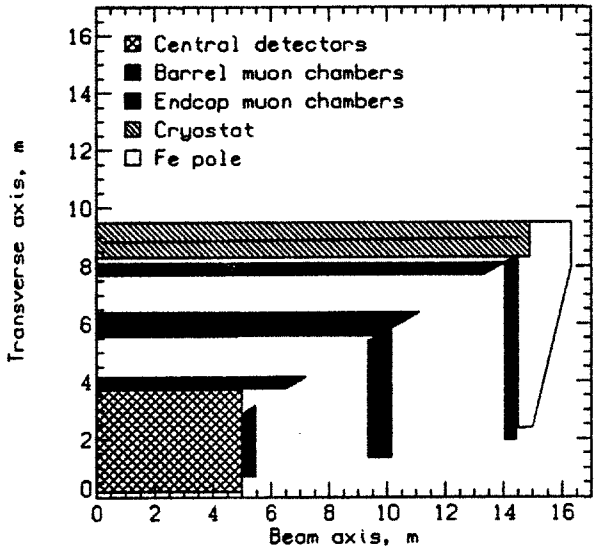

Figure 2: Quadrant side view (based on the EoI) of GEM showing: the central detectors, strawman muon chamber layout, magnet cryostat, and thick iron pole piece. The size of the central detector is dictated by calorimetry resolution and the vertex detector; the muon resolution determines the overall volume and the magnet cryostat must be outside that.

To obtain a resolving power measure[4], we consider the Lorentz force,

$$\frac{d\vec{p}}{dt} = \frac{q}{c}\vec{v} \times \vec{B}, \tag{6}$$

and assume that the particle rigidity $\mathcal{R}$ is high enough that $\rho \gg L$ where ρ is the radius of curvature ($= \mathcal{R}/B_\perp$) and L is the length scale of interest (e.g., the size of the experiment). Under this assumption, the osculating plane is fixed and (small) higher order corrections to the path are ignored. The first integral of the force equation is the impulse $\vec{\mathcal{I}}$:

$$\vec{\mathcal{I}} \equiv \frac{q}{c}\int_0^s \vec{B} \times d\vec{\ell}. \tag{7}$$

[4]A complementary analysis by Prof. Pless of M.I.T. with the same result is reproduced in Appendix B.

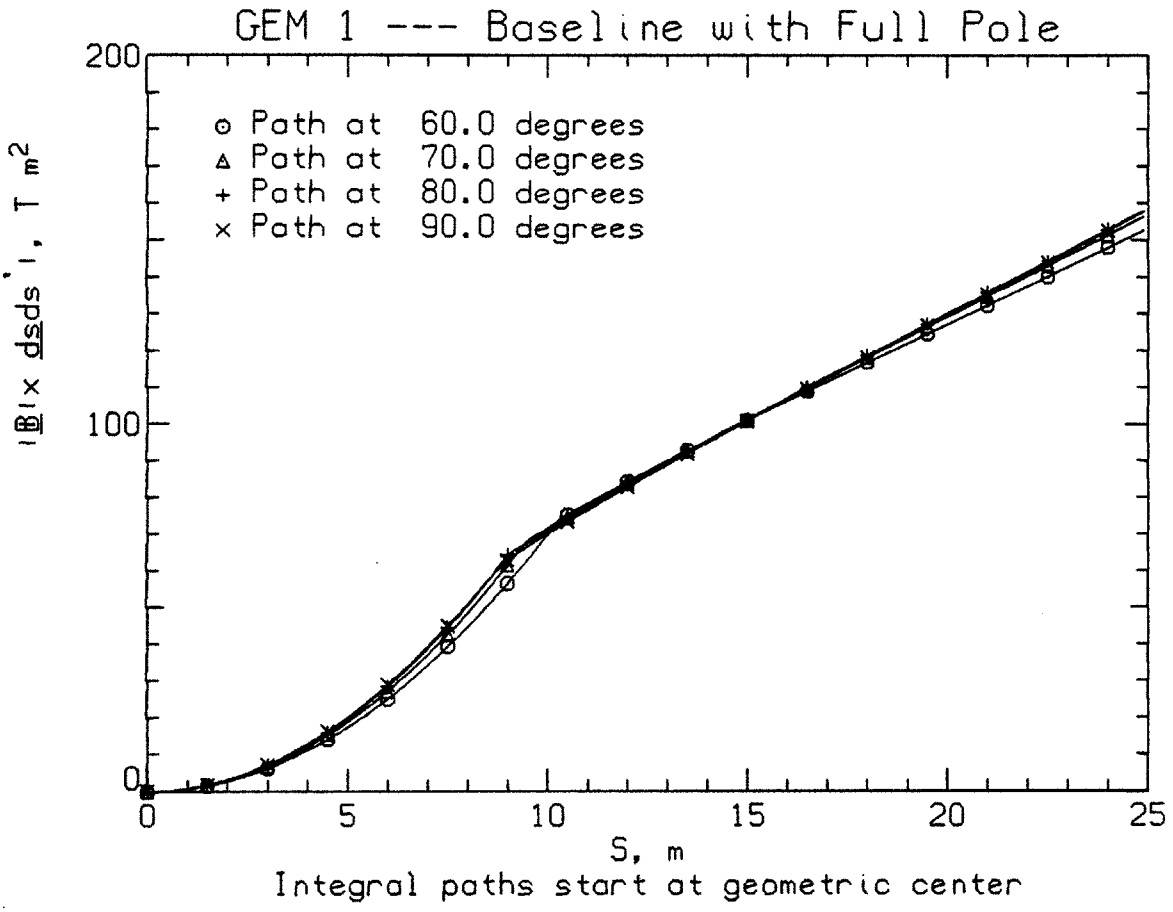

Figure 11: Plot of $|\vec{\mathcal{I}}|$ for the EoI baseline magnet versus path length from the interaction point for tracks at 60, 70, 80, and 90° (from the beam line).

4 GEM Baseline

For the uniform field (where most results are analytic), isopleths of constant $\mathcal{BL}^2$ are shown in Figure 3; the 10 T m^2 isopleth is approximately the 5% resolution level (for fixed P). However, the questions: "How well does the baseline design (cf. Figure 2) meet the con-

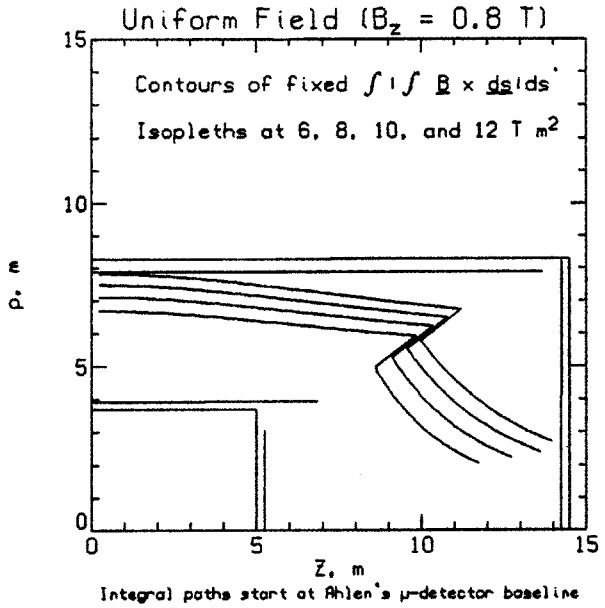

Figure 3: Isopleths of constant $\mathcal{BL}^2$ for a uniform field superposed on a sketch of GEM; isopleths increase in value with distance from the origin.

ceptual design goals?" and "Is it possible to reduce cost, to improve access, etc. of the baseline?" must be answered. We do this by considering (and comparing)

1. a uniform field,
2. a simple solenoid (cf. Appendix A.1.1),
3. the EoI baseline, a solenoid with a thick iron pole (cf. Appendix A.1.2), and
4. the LoI[9] baseline, a solenoid with a thin iron pole extending to only 7 m (cf. Appendix A.1.7).

The resolving power as a function of pseudorapidity is shown in Figure 4 for these four cases. The kink in all the curves is simply an artifact of the muon detector geometry. The uniform field has larger resolving power at all values of η and the curve for the thin pole crosses that for the baseline because the thin pole extends closer to the beamline. The differences in resolving power can be seen in a plot of their ratios (cf. Figure 5).

The resolution $(\frac{\Delta S}{S})$ for a constant P of 500 GeV is shown in Figure 6 and for a constant P_t of 500 GeV in Figure 7. Clearly for $\eta > 1.5$, the fixed P_t resolution deteriorates rapidly and this is a major drawback to both baseline magnet options.

[9]LoI — Letter of Intent (to propose an experiment); due November 30, 1991 for GEM.

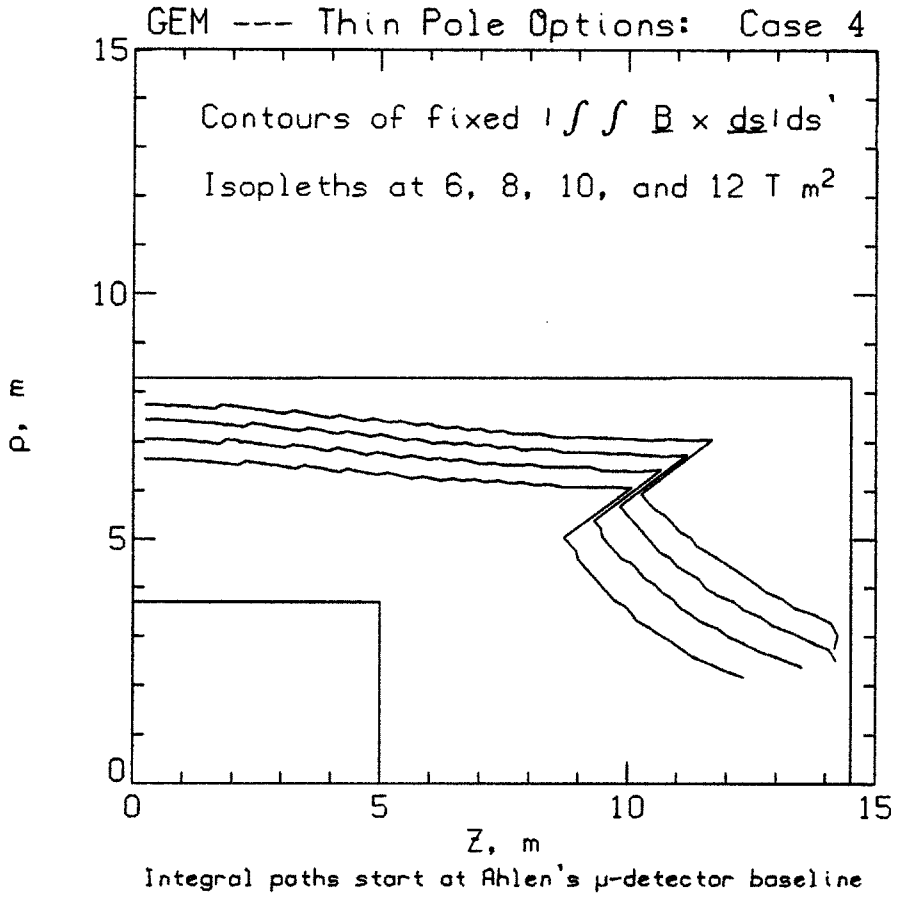

Figure 92: Isopleths of constant $\mathcal{BL}^2$ superposed on a sketch of the GEM concept; isopleths increase with distance from the origin.

A.1.4 Thin pole case 2

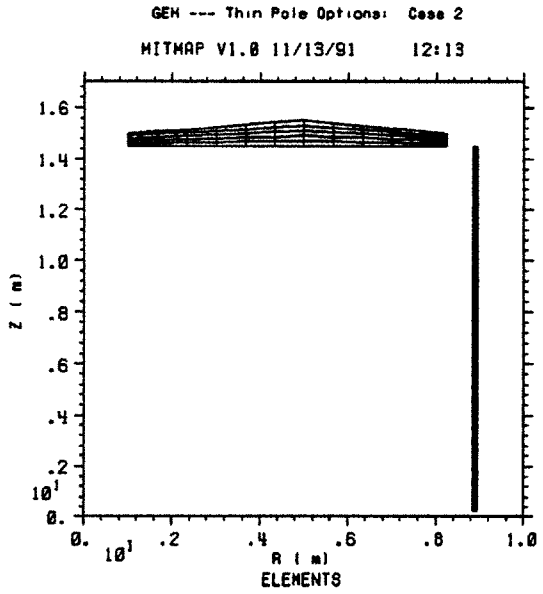

Figure 64: Side view of a superconducting solenoid with a thin pole, case #2. Note that the beam axis (the z axis) is vertical on the page and the transverse (radial) axis is horizontal.

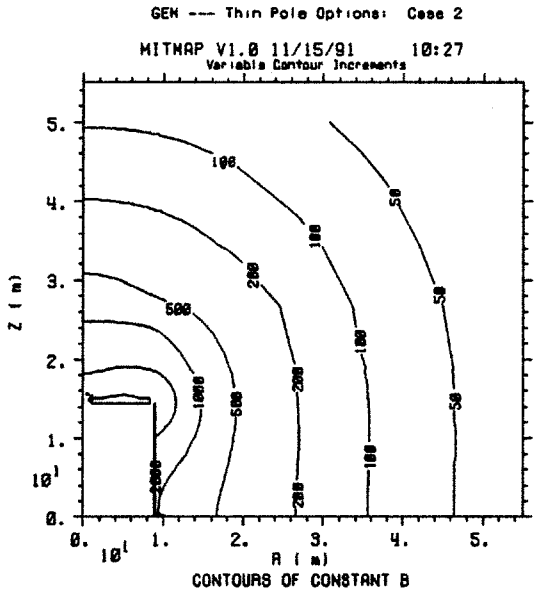

Figure 65: Contours of constant $|\vec{B}|$ superposed on a side view of the magnet; isopleths are labeled in gauss.

A.1.5 Thin pole case 3

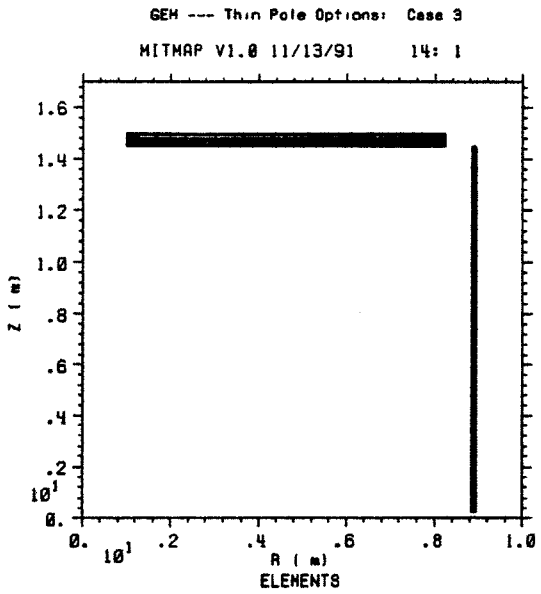

Figure 73: Side view of a superconducting solenoid with a thin pole, case #3. Note that the beam axis (the z axis) is vertical on the page and the transverse (radial) axis is horizontal.

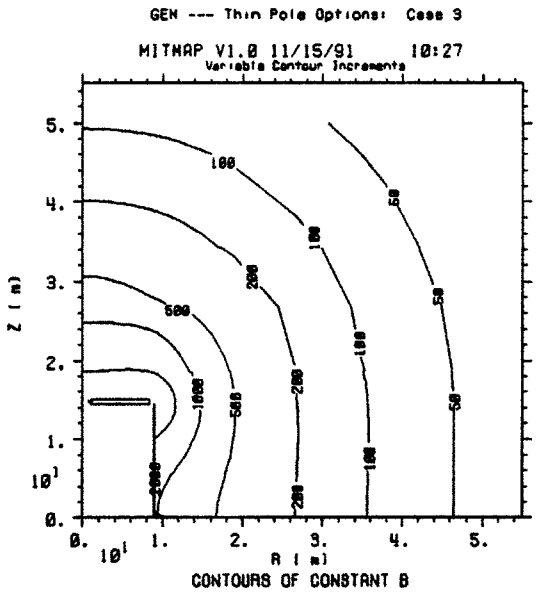

Figure 74: Contours of constant $|\vec{B}|$ superposed on a side view of the magnet; isopleths are labeled in gauss.

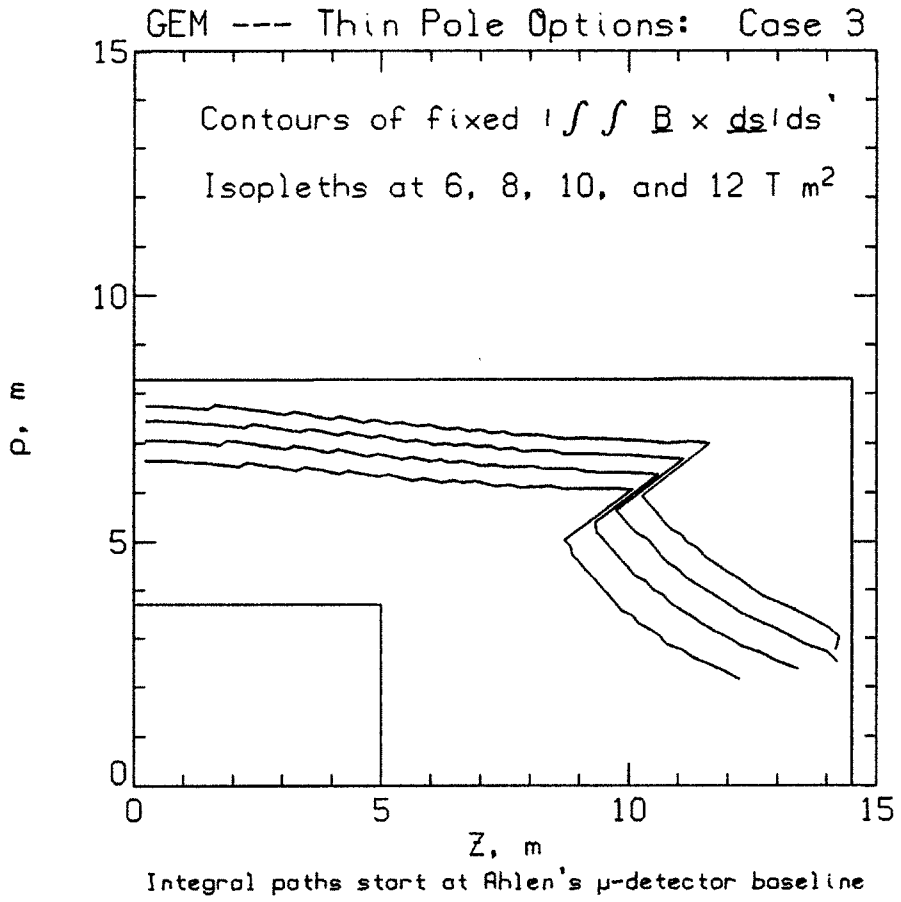

Figure 83: Isopleths of constant $\mathcal{BL}^2$ superposed on a sketch of the GEM concept; isopleths increase with distance from the origin.

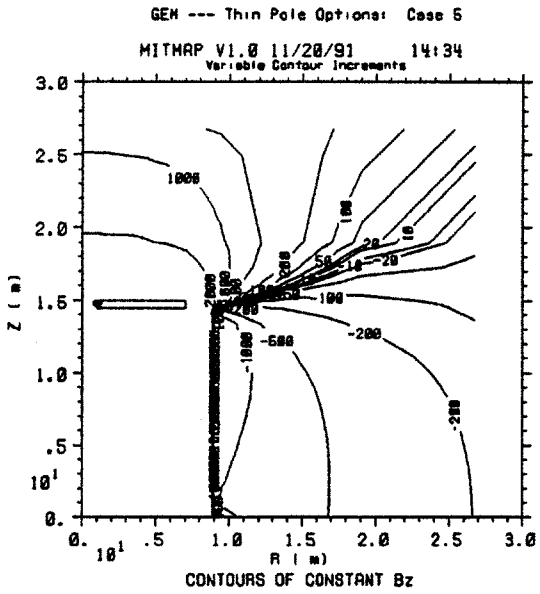

Figure 95: Contours of constant B_z superposed on a side view of the magnet; isopleths are labeled in gauss.

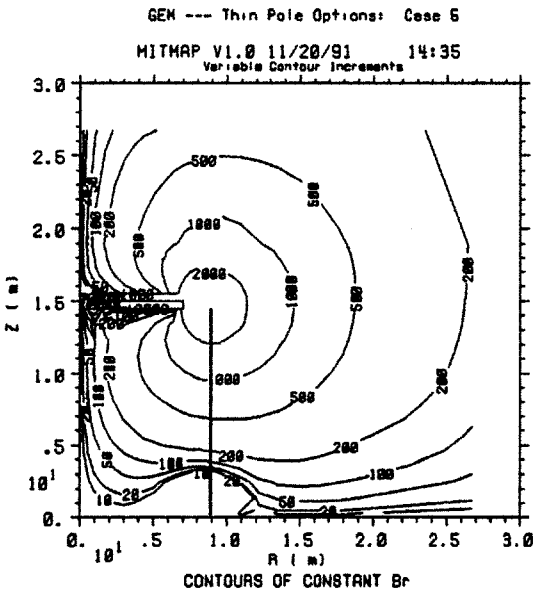

Figure 96: Contours of constant B_r superposed on a side view of the magnet; isopleths are labeled in gauss.

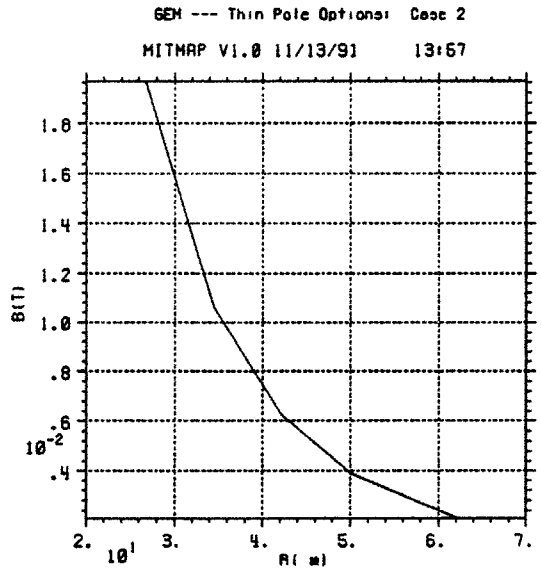

Figure 68: $|\vec{B}|$ versus radius near the surface.

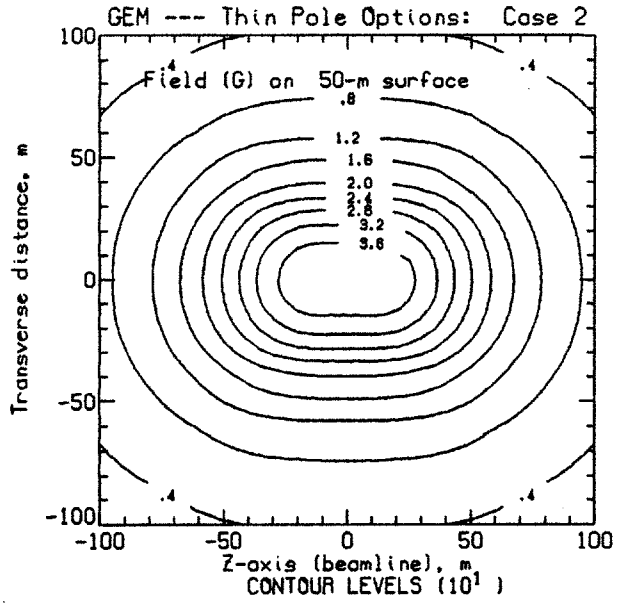

Figure 69: Isogauss contours of the field on a surface at a nominal elevation of 50 m above the beamline (centerline).

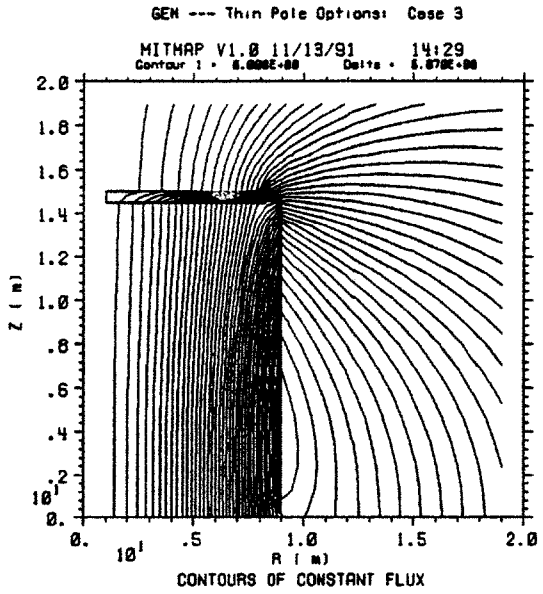

Figure 77: Flux lines superposed on a side view of the magnet design.

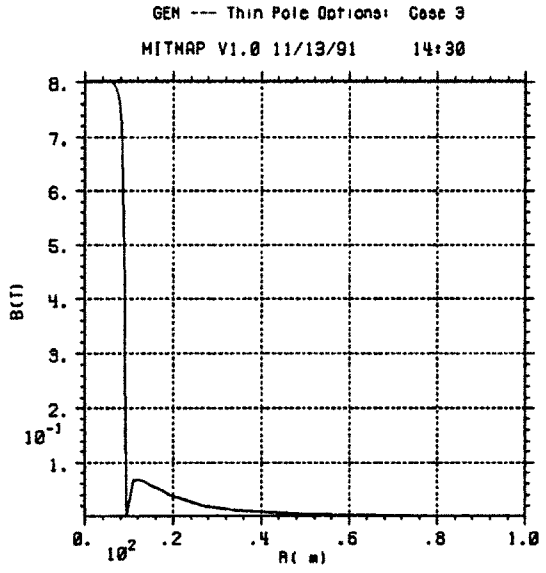

Figure 78: $|\vec{B}|$ versus radius in the hall.

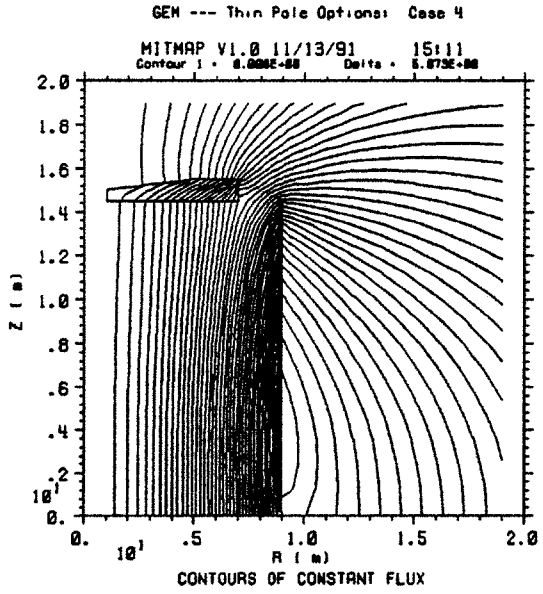

Figure 86: Flux lines superposed on a side view of the magnet design.

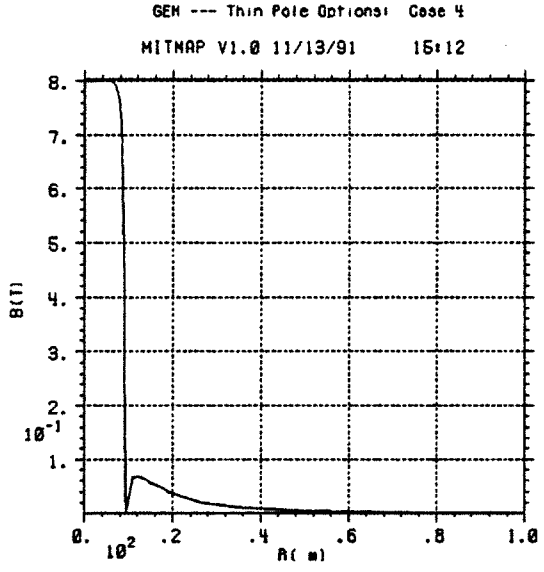

Figure 87: $|\vec{B}|$ versus radius in the hall.

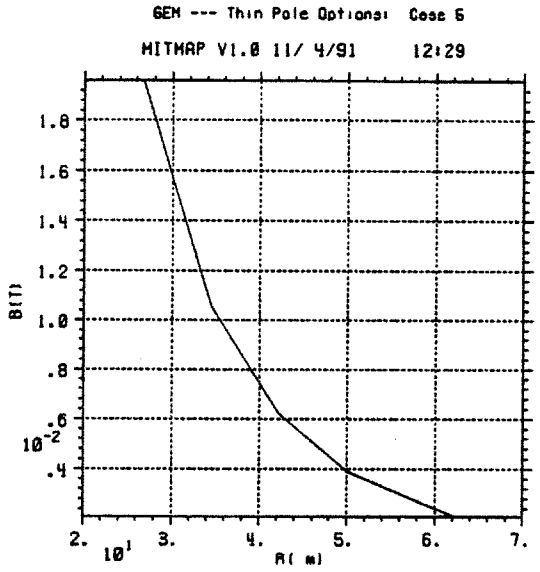

Figure 99: $|\vec{B}|$ versus radius near the surface.

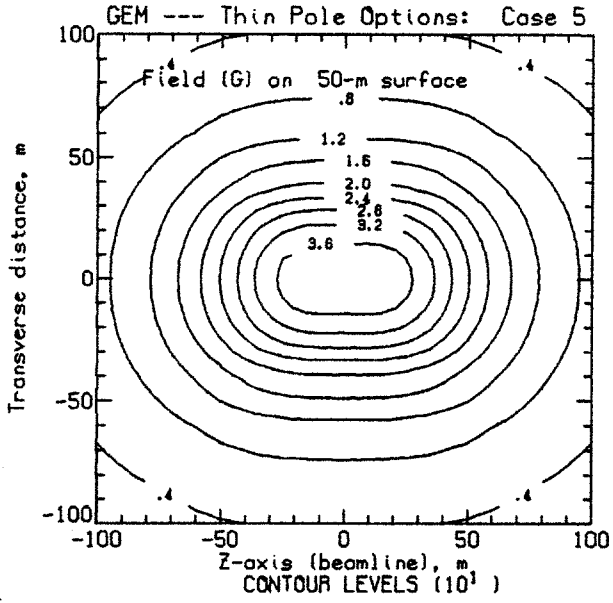

Figure 100: Isogauss contours of the field on a surface at a nominal elevation of 50 m above the beamline (centerline).

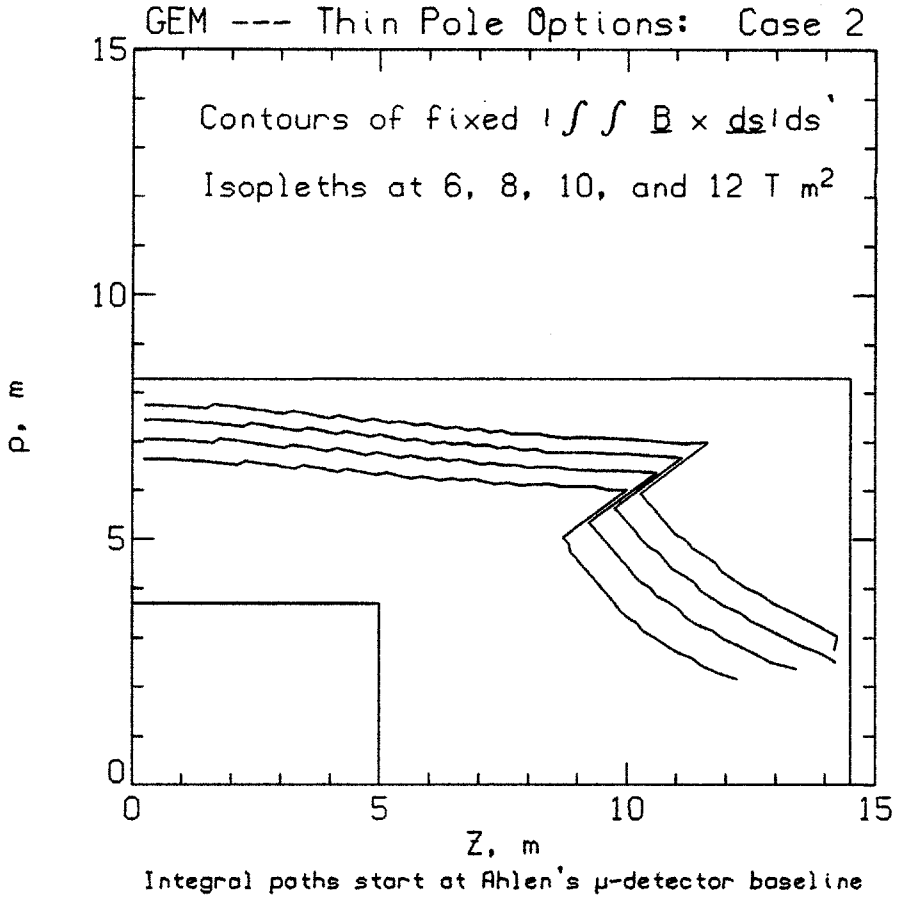

Figure 72: Isopleths of constant BL^2 superposed on a sketch of the GEM concept; isopleths increase with distance from the origin.

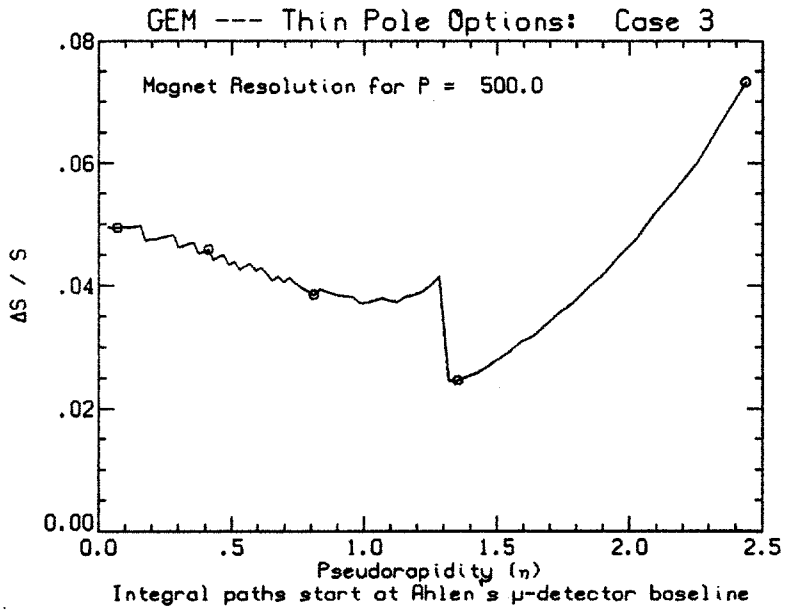

Figure 81: Resolution for constant P as a function of η.

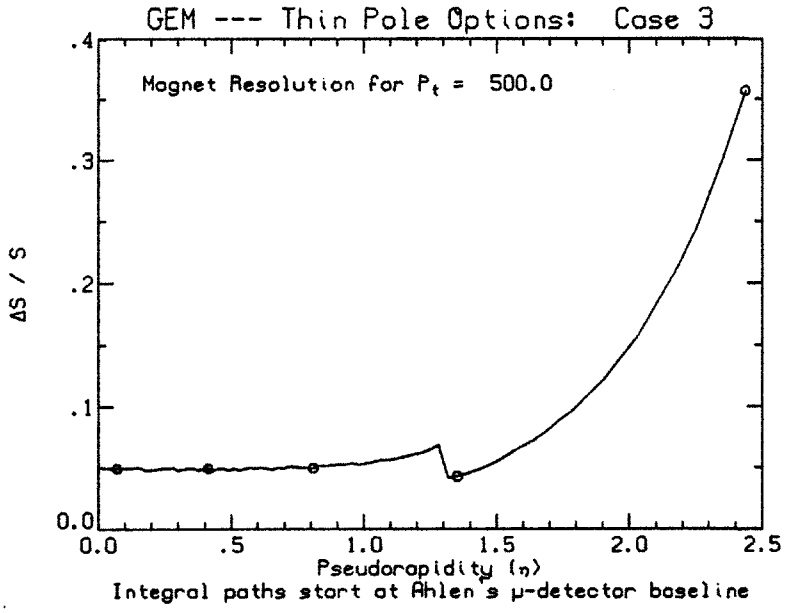

Figure 82: Resolution for constant P_t as a function of η.

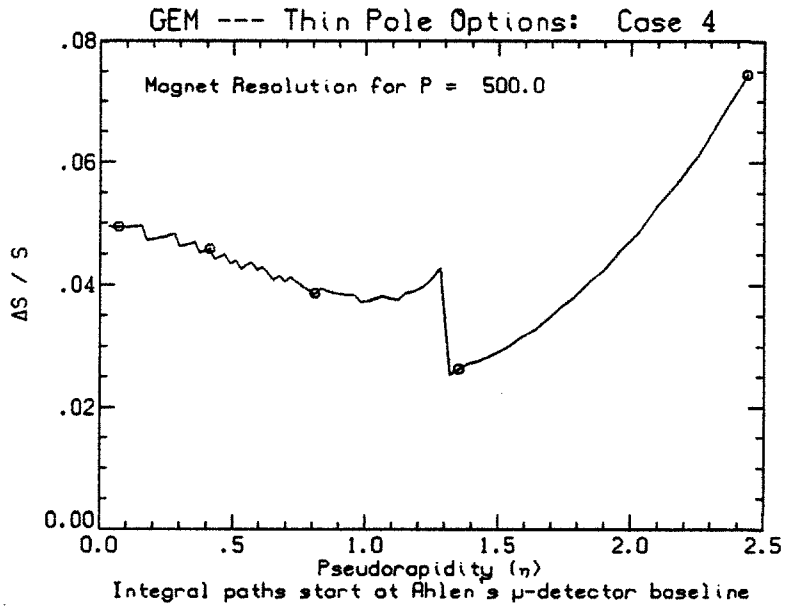

Figure 90: Resolution for constant P as a function of η.

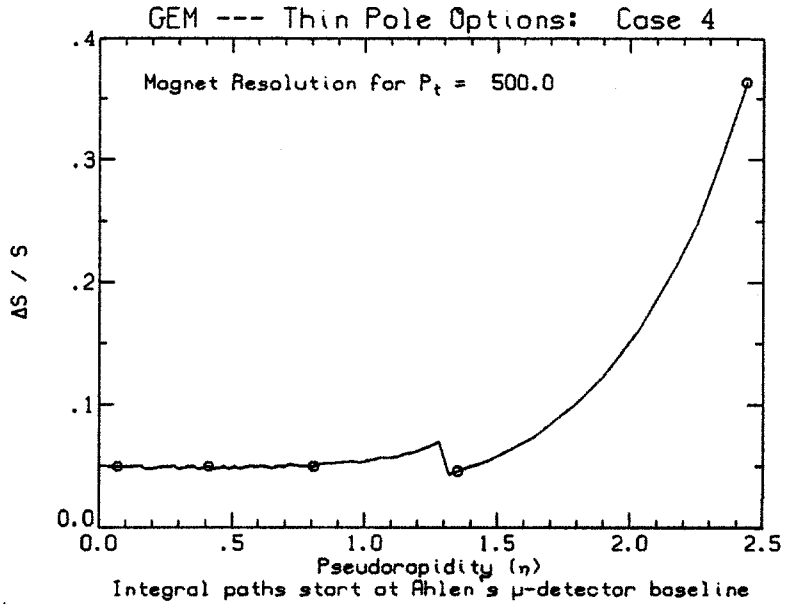

Figure 91: Resolution for constant P_t as a function of η.

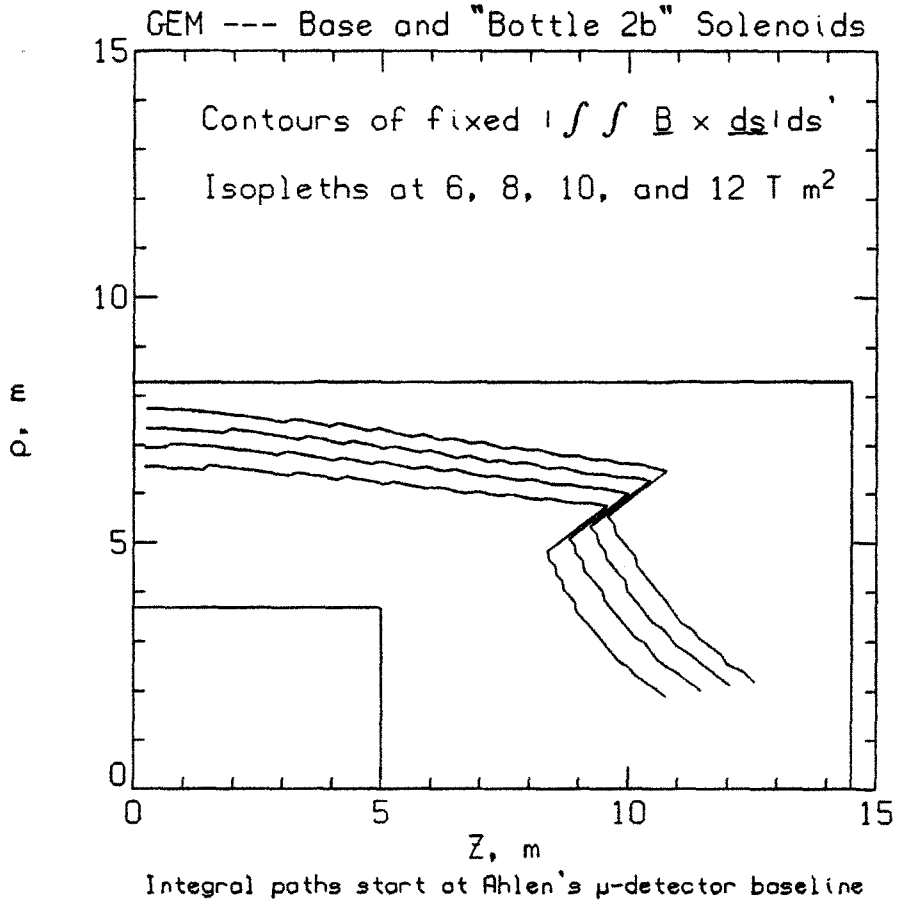

Figure 186: Isopleths of constant $\mathcal{BL}^2$ superposed on a sketch of the GEM concept; isopleths increase with distance from the origin.

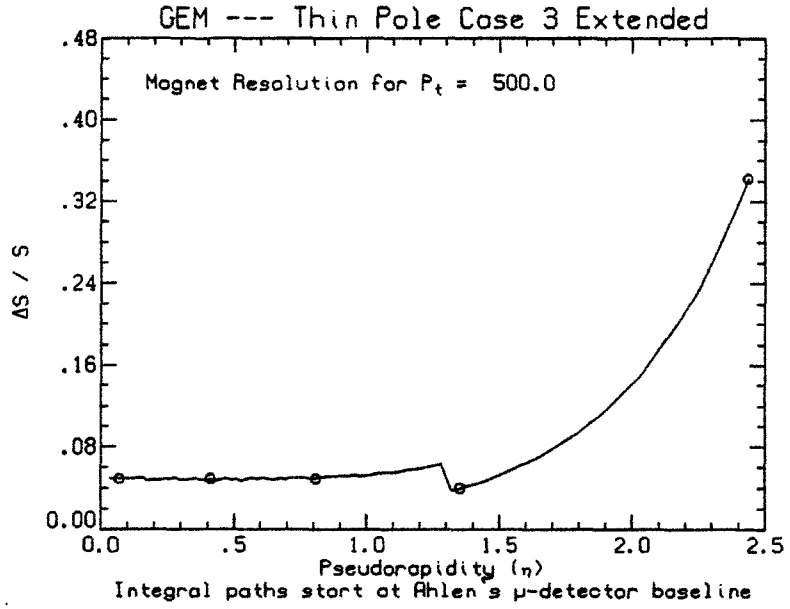

Figure 157: Resolution for constant P_t as a function of η.

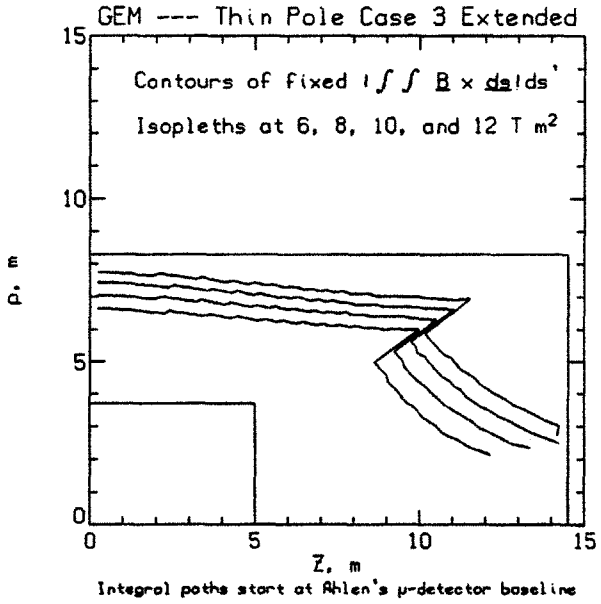

Figure 158: Isopleths of constant $\boldsymbol{BL}^2$ superposed on a sketch of the GEM concept; isopleths increase with distance from the origin.

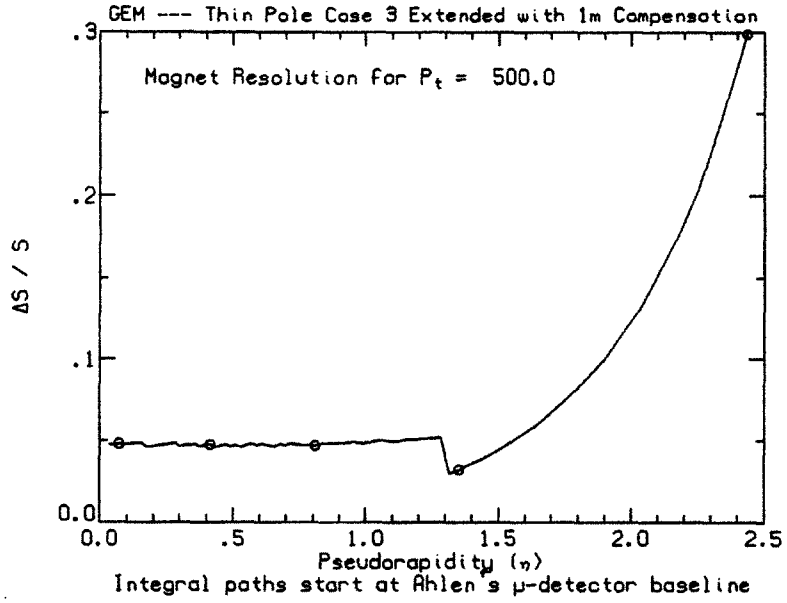

Figure 167: Resolution for constant P_t as a function of η.

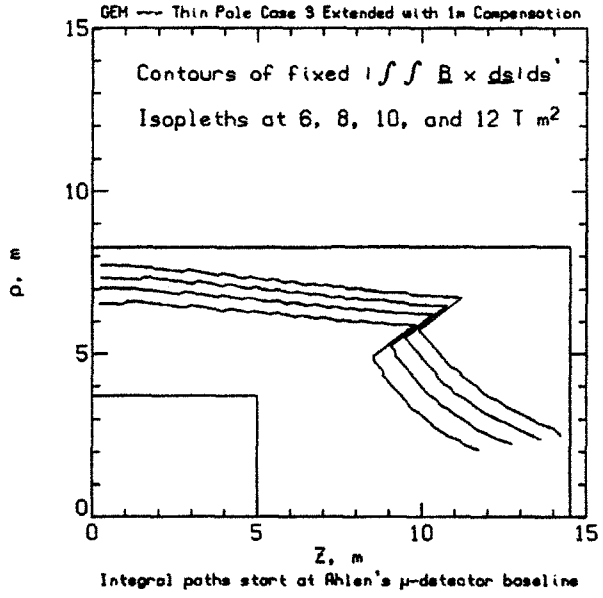

Figure 168: Isopleths of constant $\boldsymbol{BL}^2$ superposed on a sketch of the GEM concept; isopleths increase with distance from the origin.

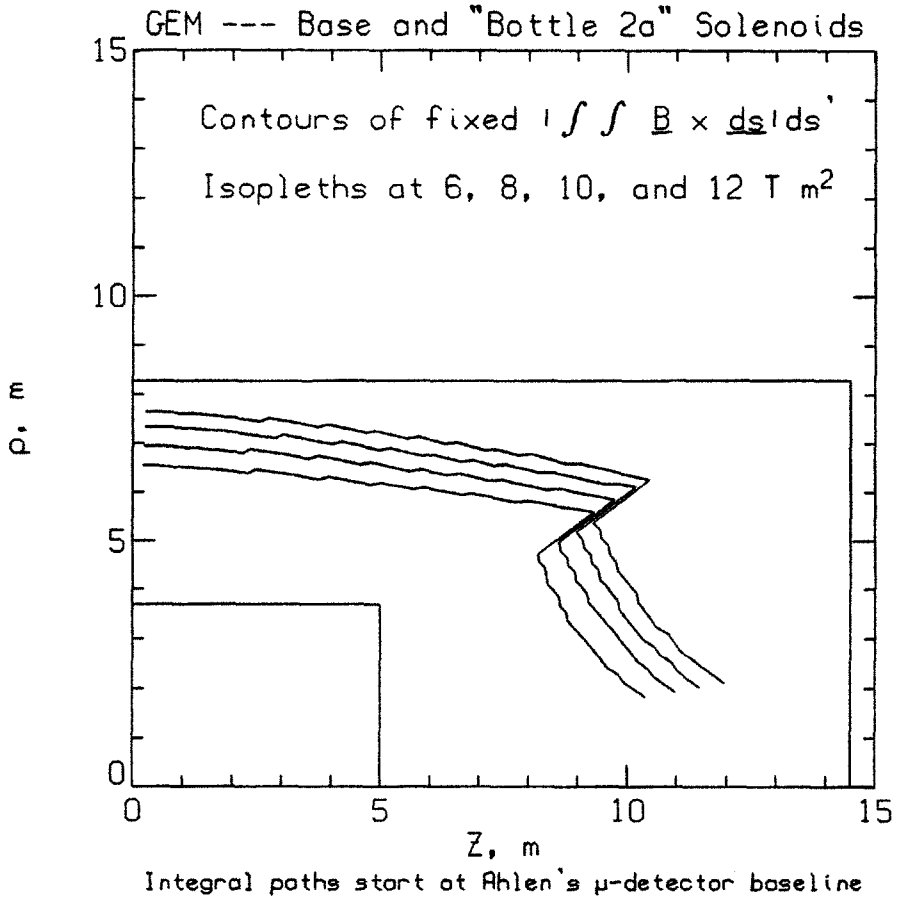

Figure 177: Isopleths of constant $\boldsymbol{BL}^2$ superposed on a sketch of the GEM concept; isopleths increase with distance from the origin.

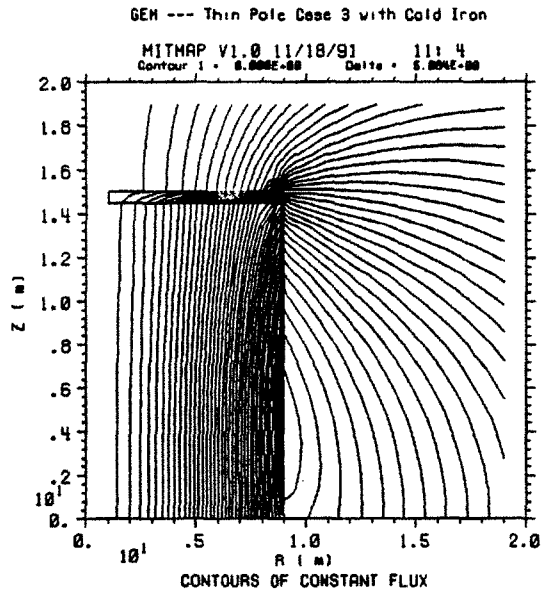

Figure 189: Flux lines superposed on a side view of the magnet design.

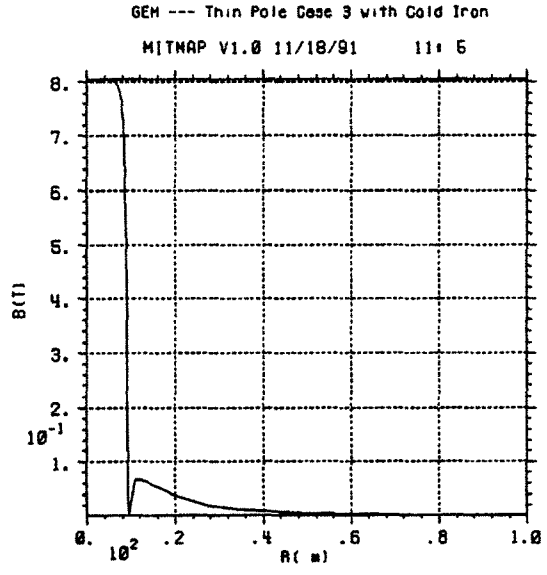

Figure 190: $|\vec{B}|$ versus radius in the hall.

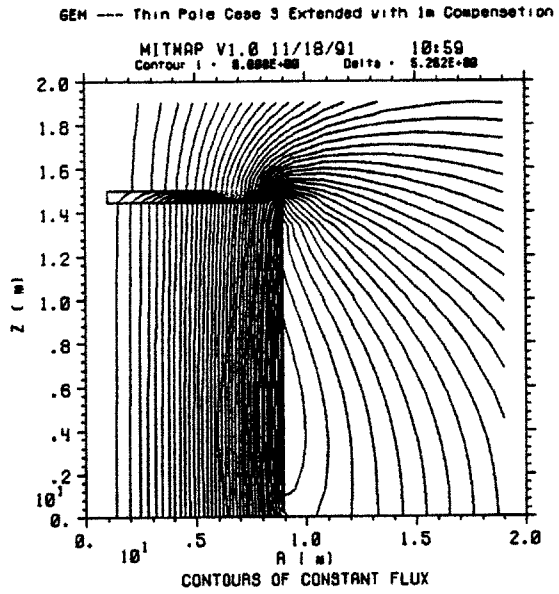

Figure 161: Flux lines superposed on a side view of the magnet design.

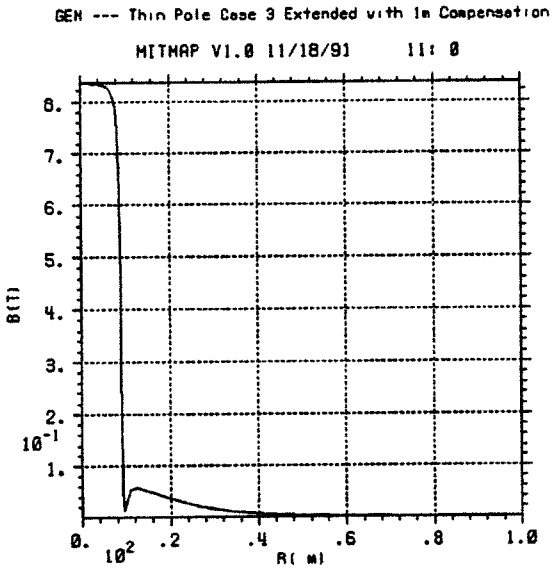

Figure 162: $|\vec{B}|$ versus radius in the hall.

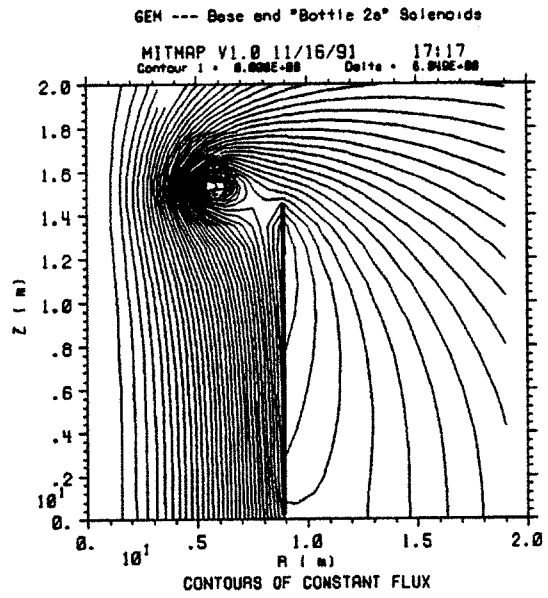

Figure 171: Flux lines superposed on a side view of the magnet design.

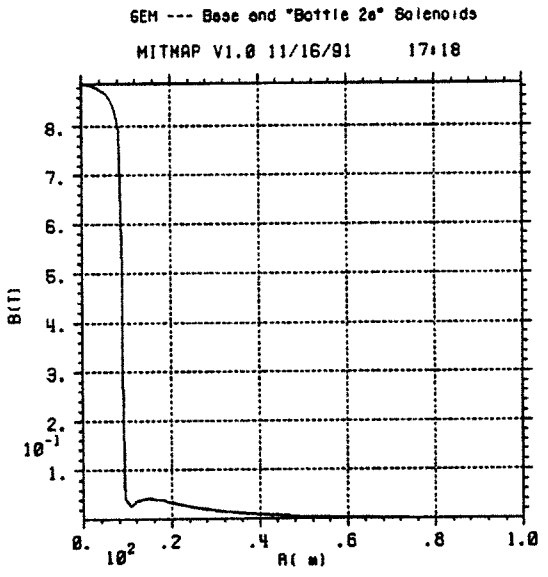

Figure 172: $|\vec{B}|$ versus radius in the hall.

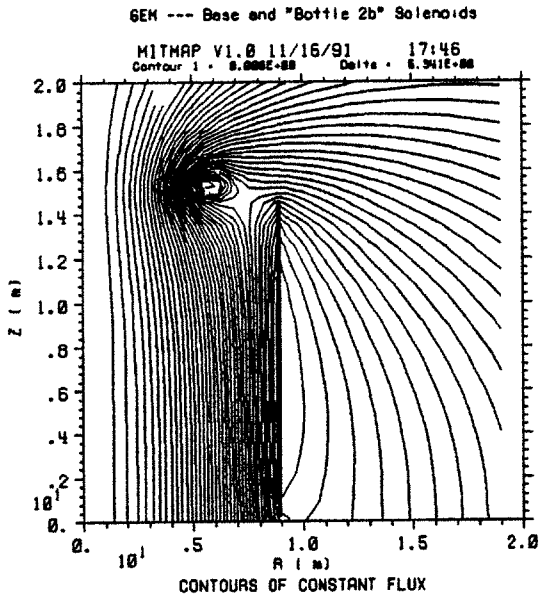

Figure 180: Flux lines superposed on a side view of the magnet design.

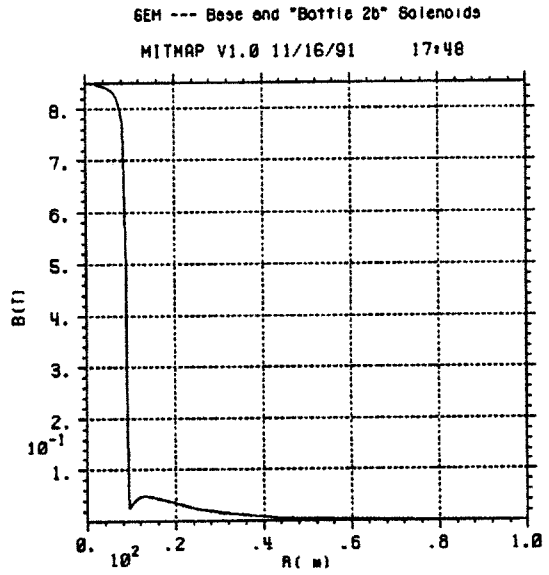

Figure 181: $|\vec{B}|$ versus radius in the hall.

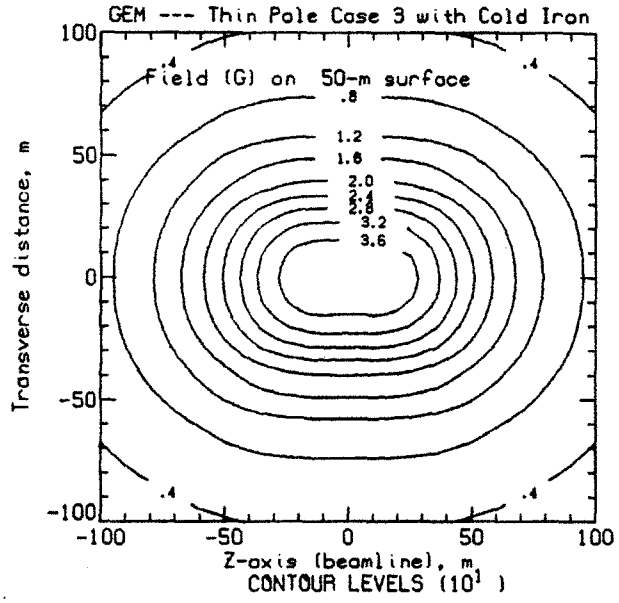

Figure 193: Isogauss contours of the field on a surface at a nominal elevation of 50 m above the beamline (centerline).

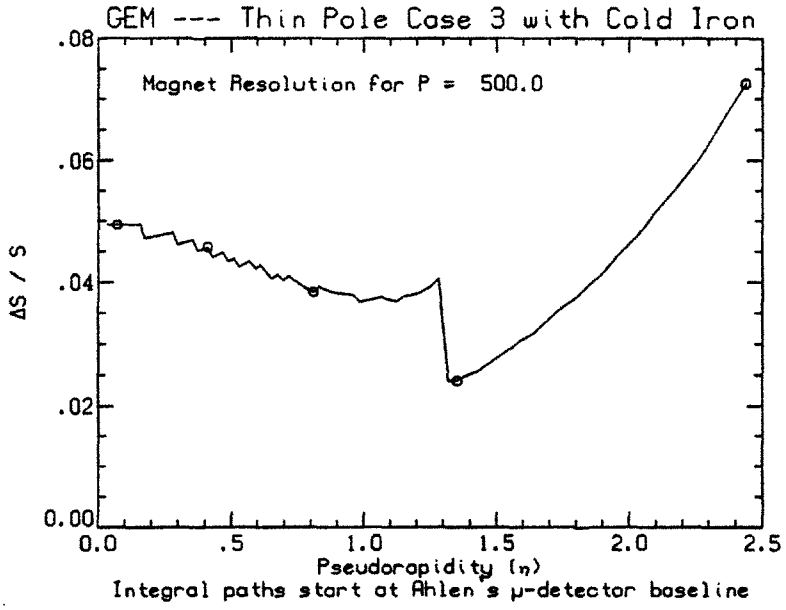

Figure 194: Resolution for constant P as a function of η.

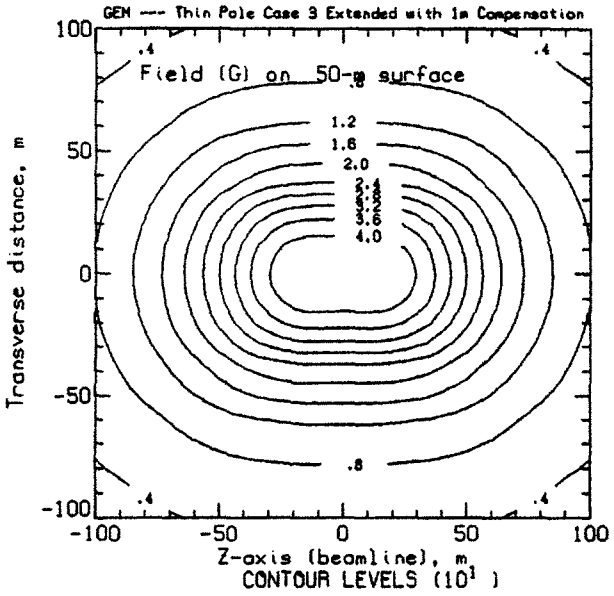

Figure 165: Isogauss contours of the field on a surface at a nominal elevation of 50 m above the beamline (centerline).

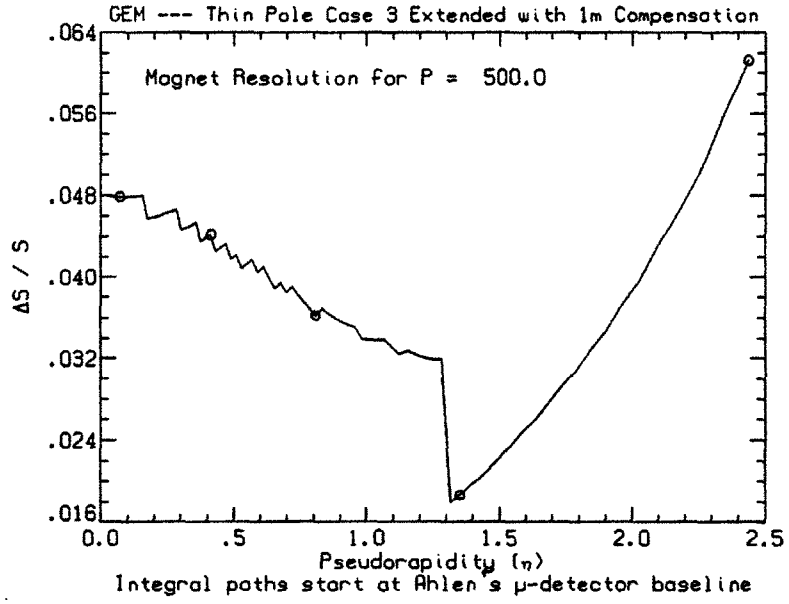

Figure 166: Resolution for constant P as a function of η.

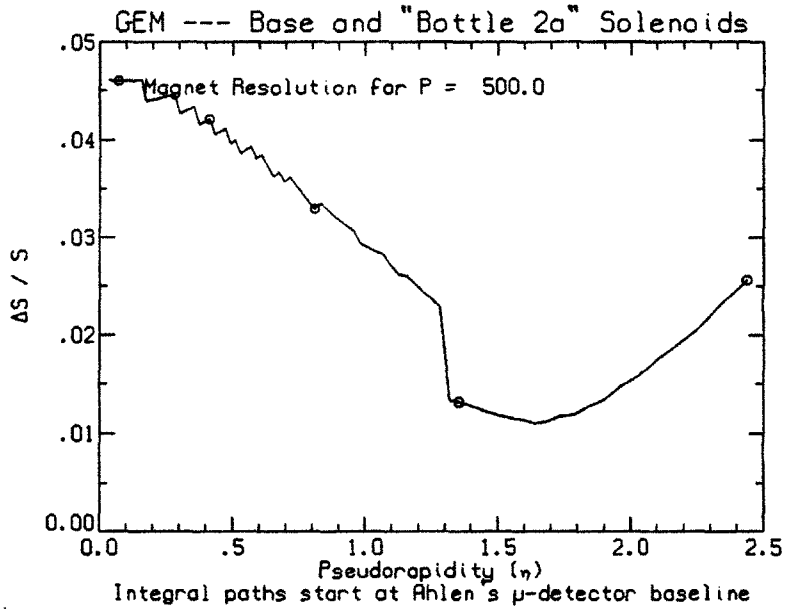

Figure 175: Resolution for constant P as a function of η.

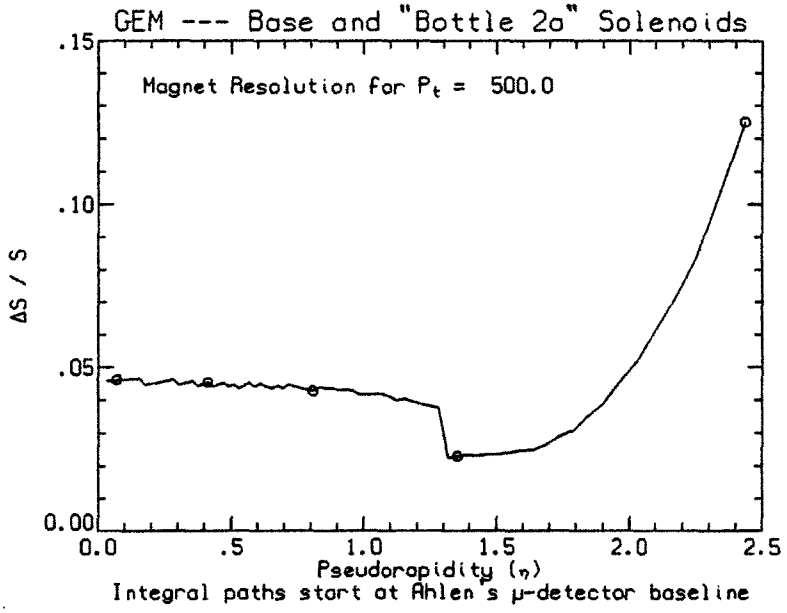

Figure 176: Resolution for constant P_t as a function of η.

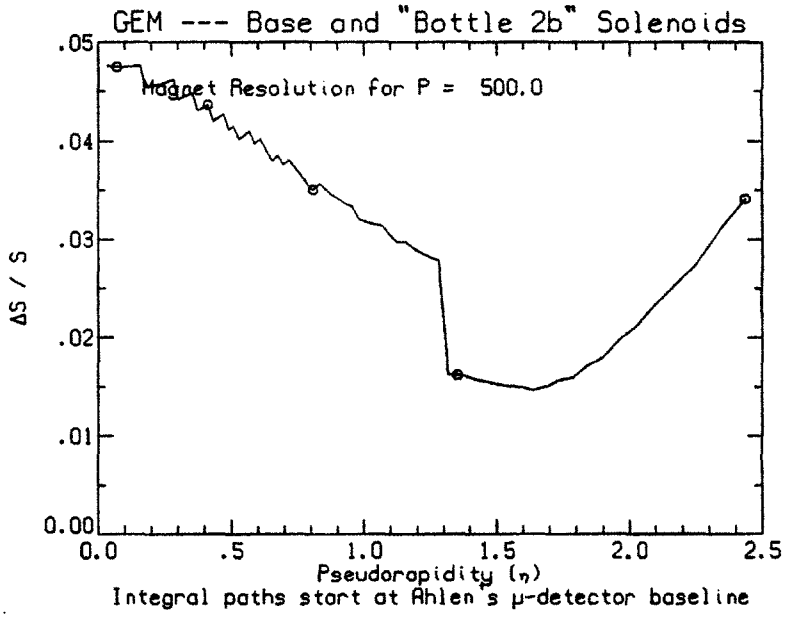

Figure 184: Resolution for constant P as a function of η.

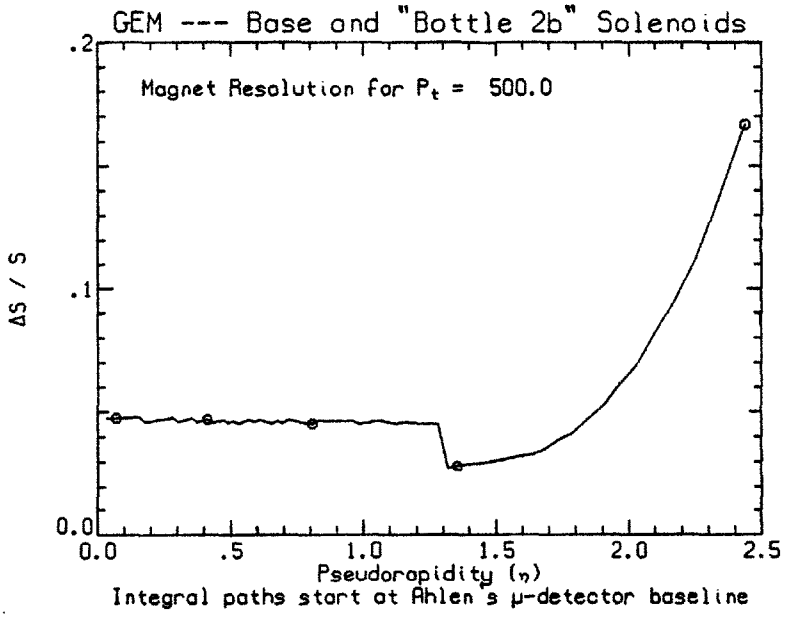

Figure 185: Resolution for constant P_t as a function of η.

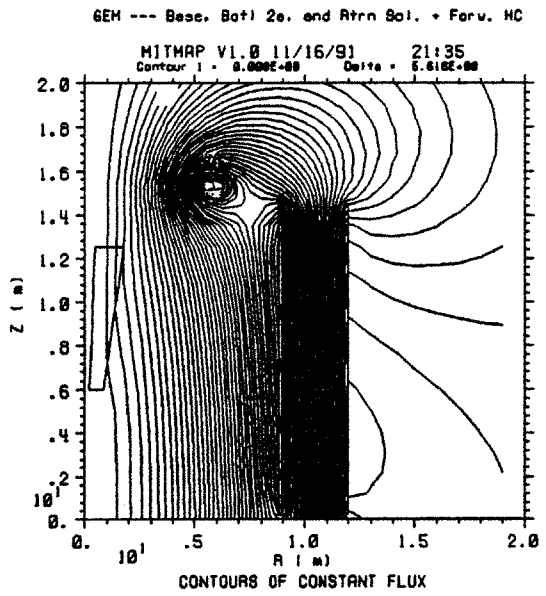

Figure 282: Flux lines superposed on a side view of the magnet design.

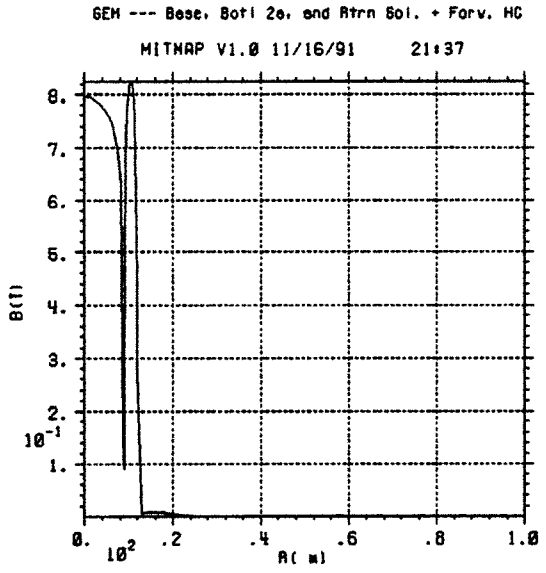

Figure 283: $|\vec{B}|$ versus radius in the hall.

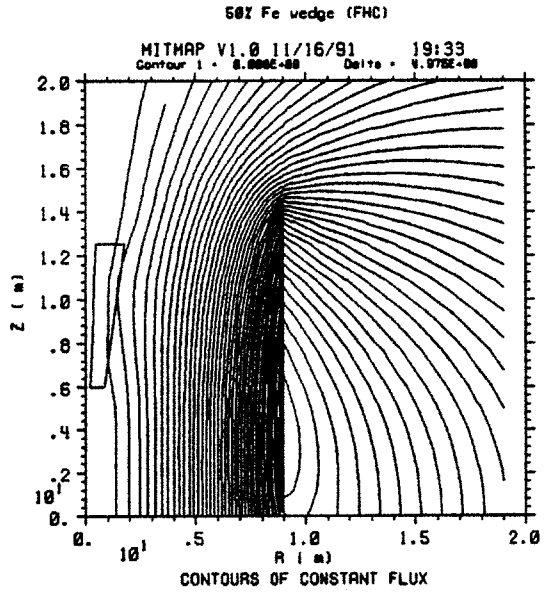

Figure 255: Flux lines superposed on a side view of the magnet design.

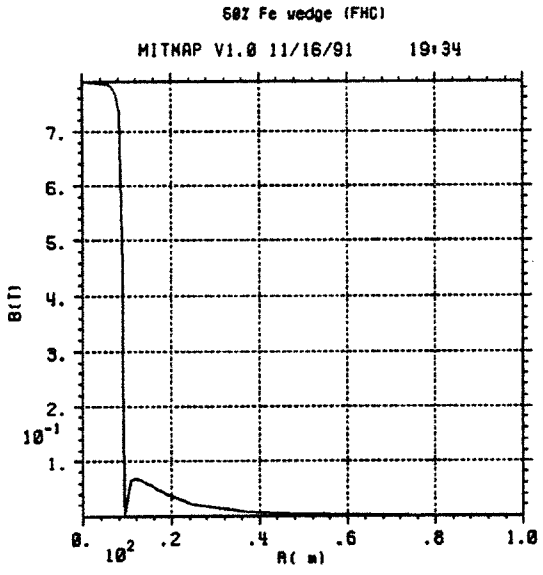

Figure 256: $|\vec{B}|$ versus radius in the hall.

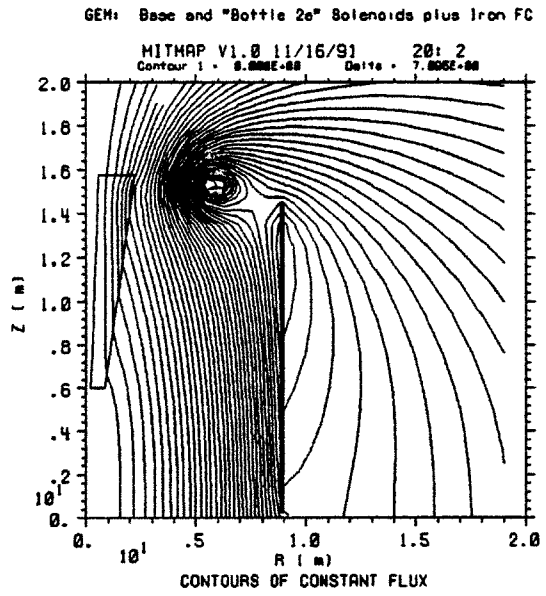

Figure 264: Flux lines superposed on a side view of the magnet design.

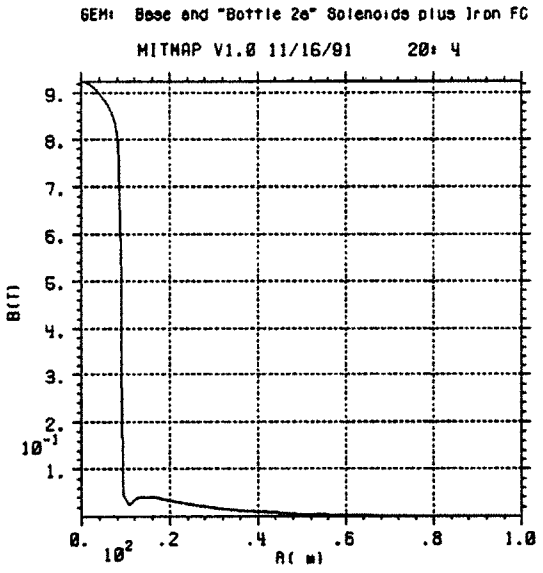

Figure 265: $|\vec{B}|$ versus radius in the hall.

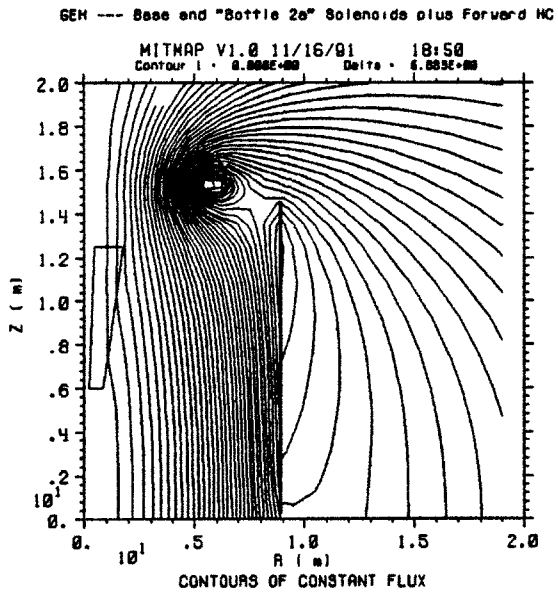

Figure 273: Flux lines superposed on a side view of the magnet design.

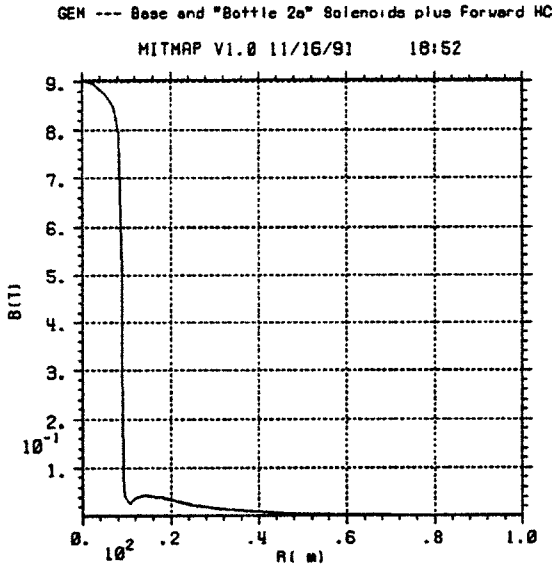

Figure 274: $|\vec{B}|$ versus radius in the hall.

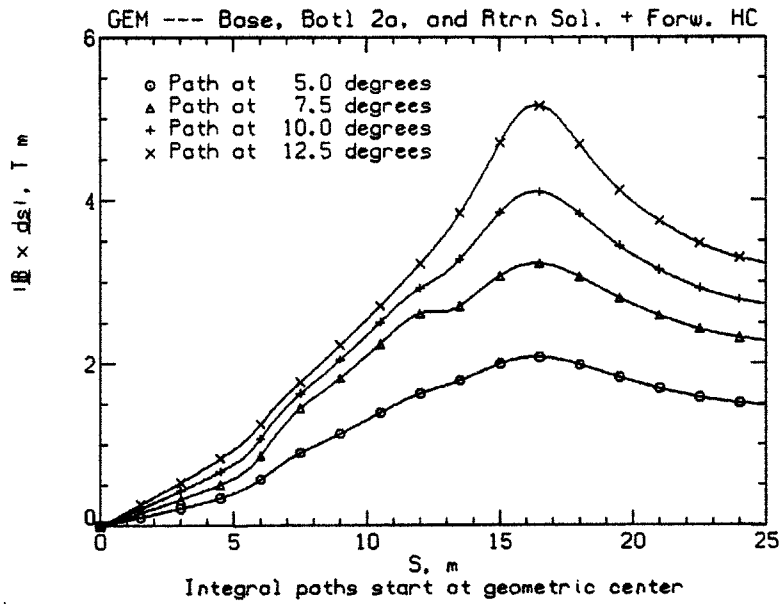

Figure 286: Plot of $|\vec{\mathcal{I}}|$ versus path length from the interaction point for tracks at 5, 7.5, 10, and 12.5° (from the beam line).

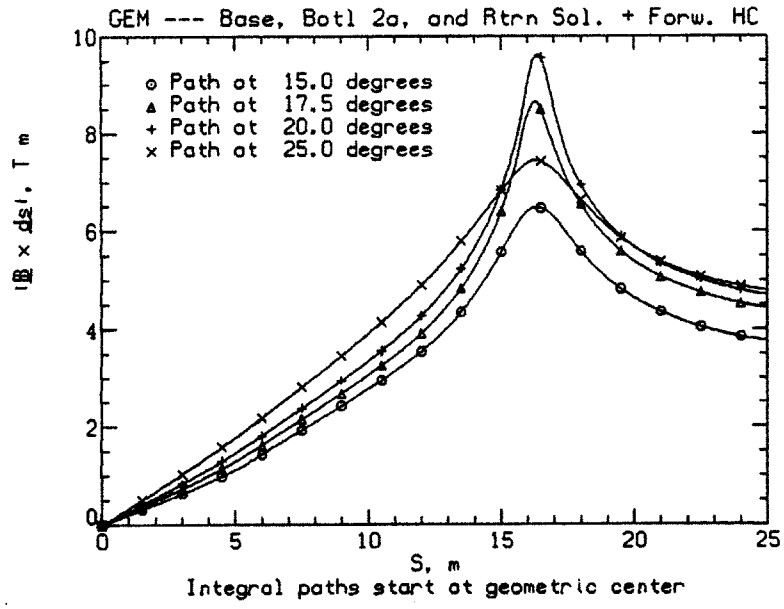

Figure 287: Plot of $|\vec{\mathcal{I}}|$ versus path length from the interaction point for tracks at 15, 17.5, 20, and 25° (from the beam line).

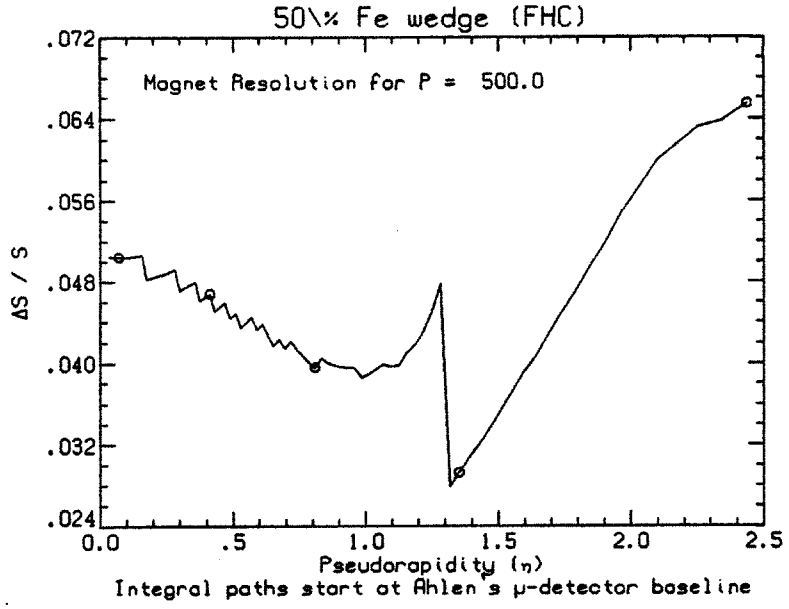

Figure 259: Resolution for constant P as a function of η.

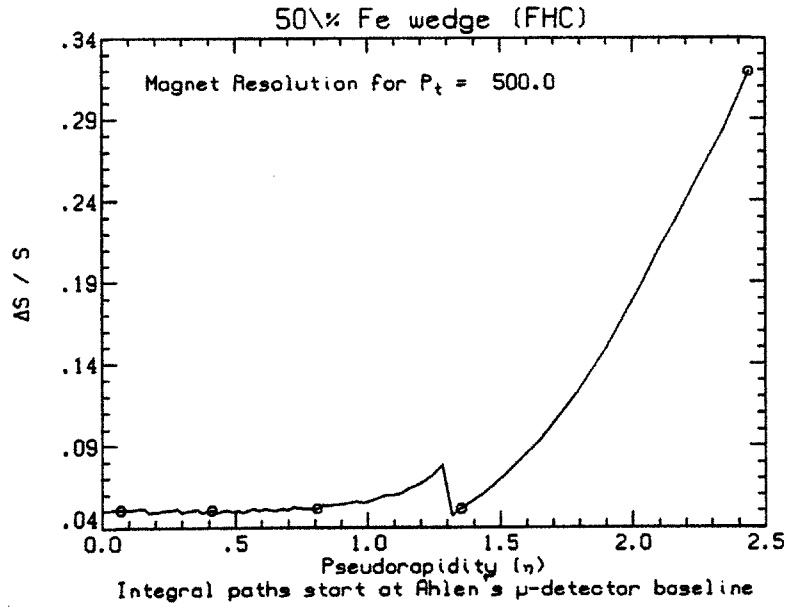

Figure 260: Resolution for constant P_t as a function of η.

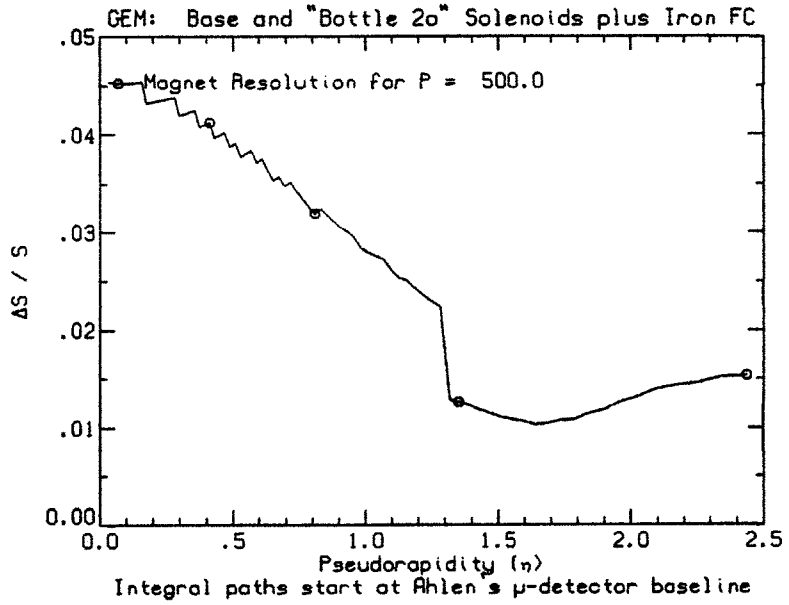

Figure 268: Resolution for constant P as a function of η.

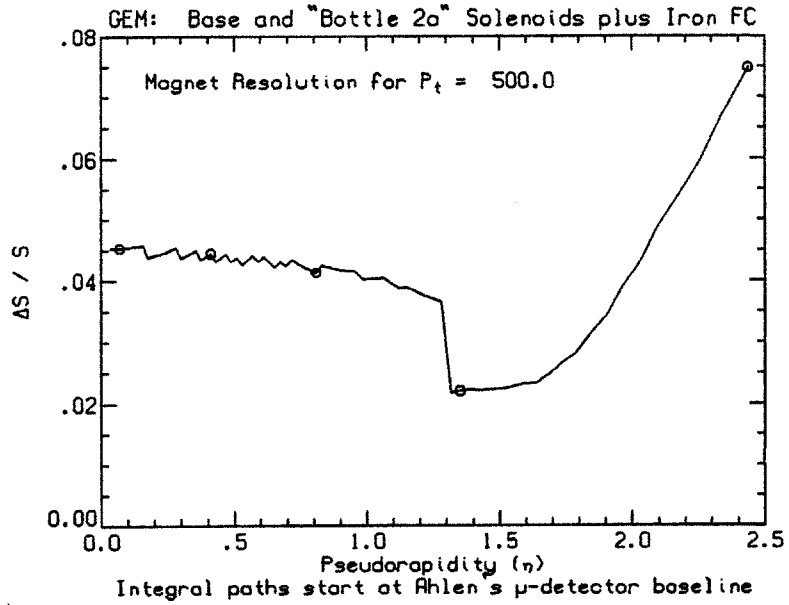

Figure 269: Resolution for constant P_t as a function of η.

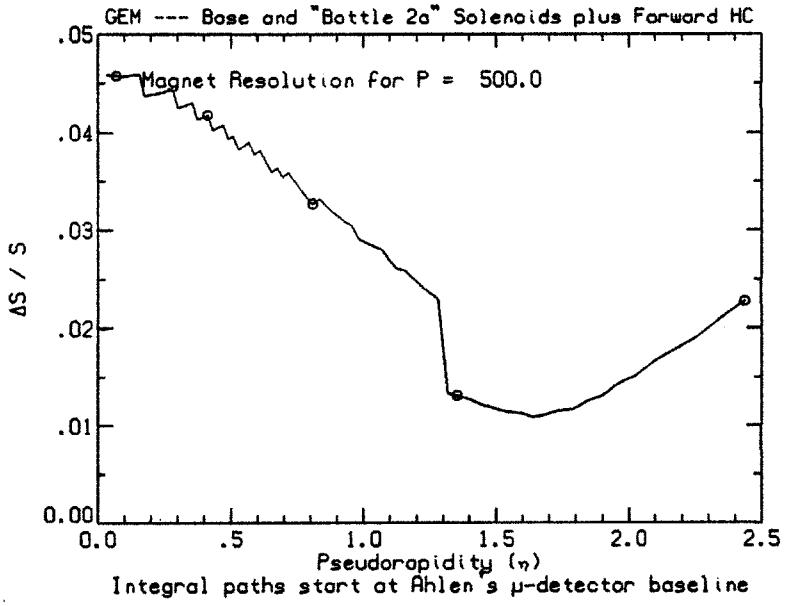

Figure 277: Resolution for constant P as a function of η.

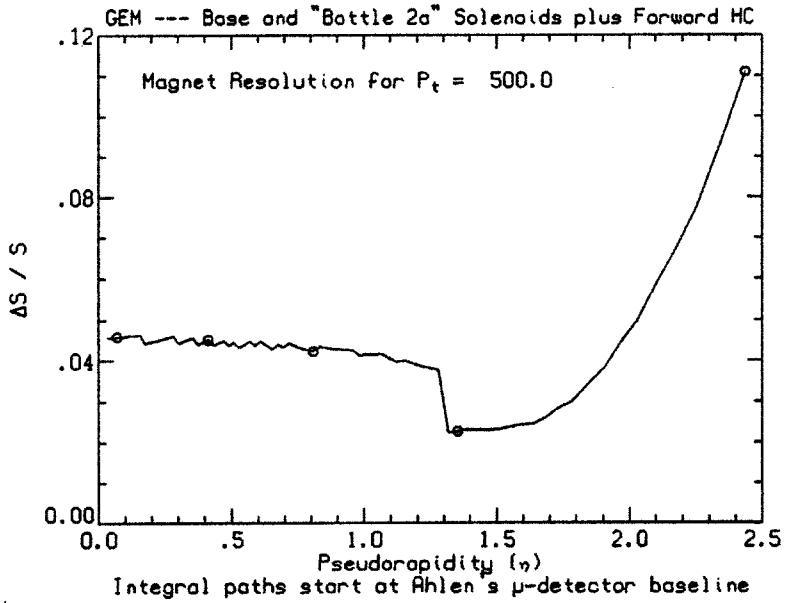

Figure 278: Resolution for constant P_t as a function of η.

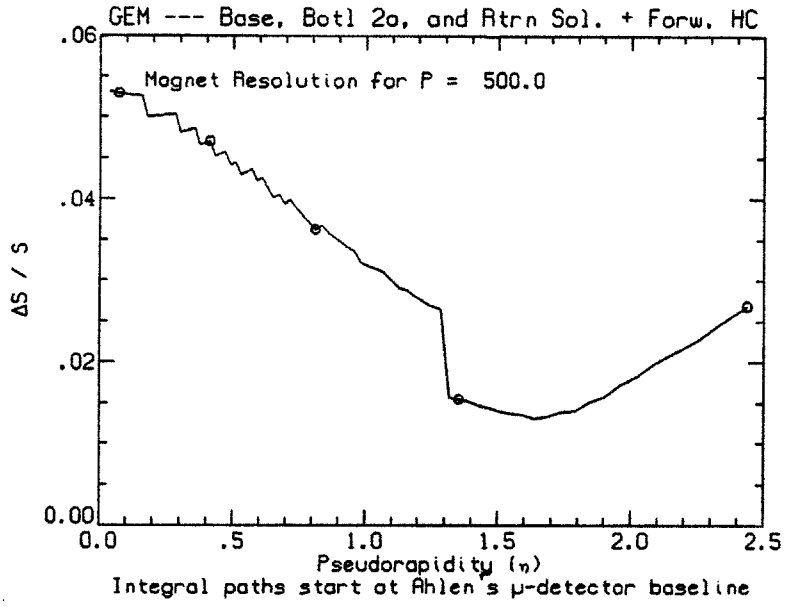

Figure 290: Resolution for constant P as a function of η.

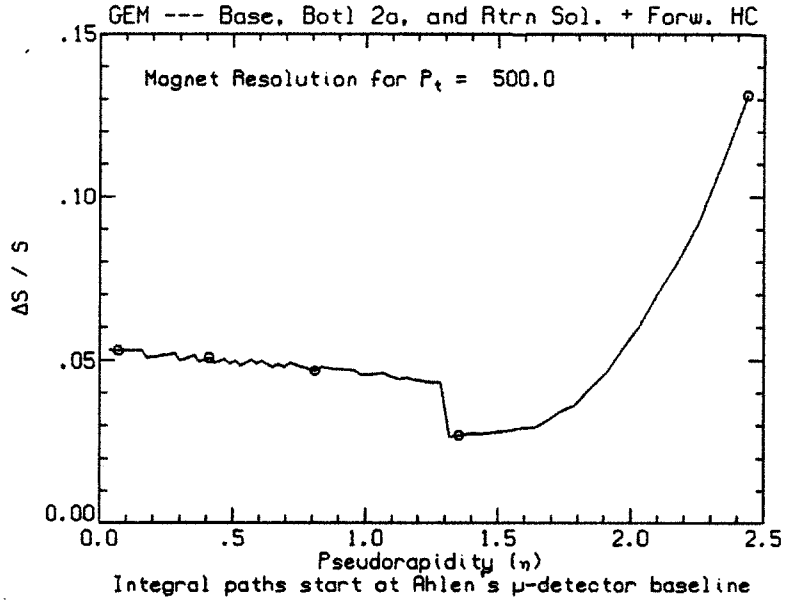

Figure 291: Resolution for constant P_t as a function of η.

A.3.3 Bottle with solid iron wedge

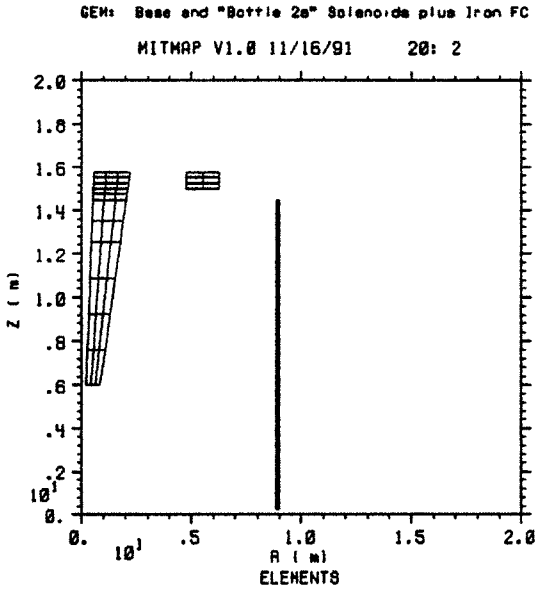

Figure 262: Side view of a superconducting solenoid with the end pole replaced by a superconducting bottle coil and with a solid iron wedge. Note that the beam axis (the z axis) is vertical on the page and the transverse (radial) axis is horizontal.

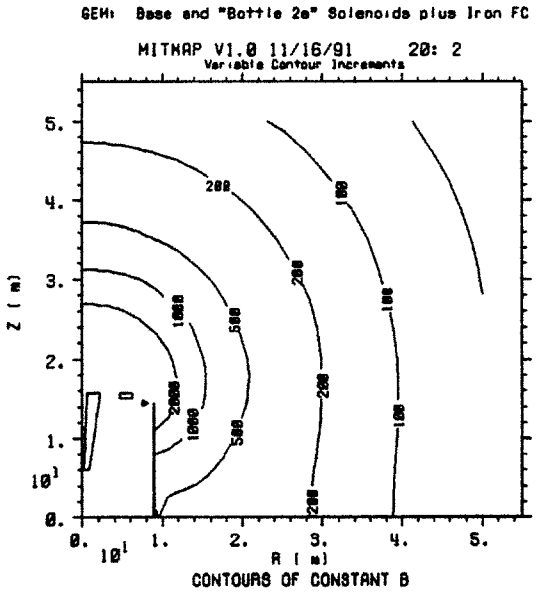

Figure 263: Contours of constant $|\vec{B}|$ superposed on a side view of the magnet; isopleths are labeled in gauss.

A.3.4 Bottle with 50% iron wedge

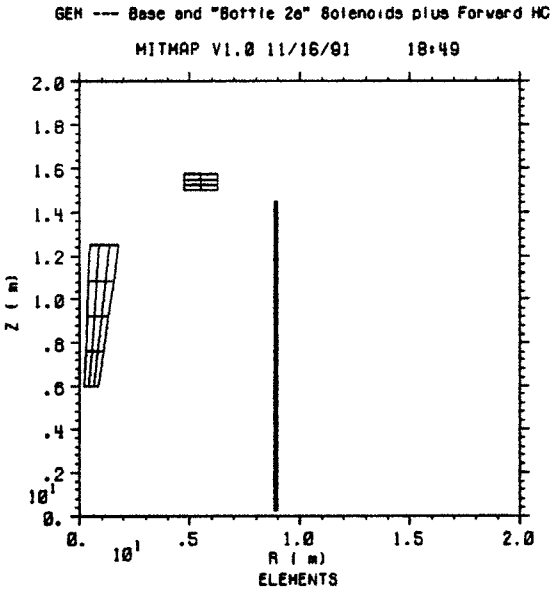

Figure 271: Side view of a superconducting solenoid with the end pole replaced by a superconducting coil and with a 50% iron wedge (calorimeter). Note that the beam axis (the z axis) is vertical on the page and the transverse (radial) axis is horizontal.

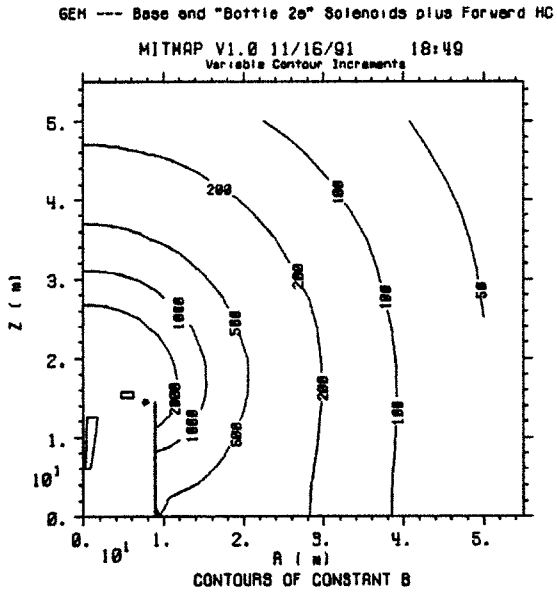

Figure 272: Contours of constant $|\vec{B}|$ superposed on a side view of the magnet; isopleths are labeled in gauss.

A.3.5 Bottle with return and 50% iron wedge

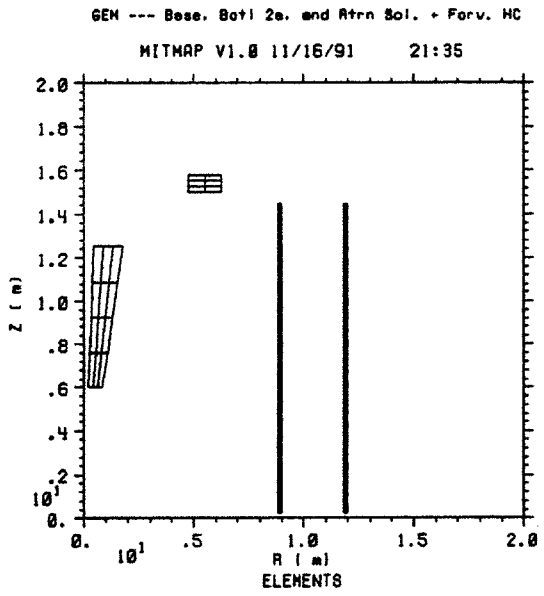

Figure 280: Side view of a superconducting solenoid with a superconducting return, with the end pole replaced by a superconducting coil, and with a 50% iron wedge (calorimeter). Note that the beam axis (the z axis) is vertical on the page and the transverse (radial) axis is horizontal.

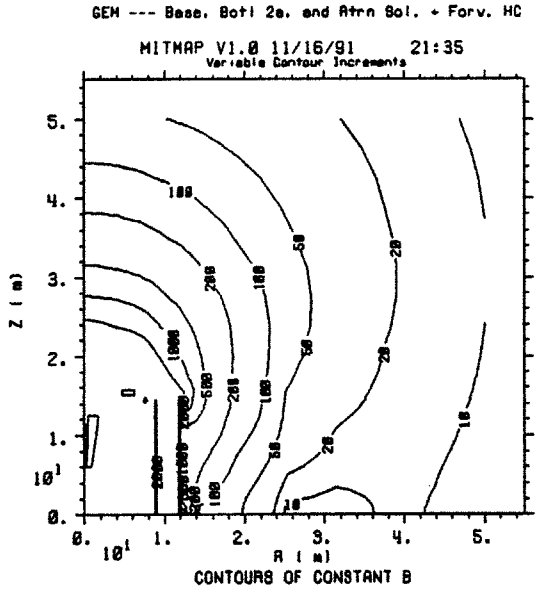

Figure 281: Contours of constant $|\vec{B}|$ superposed on a side view of the magnet; isopleths are labeled in gauss.

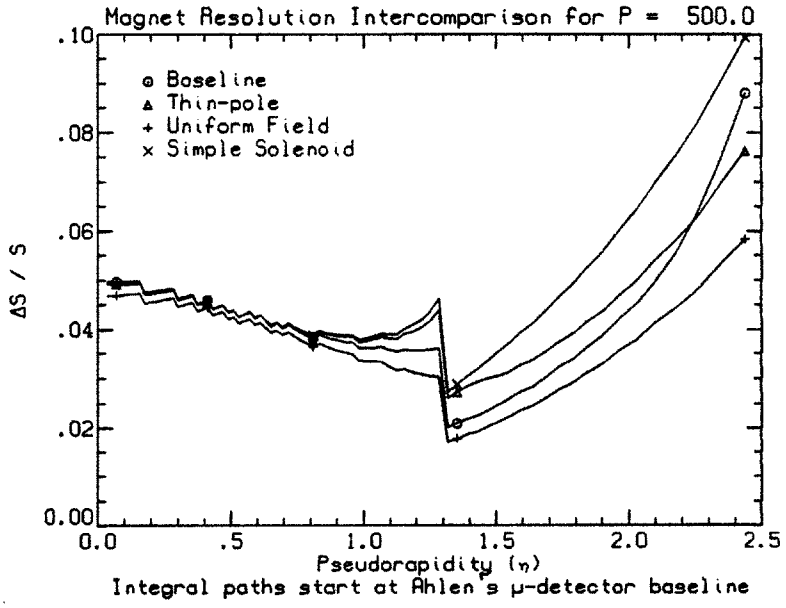

Figure 6: Comparison of the resolution of various magnet designs for constant P (500 GeV) as a function of η. The curve for a uniform field is marked with a $+$, that for a simple solenoid with $\times$, for EoI baseline $\bigcirc$, and for the LoI baseline $\triangle$.

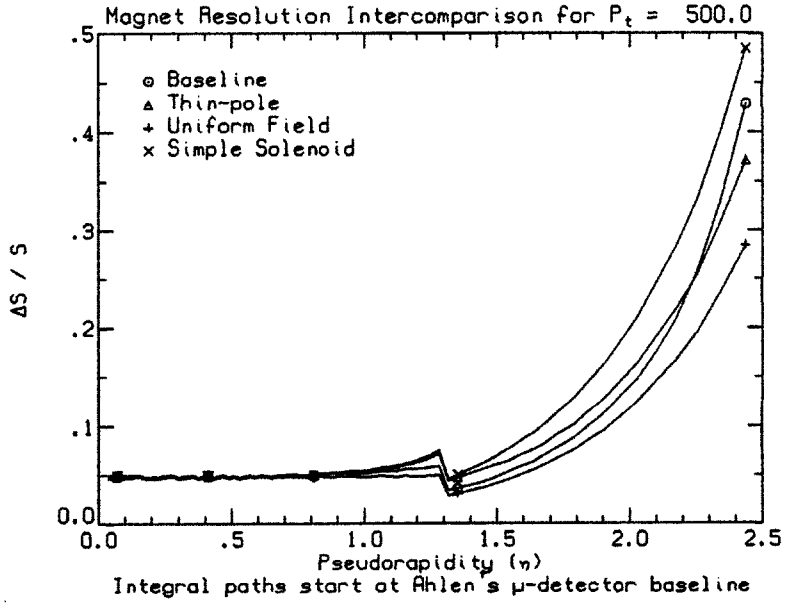

Figure 7: Comparison of the resolution of various magnet designs for constant P_t (500 GeV) as a function of η. The curve for a uniform field is marked with a $+$, that for a simple solenoid with $\times$, for EoI baseline $\bigcirc$, and for the LoI baseline $\triangle$.

2 Basis for Design Evaluation

In order to compare magnet designs fairly, the (momentum $\vec{p}$) resolution [4, 5],

$$\frac{\Delta p}{p} = \frac{\Delta p_t}{p_t} \equiv \frac{\Delta S}{S} \tag{1}$$

where $p = |\vec{p}|$, $p_t = |\vec{p}| \sin\theta$, and θ is the angle from the beam line, is computed as a function of angle (pseudorapidity[3]) given p. $S(\vec{p})$ is the sagitta given in eq. 9 and ΔS is the total uncertainty including measurement error σ_{meas} (cf. eq. 3), multiple scattering σ_{MS} (cf. eq. 4), and systematic error σ_{sys} (cf. eq. 5), e.g.,

$$\Delta S^2 = \sigma^2_{meas} + \sigma^2_{MS} + \sigma^2_{sys}. \tag{2}$$

The uncertainty in the resolution depends on the actual track (because the path length varies and the angle relative to the magnetic field changes). Thus, to compute S and ΔS a muon detector geometry must be defined, a suitable measure of the resolving power agreed upon, and adequate computer codes (software tools) made available.

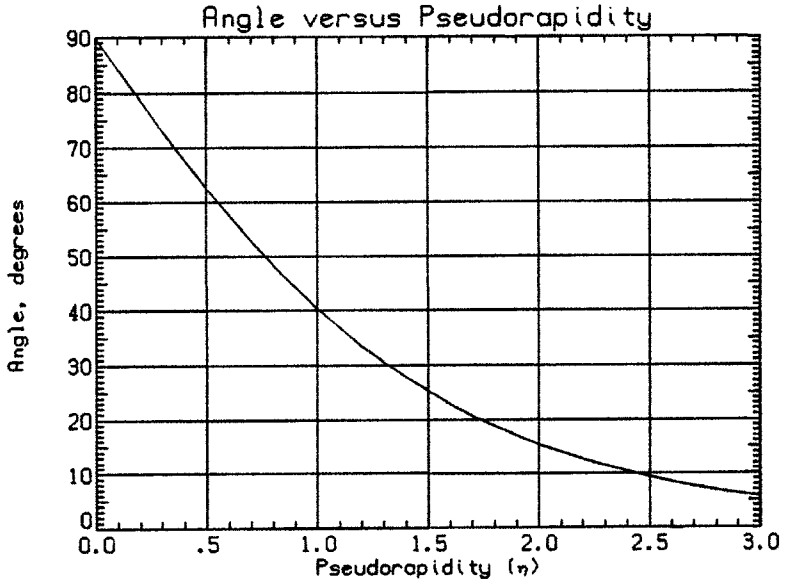

Figure 1: Reference curve: angle from the beamline versus pseudorapidity.

In general, for the results presented herein, the muon detector geometry is that shown in Figure 2 (given by S. Ahlen). The muon detectors are assumed to have a resolution σ_{layer} of 100 μm per layer, a thickness of 5 μm per layer, and a chamber layout of 8, 16, and 8 layers for the inner, central, and outer detector superlayers. Whence assuming equal spacing between superlayers and that $S = \zeta_{central} - \frac{(\zeta_{inner}+\zeta_{outer})}{2}$ where ζ is the position on a given superlayer,

$$\sigma^2_{meas} = \frac{1}{16}\sigma^2_{layer} + \frac{1}{4}\left(\frac{1}{8}\sigma^2_{layer} + \frac{1}{8}\sigma^2_{layer}\right) = \frac{1}{8}\sigma^2_{layer}. \tag{3}$$

[3]the symbol η is used for the pseudorapidity; $\eta \equiv -\ln \arctan(\theta/2)$ where θ is the (polar) angle from the beamline (cf. Figure 1 for a plot of $\theta(\eta)$).

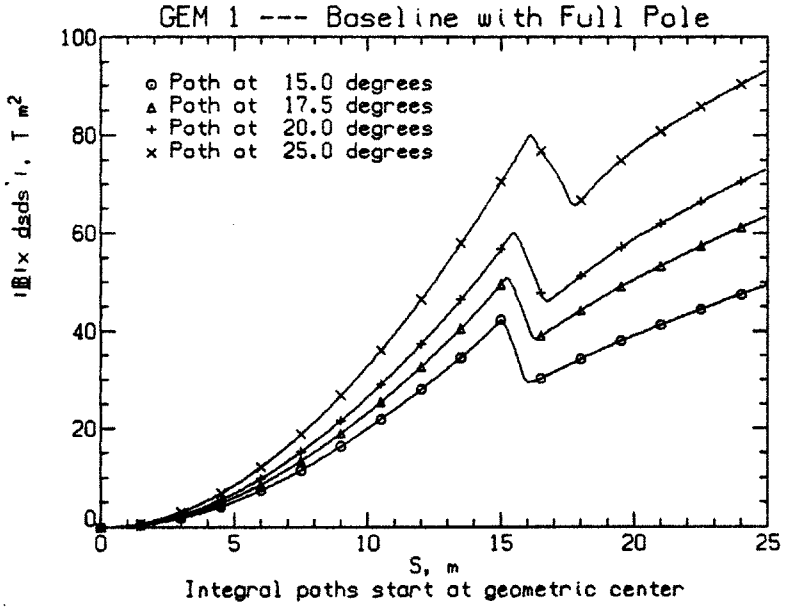

Figure 9: Plot of $|\vec{\mathcal{I}}|$ for the EoI baseline magnet versus path length from the interaction point for tracks at 15, 17.5, 20, and 25° (from the beam line).

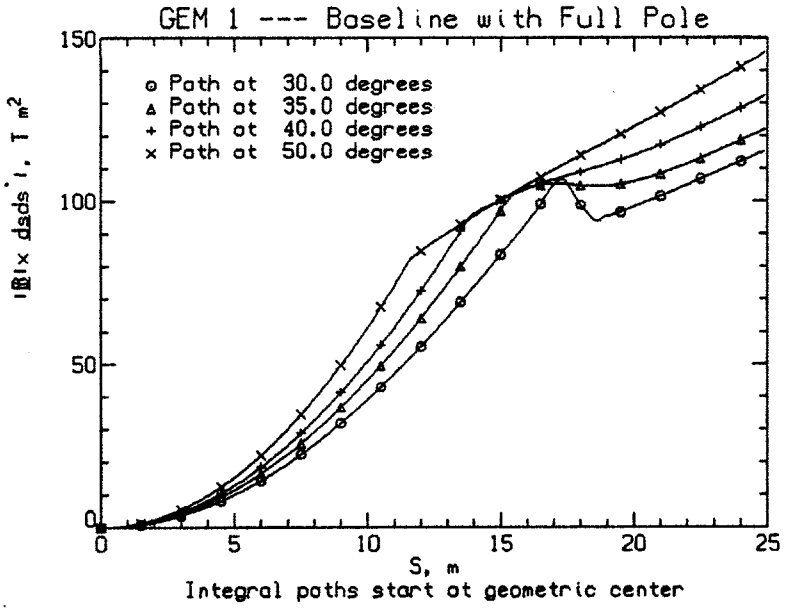

Figure 10: Plot of $|\vec{\mathcal{I}}|$ for the EoI baseline magnet versus path length from the interaction point for tracks at 30, 35, 40, and 50° (from the beam line).

The impulse between two points is a good figure of merit when considering angular change, e.g., Nier type mass spectrometer as $\Delta\vec{p} = \vec{\mathcal{I}}$ or $\Delta p_\perp = |\vec{\mathcal{I}}|$. Further, the second integral which we call $\mathcal{BL}^2$ is given by[5]:

$$\mathcal{BL}^2 \equiv 2\left|\int_0^L \int_0^s \vec{B} \times d\vec{\ell} ds\right|. \tag{8}$$

$\mathcal{BL}^2$ is a good figure of merit for linear displacements, e.g., radius of curvature or sagitta S

$$S = \frac{0.3}{8|\vec{p}|}\mathcal{BL}^2 = \frac{0.3\sin\theta}{8p_t}\mathcal{BL}^2. \tag{9}$$

Both $|\vec{\mathcal{I}}|$, sometimes referred to as BL, and $\mathcal{BL}^2$ are used as the situation dictates for comparing magnet designs.[6]

Over the years, an extensive software toolbox has been brought together at the PFC. This analysis toolbox includes

- Magnet codes [8, 9]
- Trajectory following codes upgraded from Astromag[7], SIAM[8], and L* [1]
- Error analysis codes including measurement, systematic, and multiple scattering uncertainties and the possibility of arbitrary physical structures, e.g., calorimeters, can be handled.
- Graphical [10] and/or tabular output

In addition, various commercial codes (e.g., ANSYS [11] for finite element analysis) are readily available but these are not used for most of what is reported herein.

3 Overview

Detailed plots for each design option are presented in subsections of Appendix A. The principal design options are discussed in the following sections

- GEM baseline and design options varying the pole pieces — Section 4
- Fringe field shielding (Safety/Environmental) — Section 5
- Small angle options — Section 6

A separate report on fringe field shielding for operations is in preparation; it includes analysis of forces and torques [12], of quadrupole shielding (need for current sheet), of counting room shield, etc.

[5]The factor of 2 in the definition of $\mathcal{BL}^2$ is included to agree with the naive results for a uniform field.

[6]Note that in general $\mathcal{BL}^2 \neq B_\perp L^2$ and $|\vec{\mathcal{I}}| \neq B_\perp L$.

[7]Astromag was a magnet facility planned for Space Station Freedom and intended principally for cosmic ray studies

[8]A balloon-borne cosmic ray isotope experiment

A.1.7 LoI baseline: Thin pole case 5

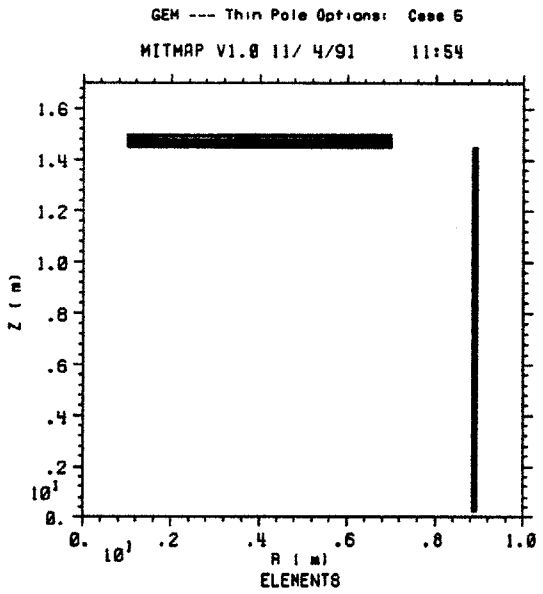

Figure 93: Side view of a superconducting solenoid with a thin pole, case #5. Note that the beam axis (the z axis) is vertical on the page and the transverse (radial) axis is horizontal.

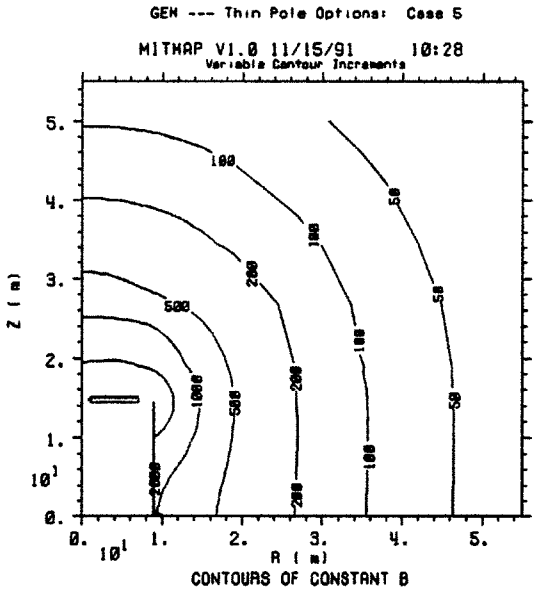

Figure 94: Contours of constant $|\vec{B}|$ superposed on a side view of the magnet; isopleths are labeled in gauss.

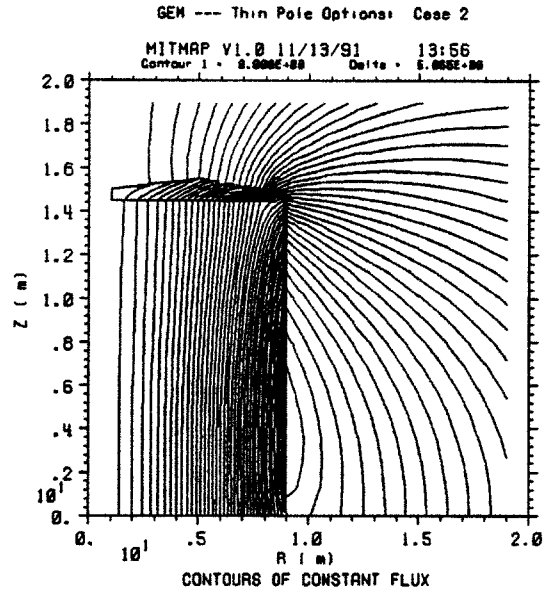

Figure 66: Flux lines superposed on a side view of the magnet design.

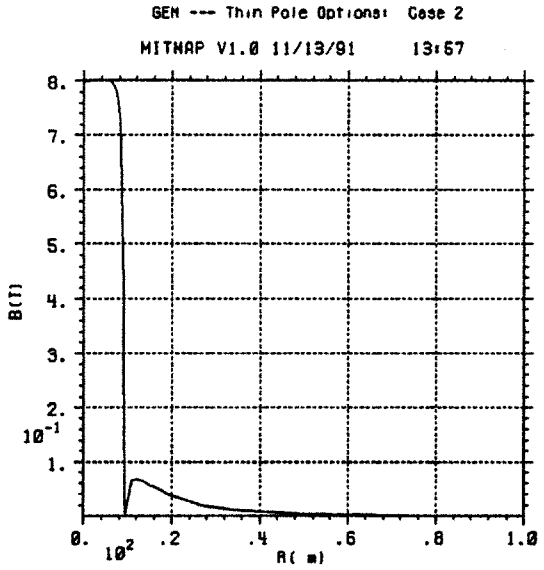

Figure 67: $|\vec{B}|$ versus radius in the hall.

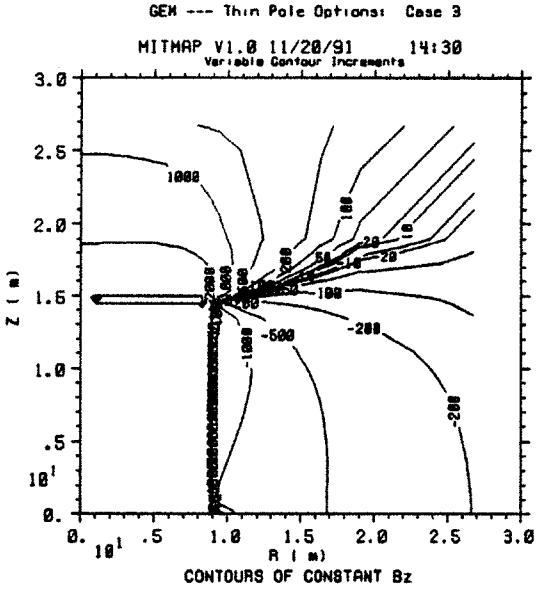

Figure 75: Contours of constant B_z superposed on a side view of the magnet; isopleths are labeled in gauss.

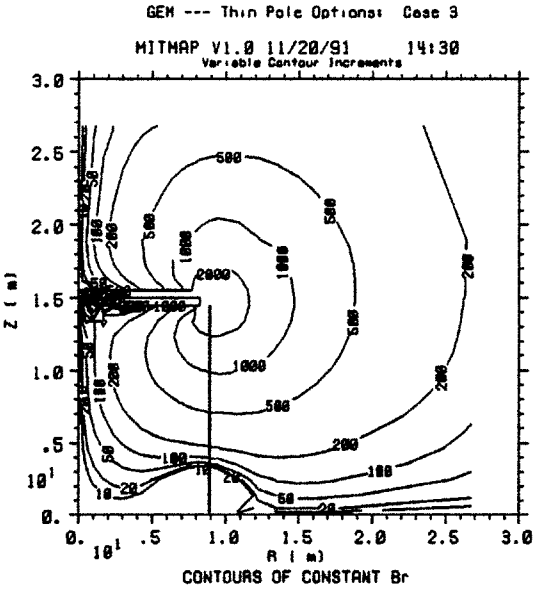

Figure 76: Contours of constant B_r superposed on a side view of the magnet; isopleths are labeled in gauss.

A.1.6 Thin pole case 4

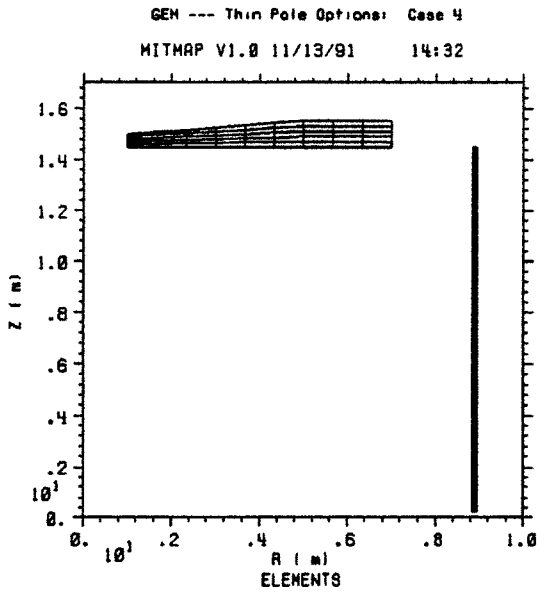

Figure 84: Side view of a superconducting solenoid with a thin pole, case #4. Note that the beam axis (the z axis) is vertical on the page and the transverse (radial) axis is horizontal.

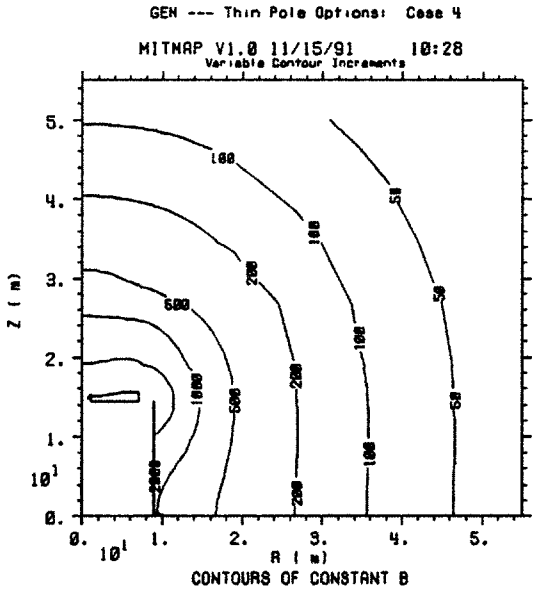

Figure 85: Contours of constant $|\vec{B}|$ superposed on a side view of the magnet; isopleths are labeled in gauss.

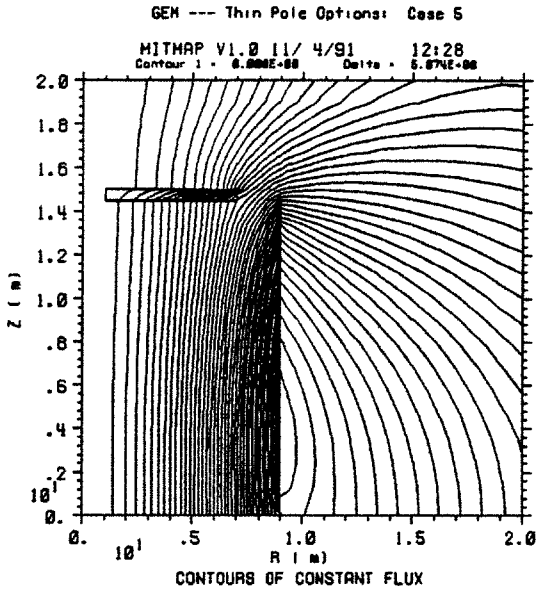

Figure 97: Flux lines superposed on a side view of the magnet design.

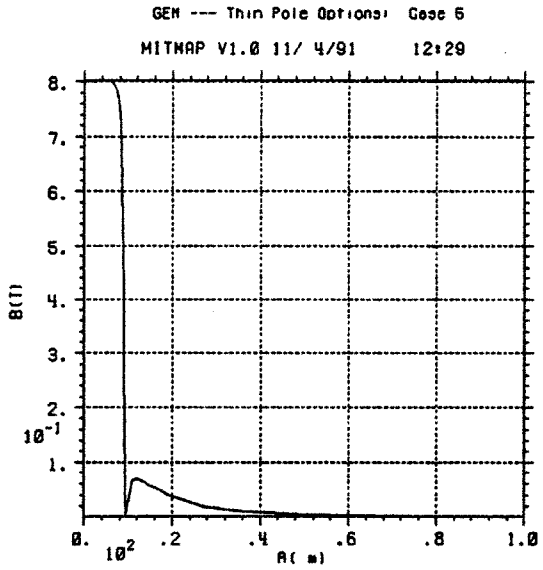

Figure 98: $|\vec{B}|$ versus radius in the hall.

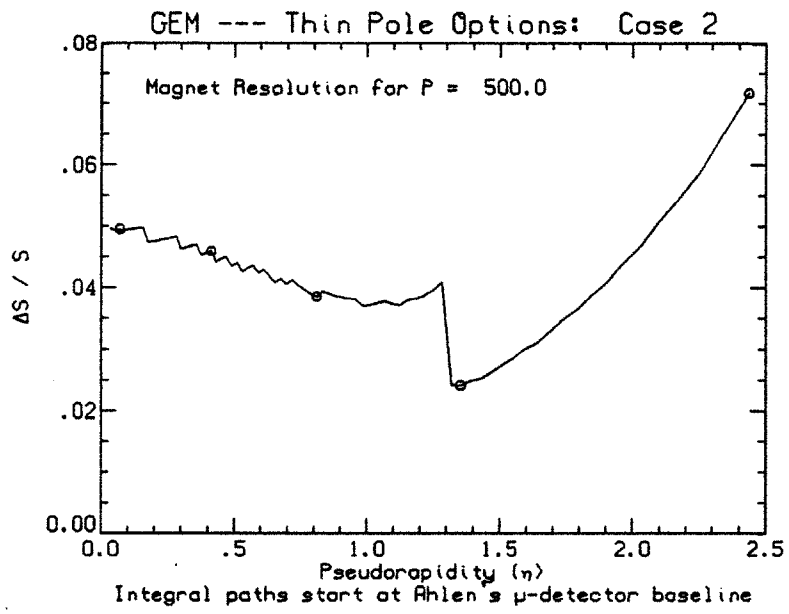

Figure 70: Resolution for constant P as a function of η.

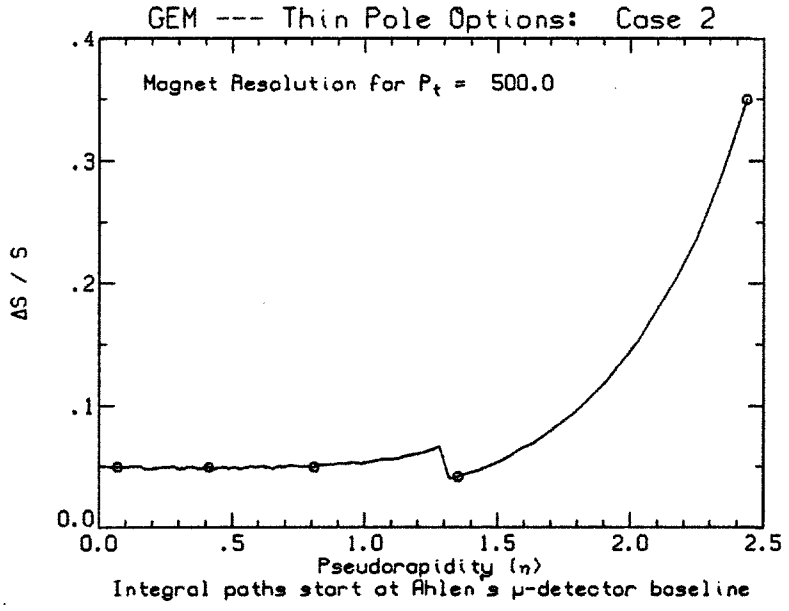

Figure 71: Resolution for constant P_t as a function of η.

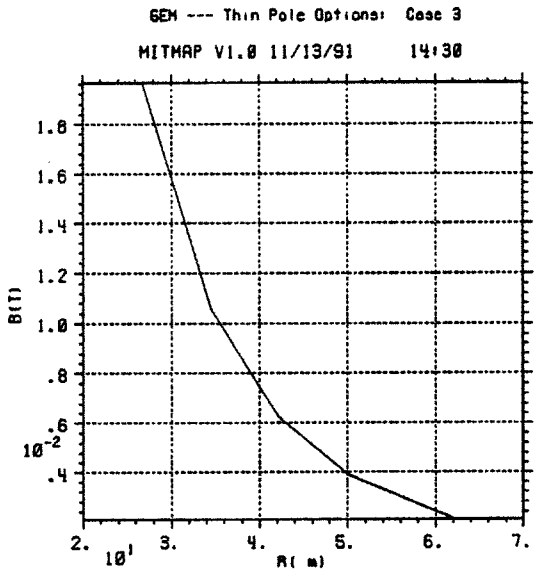

Figure 79: $|\vec{B}|$ versus radius near the surface.

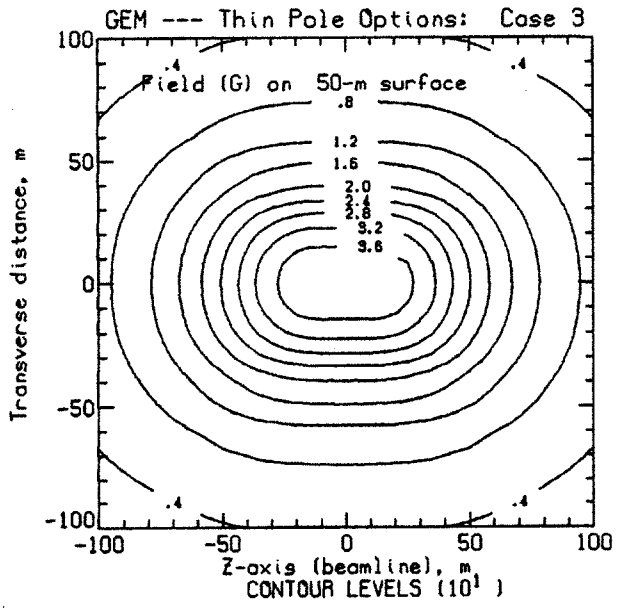

Figure 80: Isogauss contours of the field on a surface at a nominal elevation of 50 m above the beamline (centerline).

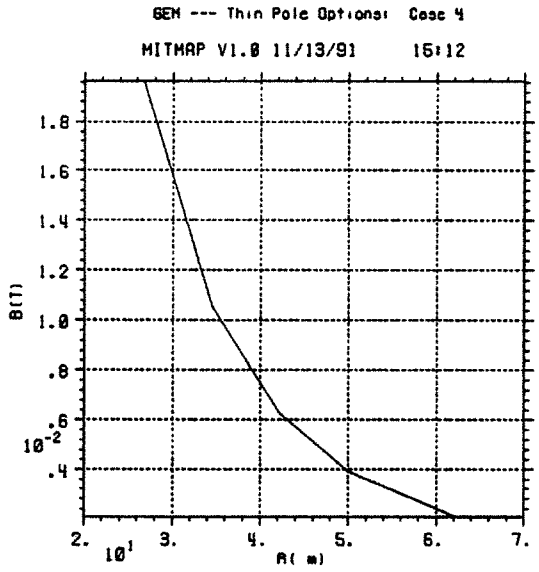

Figure 88: $|\vec{B}|$ versus radius near the surface.

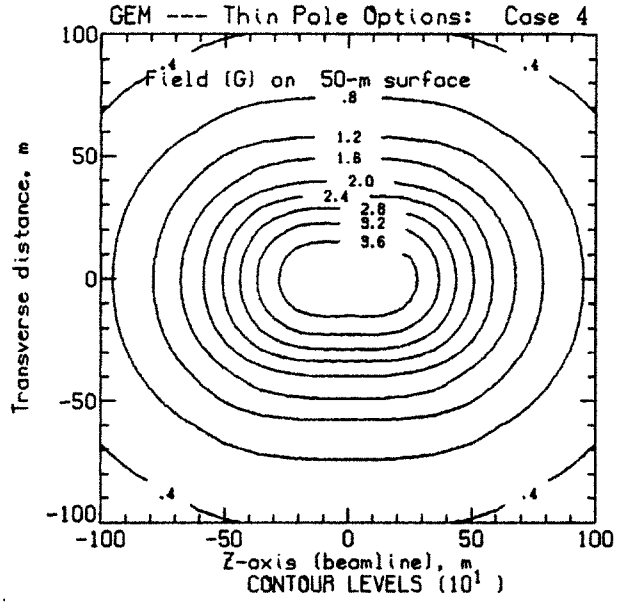

Figure 89: Isogauss contours of the field on a surface at a nominal elevation of 50 m above the beamline (centerline).

A.2.3 Complex pole pieces

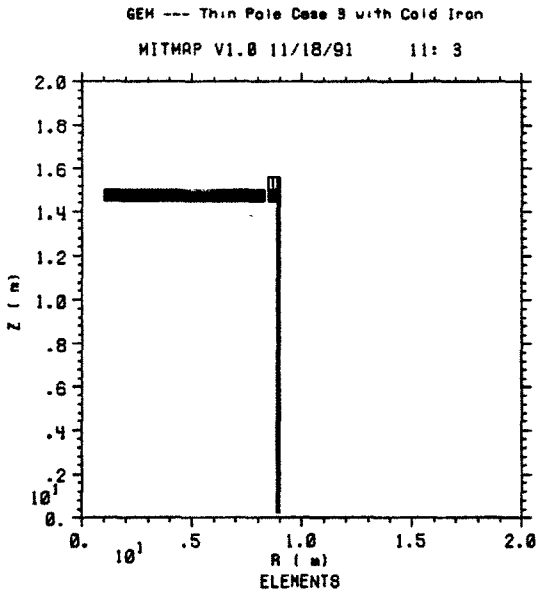

Figure 187: Side view of a superconducting solenoid with a block of iron within the cryostat. Note that the beam axis (the z axis) is vertical on the page and the transverse (radial) axis is horizontal.

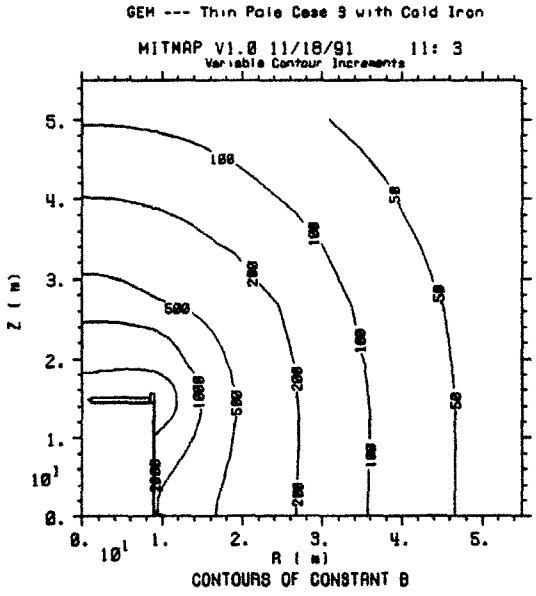

Figure 188: Contours of constant $|\vec{B}|$ superposed on a side view of the magnet; isopleths are labeled in gauss.

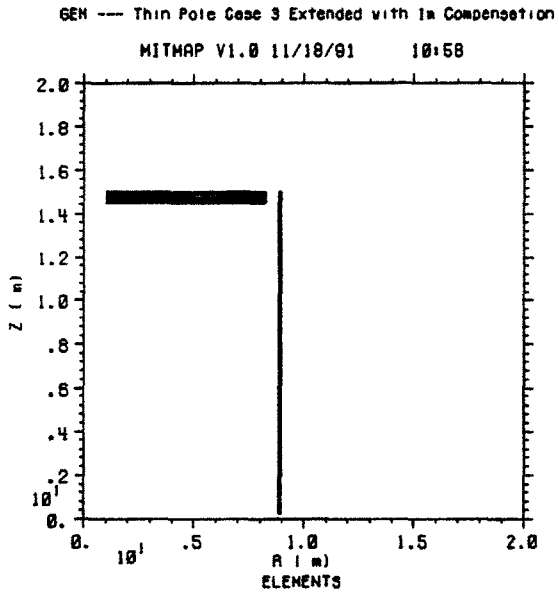

Figure 159: Side view of a superconducting solenoid with the conductor extended over the pole piece and with the current doubled in the last 1 m. Note that the beam axis (the z axis) is vertical on the page and the transverse (radial) axis is horizontal.

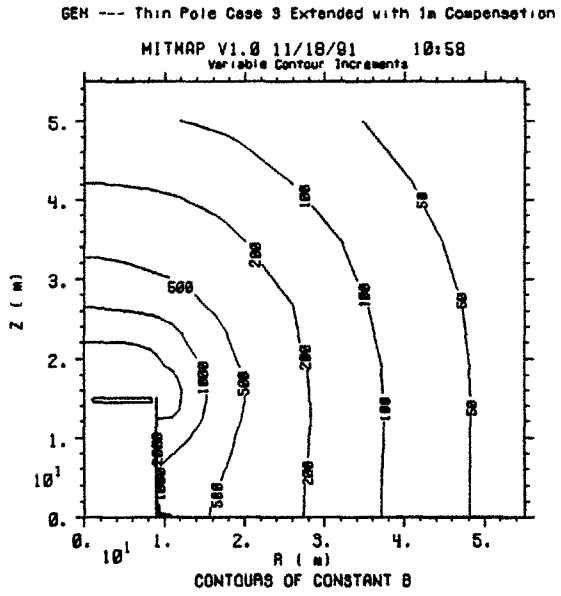

Figure 160: Contours of constant $|\vec{B}|$ superposed on a side view of the magnet; isopleths are labeled in gauss.

A.2.2 Bottle Solenoids

The "bottle" solenoid for Figures 169–177 has a larger current than that in Figures 178–186.

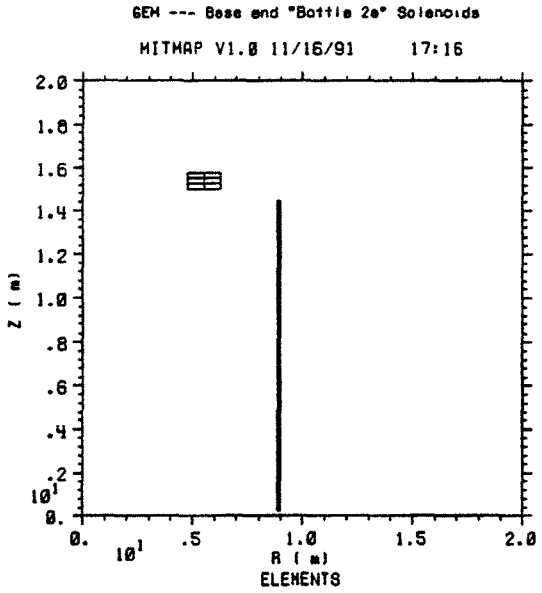

Figure 169: Side view of a superconducting solenoid with the end pole replaced by a superconducting solenoid. The "bottle" current is 133% of that for the case in Figures 178–186. Note that the beam axis (the z axis) is vertical on the page and the transverse (radial) axis is horizontal.

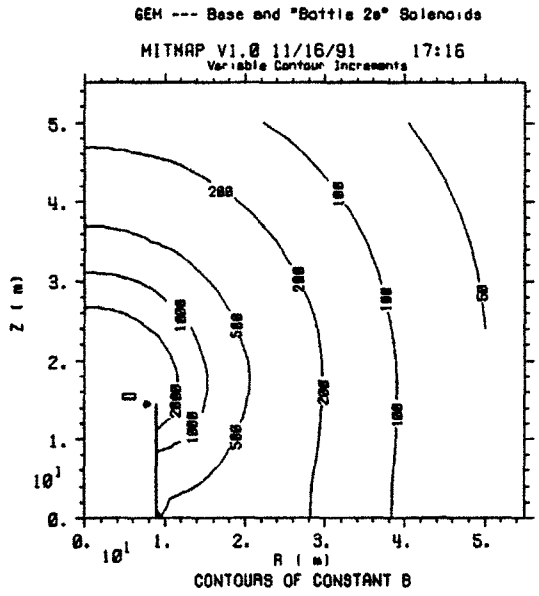

Figure 170: Contours of constant $|\vec{B}|$ superposed on a side view of the magnet design.

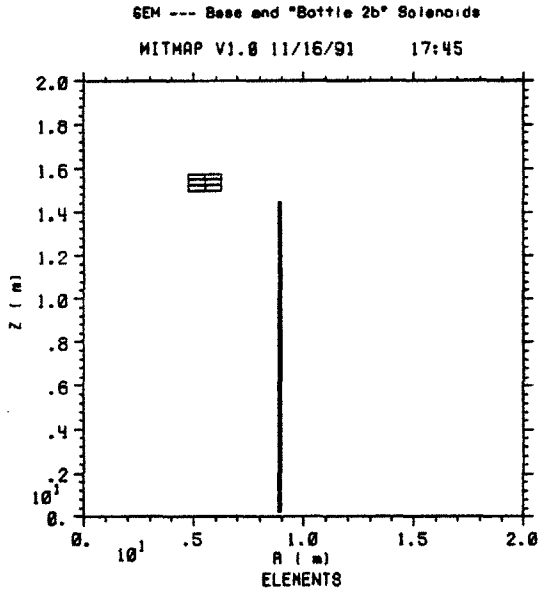

Figure 178: Side view of a superconducting solenoid with the end pole replaced by a superconducting solenoid. The "bottle" current is 75% of that for the case in Figures 169–177. Note that the beam axis (the z axis) is vertical on the page and the transverse (radial) axis is horizontal.

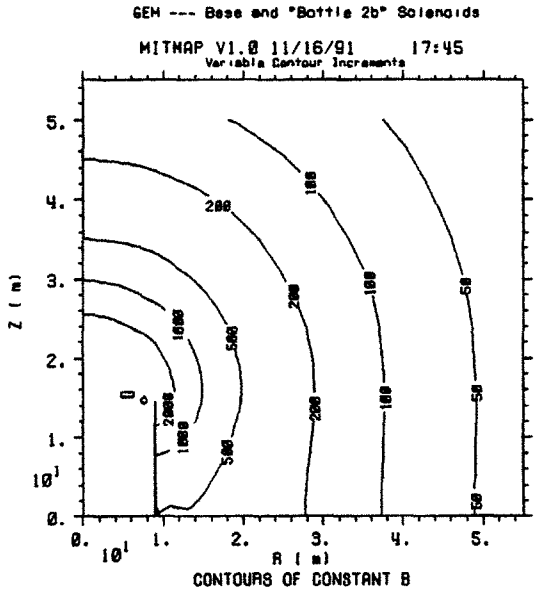

Figure 179: Contours of constant $|\vec{B}|$ superposed on a side view of the magnet design.

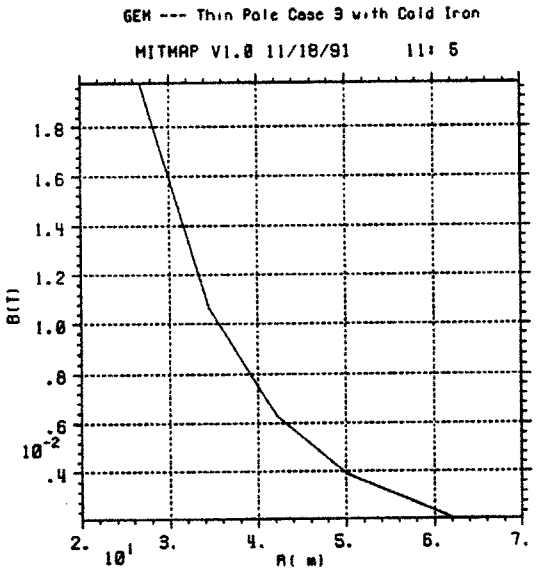

Figure 191: $|\vec{B}|$ versus radius near the surface.

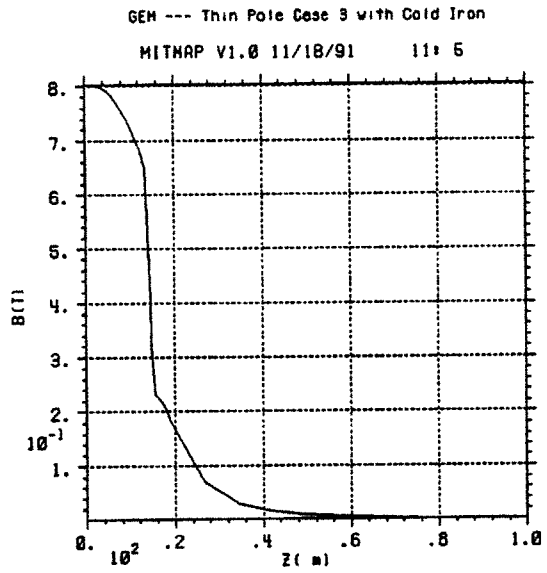

Figure 192: $|\vec{B}|$ versus z on axis in the hall.

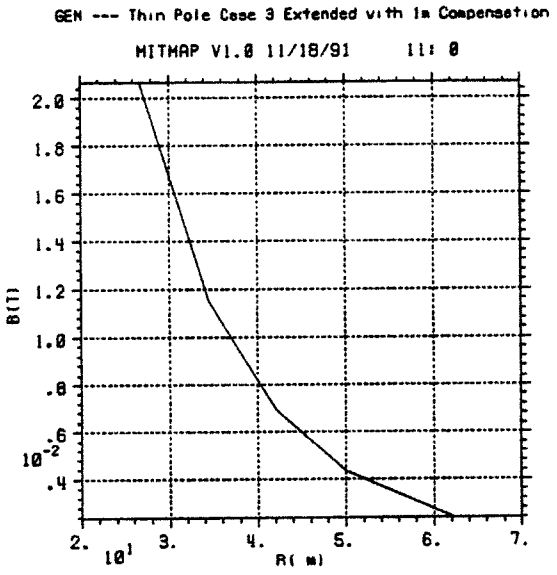

Figure 163: $|\vec{B}|$ versus radius near the surface.

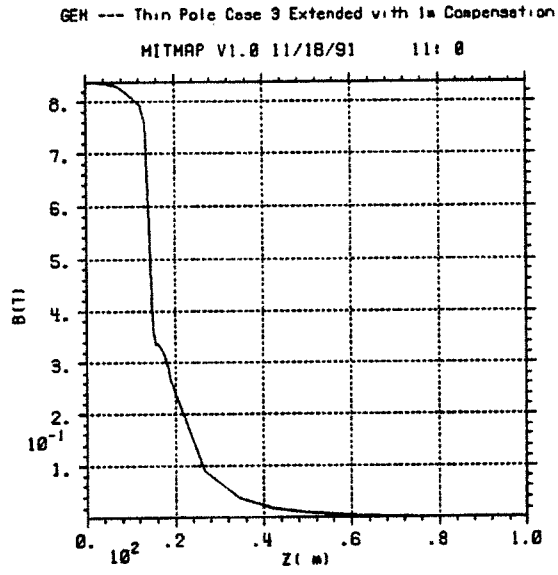

Figure 164: $|\vec{B}|$ versus z on axis in the hall.

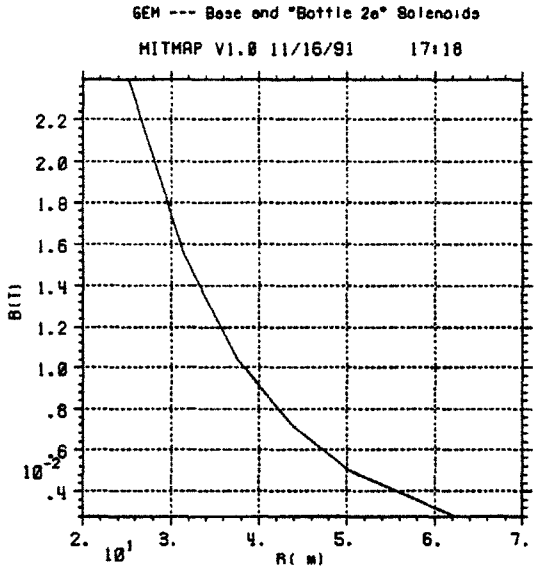

Figure 173: $|\vec{B}|$ versus radius near the surface.

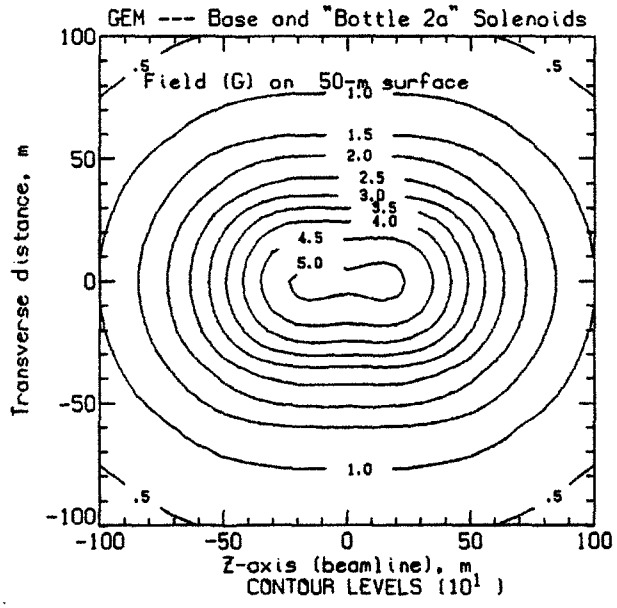

Figure 174: Isogauss contours of the field on a surface at a nominal elevation of 50 m above the beamline (centerline).

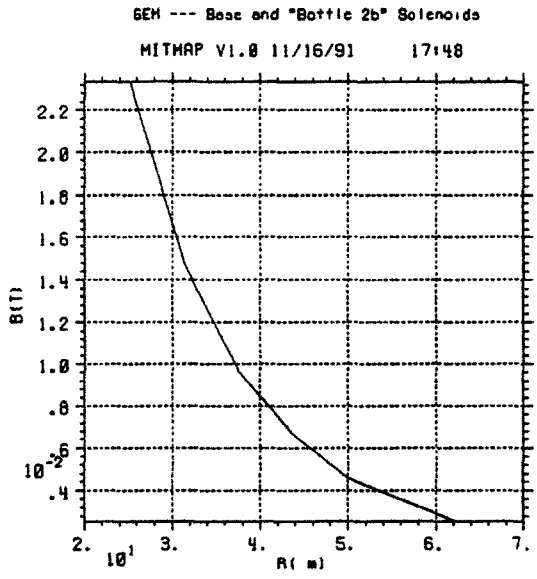

Figure 182: $|\vec{B}|$ versus radius near the surface.

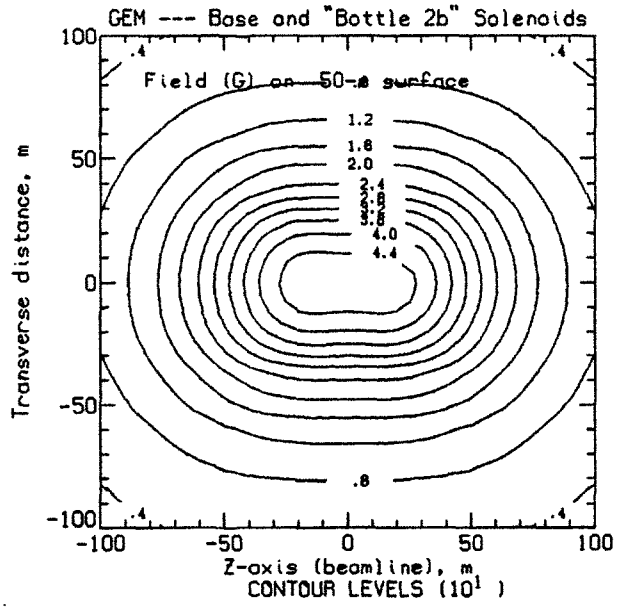

Figure 183: Isogauss contours of the field on a surface at a nominal elevation of 50 m above the beamline (centerline).

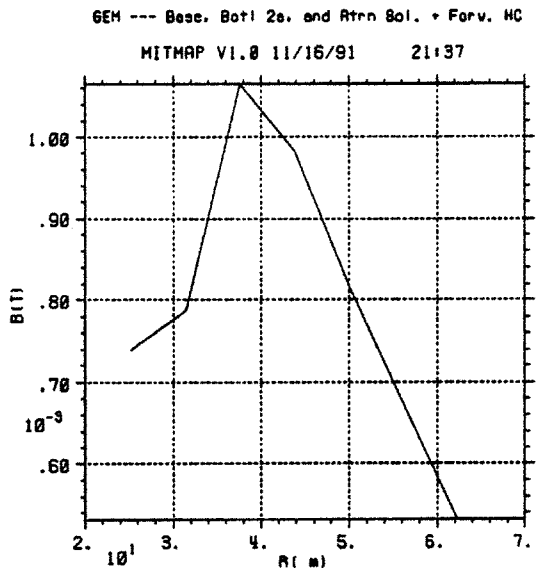

Figure 284: $|\vec{B}|$ versus radius near the surface.

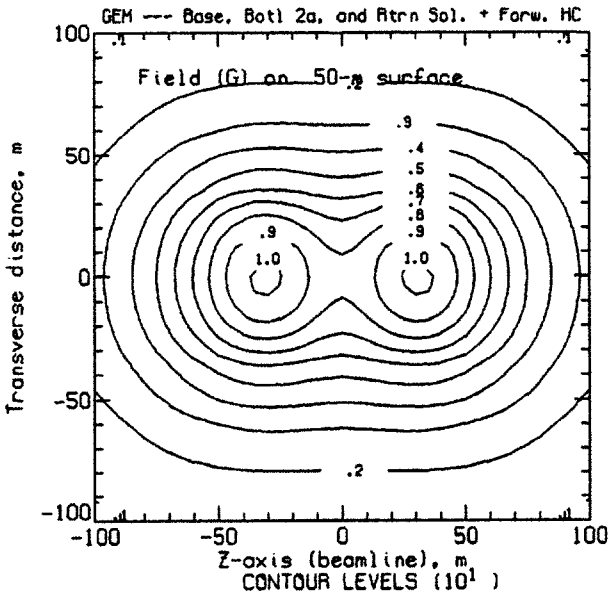

Figure 285: Isogauss contours of the field on a surface at a nominal elevation of 50 m above the beamline (centerline).

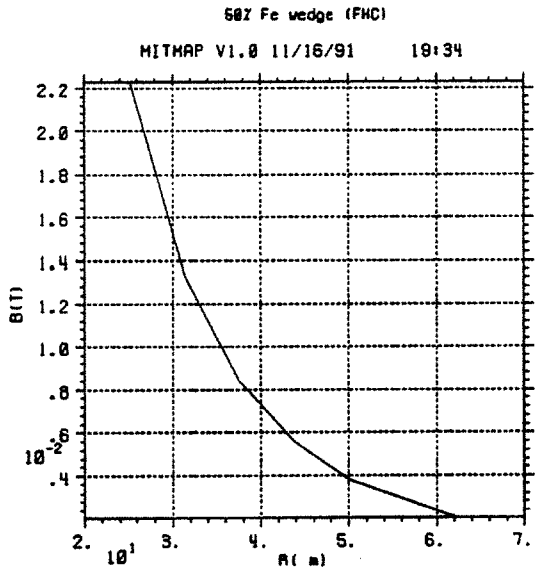

Figure 257: $|\vec{B}|$ versus radius near the surface.

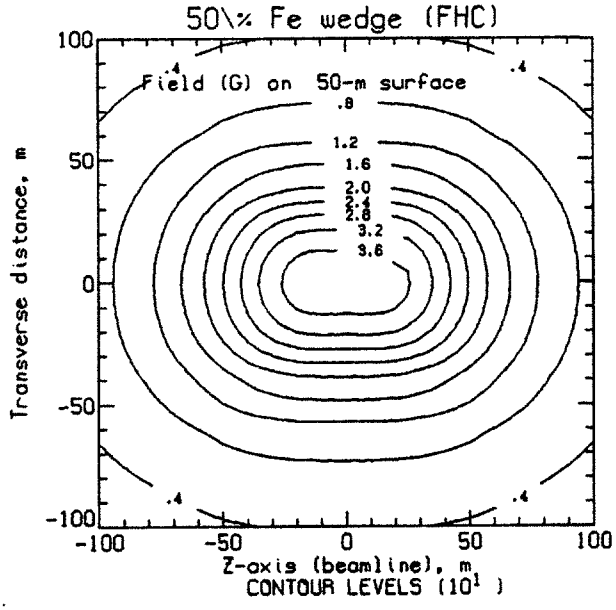

Figure 258: Isogauss contours of the field on a surface at a nominal elevation of 50 m above the beamline (centerline).

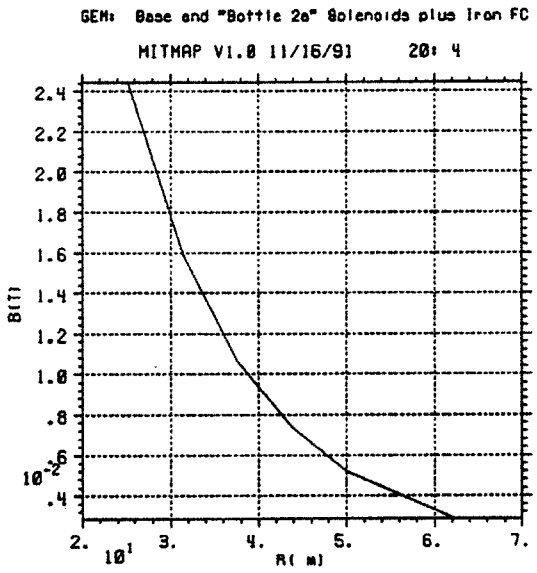

Figure 266: $|\vec{B}|$ versus radius near the surface.

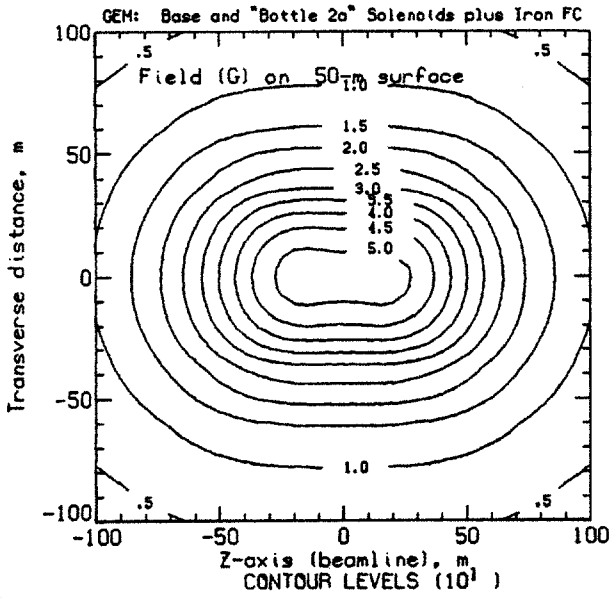

Figure 267: Isogauss contours of the field on a surface at a nominal elevation of 50 m above the beamline (centerline).

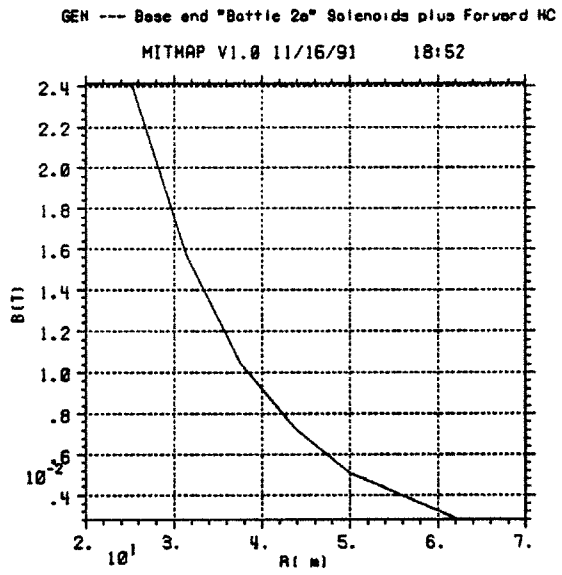

Figure 275: $|\vec{B}|$ versus radius near the surface.

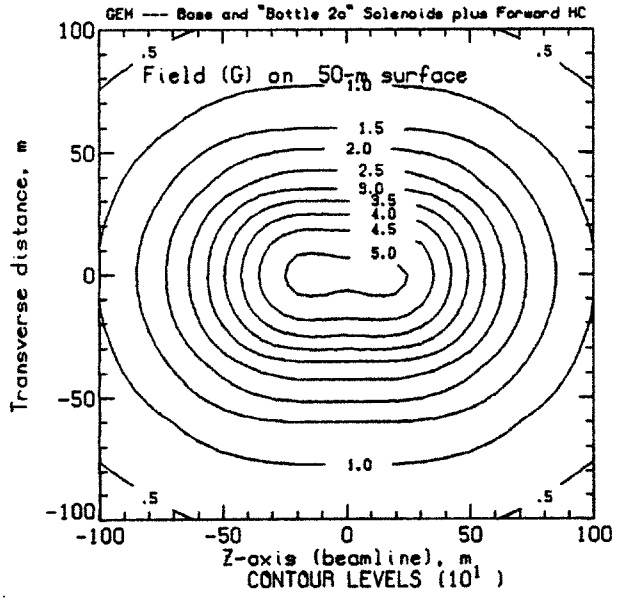

Figure 276: Isogauss contours of the field on a surface at a nominal elevation of 50 m above the beamline (centerline).

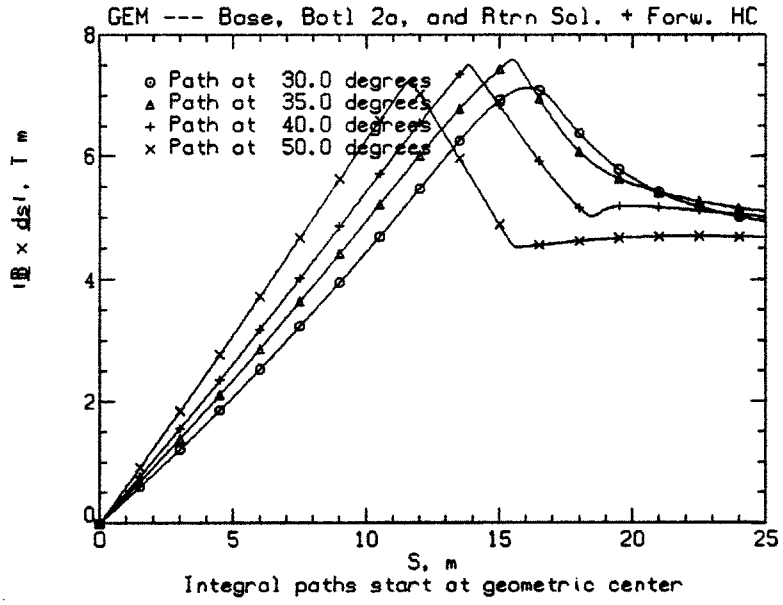

Figure 288: Plot of $|\vec{\mathcal{I}}|$ versus path length from the interaction point for tracks at 30, 35, 40, and 50° (from the beam line).

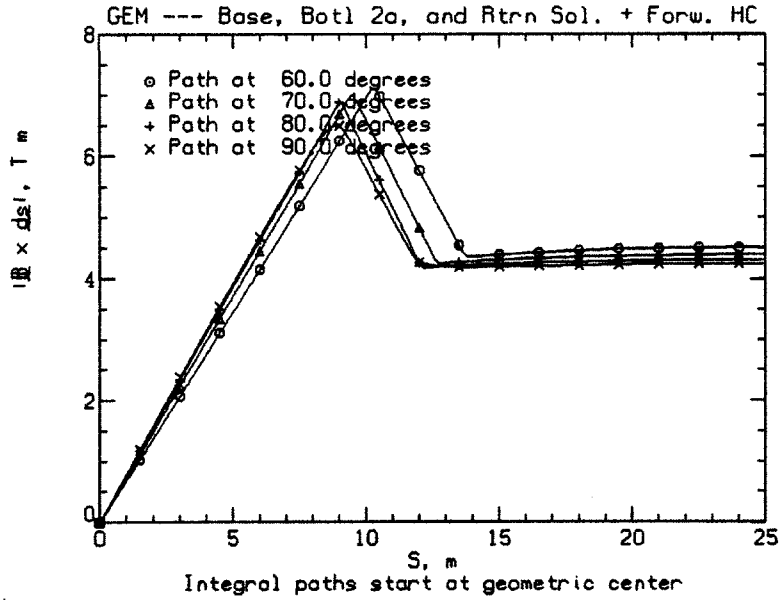

Figure 289: Plot of $|\vec{\mathcal{I}}|$ versus path length from the interaction point for tracks at 60, 70, 80, and 90° (from the beam line).

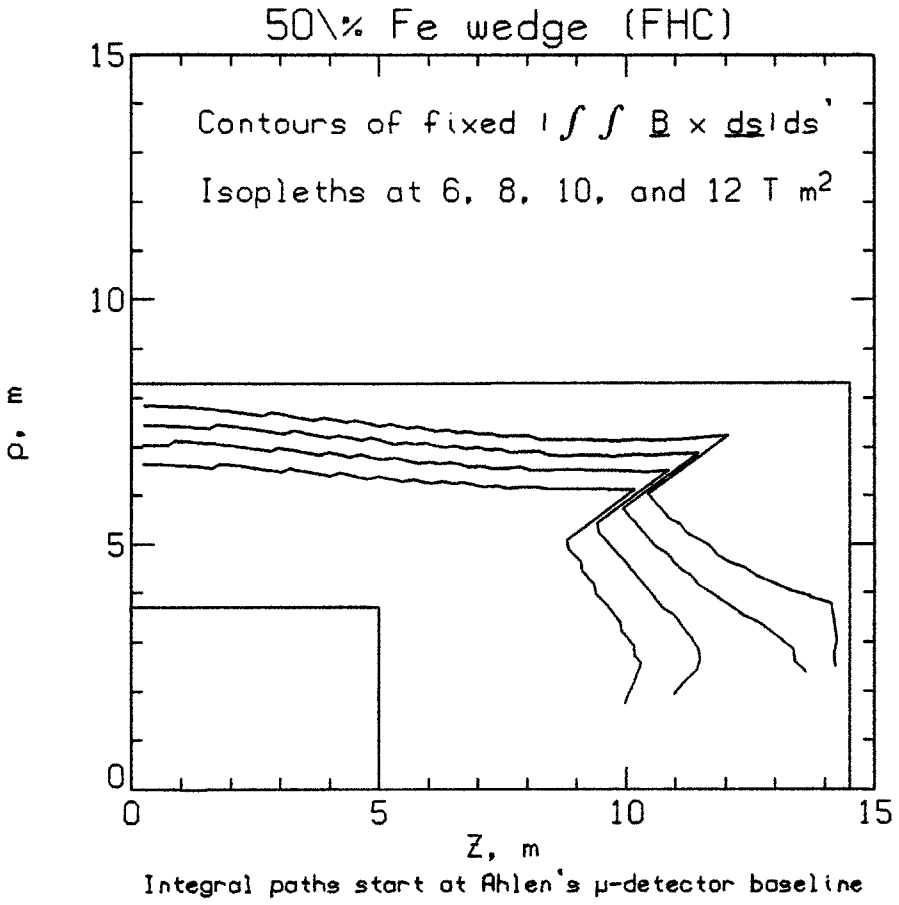

Figure 261: Isopleths of constant BL^2 superposed on a sketch of the GEM concept; isopleths increase with distance from the origin.

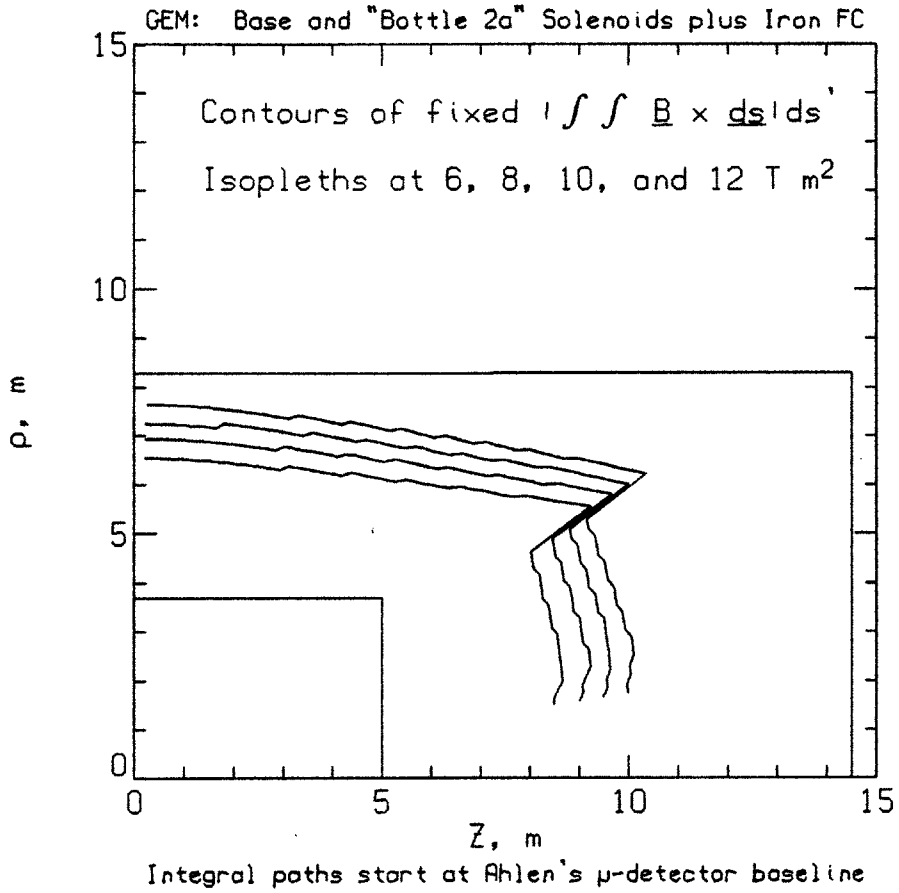

Figure 270: Isopleths of constant $\mathcal{BL}^2$ superposed on a sketch of the GEM concept; isopleths increase with distance from the origin.

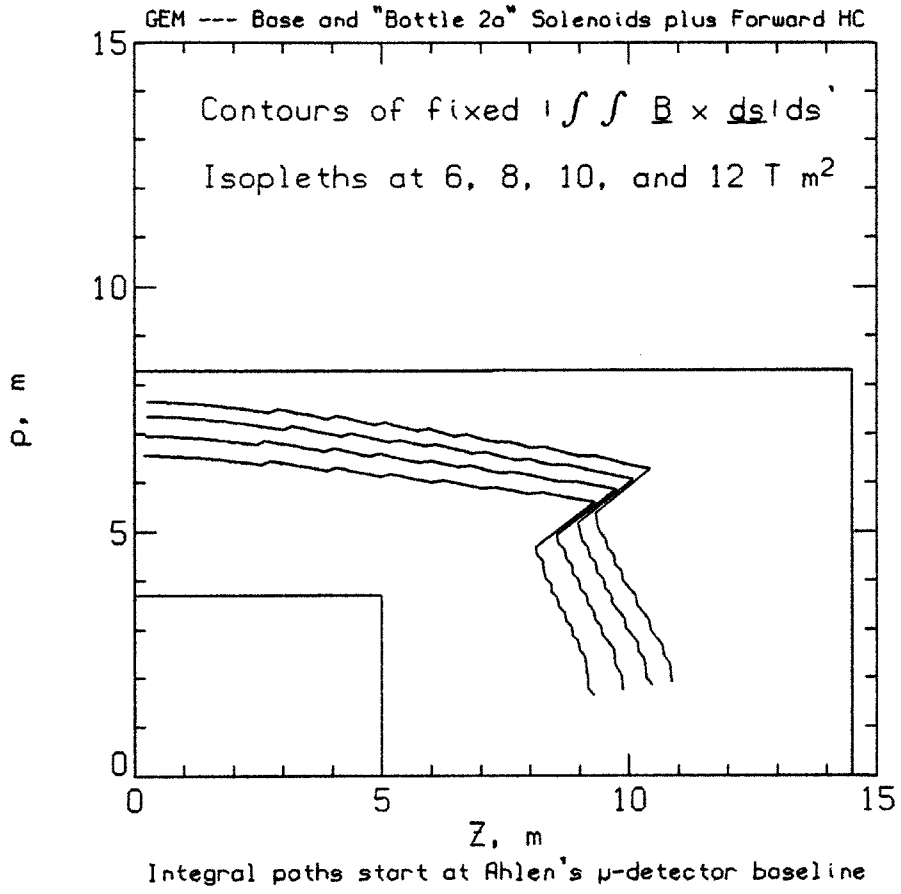

Figure 279: Isopleths of constant $\mathcal{BL}^2$ superposed on a sketch of the GEM concept; isopleths increase with distance from the origin.

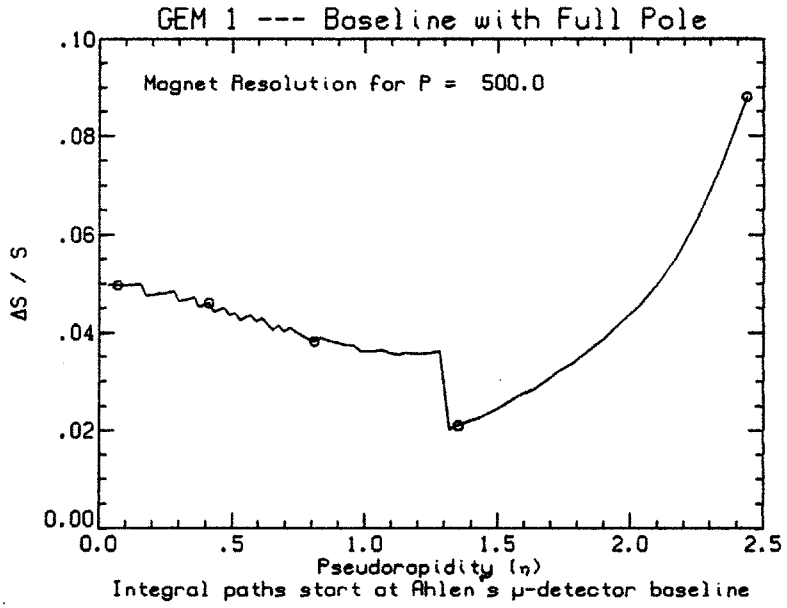

Figure 45: Resolution for constant P as a function of η.

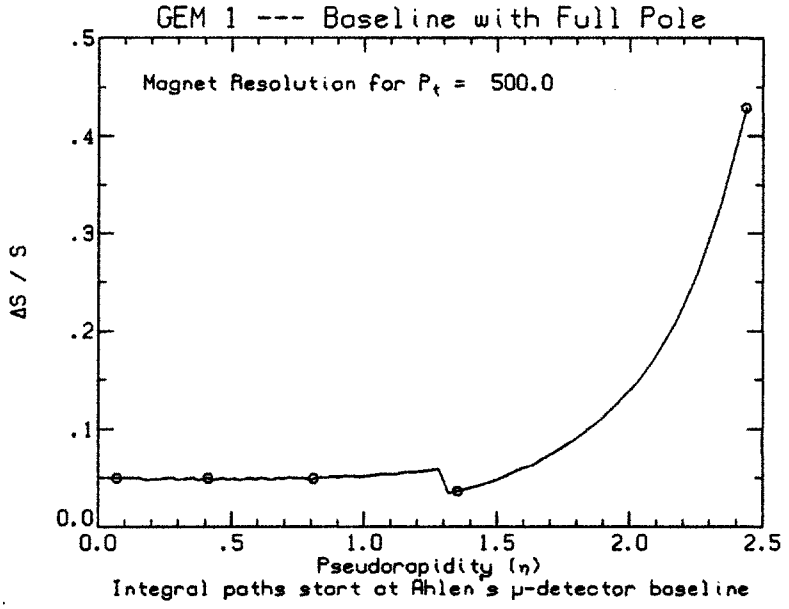

Figure 46: Resolution for constant P_t as a function of η.

A.1.3 Thin pole case 1

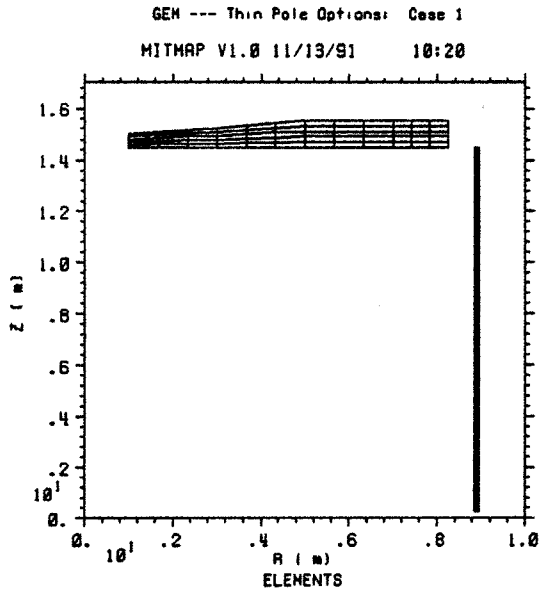

Figure 55: Side view of a superconducting solenoid with a thin pole, case #1. Note that the beam axis (the z axis) is vertical on the page and the transverse (radial) axis is horizontal.

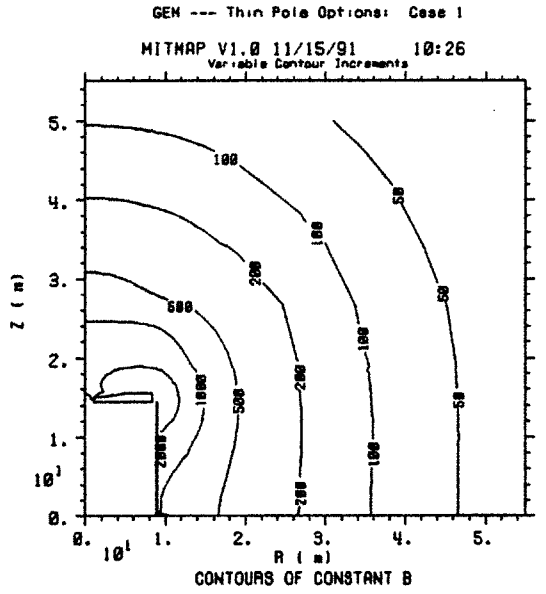

Figure 56: Contours of constant $|\vec{B}|$ superposed on a side view of the magnet; isopleths are labeled in gauss.

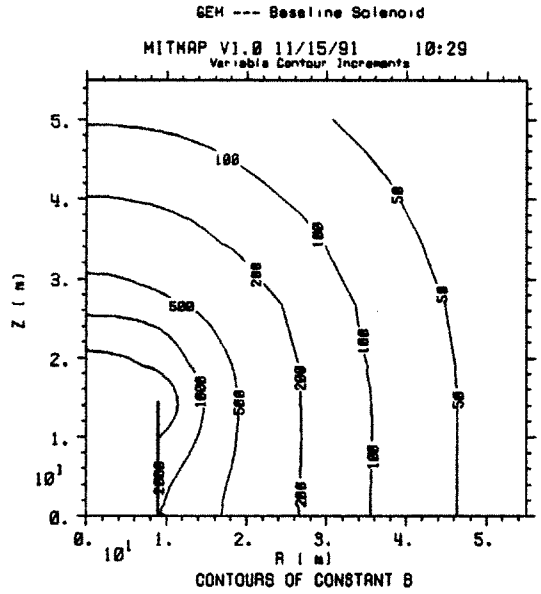

Figure 25: Contours of constant $|\vec{B}|$ superposed on a side view of the magnet; isopleths are labeled in gauss.

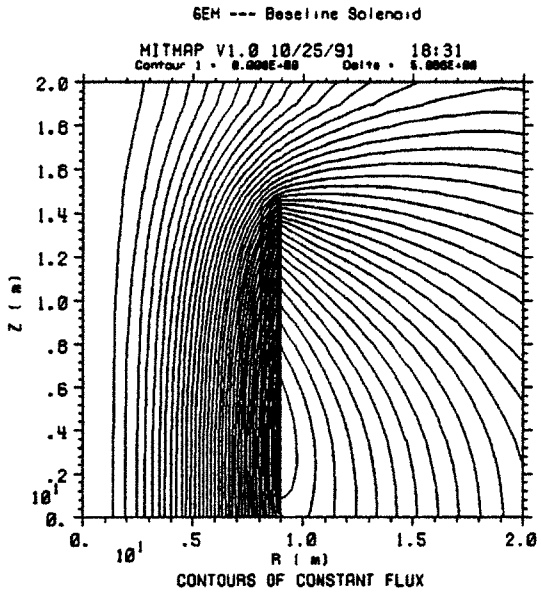

Figure 26: Flux lines superposed on a side view of the magnet design.

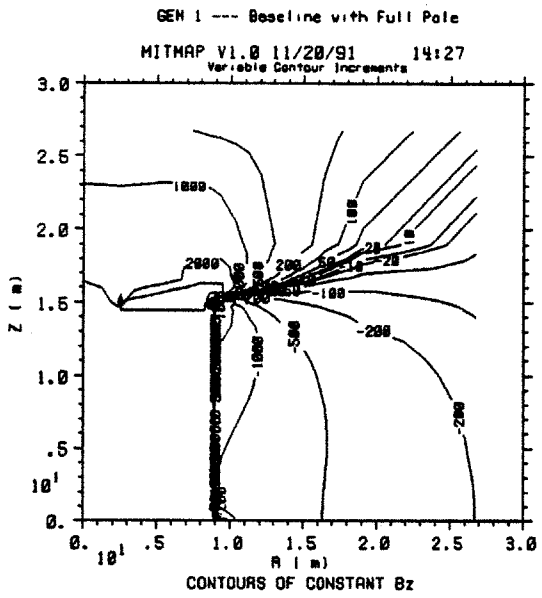

Figure 35: Contours of constant B_z superposed on a side view of the magnet; isopleths are labeled in gauss.

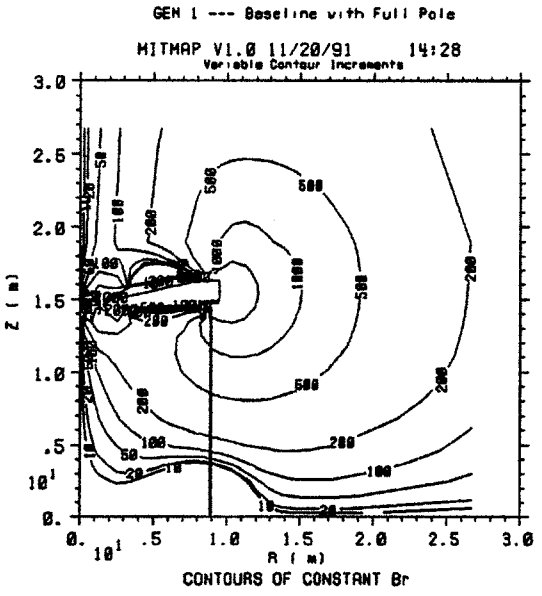

Figure 36: Contours of constant B_r superposed on a side view of the magnet; isopleths are labeled in gauss.

5 Fringe Field Shielding

As the surface field (cf. Figure 12) for the unshielded baseline magnet (either EoI or LoI) is measured in 10s of gauss, various options to reduce the surface field below 10 G or 5 or ... have been investigated to address both safety and environmental concerns. Basically, there

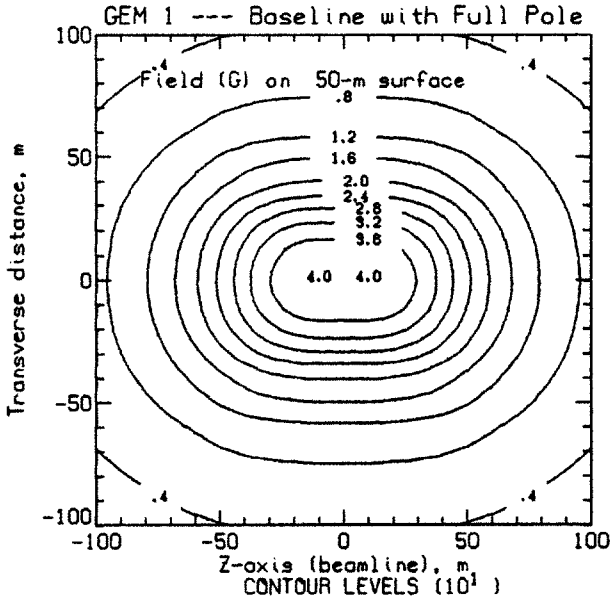

Figure 12: Isogauss contours of the field on a surface at a nominal elevation of 50 m from above the center (beam) line of the EoI baseline magnet. Note the peak field at an elevation of 50 m does not occur on the midplane and is about 40 G.

are four approaches:

1. Full iron return frame (in the hall) cf. Appendix A.4.1,
2. Superconducting shield (second coil) cf. Appendix A.4.2,
3. Local shielding with an iron plate at the surface (or at some intermediate elevation), and
4. Construct an earthen mound (hill) to physically exclude access to the increased fields.

Shown in Figure 13 is a side view of a full iron return frame with a thickness of 1.3 m which is sufficient to reduce the surface (50 m) field to < 10 G (cf. Figure 14). The flux lines for this case are essentially identical to the unshielded case and the resolution is unaffected (cf. Figure 15). A 1.6 m thick return frame will reduce the surface field to 5 G. Shown in Figure 16 is a side view of a full iron return frame with a thickness of 2.0 m which is sufficient to reduce the surface (50 m) field to ~ 1 G (cf. Figure 17). The flux lines for this case are essentially identical to the unshielded case and the resolution is unaffected (cf. Figure 18). Of course the resolution at small angles is still a problem but at least the surface field is negligible. A superconducting coil to return the flux adds some complexity but also suffices to limit the surface field (cf. Section 6 and Appendix A.4.2). Either method of returning

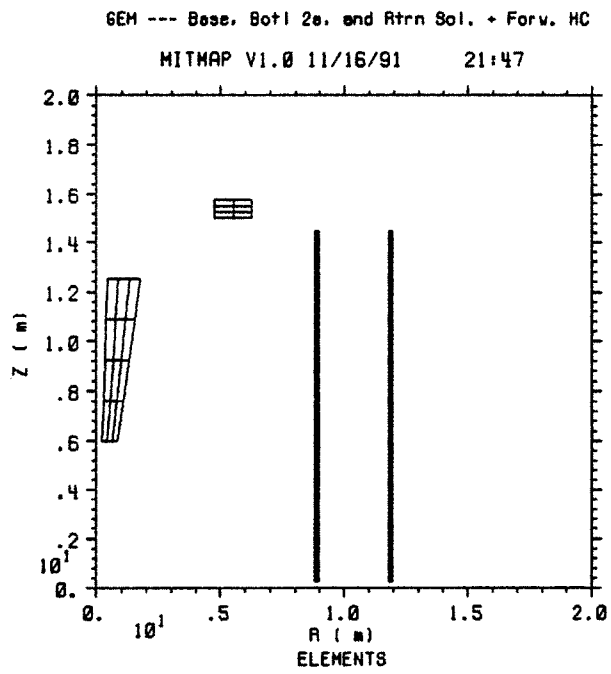

Figure 19: Side view (one quadrant) of superconducting solenoid with superconducting return, with the end poles replaced with a solenoid, and with a conical iron wedge (forward calorimeter) to draw flux towards the axis; the figure is rotationally symmetric.

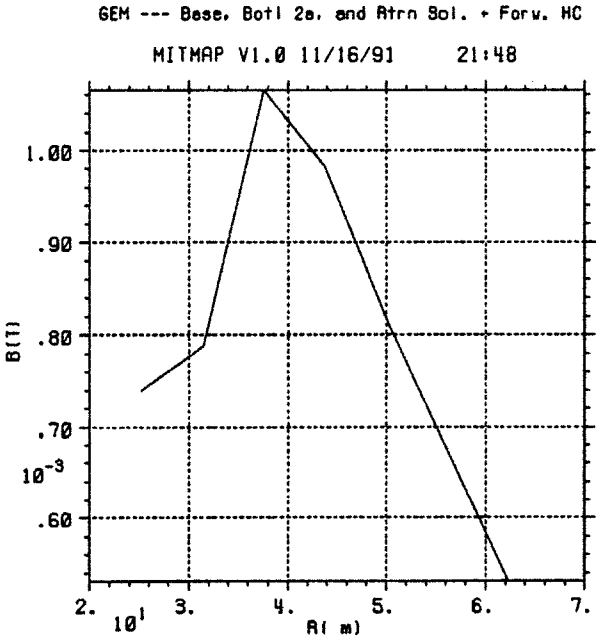

Figure 20: $|\vec{B}|$ versus radius near the surface for the magnet design shown in Figure 19.

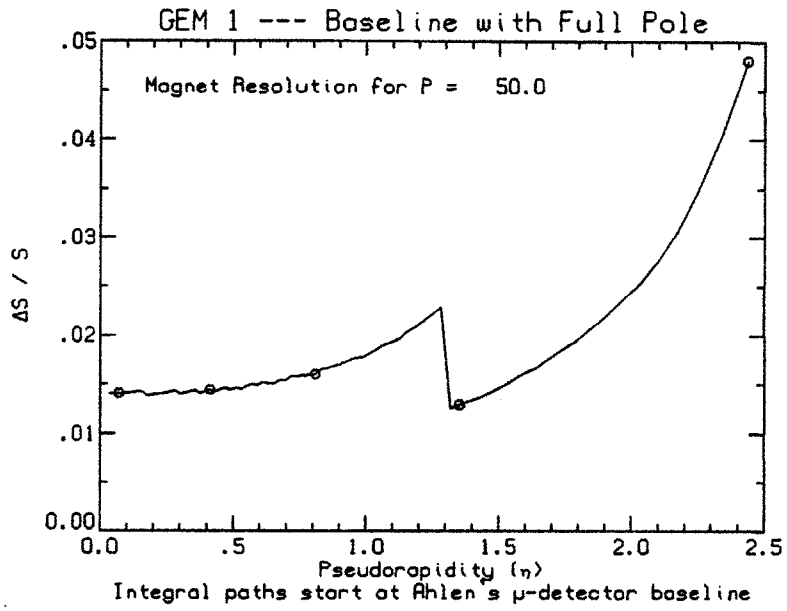

Figure 49: Resolution for constant P as a function of η.

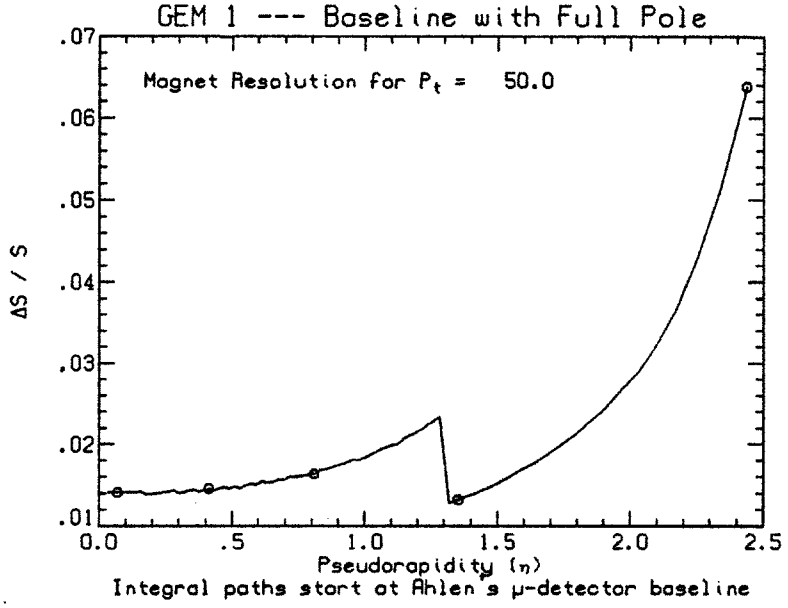

Figure 50: Resolution for constant P_t as a function of η.

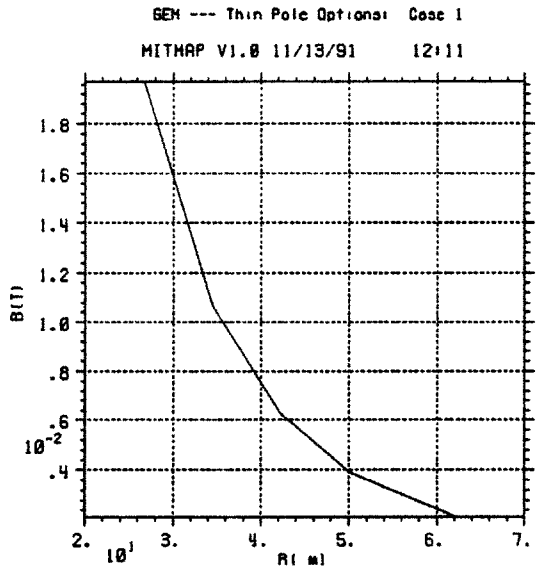

Figure 59: $|\vec{B}|$ versus radius near the surface.

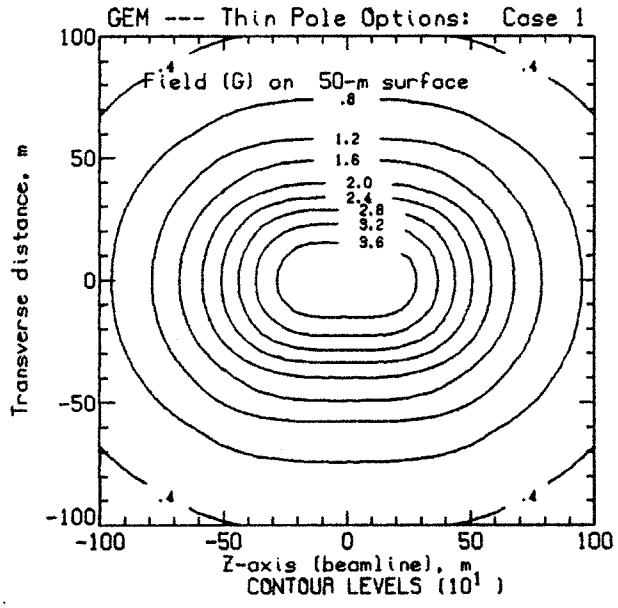

Figure 60: Isogauss contours of the field on a surface at a nominal elevation of 50 m above the beamline (centerline).

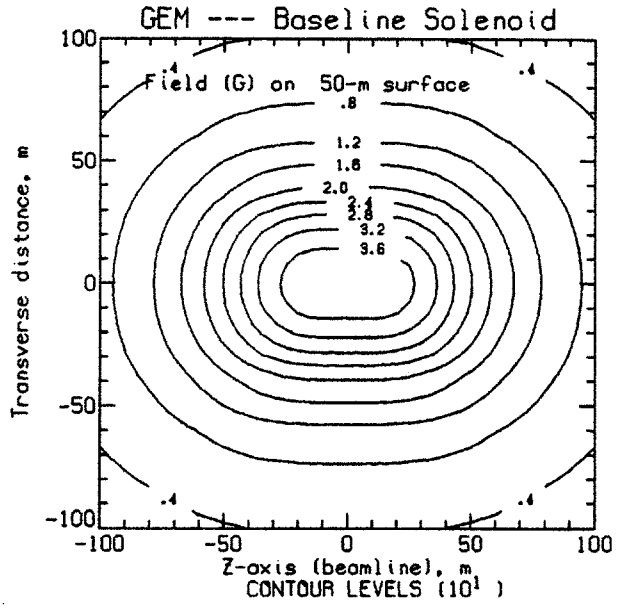

Figure 29: Isogauss contours of the field on a surface at a nominal elevation of 50 m above the beamline (centerline).

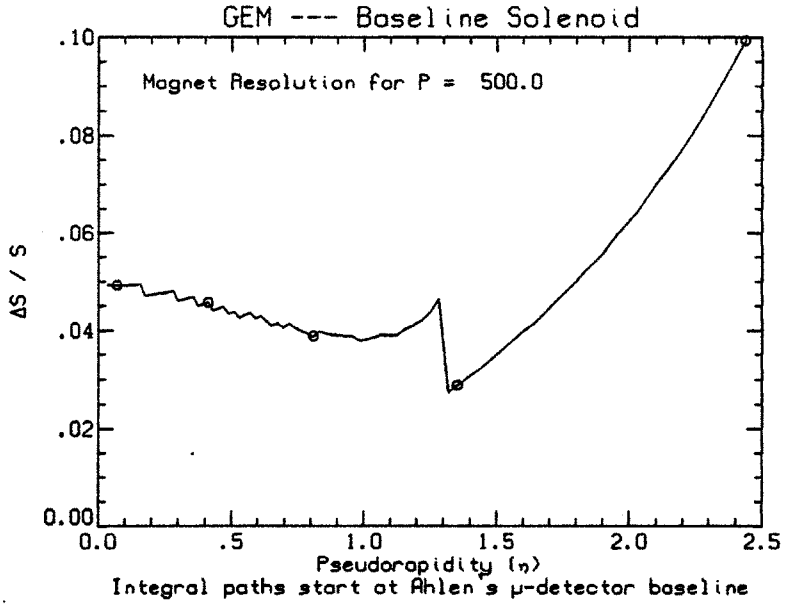

Figure 30: Resolution for constant P as a function of η.

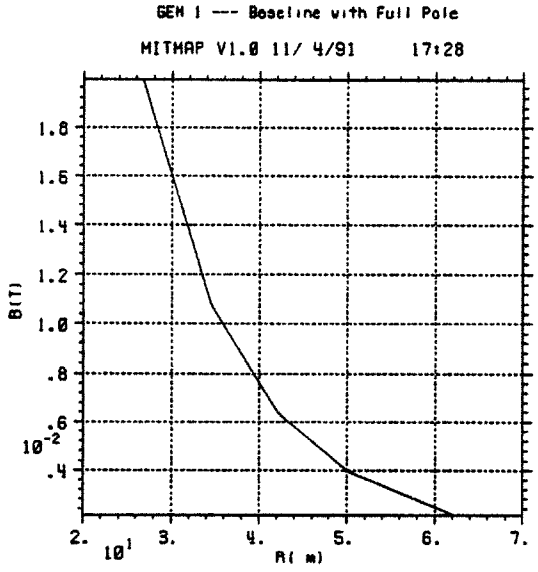

Figure 39: $|\vec{B}|$ versus radius near the surface.

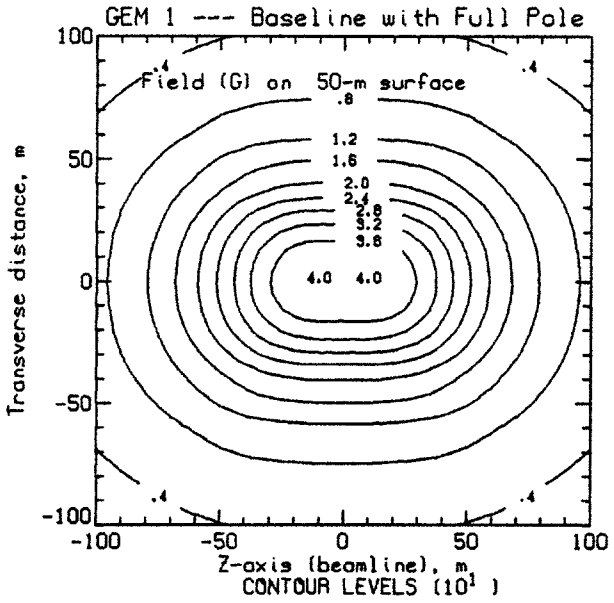

Figure 40: Isogauss contours of the field on a surface at a nominal elevation of 50 m above the beamline (centerline).

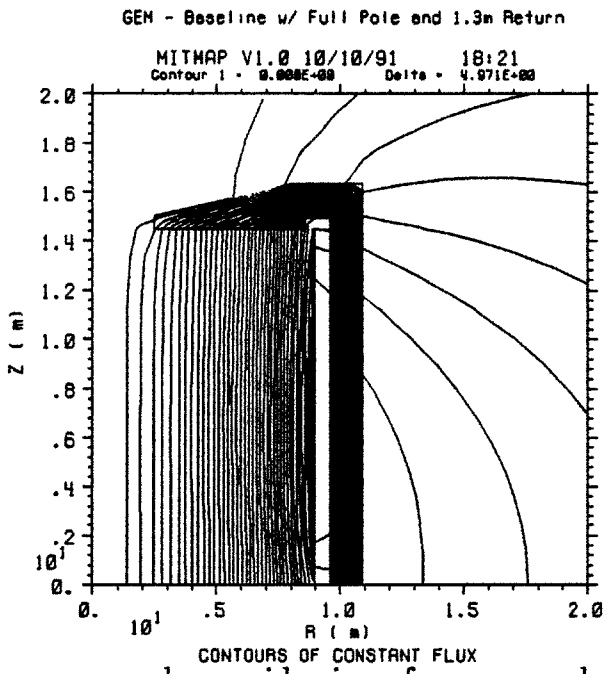

Figure 15: Flux lines superposed on a side view of a superconducting solenoid with a 1.3 m iron return frame. Note that the beam axis (the z axis) is vertical on the page and the transverse (radial) axis is horizontal.

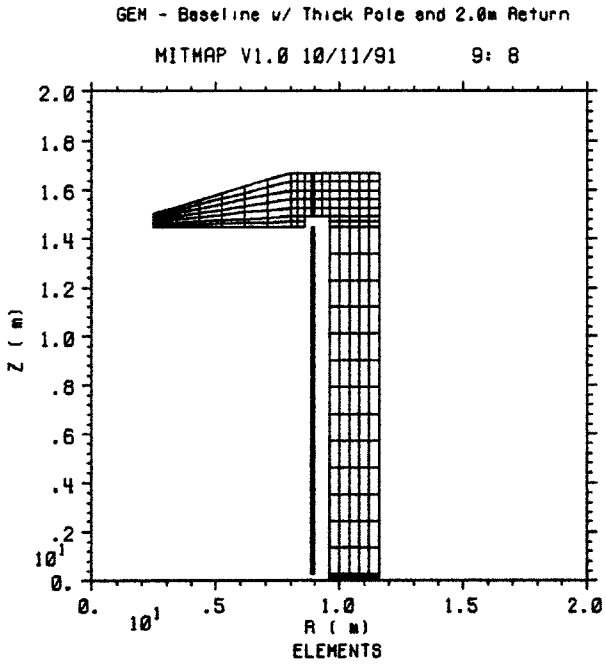

Figure 16: Side view of superconducting solenoid with a 2.0 m full iron return frame (the figure is rotationally symmetric about the z-axis). Note that the beam axis (the z axis) is vertical on the page and the transverse (radial) axis is horizontal.

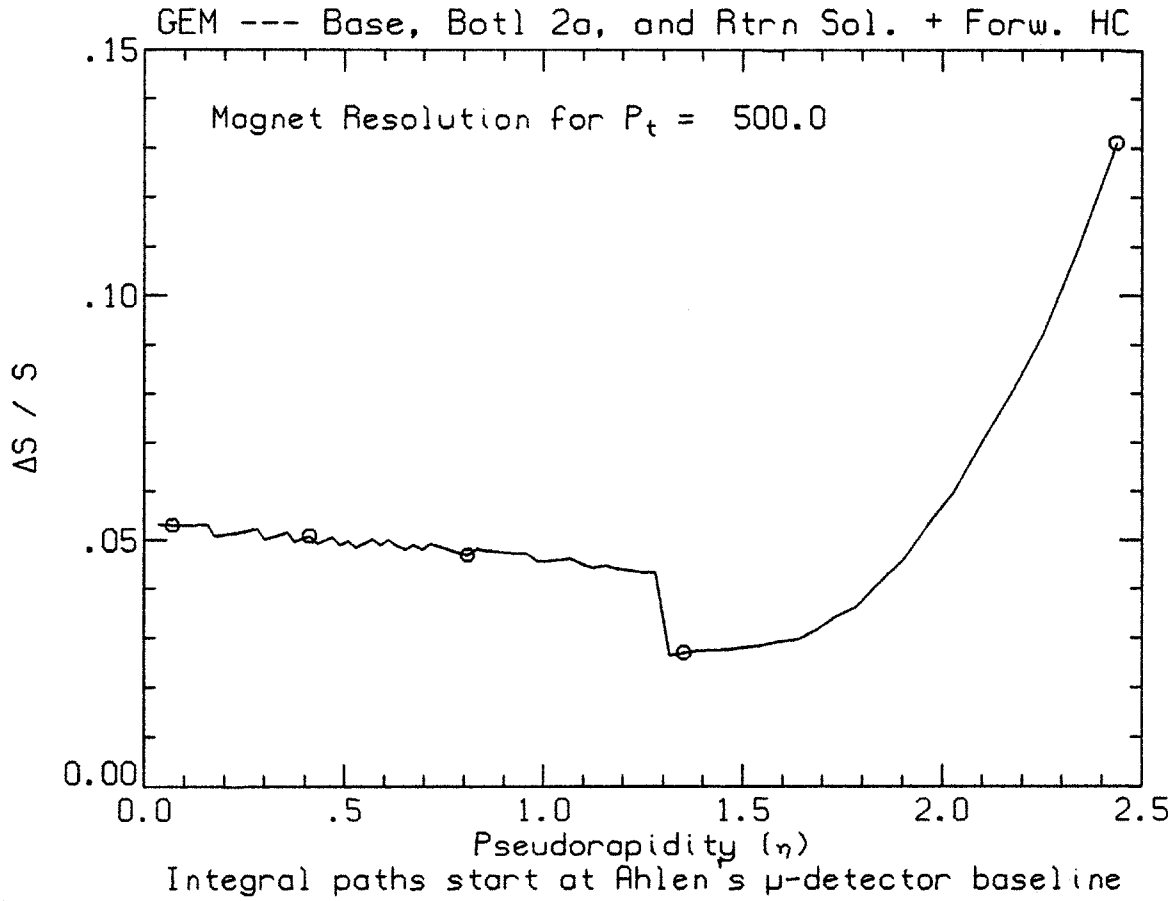

Figure 23: Resolution for constant P_t (500 GeV) as a function of η for the design shown in Figure 19.

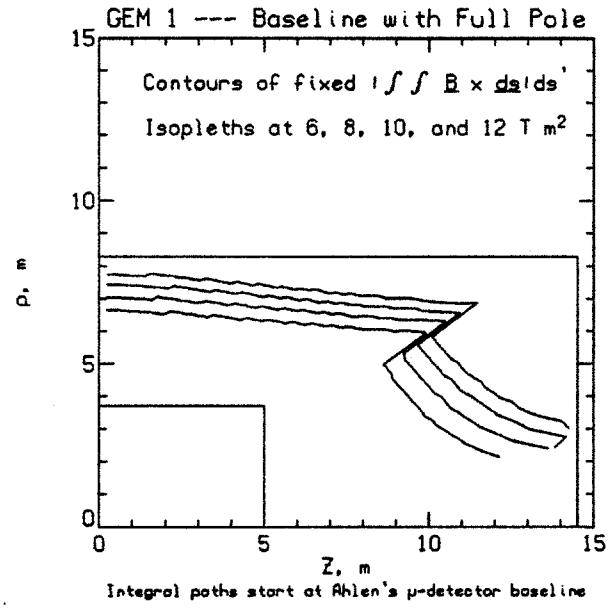

Figure 53: Isopleths of constant $\mathcal{BL}^2$ superposed on a sketch of the GEM concept; isopleths increase with distance from the origin.

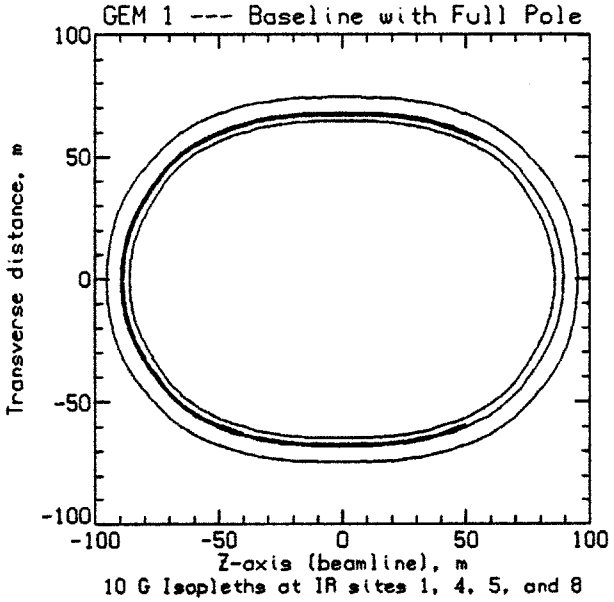

Figure 54: Superposed 10 G contours of the field on the surface for nominal interaction regions.

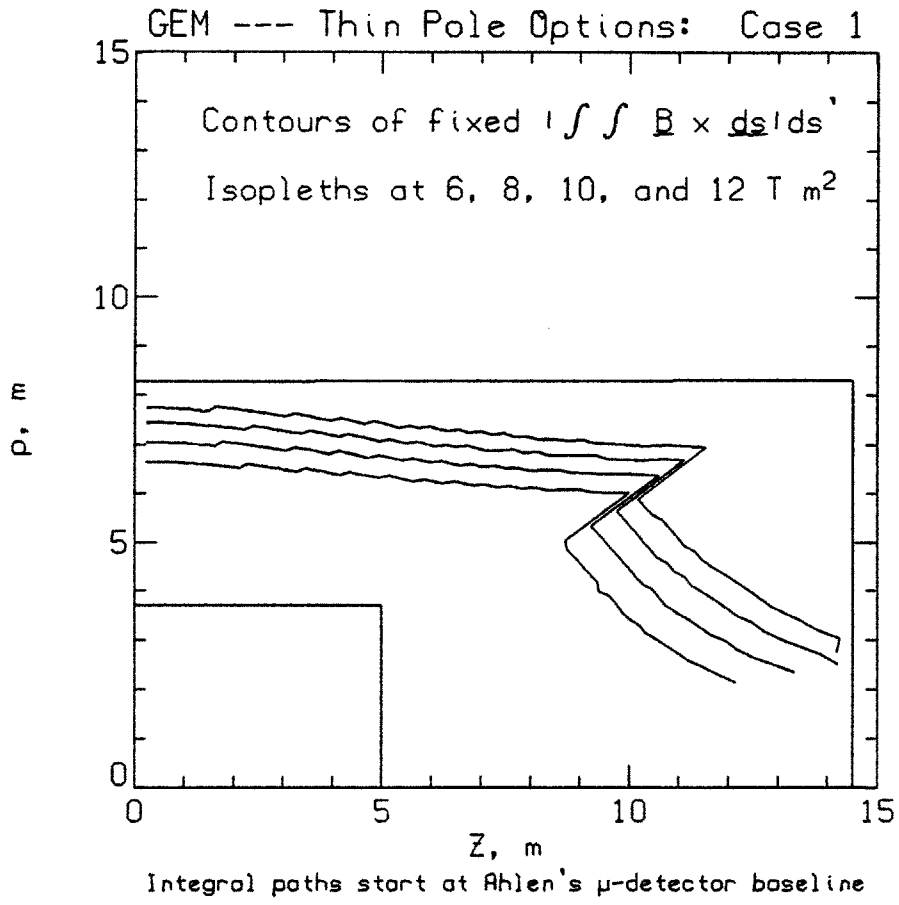

Figure 63: Isopleths of constant BL^2 superposed on a sketch of the GEM concept; isopleths increase with distance from the origin.

A.1.2 EoI baseline: Solenoid with thick end poles

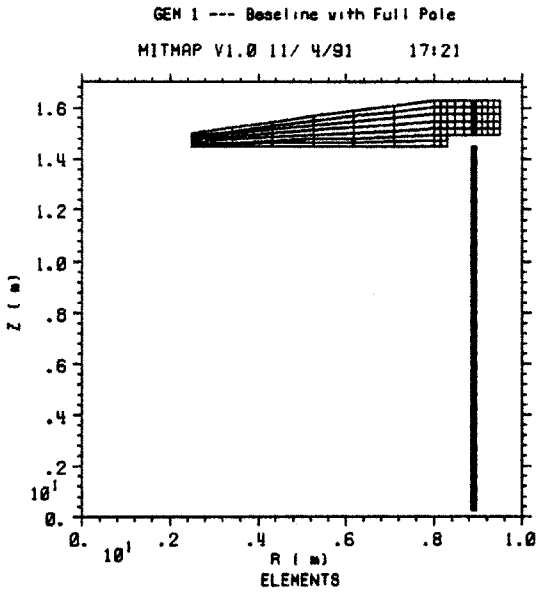

Figure 33: Side view of a superconducting solenoid with thick end poles (EoI baseline). Note that the beam axis (the z axis) is vertical on the page and the transverse (radial) axis is horizontal.

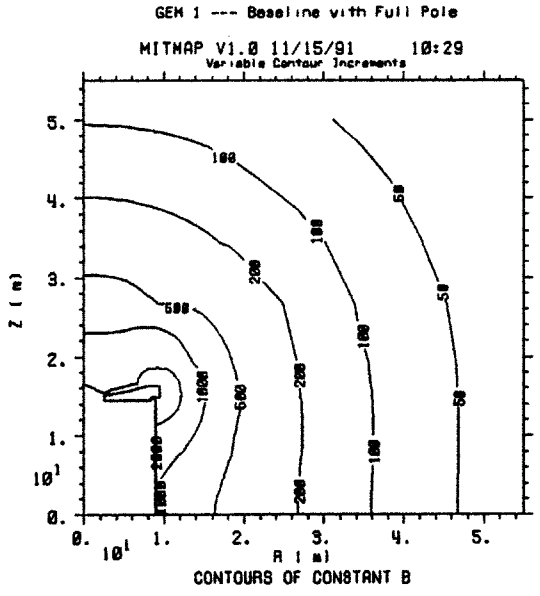

Figure 34: Contours of constant $|\vec{B}|$ superposed on a side view of the magnet; isopleths are labeled in gauss.

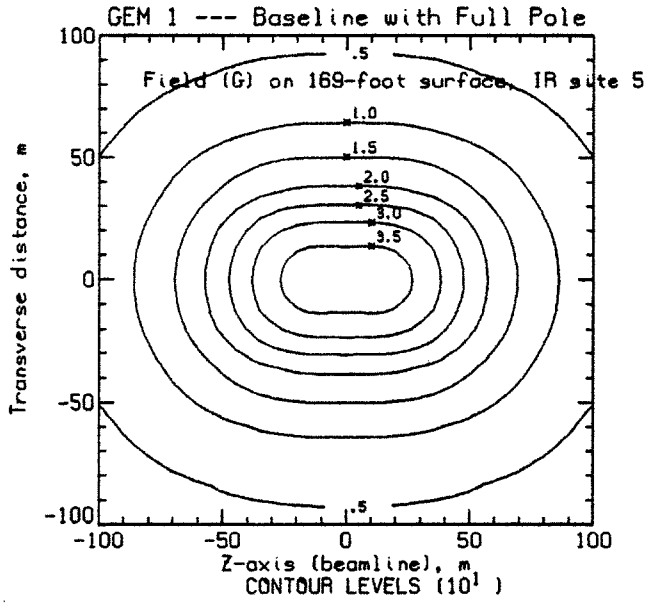

Figure 43: Isogauss contours of the field on a surface at the nominal elevation of IR site 5.

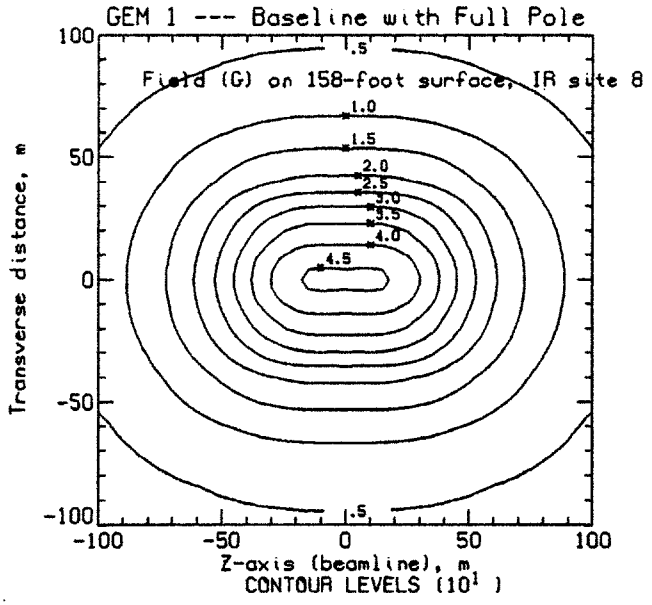

Figure 44: Isogauss contours of the field on a surface at the nominal elevation of IR site 8.

the flux reduces the field in the experiment hall; the other two methods, e.g., local shielding and surface mound, do not. Local shielding is discussed in a separate report [13]; a surface mound would need to extend either to $\sim$ 80 m to reduce the field to 10 G or to $\sim$ 100 m for 5 G; the corresponding volumes are $\sim 3 \times 10^5$ m^3 and $\sim 5 \times 10^5$ m^3 assuming 100 m radius and 50 m surface. The Earth's field of $\sim$ 0.57 G has been neglected and the surface is assumed to be at a nominal elevation of 50 m although explicit curves corresponding to the different interaction regions have been generated for several of the options and are included in the appendices. Essentially, any of the approaches can be made to work and it becomes a question of cost, schedule, (and taste).

6 Small Angle Resolution

Several options have been generated in the effort to solve the resolution problem below 20° for fixed P_t. The most interesting are

1. Addition of solid iron conical wedge (cf. Appendix A.3.1),
2. Addition of 50% iron wedge, e.g., forward hadron calorimeter (cf. Appendix A.3.2),
3. Replacement of pole with "bottle" solenoid plus solid iron wedge (cf. Appendix A.3.3),
4. Replacement of pole with "bottle" solenoid with 50% iron wedge (cf. Appendix A.3.4), and
5. Replacement of pole with "bottle" solenoid with 50% iron wedge and a superconducting return coil (cf. Appendix A.3.5);

these are discussed here with more details[10] in Appendix A.3. Clearly, the approach is twofold. First, conical iron wedges are added to further shape the field by drawing the flux towards the axis and, second, the iron pole piece is replaced with a small superconducting solenoid (the "bottle"). It should be noted that if a forward hadron calorimeter is planned and its absorber is chosen to be iron, then it will also serve as a wedge (these are the 50% iron options). Both approaches have the beneficial effect of inducing field curvature orthogonal to the particle trajectories at low and intermediate angles. That is, $\boldsymbol{BL}^2$ is increased. Finally, a superconducting return coil can be added to address the fringe field problems (cf. Section 5); a side view for this option is shown in Figure 19. With the return solenoid chosen, the surface (50 m) field is reduced to $\sim$ 10 G (cf. Figure 20); an isogauss field map at the surface is shown in Figure 21. The flux lines (lines of force) are shown in Figure 22 where they can be seen to differ significantly from those of the baseline (cf. Appendix A.1.2). Finally, the resolution can be seen in Figure 23 which should be compared with Figure 7 — **the improvement is obvious!**

[10] A number of other options are included in Appendix A.2, options with either end winding compensation or an extended solenoid or additional solenoids or complex pole pieces to further shape the field. Miscellaneous alternatives to improve the small angle resolution including toroids are discussed briefly in Appendix B.

A Options

Except for the high field designs shown in Appendix A.5, the central field is 0.8 T, and the following summary graphs are normally shown:

1. basic geometry
2. contours of $|\vec{B}|$
3. flux contours (lines of force)
4. plots of $|\vec{B}|$ vs ρ or z
5. surface field plot (at either a nominal 50 m and/or the elevations of the various IRs)
6. plots of $\left(\frac{\Delta S}{S}\right)_{P \text{ or } P_t}$ vs. η
7. isopleths of $\mathcal{BL}^2$ at 6, 8, 10, and 12 T m^2

A.1 Solenoids with field shaping

A.1.1 Solenoid without end poles

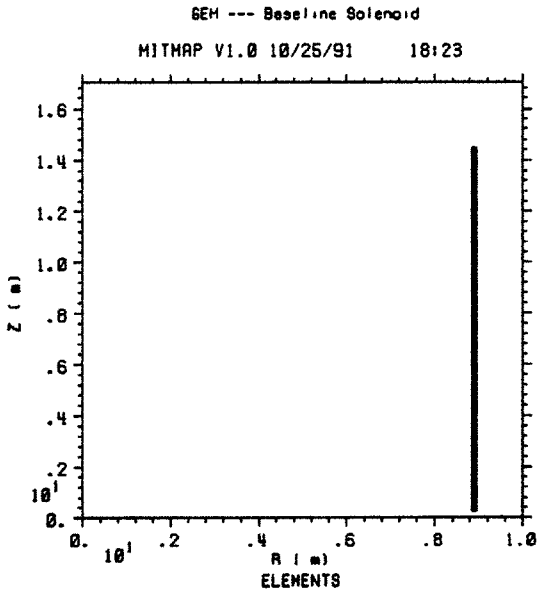

Figure 24: Side view of a simple superconducting solenoid. Note that the beam axis (the z axis) is vertical on the page and the transverse (radial) axis is horizontal.

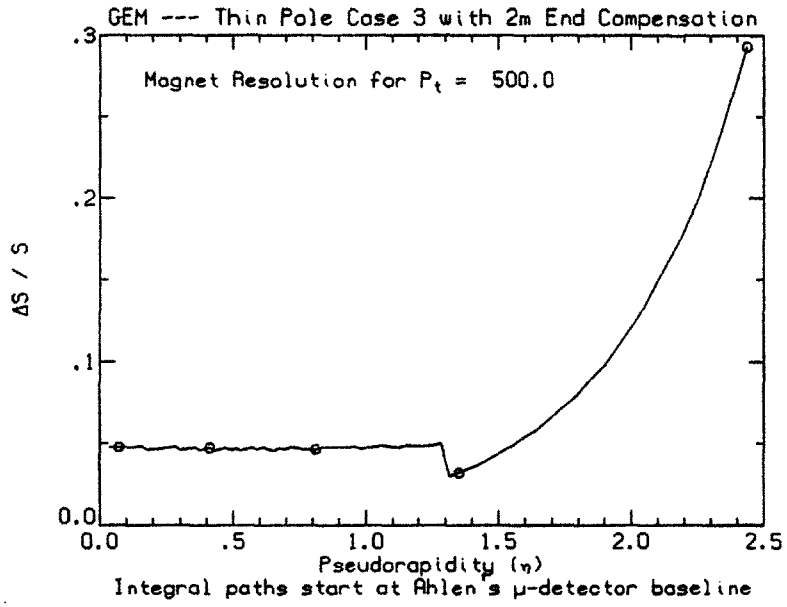

Figure 137: Resolution for constant P_t as a function of η.

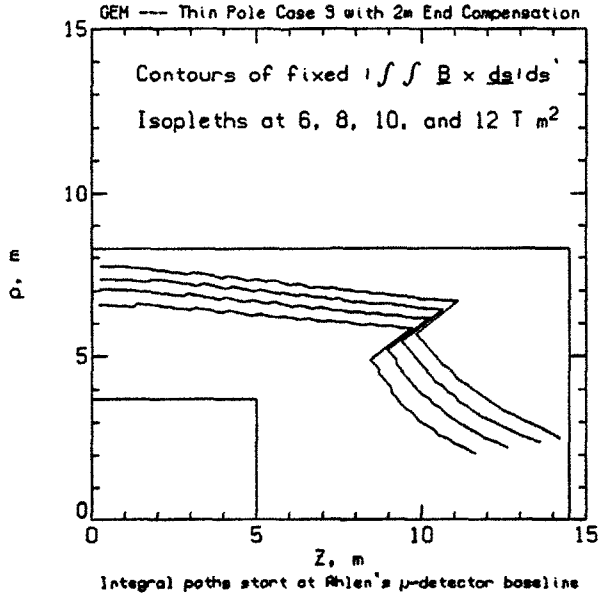

Figure 138: Isopleths of constant $\mathcal{BL}^2$ superposed on a sketch of the GEM concept; isopleths increase with distance from the origin.

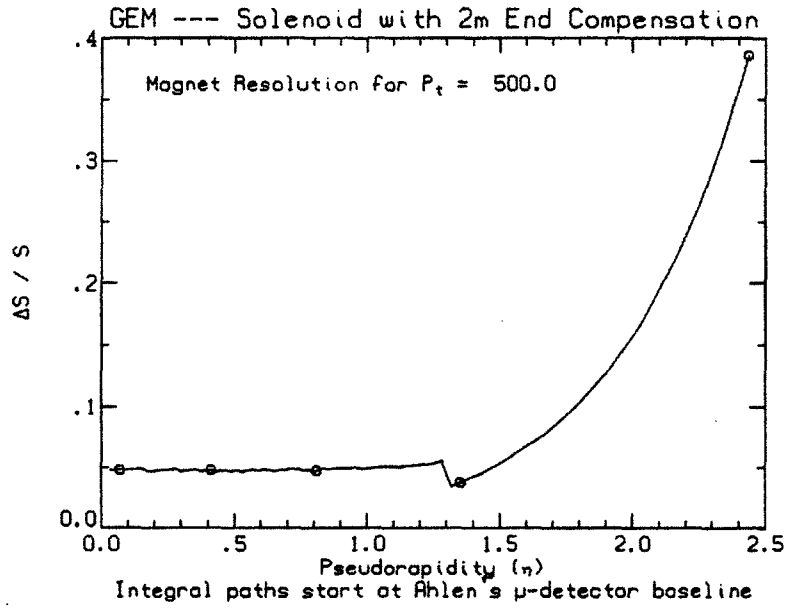

Figure 147: Resolution for constant P_t as a function of η.

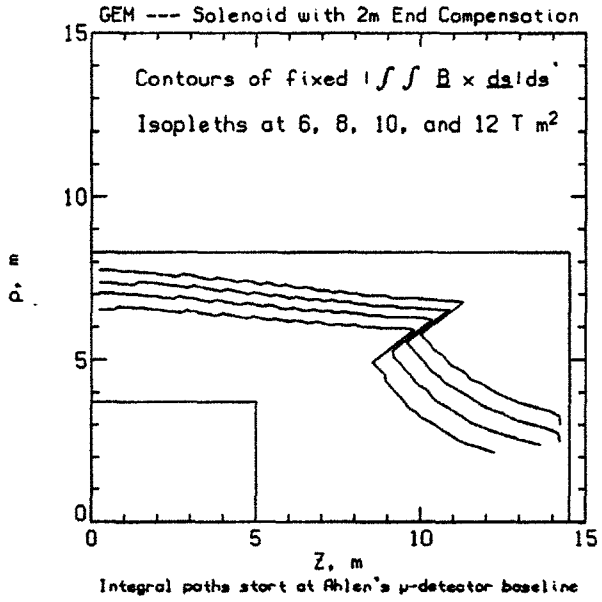

Figure 148: Isopleths of constant $\mathcal{BL}^2$ superposed on a sketch of the GEM concept; isopleths increase with distance from the origin.

A.2 Further shaping and shielding

A wide range of possible options has been considered. The options discussed in Section 4 did not include end winding compensation as a method to approximate more closely a uniform field (in the desired detector volume). Using the option in Appendix A.1.5 as a basis, alternatives with the current increased in the last 1 m (cf. Figures 119–128) or 2 m (cf. Figures 129–138) of the solenoid have been run along with cases where the solenoid is extended (cf. Figures 149–158) over the pole piece or extended and compensated (cf. Figures 159–168). While simple end compensation (cf. Appendix A.2.1) better approximates a uniform field, the replacement of the end poles with a "bottle" solenoid has the beneficial effect of inducing field curvature orthogonal to the particle trajectories; that is, $\mathcal{BL}^2$ is increased (cf. Appendix A.2.2). Another way to induce field curvature (i.e., draw the flux lines toward the axis) is to use complex pole pieces including conical iron wedges; several variants are presented in Appendix A.2.3 where current sheets (solenoids) are frequently used to model the iron wedges. If a forward hadron calorimeter is planned and its absorber is chosen to be iron, then it will also be an iron wedge. Finally, a few other options are presented in Appendix A.2.4.

A.2.1 Compensation

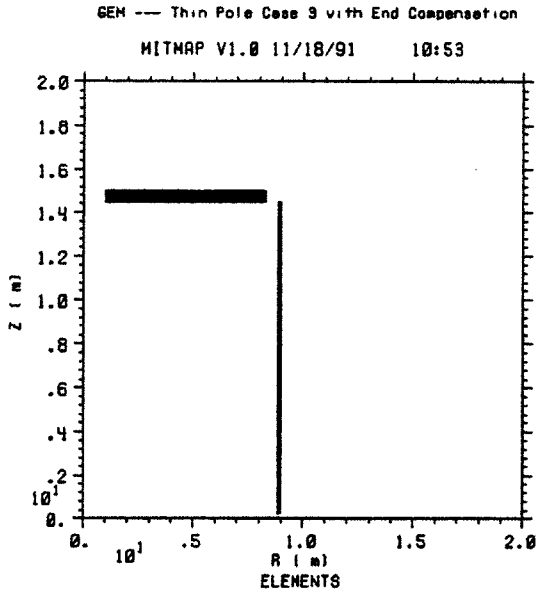

Figure 119: Side view of a superconducting solenoid with the current doubled in the last 1 m. Note that the beam axis (the z axis) is vertical on the page and the transverse (radial) axis is horizontal.

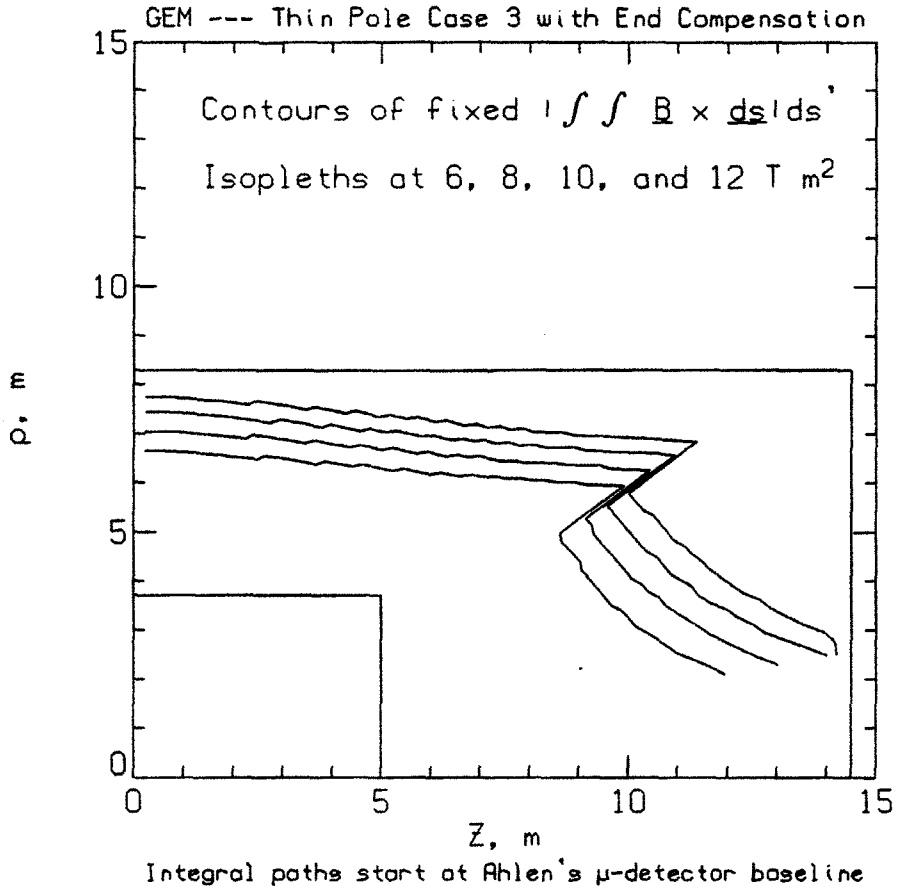

Figure 128: Isopleths of constant $\mathcal{BL}^2$ superposed on a sketch of the GEM concept; isopleths increase with distance from the origin.

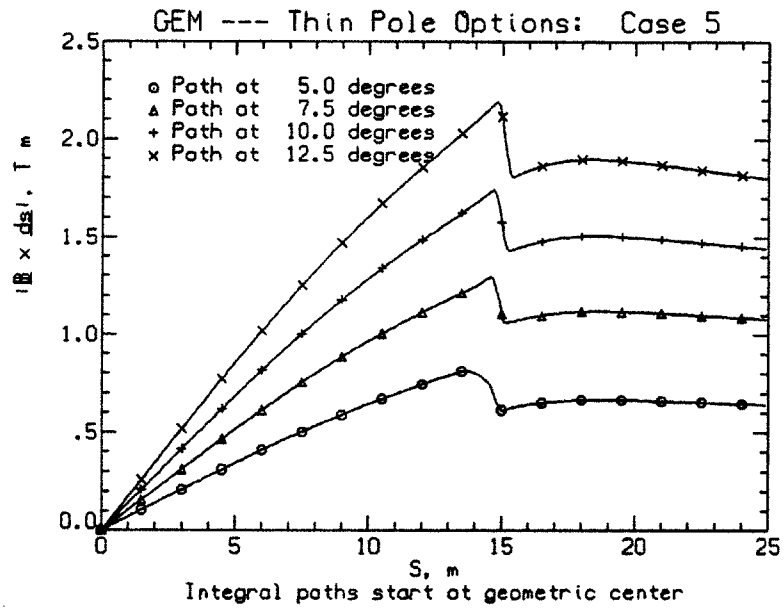

Figure 101: Plot of $|\vec{\mathcal{I}}|$ for the LoI baseline magnet versus path length from the interaction point for tracks at 5, 7.5, 10, and 12.5° (from the beam line).

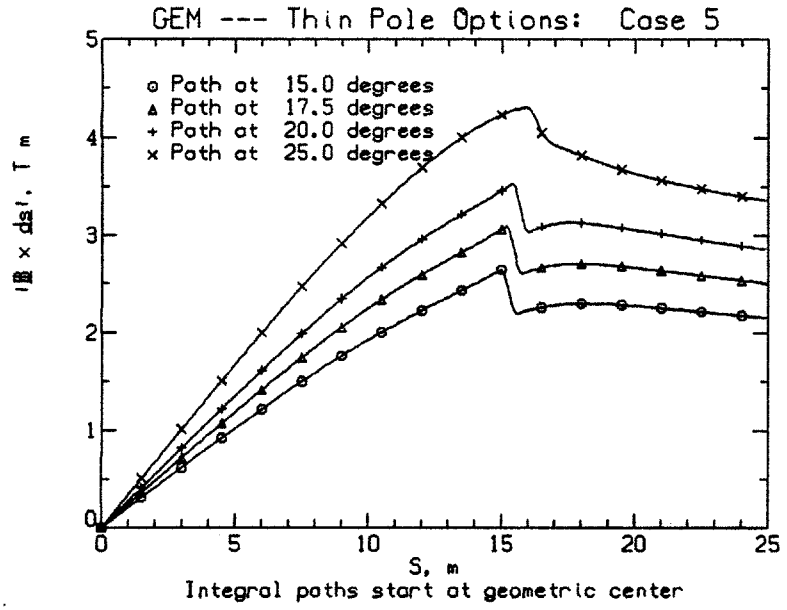

Figure 102: Plot of $|\vec{\mathcal{I}}|$ for the LoI baseline magnet versus path length from the interaction point for tracks at 15, 17.5, 20, and 25° (from the beam line).

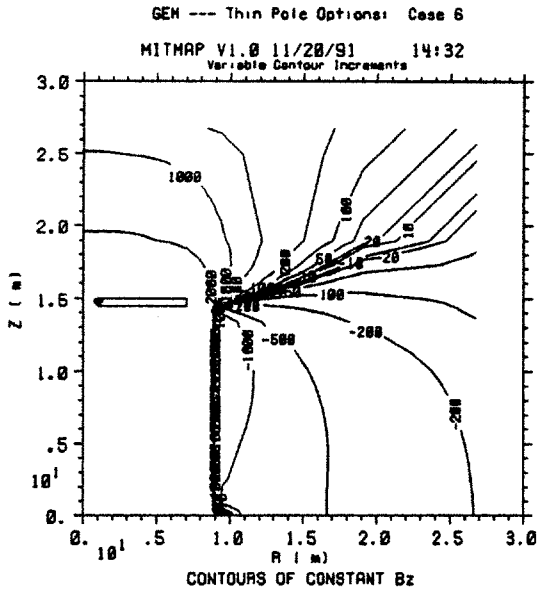

Figure 110: Contours of constant B_z superposed on a side view of the magnet; isopleths are labeled in gauss.

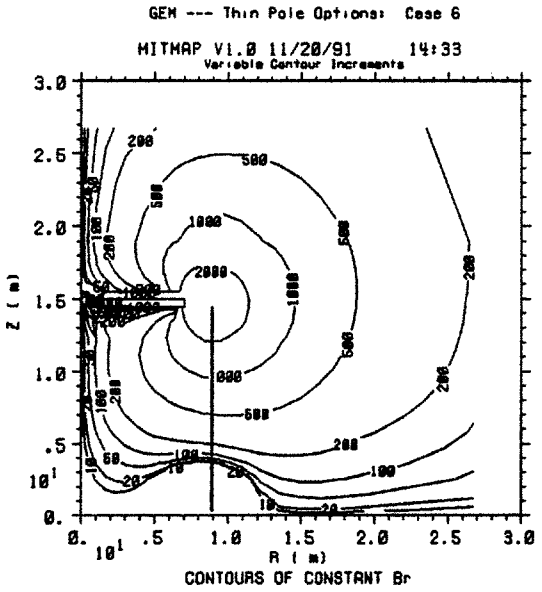

Figure 111: Contours of constant B_r superposed on a side view of the magnet; isopleths are labeled in gauss.

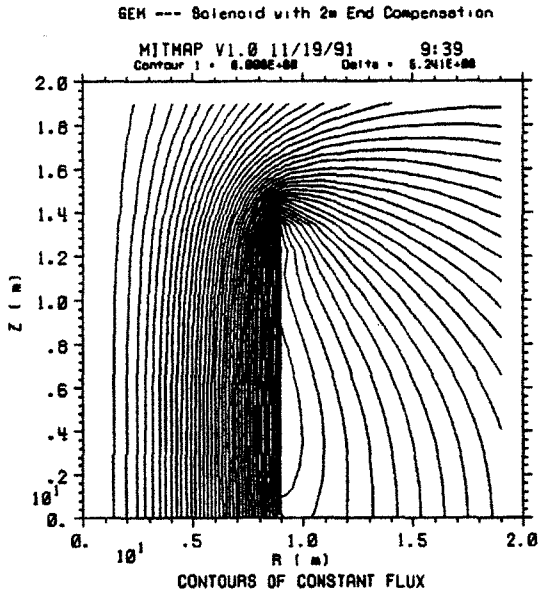

Figure 141: Flux lines superposed on a side view of the magnet design.

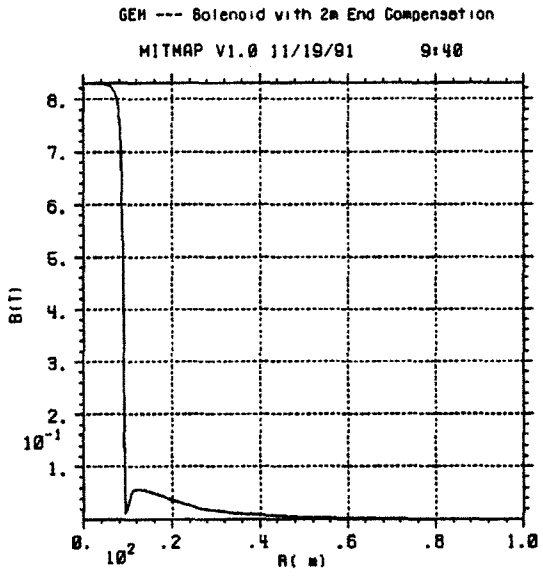

Figure 142: $|\vec{B}|$ versus radius in the hall.

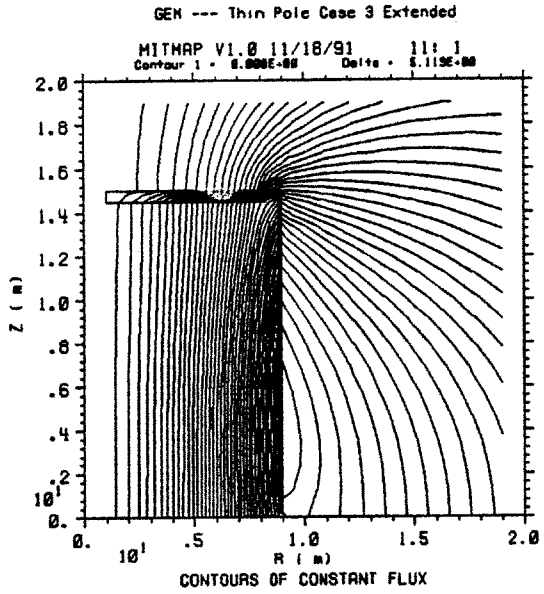

Figure 151: Flux lines superposed on a side view of the magnet design.

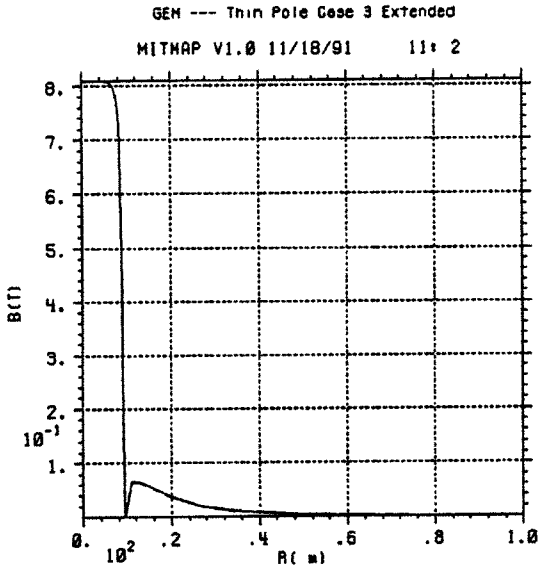

Figure 152: $|\vec{B}|$ versus radius in the hall.

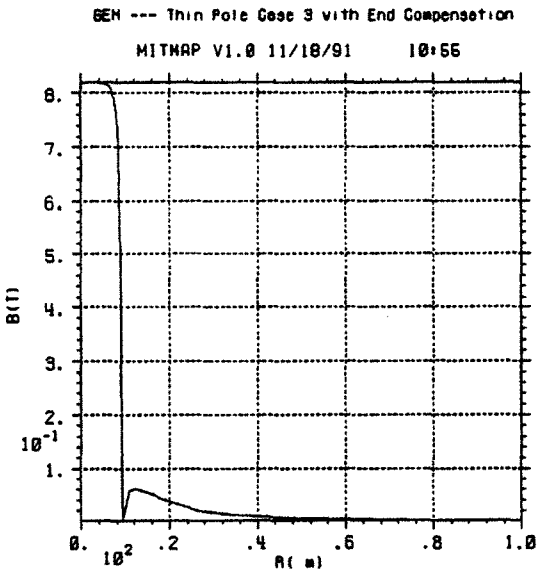

Figure 122: $|\vec{B}|$ versus radius in the hall.

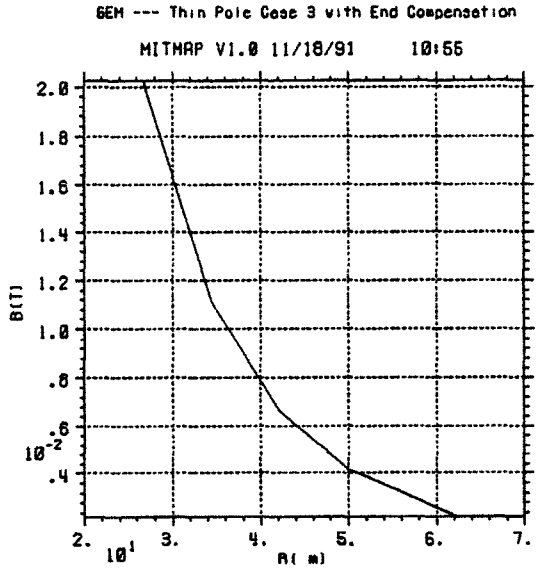

Figure 123: $|\vec{B}|$ versus radius near the surface.

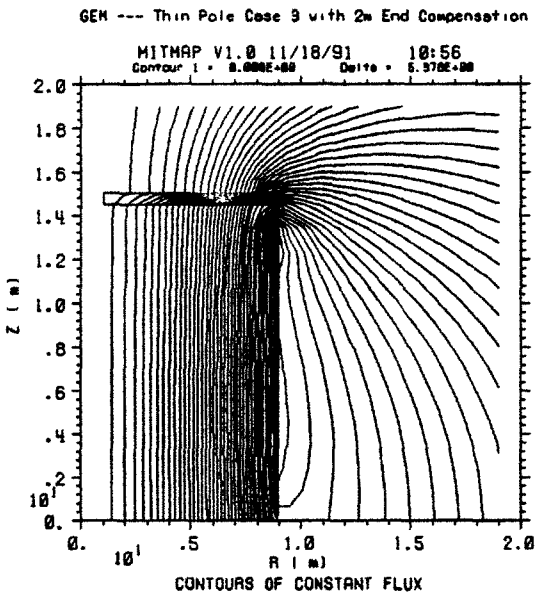

Figure 131: Flux lines superposed on a side view of the magnet design.

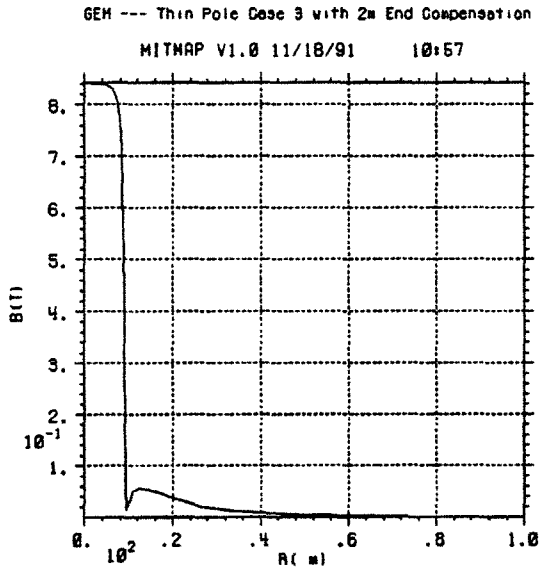

Figure 132: $|\vec{B}|$ versus radius in the hall.

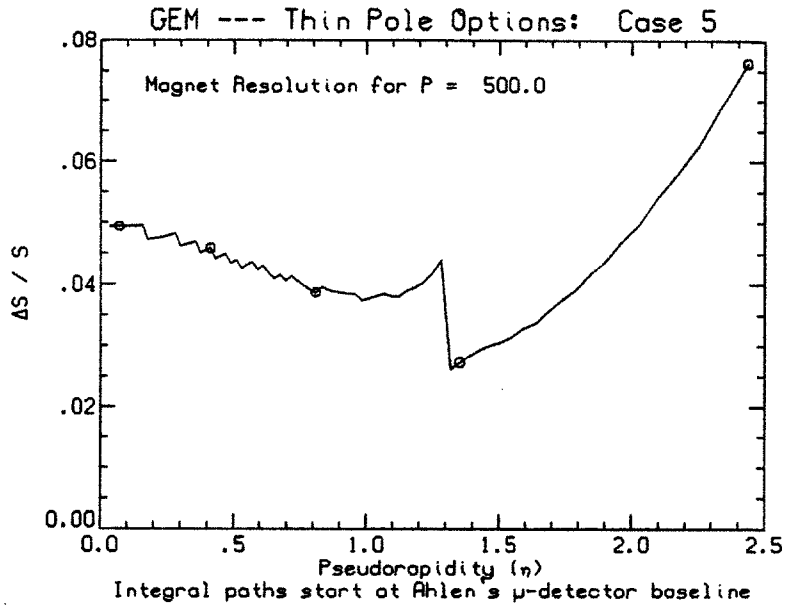

Figure 105: Resolution for constant P as a function of η.

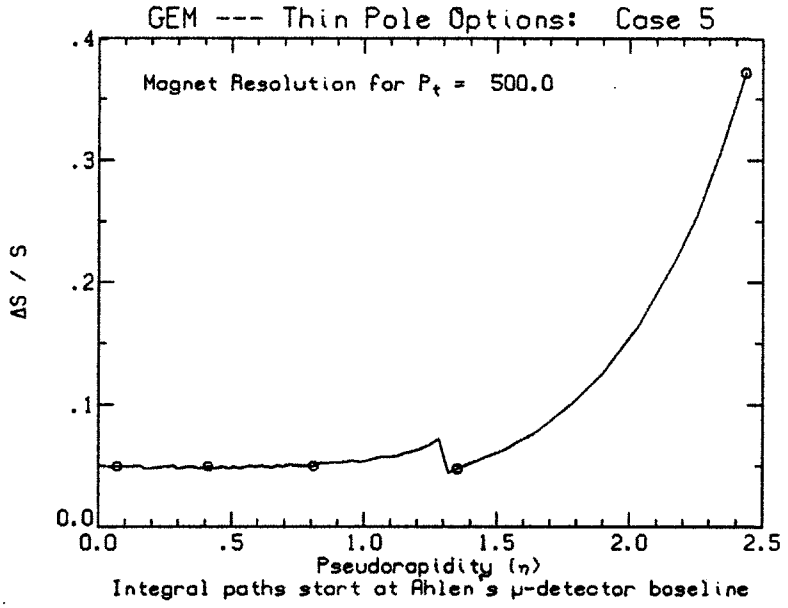

Figure 106: Resolution for constant P_t as a function of η.

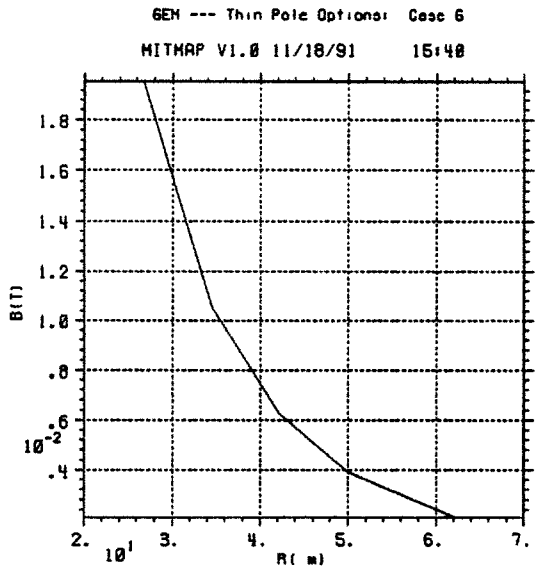

Figure 114: $|\vec{B}|$ versus radius near the surface.

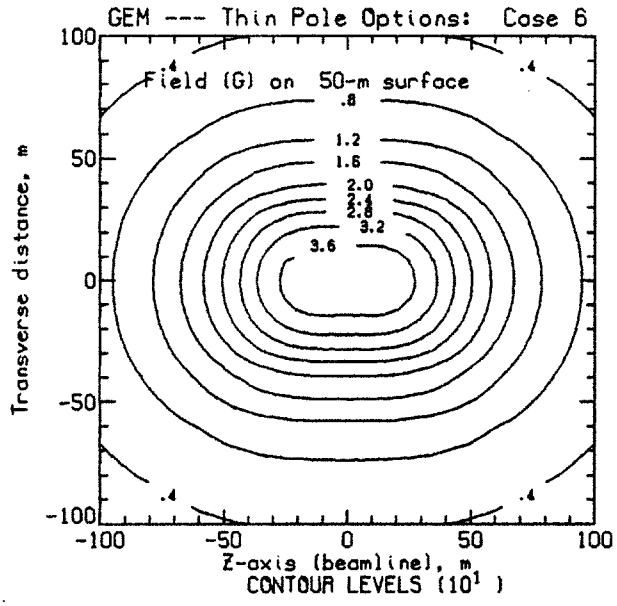

Figure 115: Isogauss contours of the field on a surface at a nominal elevation of 50 m above the beamline (centerline).

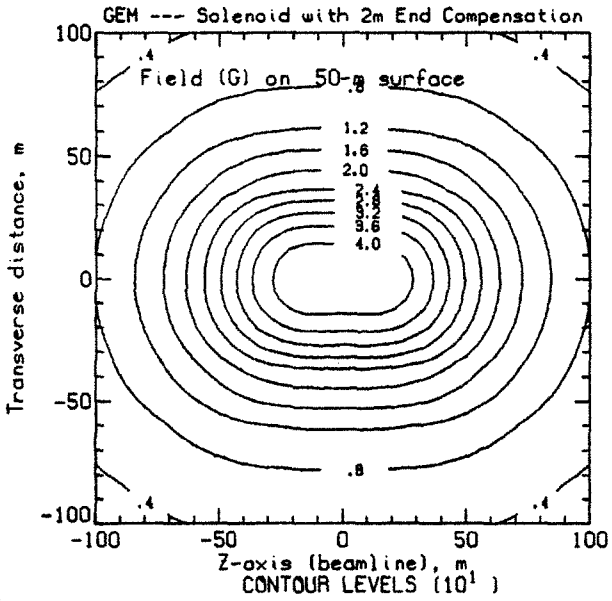

Figure 145: Isogauss contours of the field on a surface at a nominal elevation of 50 m above the beamline (centerline).

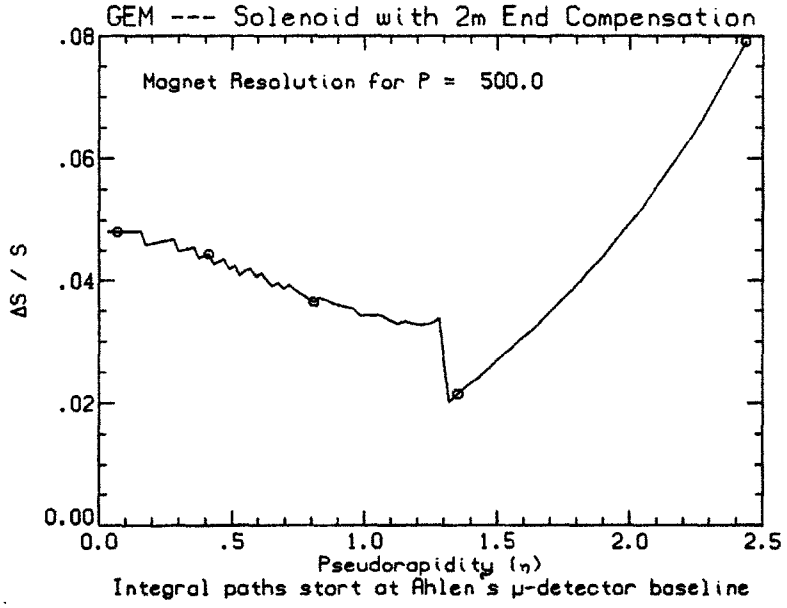

Figure 146: Resolution for constant P as a function of η.

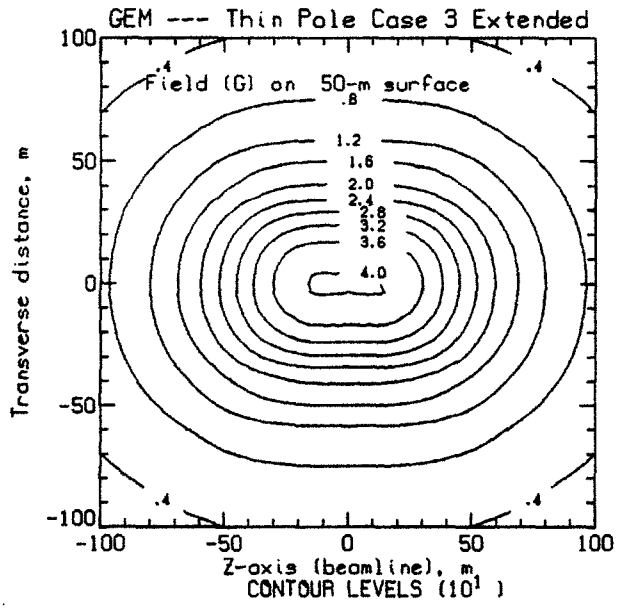

Figure 155: Isogauss contours of the field on a surface at a nominal elevation of 50 m above the beamline (centerline).

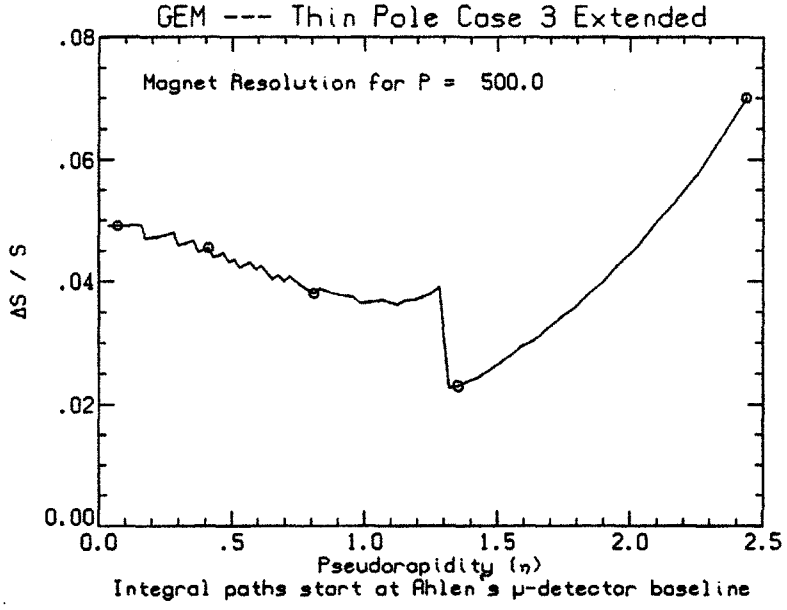

Figure 156: Resolution for constant P as a function of η.

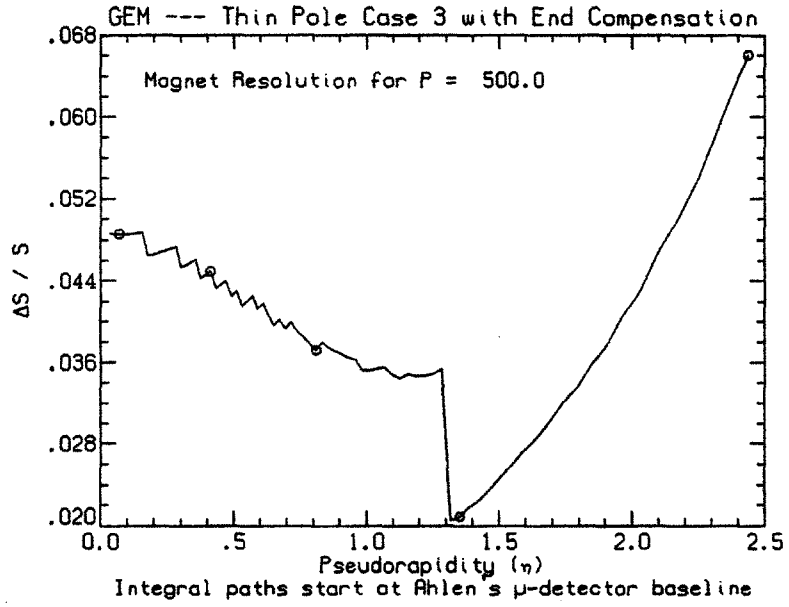

Figure 126: Resolution for constant P as a function of η.

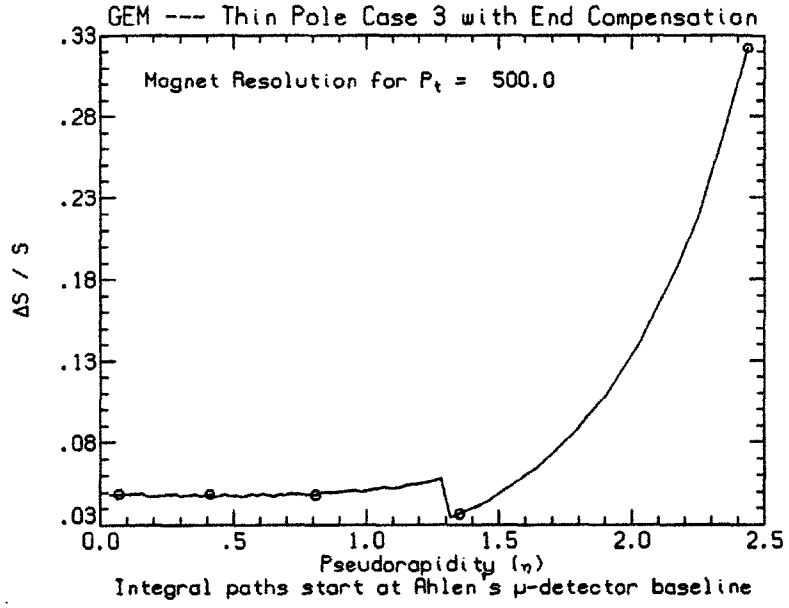

Figure 127: Resolution for constant P_t as a function of η.

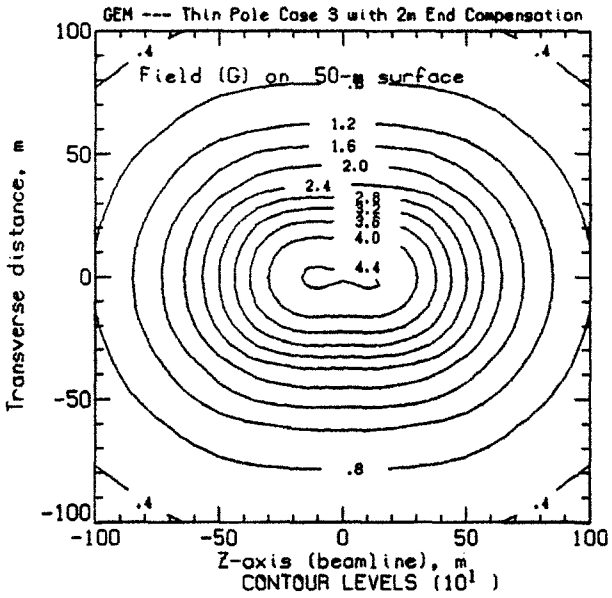

Figure 135: Isogauss contours of the field on a surface at a nominal elevation of 50 m above the beamline (centerline).

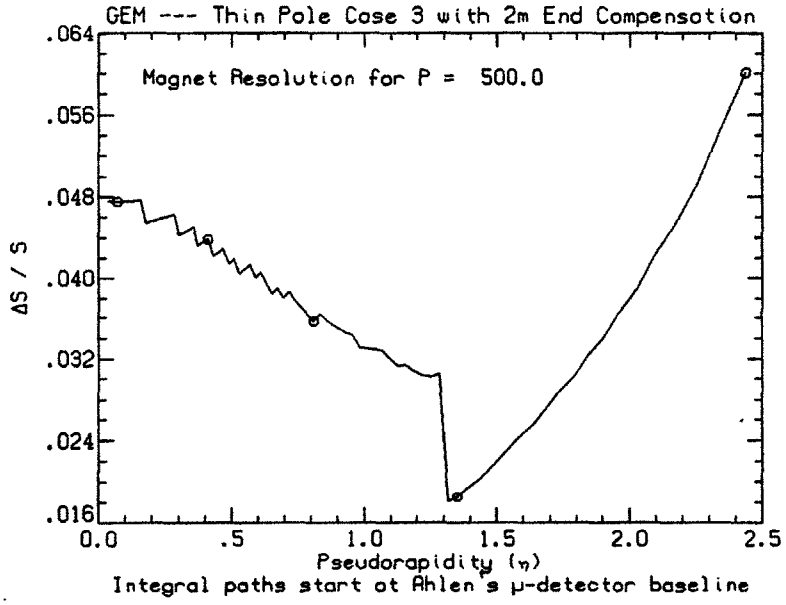

Figure 136: Resolution for constant P as a function of η.

A.1.8 Thin pole case 6

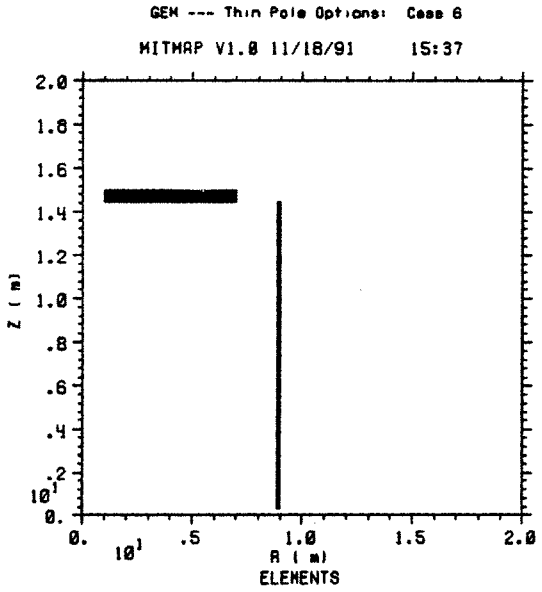

Figure 108: Side view of a superconducting solenoid with a thin pole (cf. Appendix A.1.5) but with an 0.7 m center gap in the solenoid. Note that the beam axis (the z axis) is vertical on the page and the transverse (radial) axis is horizontal.

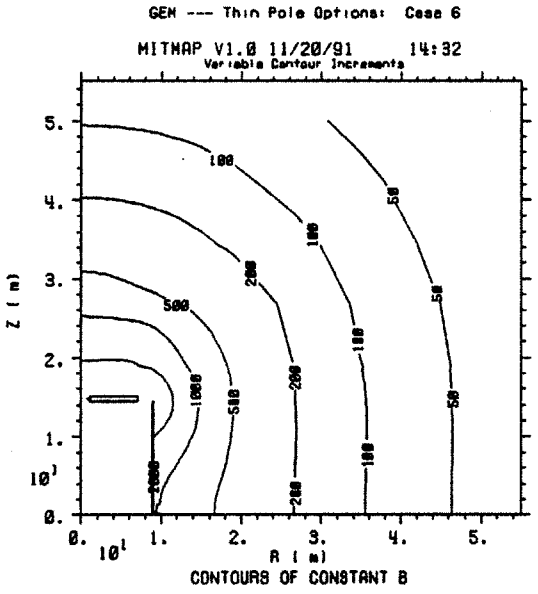

Figure 109: Contours of constant $|\vec{B}|$ superposed on a side view of the magnet; isopleths are labeled in gauss.

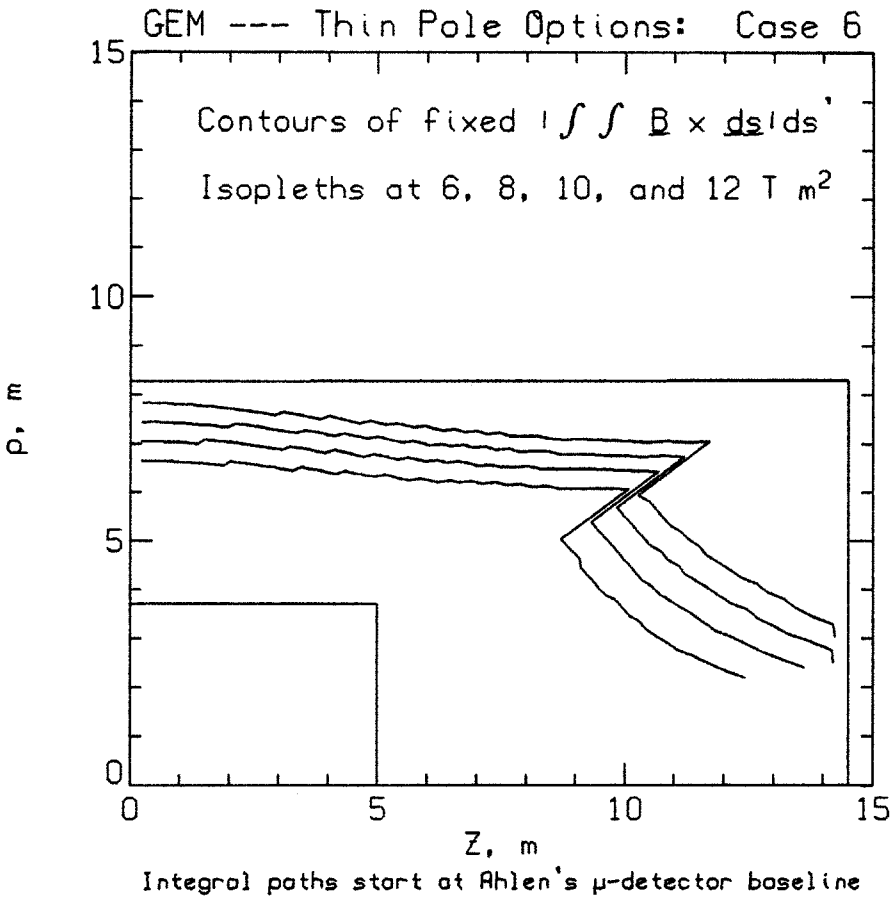

Figure 118: Isopleths of constant $\mathcal{BL}^2$ superposed on a sketch of the GEM concept; isopleths increase with distance from the origin.

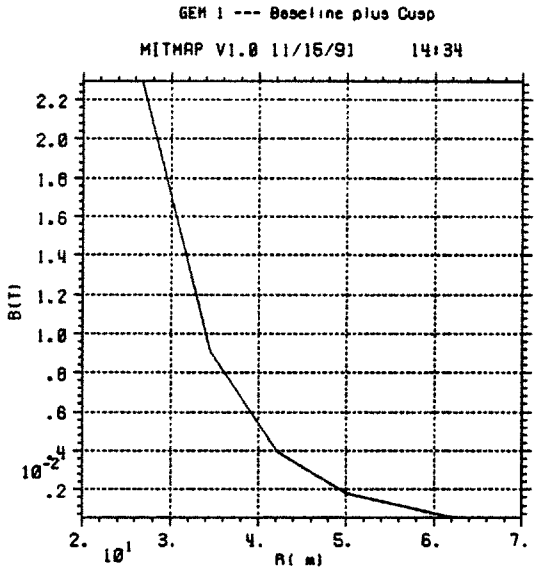

Figure 234: $|\vec{B}|$ versus radius near the surface.

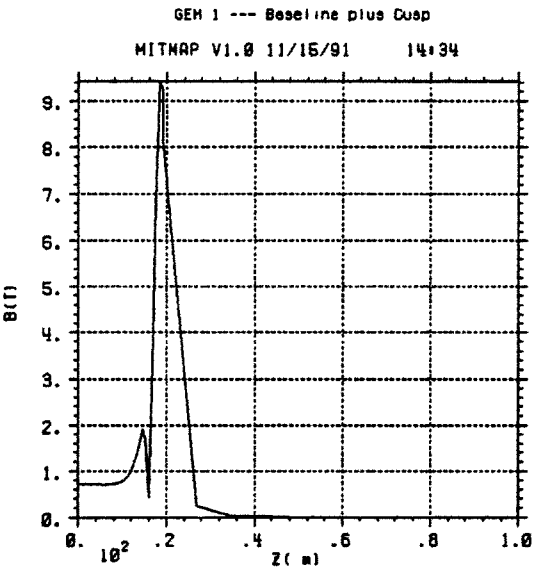

Figure 235: $|\vec{B}|$ versus z on axis in the hall.

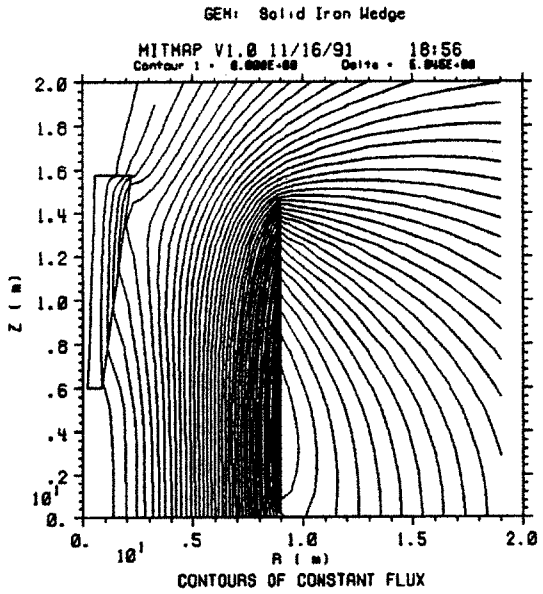

Figure 246: Flux lines superposed on a side view of the magnet design.

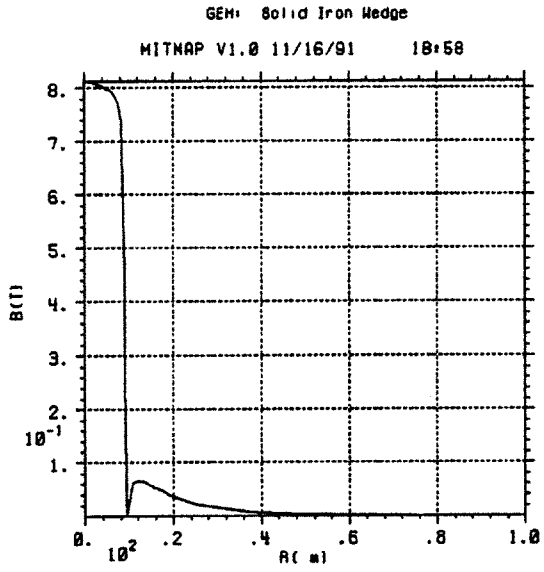

Figure 247: $|\vec{B}|$ versus radius in the hall.

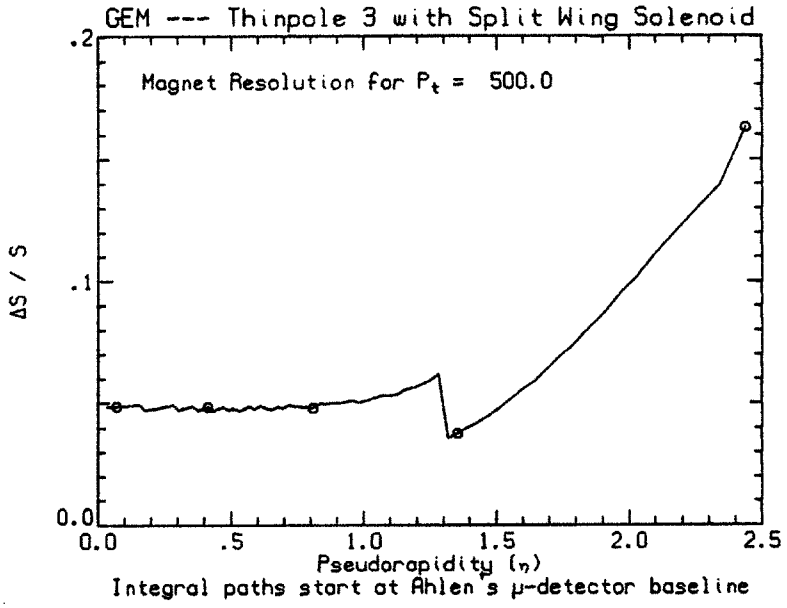

Figure 215: Resolution for constant P_t as a function of η.

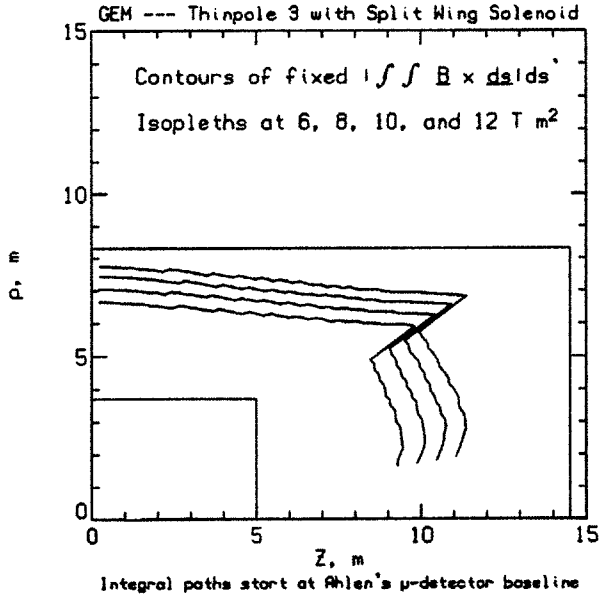

Figure 216: Isopleths of constant $\mathcal{BL}^2$ superposed on a sketch of the GEM concept; isopleths increase with distance from the origin.

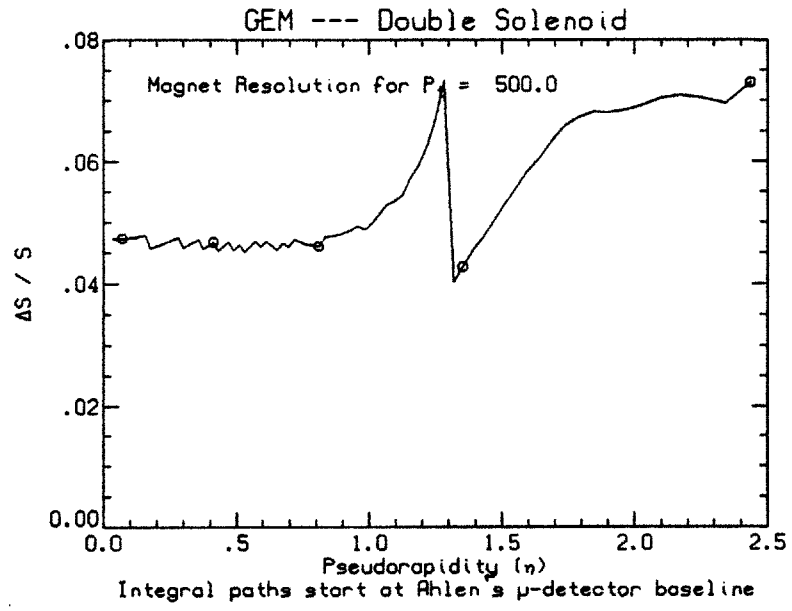

Figure 225: Resolution for constant P_t as a function of η.

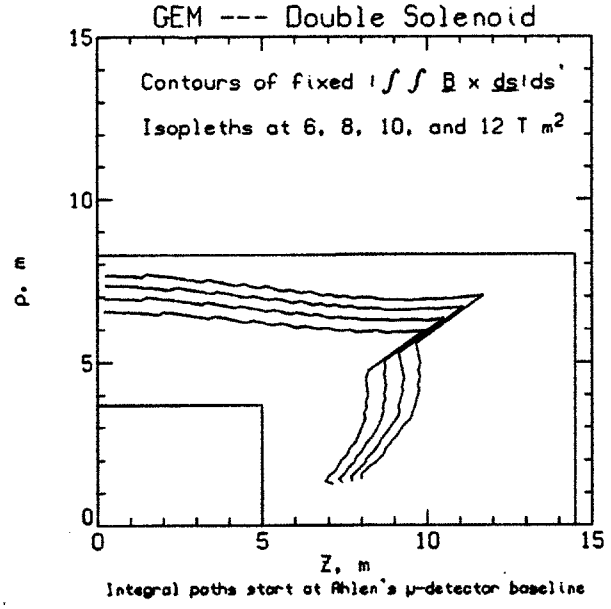

Figure 226: Isopleths of constant $\mathcal{BL}^2$ superposed on a sketch of the GEM concept; isopleths increase with distance from the origin.

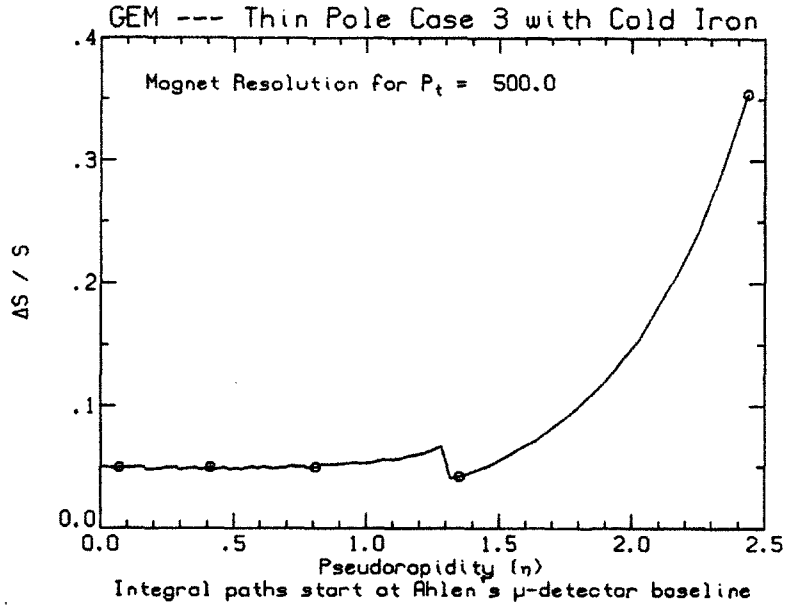

Figure 195: Resolution for constant P_t as a function of η.

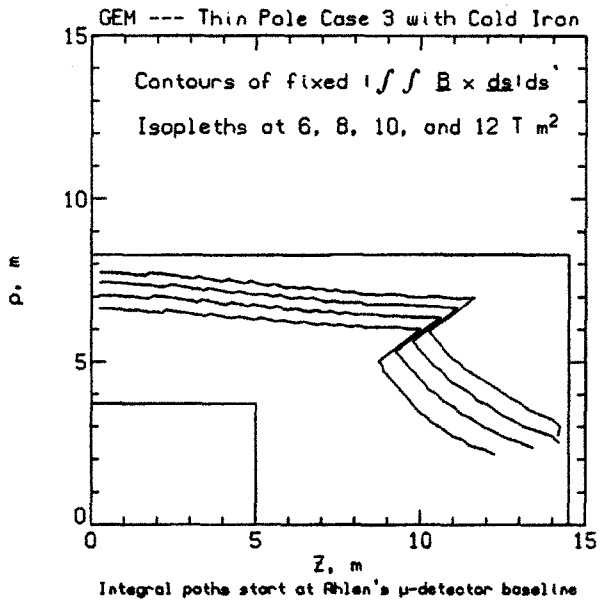

Figure 196: Isopleths of constant $\mathcal{BL}^2$ superposed on a sketch of the GEM concept; isopleths increase with distance from the origin.

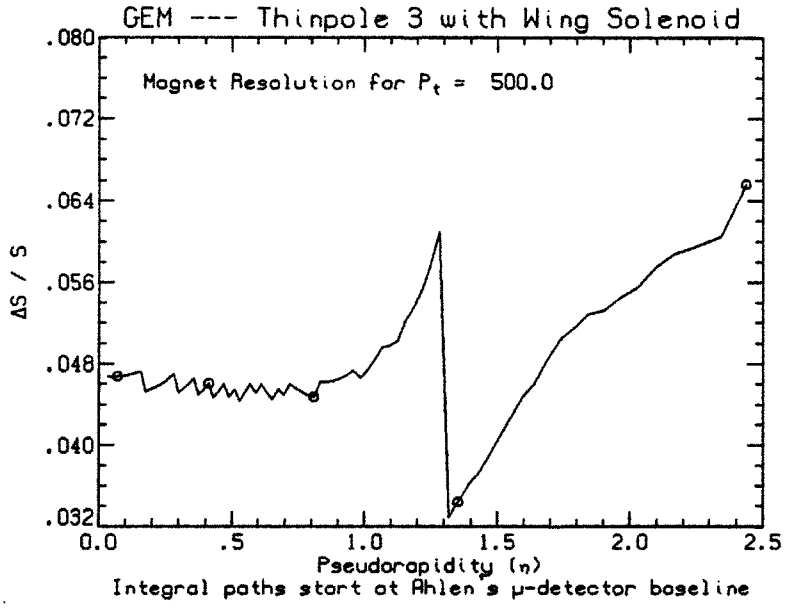

Figure 205: Resolution for constant P_t as a function of η.

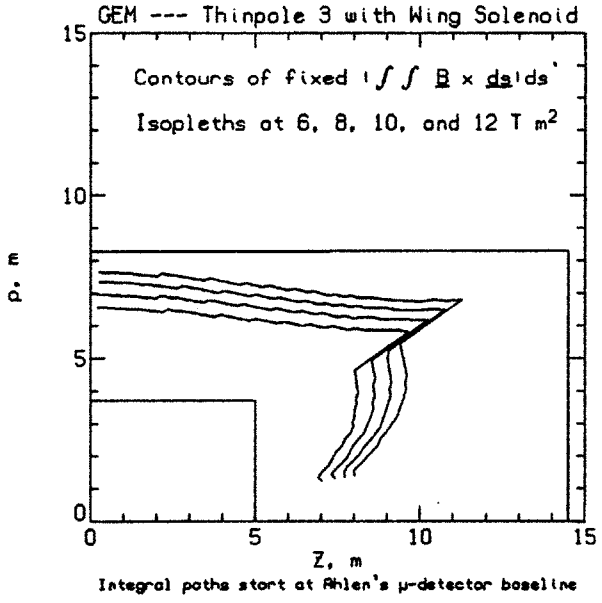

Figure 206: Isopleths of constant BL^2 superposed on a sketch of the GEM concept; isopleths increase with distance from the origin.

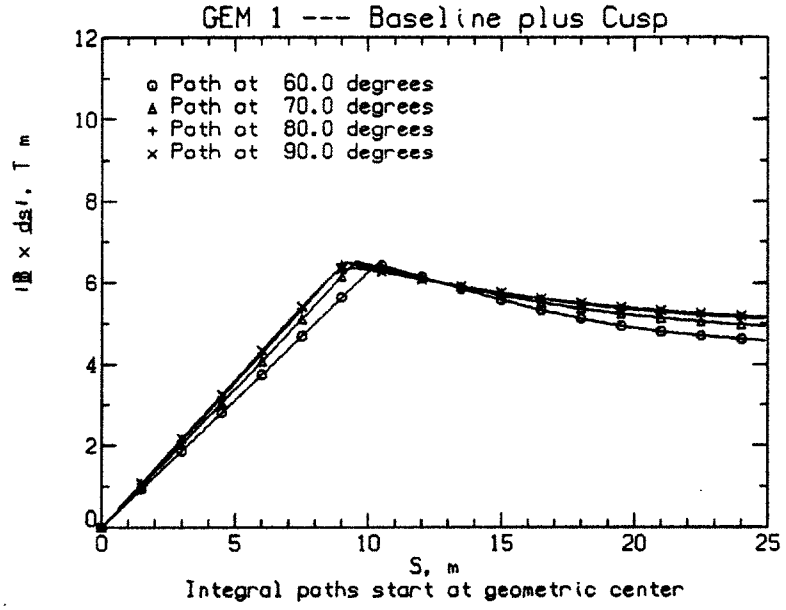

Figure 240: Plot of $|\vec{\mathcal{I}}|$ versus path length from the interaction point for tracks at 60, 70, 80, and 90° (from the beam line).

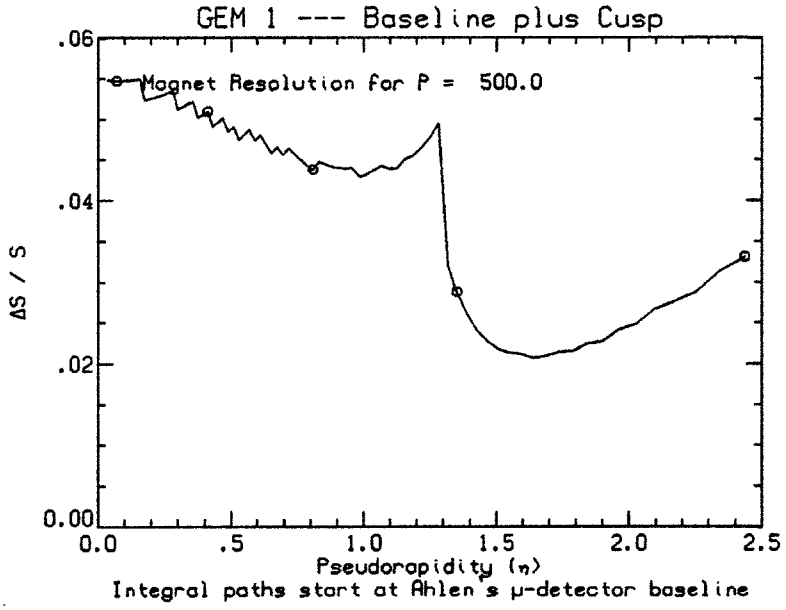

Figure 241: Resolution for constant P as a function of η.

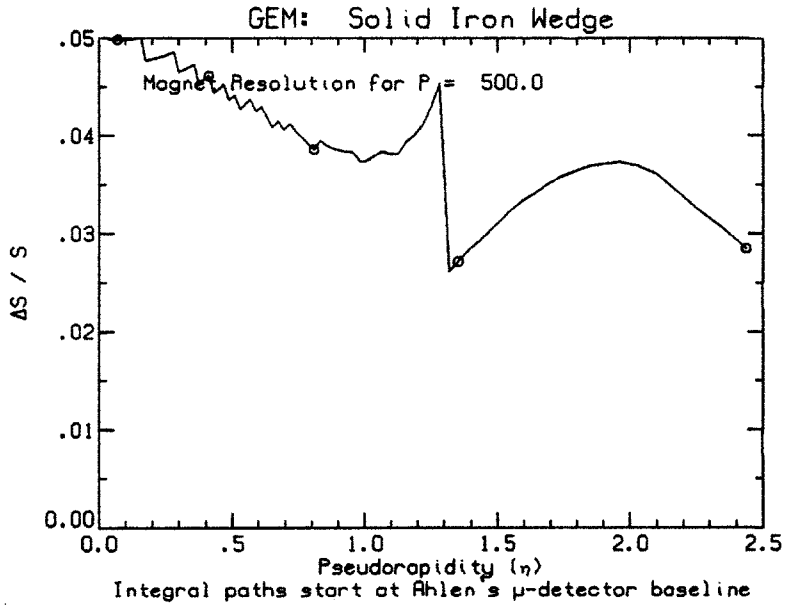

Figure 250: Resolution for constant P as a function of η.

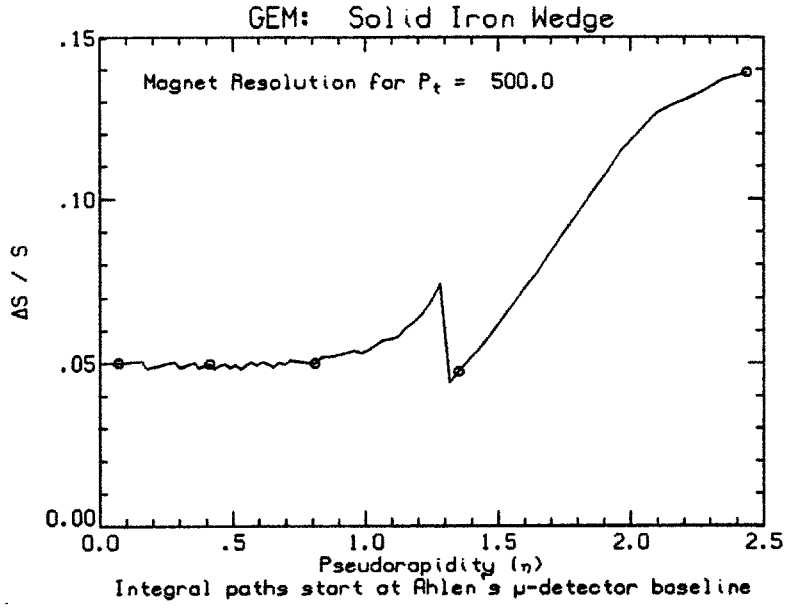

Figure 251: Resolution for constant P_t as a function of η.

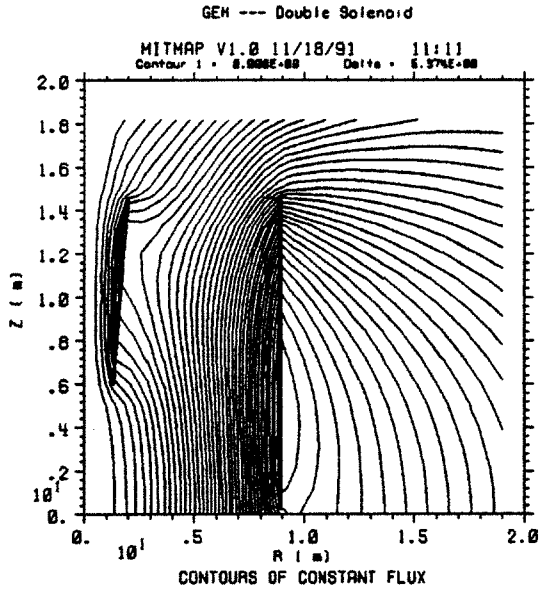

Figure 219: Flux lines superposed on a side view of the magnet design.

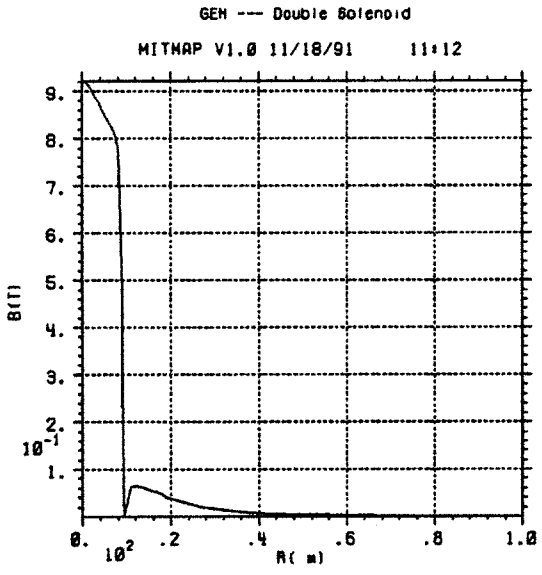

Figure 220: $|\vec{B}|$ versus radius in the hall.

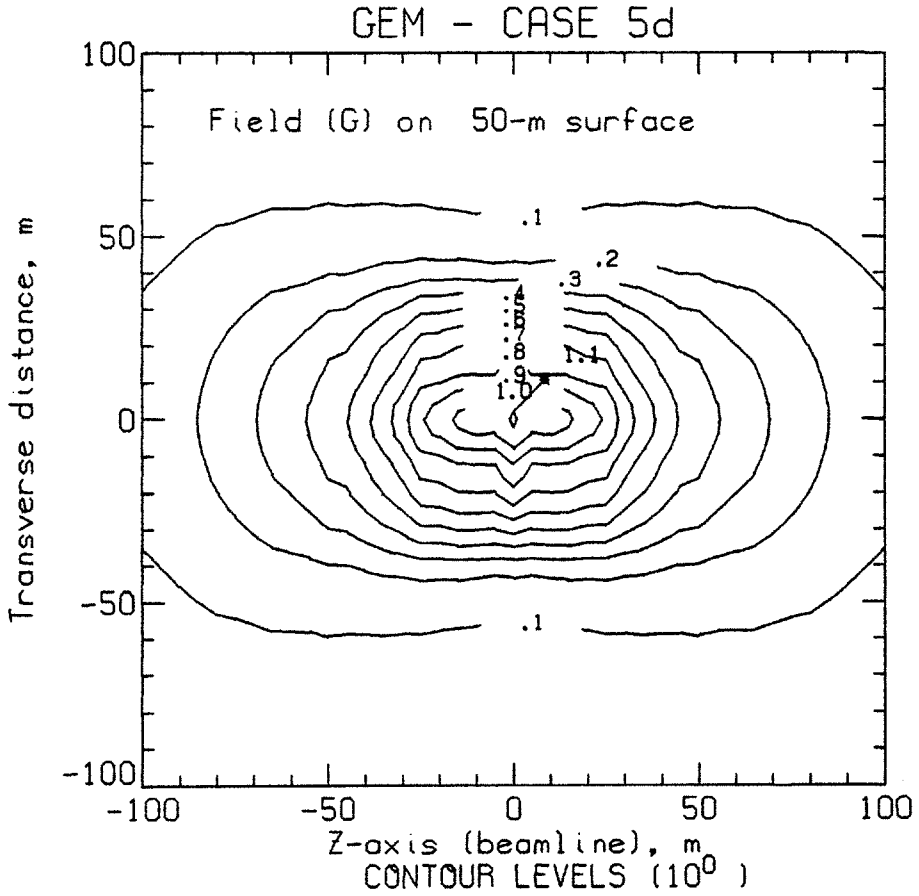

Figure 229: Isogauss contours of the field on a surface at a nominal elevation of 50 m above the beamline (centerline).

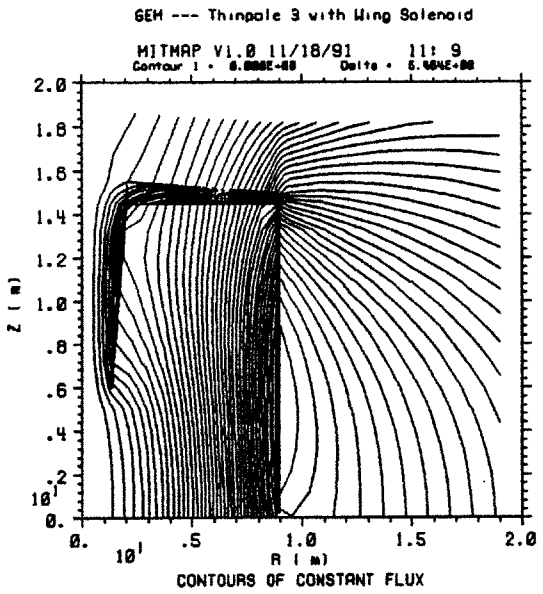

Figure 199: Flux lines superposed on a side view of the magnet design.

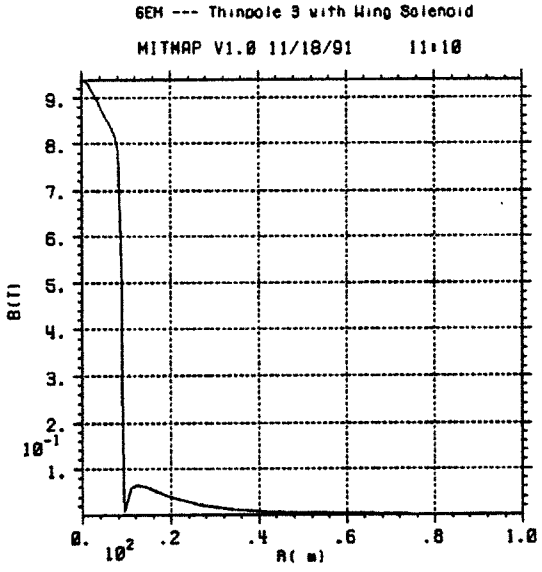

Figure 200: $|\vec{B}|$ versus radius in the hall.

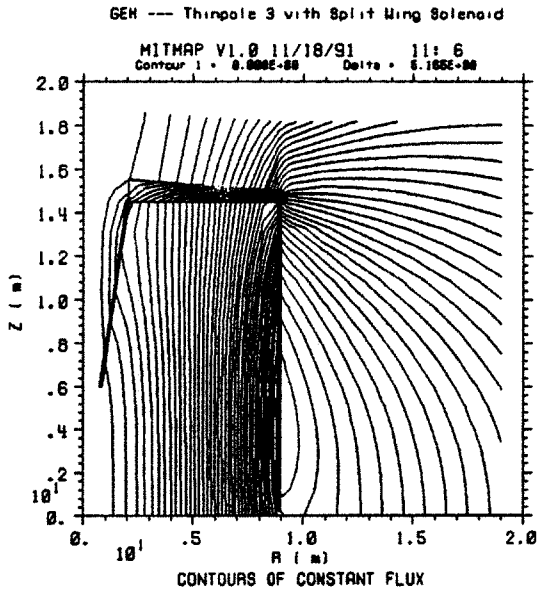

Figure 209: Flux lines superposed on a side view of the magnet design.

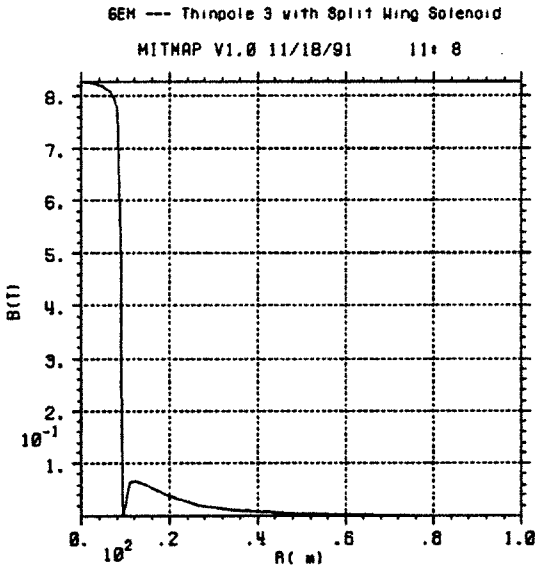

Figure 210: $|\vec{B}|$ versus radius in the hall.

A.3 Alternatives of some interest

A.3.1 Solid iron wedge

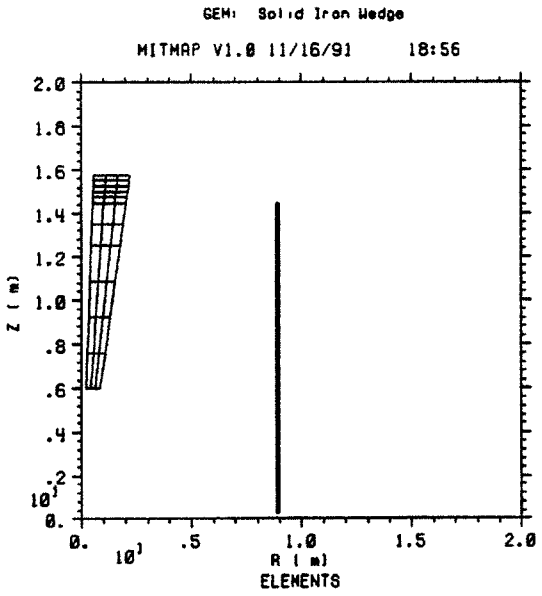

Figure 244: Side view of a superconducting solenoid with a solid iron wedge. Note that the beam axis (the z axis) is vertical on the page and the transverse (radial) axis is horizontal.

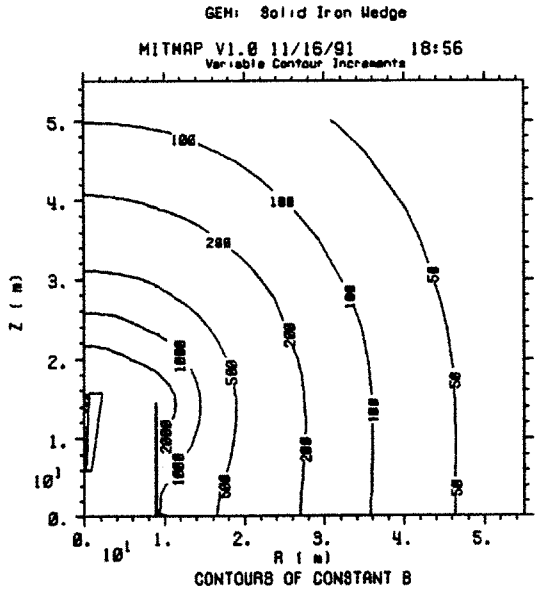

Figure 245: Contours of constant $|\vec{B}|$ superposed on a side view of the magnet; isopleths are labeled in gauss.

A.3.2 50% iron wedge

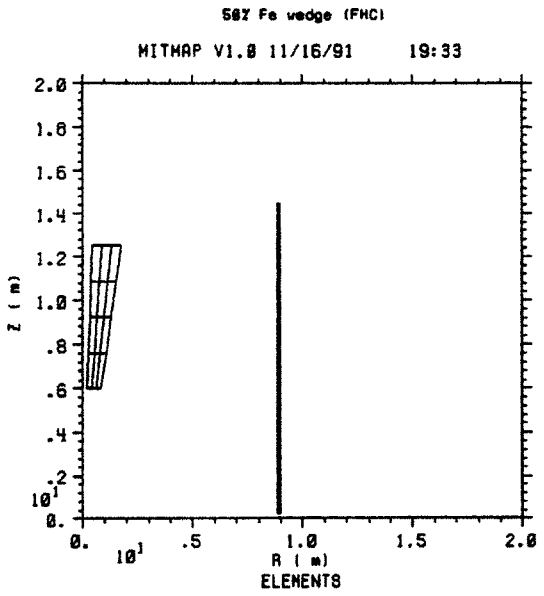

Figure 253: Side view of a superconducting solenoid with a 50% iron forward hadron calorimeter (half iron wedge). Note that the beam axis (the z axis) is vertical on the page and the transverse (radial) axis is horizontal.

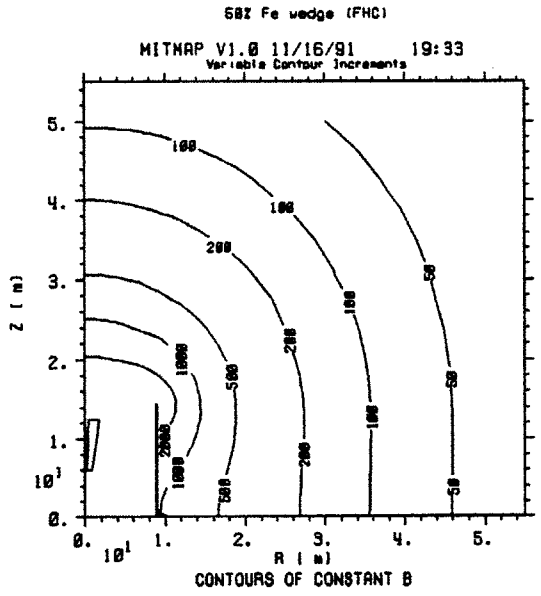

Figure 254: Contours of constant $|\vec{B}|$ superposed on a side view of the magnet; isopleths are labeled in gauss.

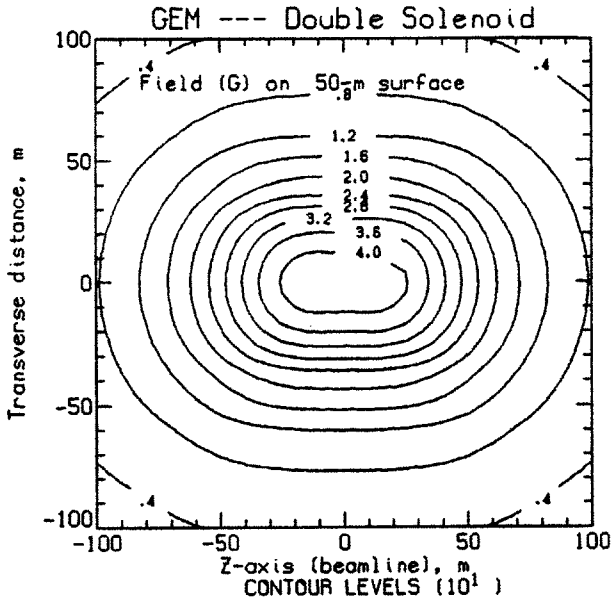

Figure 223: Isogauss contours of the field on a surface at a nominal elevation of 50 m above the beamline (centerline).

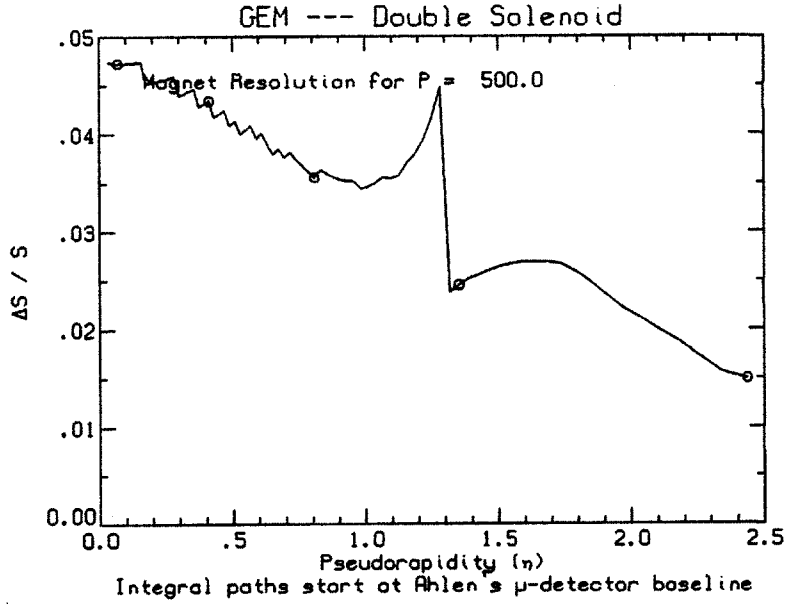

Figure 224: Resolution for constant P as a function of η.

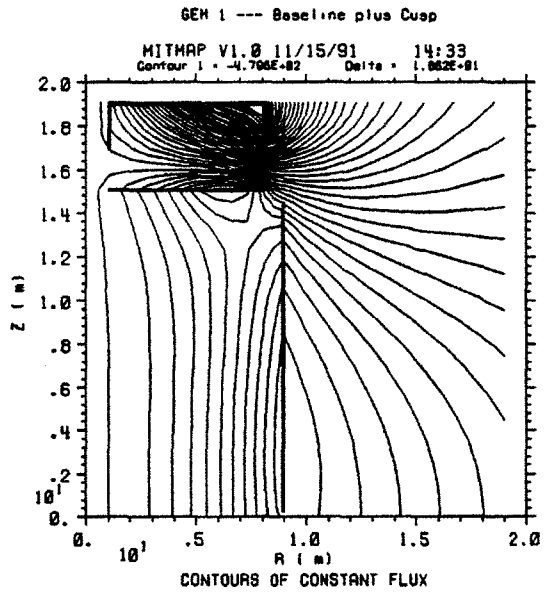

Figure 232: Flux lines superposed on a side view of the magnet design.

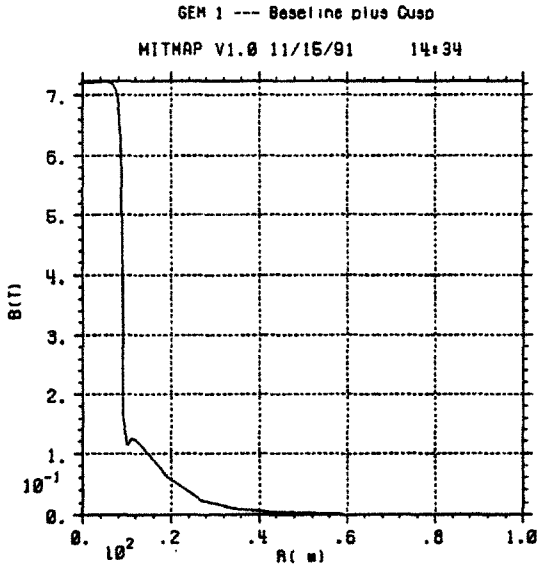

Figure 233: $|\vec{B}|$ versus radius in the hall.

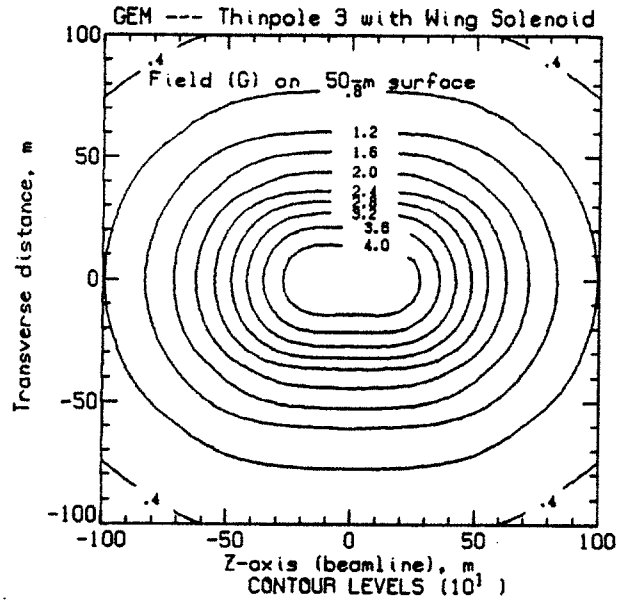

Figure 203: Isogauss contours of the field on a surface at a nominal elevation of 50 m above the beamline (centerline).

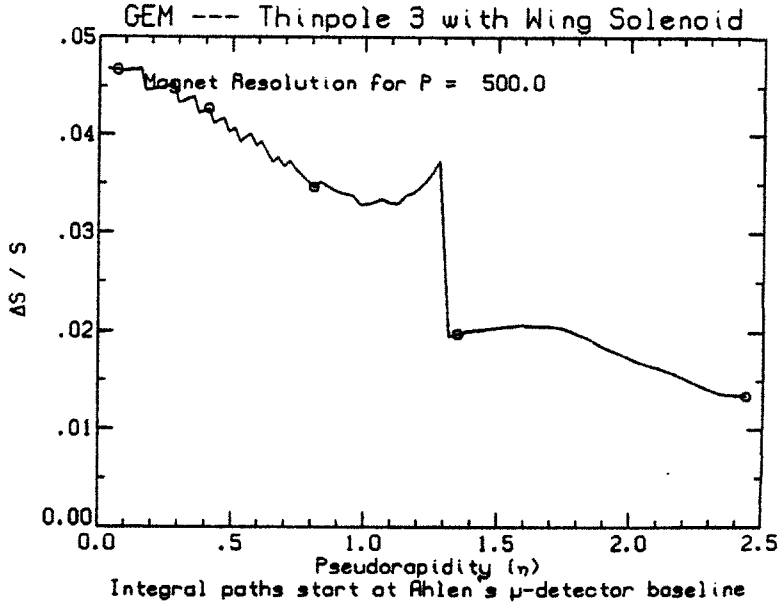

Figure 204: Resolution for constant P as a function of η.

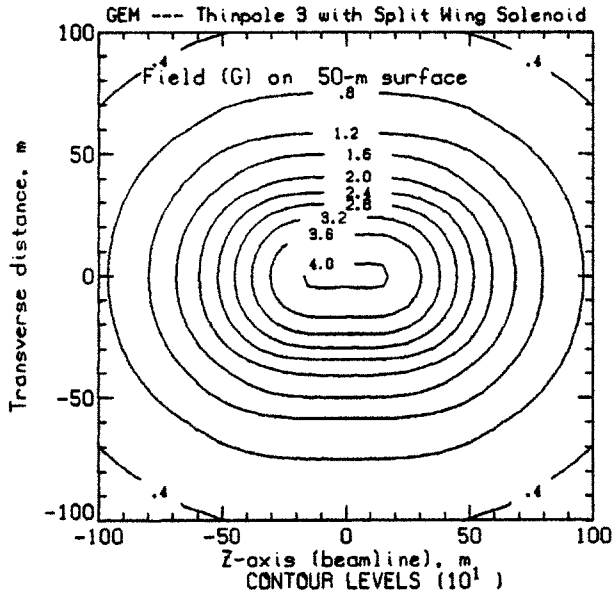

Figure 213: Isogauss contours of the field on a surface at a nominal elevation of 50 m above the beamline (centerline).

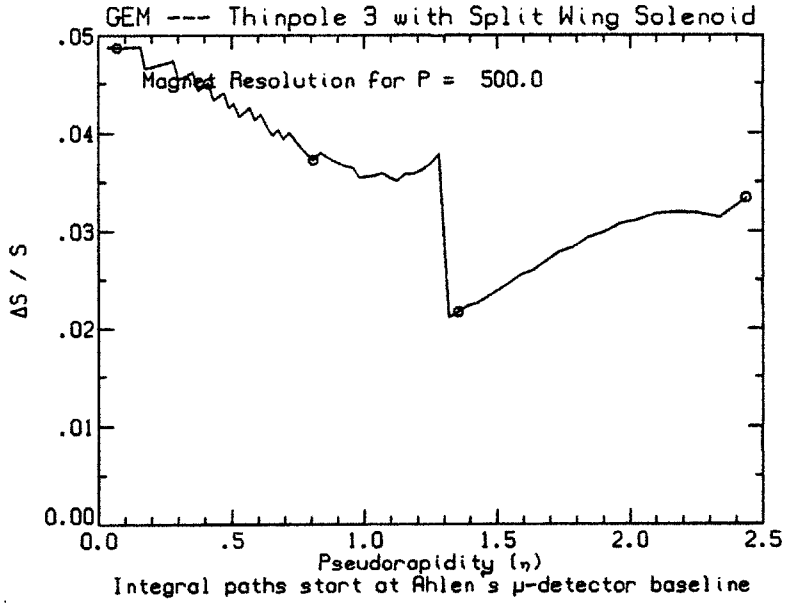

Figure 214: Resolution for constant P as a function of η.

stops) for a 500 GeV track:

$$S = .3 / 8(500)\ (.823)\ [4.93]^2 / \sin\theta = 1.48 \times 10^{-3} \text{ meters} / \sin\theta = 1.48 \text{ mm} / \sin\theta$$

The Sagitta grows from 1.48 mm to 2.85 mm. From 90° down to 31.3°.

Since the NDC magnet has a finite length of 14.5 - 6 = 8.5 meters, we have for angles below 31.3 (which is the angle where the solenoid stops):

$$L = L(0°) / \cos\theta = 8.5 / \cos\theta$$

$$S = (.3 / (8\ |P|))\ |B|\ \sin\theta\ (L\ (0°))^2 / \cos^2\theta = (.3 / (8(500)))\ (.823)\ \tan\theta\ (8.5)^2 / \cos\theta$$

$S = (.3 / (8(500))\ (.823)\ (.176)\ (8.5)^2 / .99 = 7.93 \times 10^{-4}$ meters or about .793 mm

Even in this case, $B\perp L^2$ is a useful figure of merit. If we assume an overall resolution of 35 microns then the resolution of a 500 GeV/c track at 10° is ~ 35 / 793 ~ 5%, which is an often quoted design parameter. If we wished to keep the Sagitta at 10°, equal to 1.48 mm, we would have to increase the coil length to = 35.2 meter, which is clearly practical.

Hence it seems the baseline magnet will provide resolution of at least 5% at a momentum of 500 GeV down to an angle of about 10°. It seems reasonable to consider an outside toroid for angles smaller than about 10°

Figure 2 shows the basic concept.

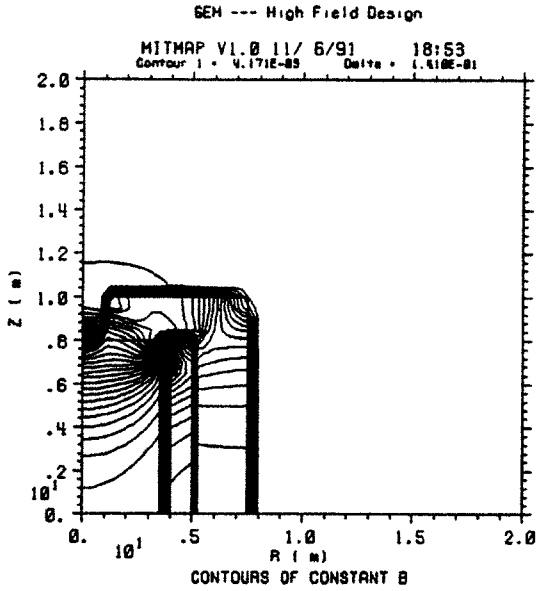

Figure 308: Contours of constant $|\vec{B}|$ superposed on a side view of the "Ko" option.

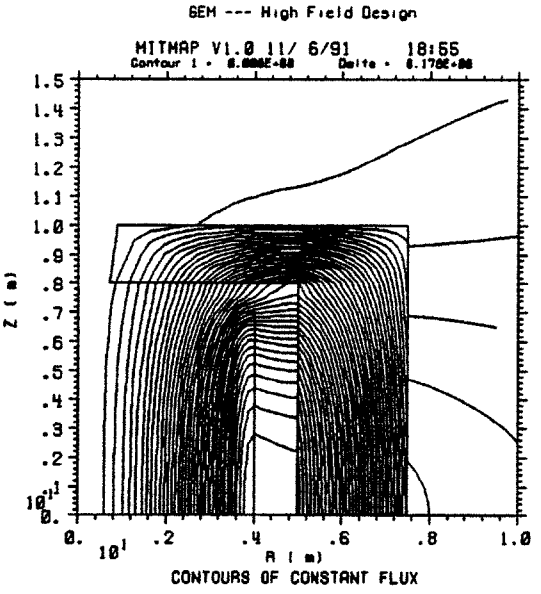

Figure 309: Flux lines superposed on a side view of the "Ko" option.

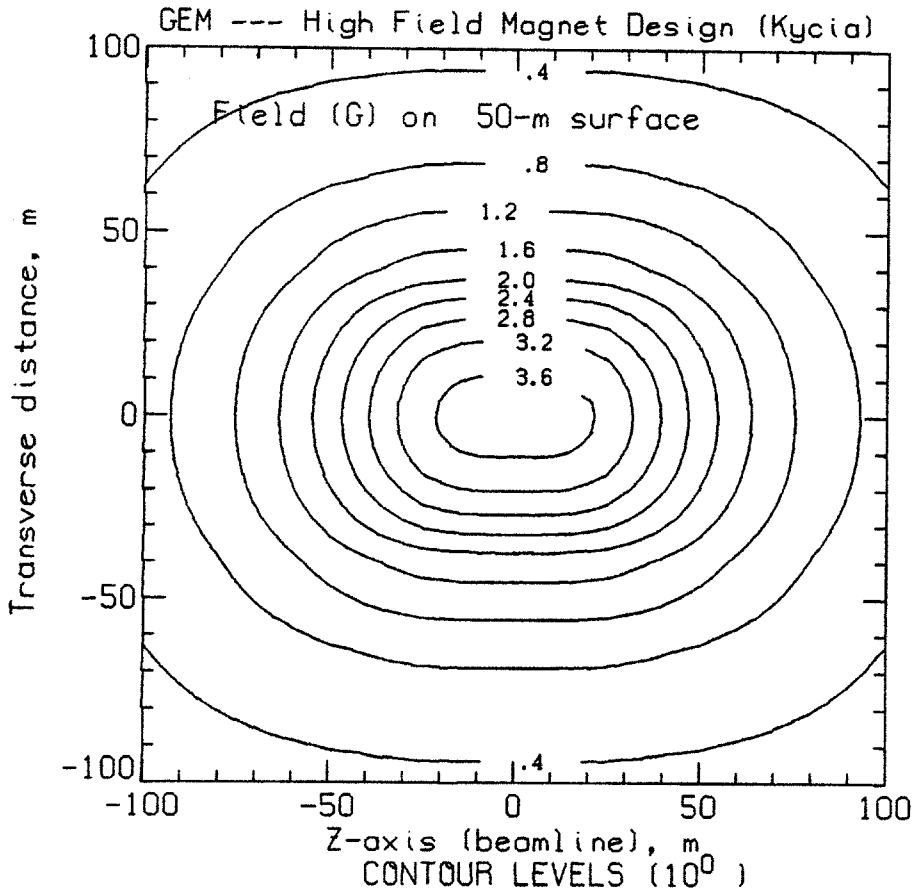

Figure 318: Isogauss contours of the field from the "Kycia" option on a surface at a nominal elevation of 50 m above the beamline (centerline). Note the peak field at an elevation of 50 m is less than 4 G.

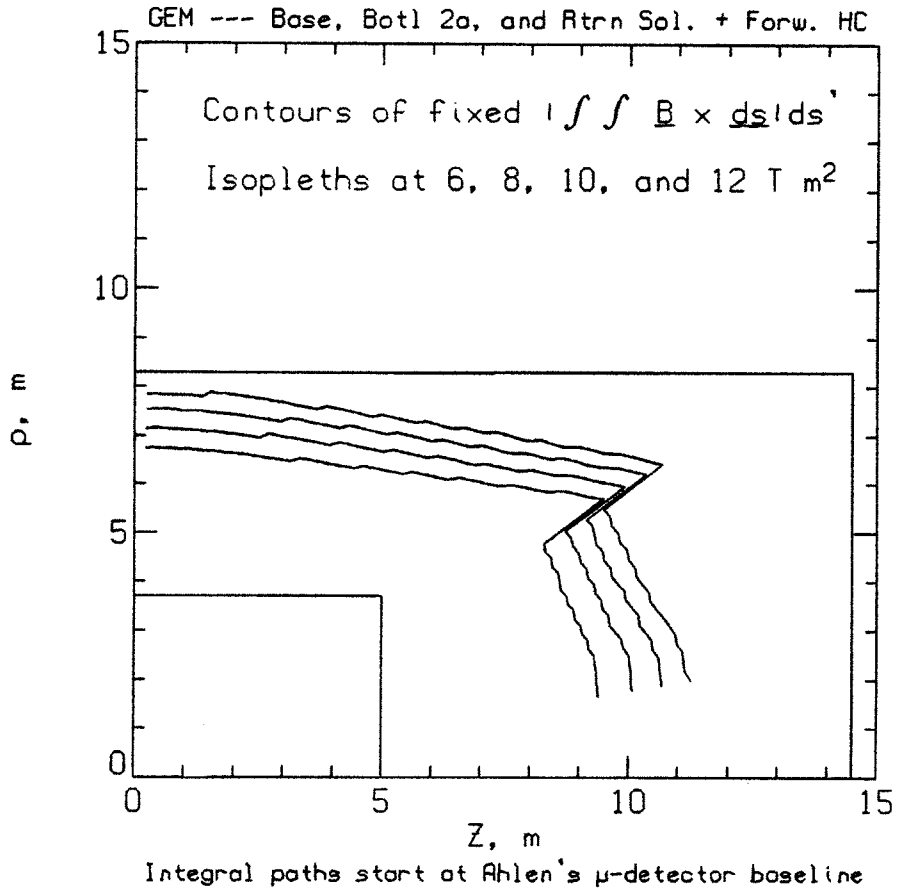

Figure 292: Isopleths of constant $\mathcal{BL}^2$ superposed on a sketch of the GEM concept; isopleths increase with distance from the origin.

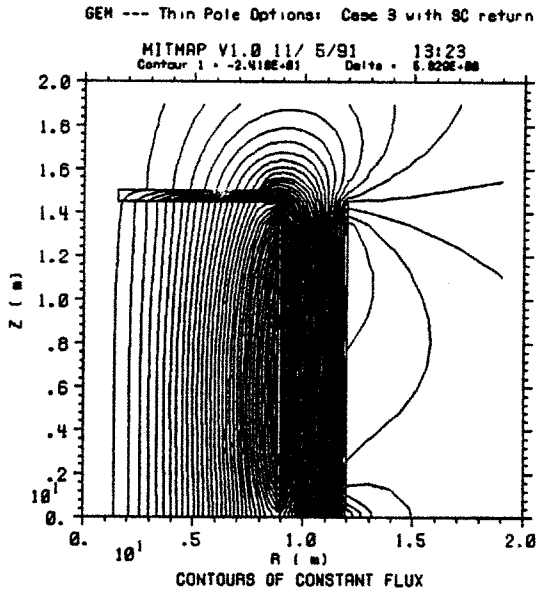

Figure 300: Flux lines superposed on a side view of the magnet design.

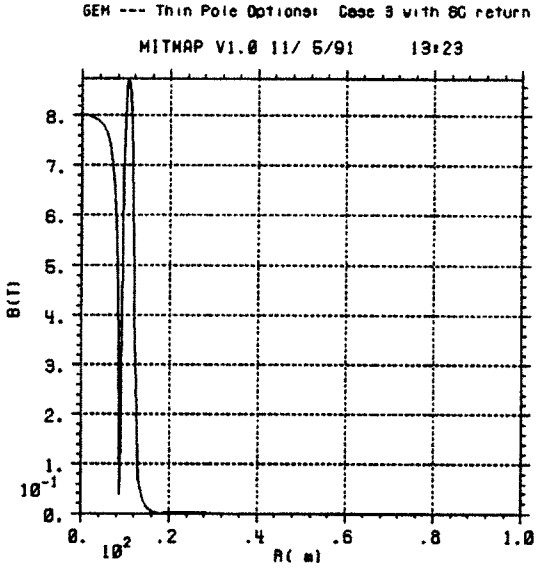

Figure 301: $|\vec{B}|$ versus radius in the hall.

We will show that:

$$S = (.3 / (2P))\ BL^2 / \cos\theta = (.3 / (2P))\ B\ t^2 / \cos^3\theta$$

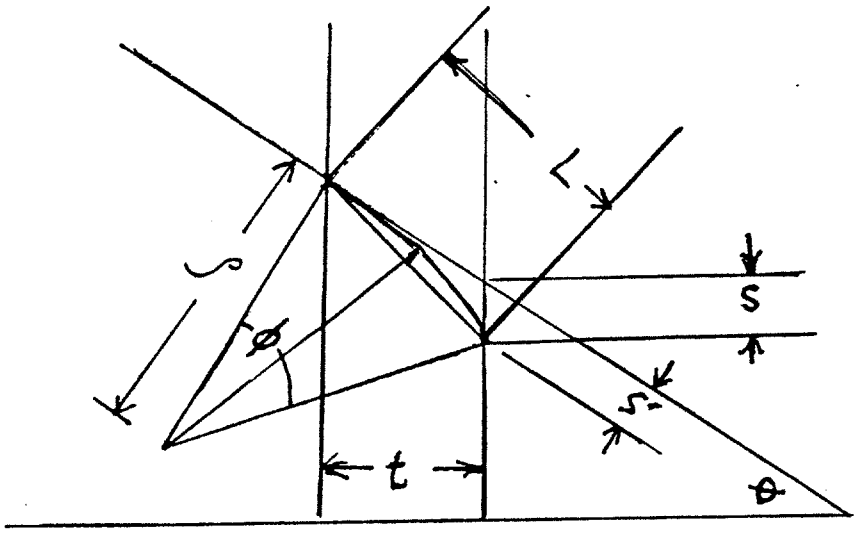

FIG 3

$$\phi = L / \rho = .3\ BL / P$$

$$S' = \phi\ L / 2 = (.3\ B / 2P)\ L^2$$

$$L = t / \cos\theta$$

$$S = S' / \cos\theta$$

$$S = (.3 / (2P))\ B\ t^2 / \cos^3\theta$$

Let us choose the following parameters:

$t = 3$
$B = 1$
$\theta = 10°, 2°$
$P = 500$

$$S = (.3 / ((2)(500)))\ (3)^2 / \cos^3(10) = 3 \times 10^{-3} = 2.8 \text{ mm for } 10°$$

$$S = (.3 / ((2)\ (500)))\ (3)^2 / \cos^3\ (2) = 2.7 \text{ mm for } 2°$$

At both angles the toroid has as good or better resolution than the solenoid at the same momentum.

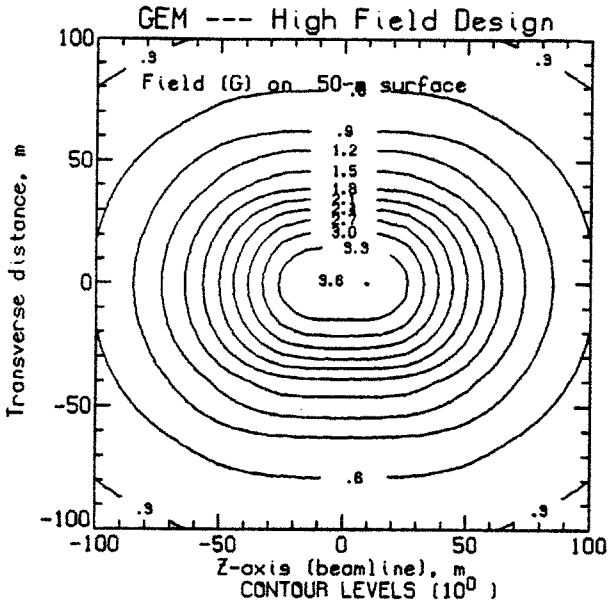

Figure 312: Isogauss contours of the field from the "Ko" option on a surface at a nominal elevation of 50 m above the beamline (centerline). Note the peak field at an elevation of 50 m is less than 4 G.

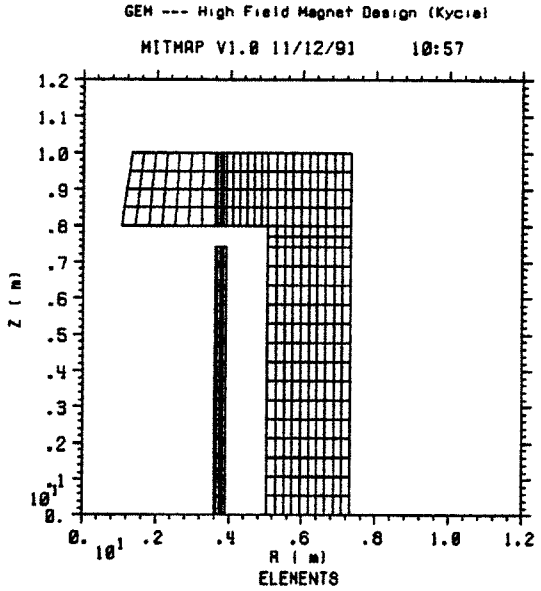

Figure 313: Side view of one quadrant of the "Kycia" option; the high field superconducting solenoid and iron return frame are shown.

DRAFT

MAGNETIC FIELDS AND MOMENTUM MEASUREMENT AND ERROR ANALYSIS FOR FRESHMEN

Irwin A. Pless

16 July 1991

Charged particles bend in magnetic fields. It is the measurement of this bend and the error on the measurement of this bend that leads to the evaluation of the momentum of charged particles and the error on that momentum.

For the New Detector Collaboration (NDC) a resolution parameter, $B\perp \cdot L^2$ $(T \cdot M^2)$, is used to compare various magnetic field geometries and the utility of a given magnetic field geometry for various particle trajectories inside that geometry. $B\perp$ is the component of the field perpendicular to the trajectory and L is the length of the trajectory.

The following is a simplified explanation and derivation of that parameter.

As a starting point we use the familiar Lorentz force equation (neglecting units):

$F = K\ P \times B$

F is the force on the particle
P is the three momentum
B is the magnetic field

From this one easily derives, for a particle of unit charge, the following:

$$|P| = 0.3\ \rho\ |B|\ \sin\theta \qquad (1)$$
$$\rho = P / .3\ B\ \sin\theta$$

Again $|P|$ is the magnitude of the momentum in GeV/c.
$|B|$ is the magnitude of the magnetic field in tesla.
$\sin\theta$ is the sine of the angle between P and B.
ρ is the instantaneous radius of curvature in meters of the particle trajectory in the osculating (kissing) plane. The osculating plane at a point on a track contains the tangent to the track at that point and the Lorenz force vector. The Sagittas calculated in this note are also contained in the osculating plane. For the small Sagittas and turning angles considered in this note one can assume, without loss of

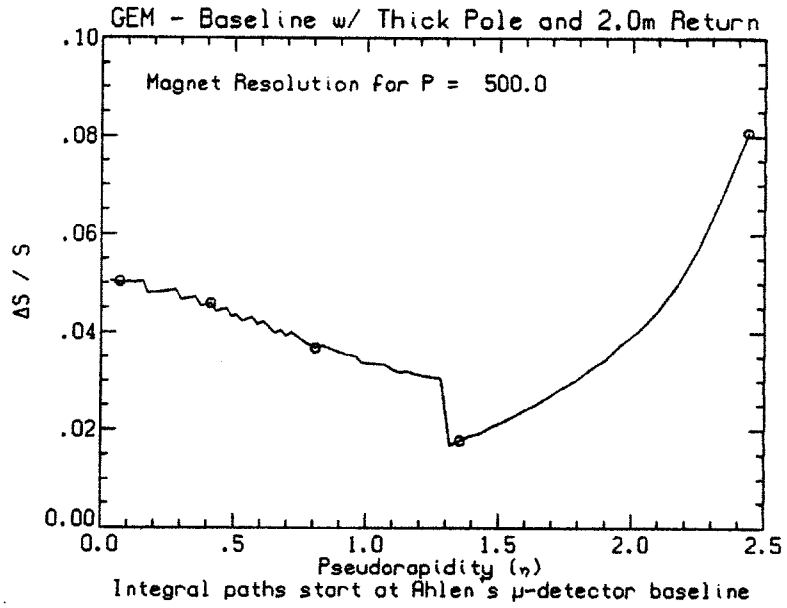

Figure 295: Resolution for constant P as a function of η.

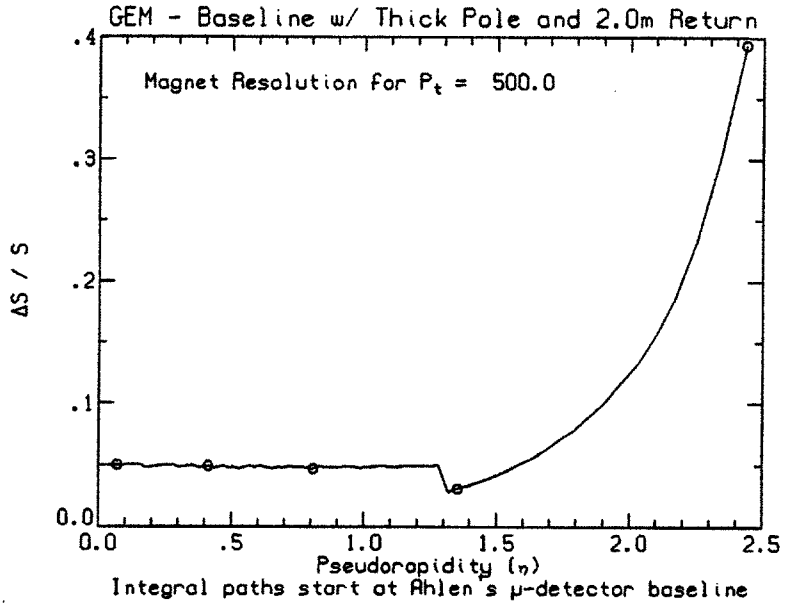

Figure 296: Resolution for constant P_t as a function of η.

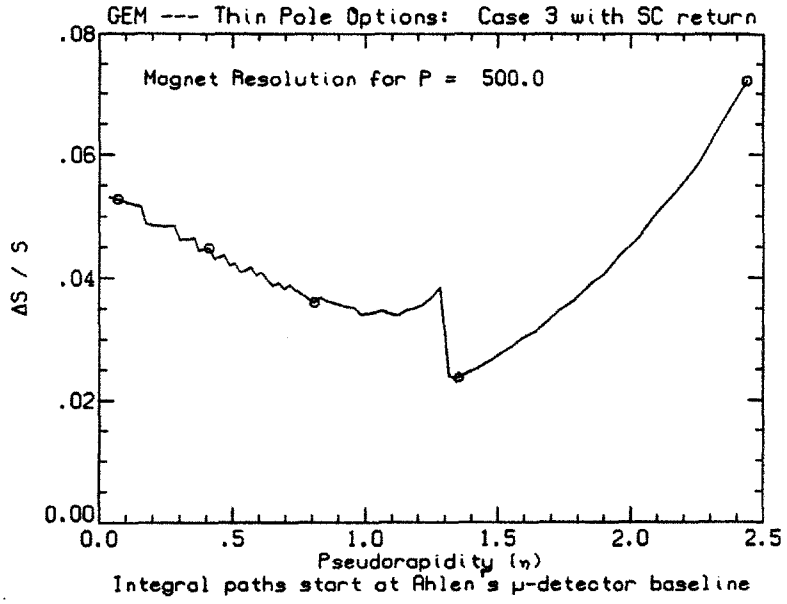

Figure 304: Resolution for constant P as a function of η.

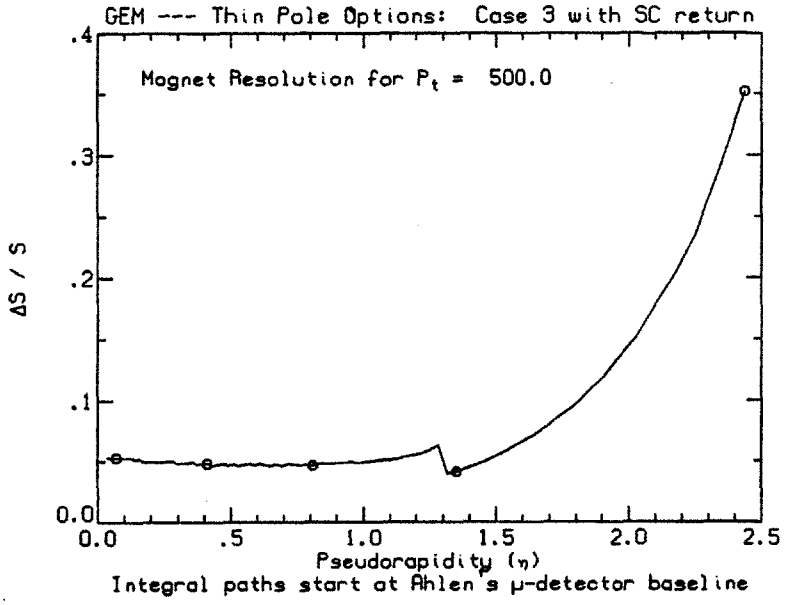

Figure 305: Resolution for constant P_t as a function of η.

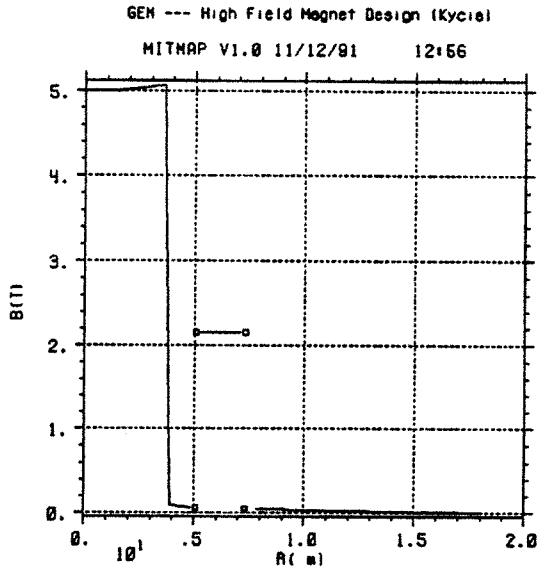

Figure 316: $|\vec{B}|$ versus radius in the hall for the "Kycia" option.

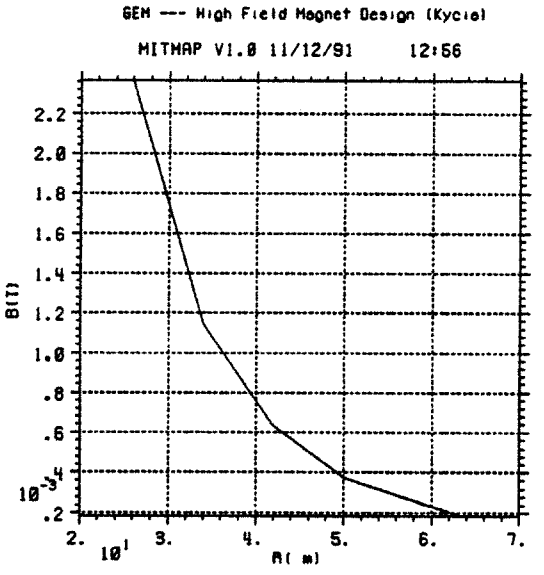

Figure 317: $|\vec{B}|$ versus radius near the surface for the "Kycia" option.

To derive formula (2) we start with:

$$d\phi = |d\mathbf{l}| / \rho(L) = .3\,|\mathbf{B} \times d\mathbf{l}| / |P|$$

$$\phi = .3 / |P| \int |\mathbf{B} \times d\mathbf{l}|$$

$$S = \rho\,(1 - \cos(\phi / 2)) = \rho / 2\,(\phi^2 / 4) = (\rho / 8)\,(.3 / P)^2\,[\int |\mathbf{B} \times d\mathbf{l}|]^2$$

Using the mean value theorem we have:

$$S = (\rho / 8)\,(.3 / |P|)^2\,(< |B| > < \sin\theta > L)^2$$

$$S = .3 / (8\,|P|) < B > < \sin\theta > L^2 \qquad (3)$$

Note $B \sin\theta = B\perp$

Setting $\sin\theta = 1$ recovers formula 2.

As an example of the use of formula (3) let us consider the base line magnet for the NDC. We restrict our study, as always, to small Sagittas, or high |P|.

R_o = 8.830 meters
R_i = 3.900 meters
} For muon detection

L (90) = 8.830 - 3.900 = 4.93 meters

Length of magnet short 6 meters
Length of magnet long 14.5 meters
} For muon detection

L (0) = 14.5 - 6 = 8.8 meters

|B| = .823 tesla

Let us calculate at the Sagitta for a 500 GeV particle between angles of 90° and 10°.

First we will look at angles from 90° to 31.3° (where the solenoid stops).

$$S = (.3 / (8P))\,B \sin\theta\,L^2\,(90) / \sin^2\theta = (.3 / 8P))\,B\,(L\,(90))^2 / \sin\theta$$

Hence for angles down to about 31.3° (which is where the solenoid

A.4.2 Superconducting return

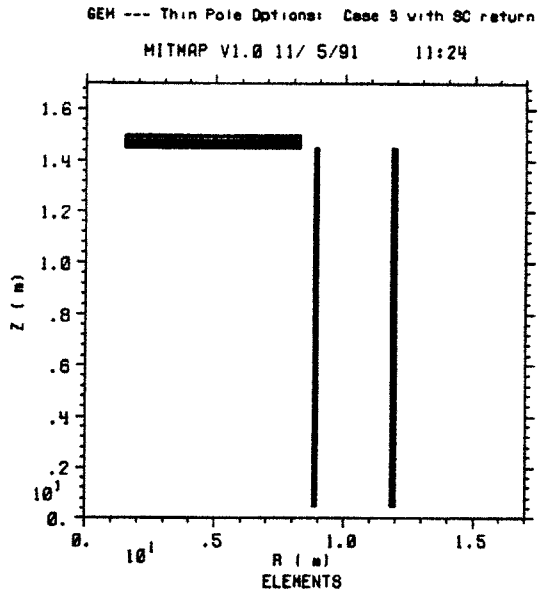

Figure 298: Side view of a superconducting solenoid with a thin end pole (cf. Appendix A.1.5) and with a superconducting return coil. Note that the beam axis (the z axis) is vertical on the page and the transverse (radial) axis is horizontal.

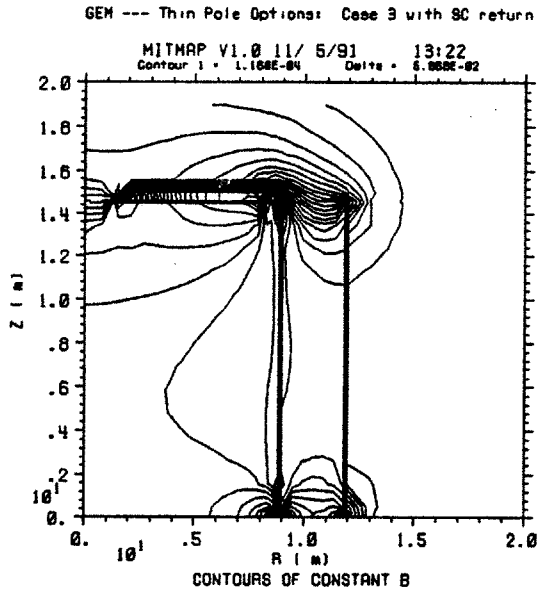

Figure 299: Contours of constant $|\vec{B}|$ superposed on a side view of the magnet design.

A.5 High Field Options

A fundamentally different approach, the "high field" approach, has been proposed by part of the collaboration. The design concept is to have a much higher uniform field (5 T) in a smaller volume with an iron return frame and use external toroids for measurements at small angles. In initial support of this work two cases were run (without toroids):

1. the original concept called the "Ko" option here (Figures 307–312), and
2. a revised approach called "Kycia" (Figures 313–318).

As the first "Ko" option was not iterated, its field is high by about 12% (cf. Figure 310 and Figure 316).

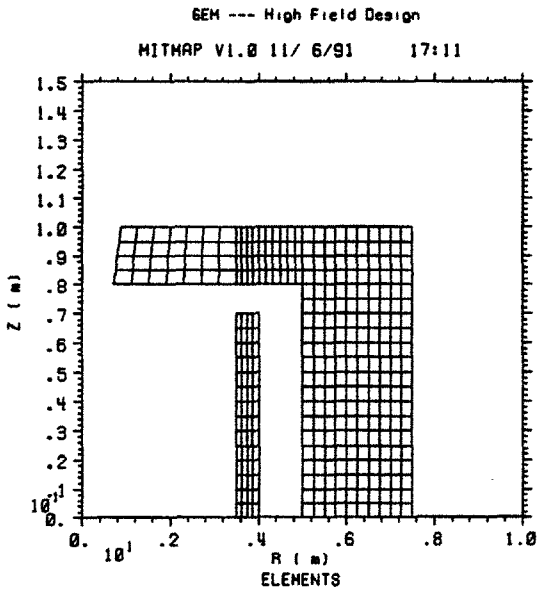

Figure 307: Side view of one quadrant of the "Ko" option; the high field superconducting solenoid and iron return frame are shown.

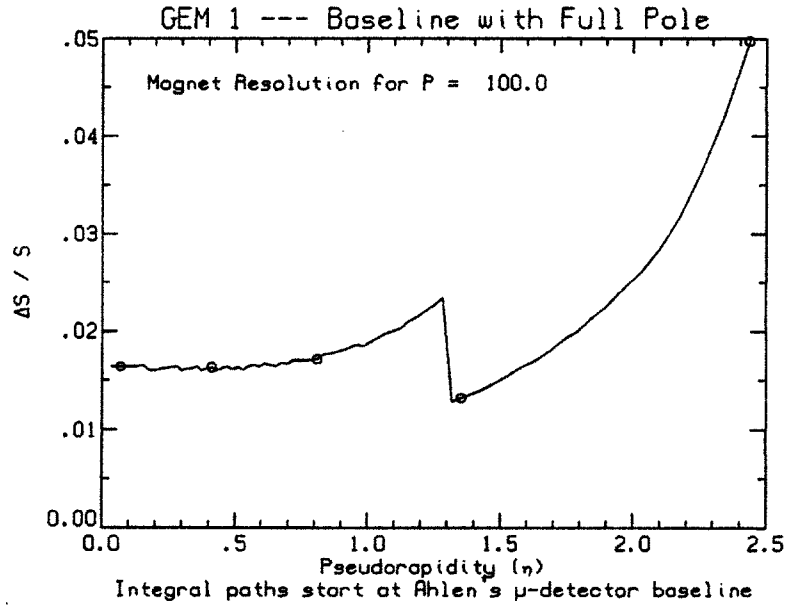

Figure 47: Resolution for constant P as a function of η.

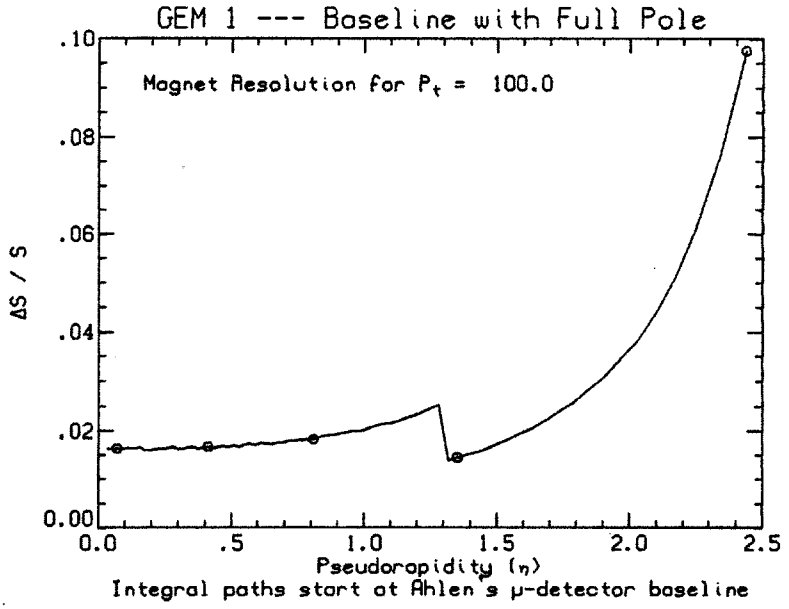

Figure 48: Resolution for constant P_t as a function of η.

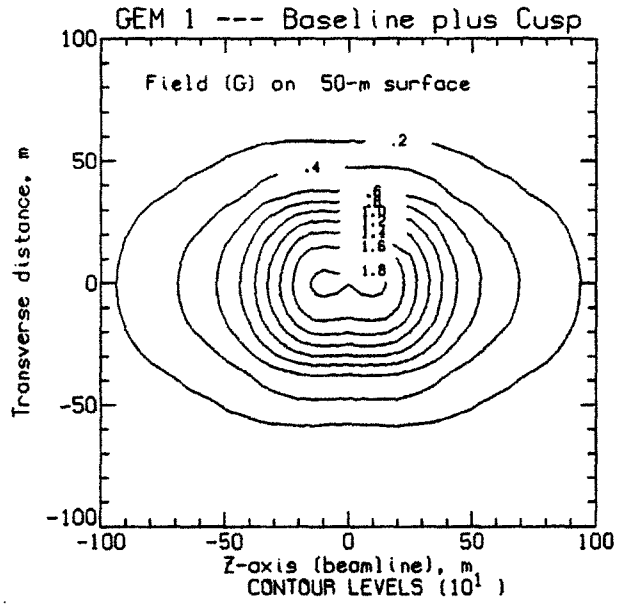

Figure 236: Isogauss contours of the field on a surface at a nominal elevation of 50 m above the beamline (centerline).

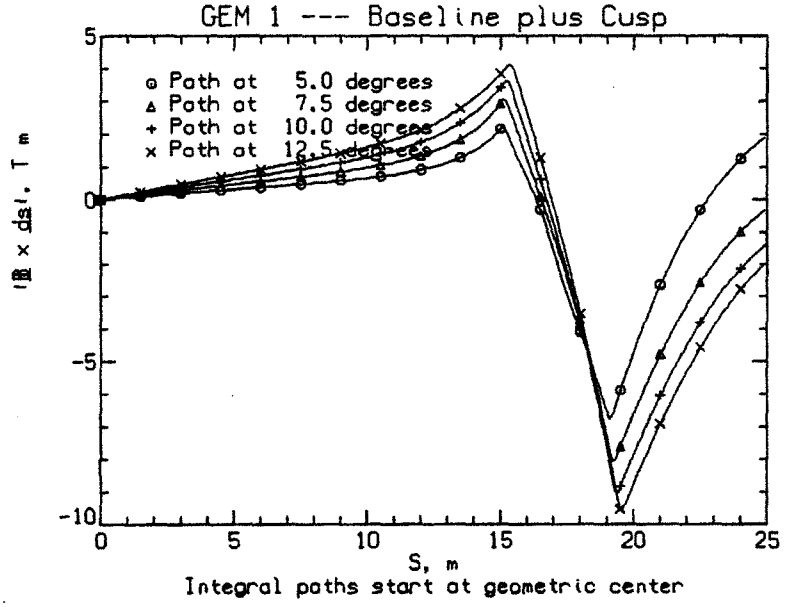

Figure 237: Plot of $|\vec{\mathcal{I}}|$ versus path length from the interaction point for tracks at 5, 7.5, 10, and 12.5° (from the beam line).

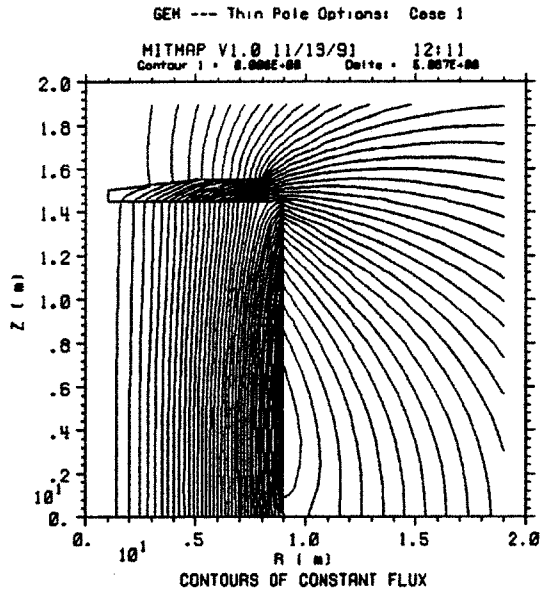

Figure 57: Flux lines superposed on a side view of the magnet design.

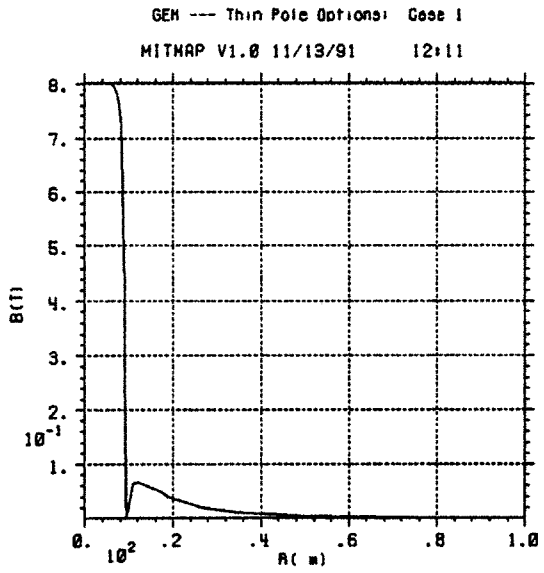

Figure 58: $|\vec{B}|$ versus radius in the hall.

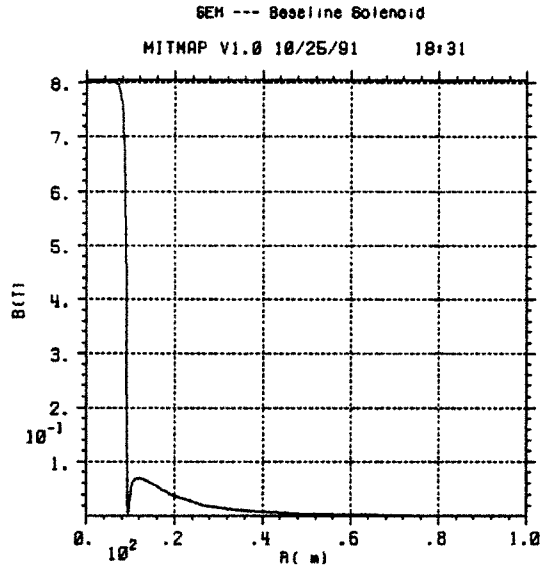

Figure 27: $|\vec{B}|$ versus radius in the hall.

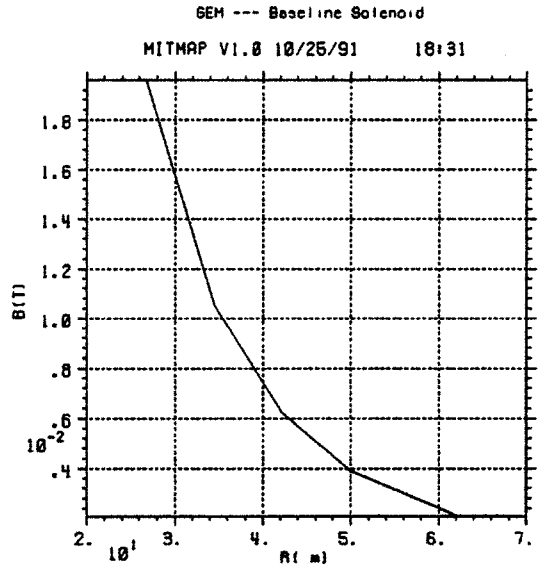

Figure 28: $|\vec{B}|$ versus radius near the surface.

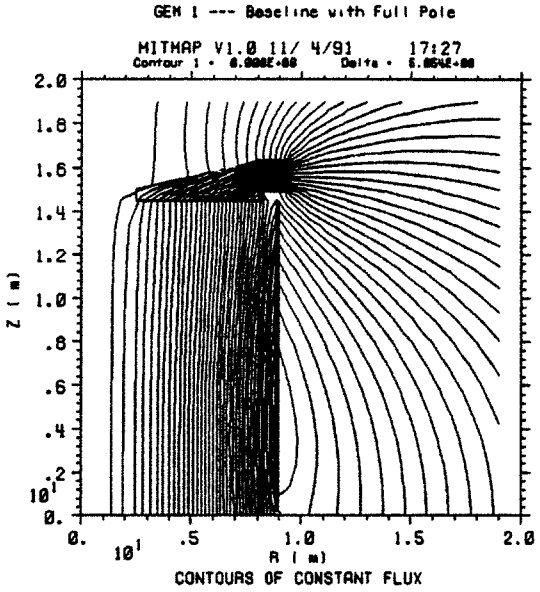

Figure 37: Flux lines superposed on a side view of the magnet design.

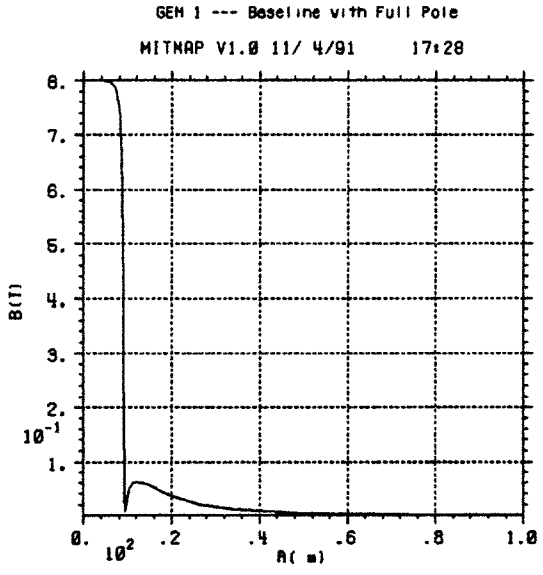

Figure 38: $|\vec{B}|$ versus radius in the hall.

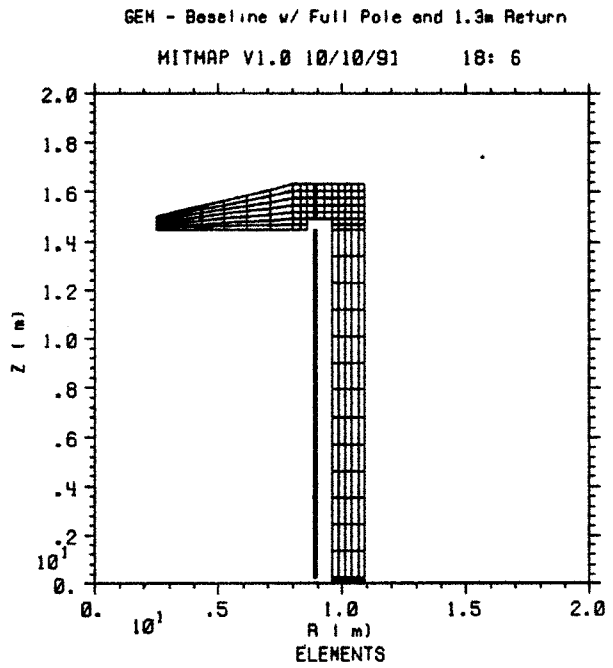

Figure 13: Side view of superconducting solenoid with a 1.3 m full iron return frame (the figure is rotationally symmetric about the z-axis). Note that this figure is rotated 90° relative to earlier figures; that is, the beam axis (the z axis) is vertical on the page and the transverse (radial) axis is horizontal.

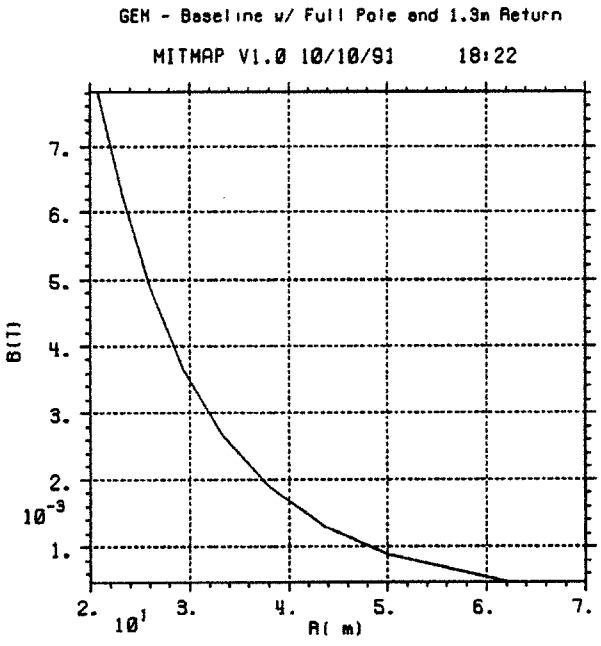

Figure 14: $|\vec{B}|$ versus radius near the surface for 1.3 m return frame.

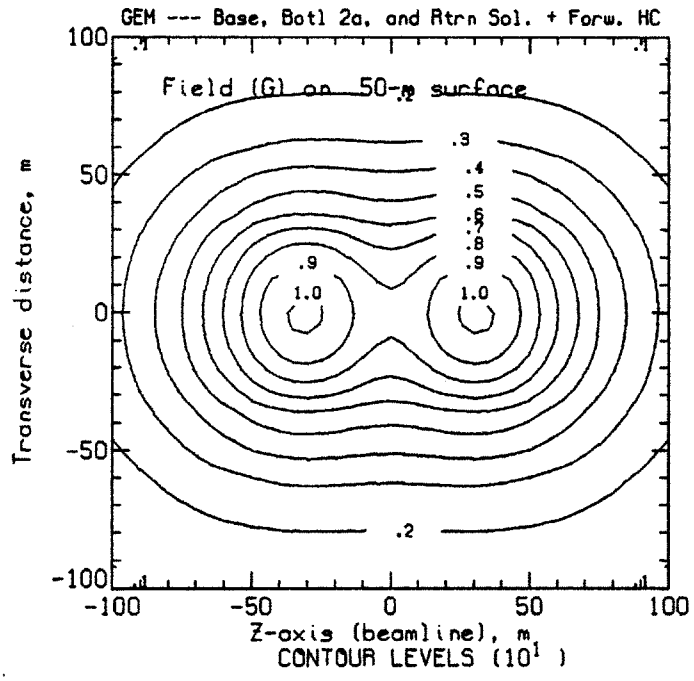

Figure 21: Isogauss contours of the field on a surface at an elevation of 50 m above the center (beam) line of the design shown in Figure 19.

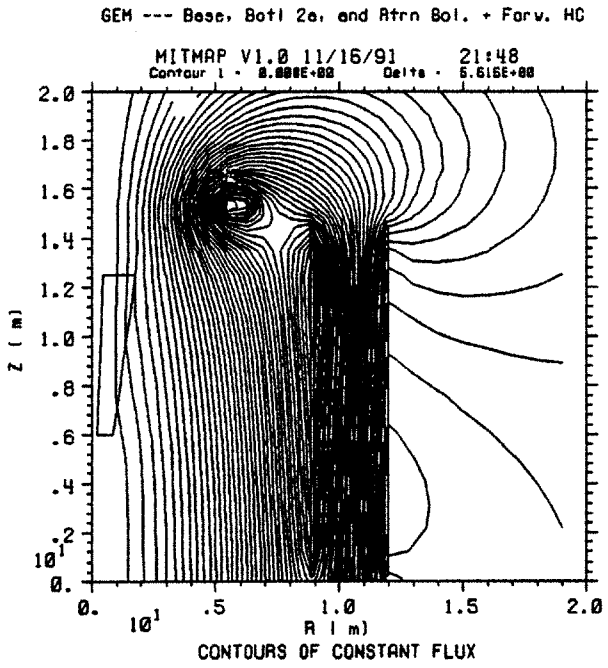

Figure 22: Flux lines superposed on a side view of superconducting solenoid with superconducting return (cf. Figure 19).

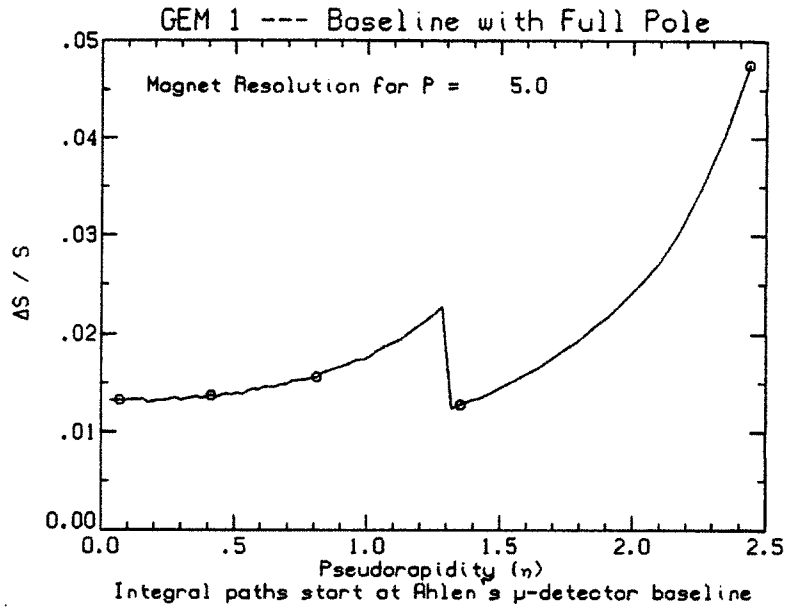

Figure 51: Resolution for constant P as a function of η.

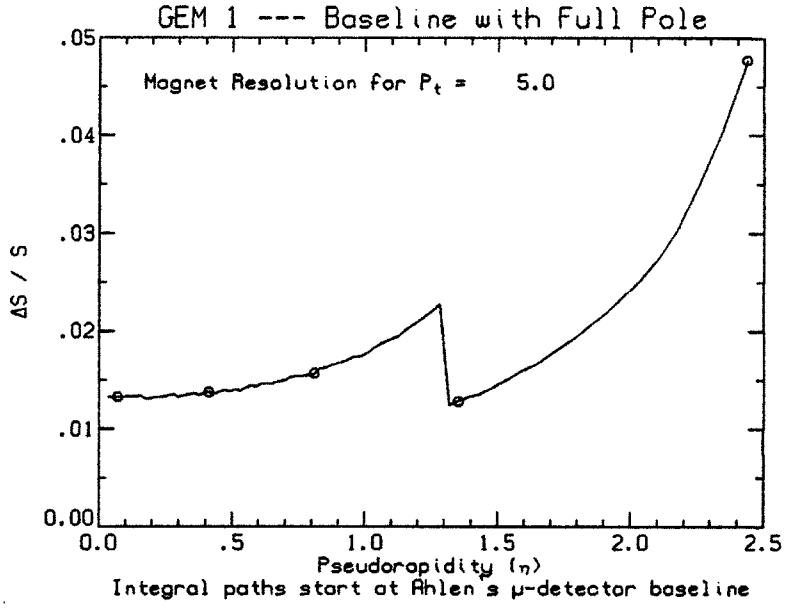

Figure 52: Resolution for constant P_t as a function of η.

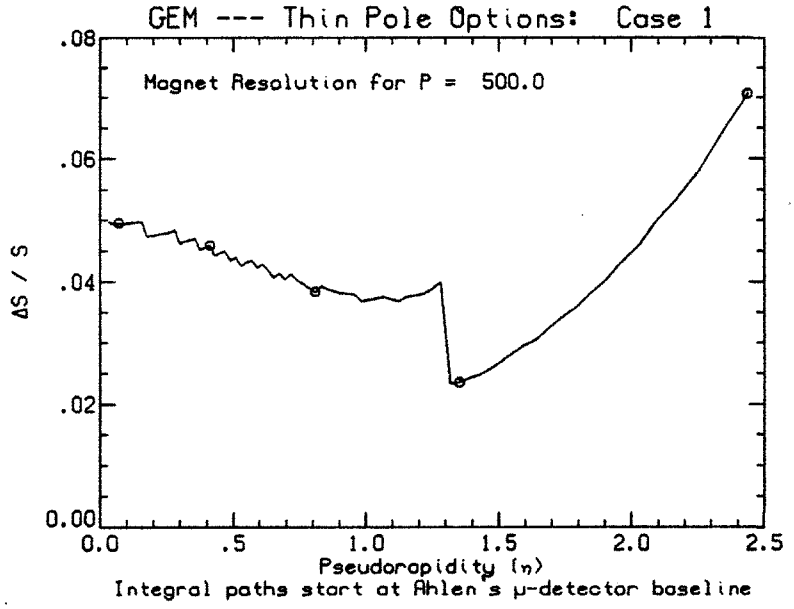

Figure 61: Resolution for constant P as a function of η.

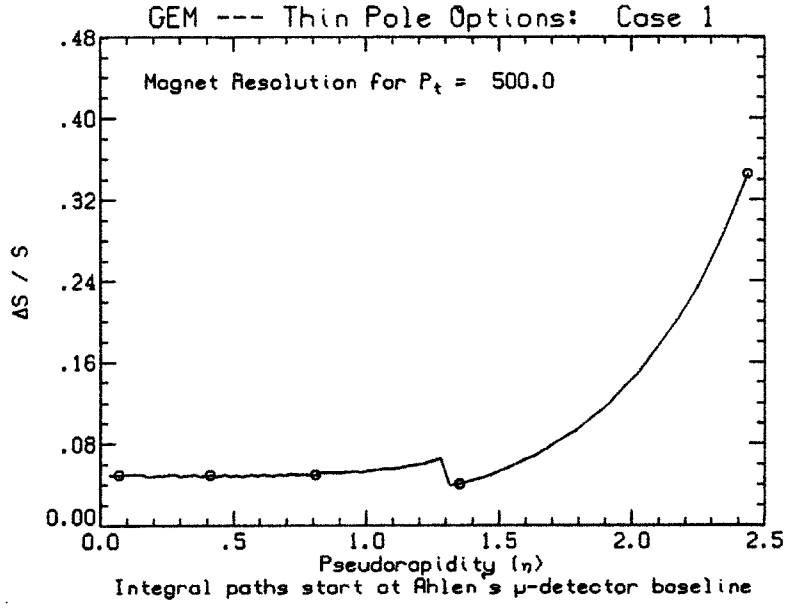

Figure 62: Resolution for constant P_t as a function of η.

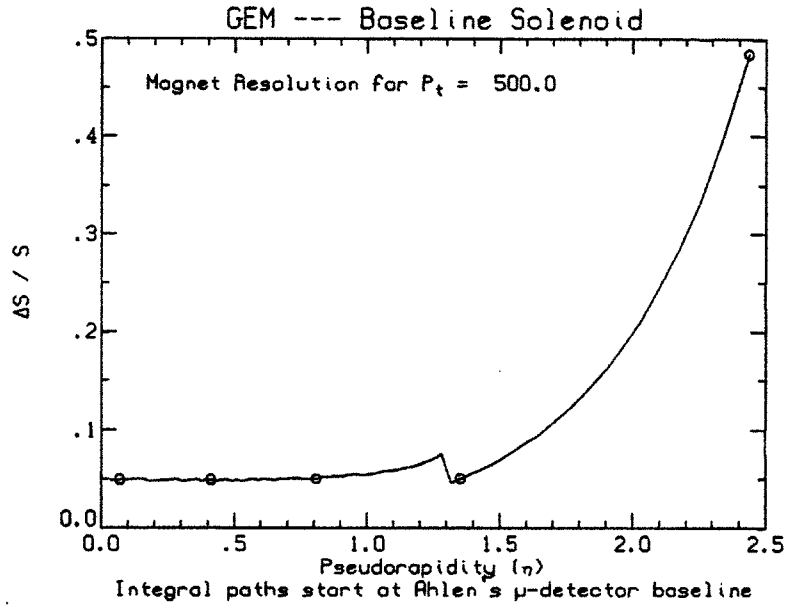

Figure 31: Resolution for constant P_t as a function of η.

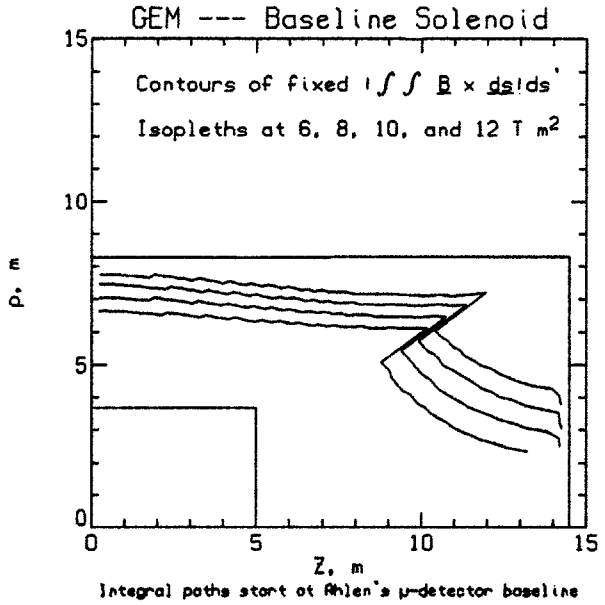

Figure 32: Isopleths of constant BL^2 for a simple solenoid superposed on a sketch of the GEM concept; isopleths increase with distance from the origin.

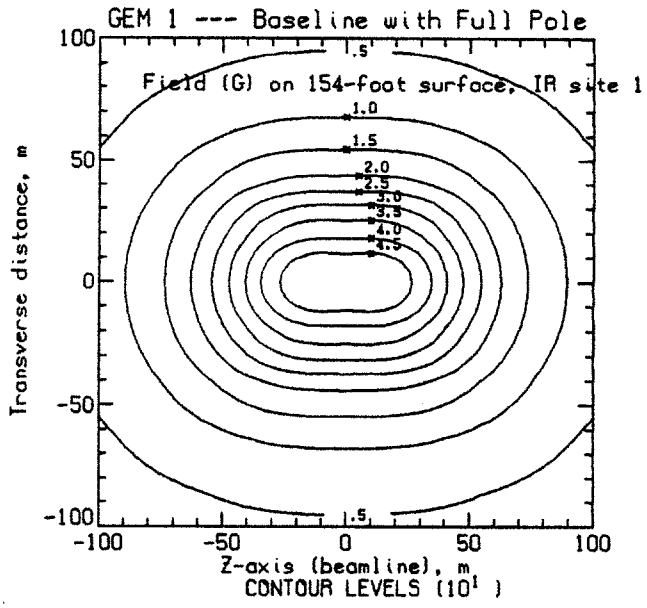

Figure 41: Isogauss contours of the field on a surface at the nominal elevation of IR site 1.

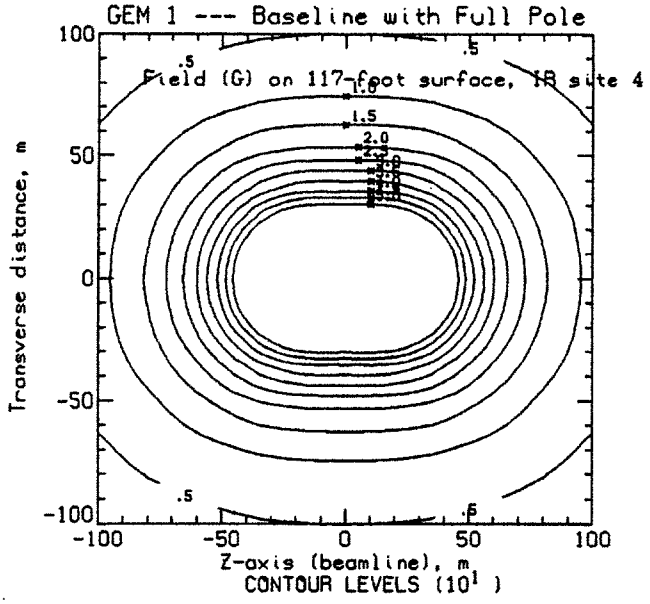

Figure 42: Isogauss contours of the field on a surface at the nominal elevation of IR site 4.

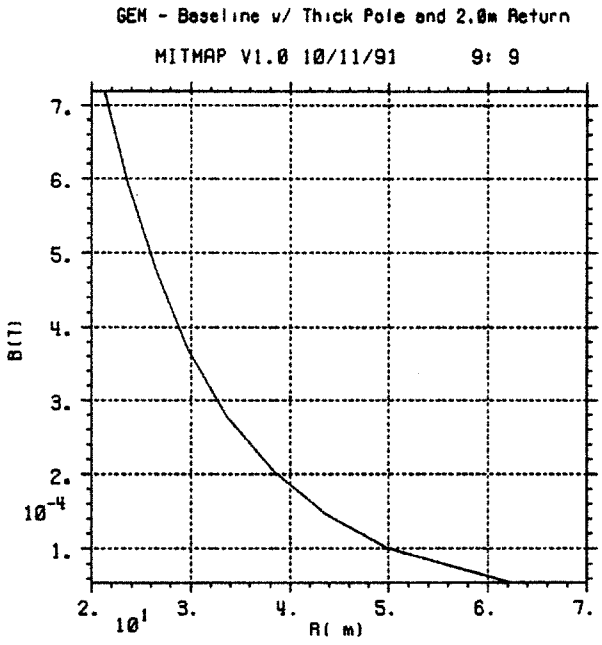

Figure 17: $|\vec{B}|$ versus radius near the surface for 2.0 m return frame.

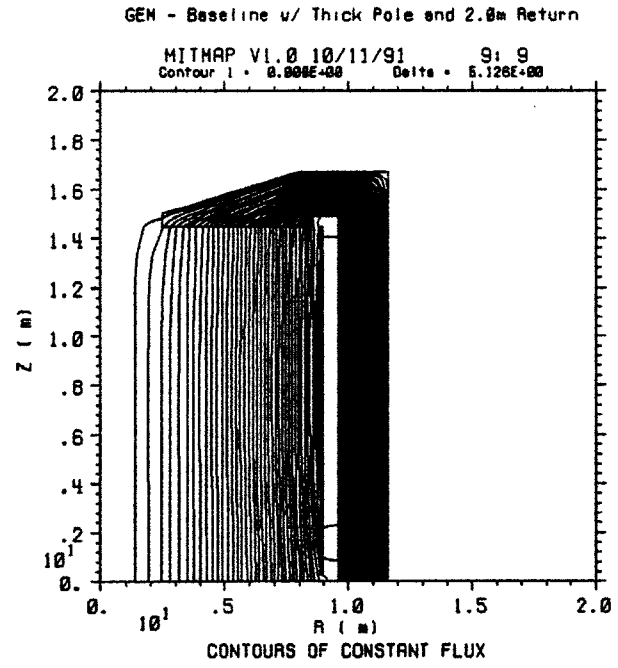

Figure 18: Flux lines superposed on a side view of a superconducting solenoid with a 2.0 m iron return frame. Note that the beam axis (the z axis) is vertical on the page and the transverse (radial) axis is horizontal.

References

[1] The L* Collaboration. Letter of intent to the SSC laboratory, November 1990.

[2] The L* Collaboration. Expression of interest to the SSC laboratory, May 1990.

[3] Second Detector Collaboration (GEM). Expression of interest to construct a major SSC detector, July 1991.

[4] U. Becker, J. Branson, M. White, B. Wyslouch, et al. Accurate measurements of high momenta. *Nuclear Instruments and Methods*, A263:14–19, 1988.

[5] S. Ahlen. private communication.

[6] V.L. Highland. *Nuclear Instruments and Methods*, 129:49, 1975.

[7] V.L. Highland. *Nuclear Instruments and Methods*, 161:171, 1979.

[8] R.D. Pillsbury, Jr. Soldesign user's manual. Technical Report PFC/RR-91-3, MIT Plasma Fusion Center, Cambridge MA, February 1991.

[9] R.D. Pillsbury, Jr. MAP user's manual. Technical Report PFC/RR-91-4, MIT Plasma Fusion Center, Cambridge MA, February 1991.

[10] J.D. Sullivan. Graphics package version 4: User's reference manual. Technical Report PFC/RR-84-4, MIT Plasma Fusion Center, Cambridge, 1984.

[11] Swanson Analysis Systems, Inc., Houston, PA. ANSYS revision 4.4a.

[12] R.D. Pillsbury, Jr. Fringe field dipole-dipole force interaction. Internal Memorandum MIT-GEM-EM-01, MIT Plasma Fusion Center, Cambridge MA, November 1991.

[13] R.D. Pillsbury, Jr., L. Myatt, and J.D. Sullivan. Shielding of the magnetic fields from the GEM magnet. Internal Memorandum MIT-GEM-EM-02, MIT Plasma Fusion Center, Cambridge MA, November 1991.

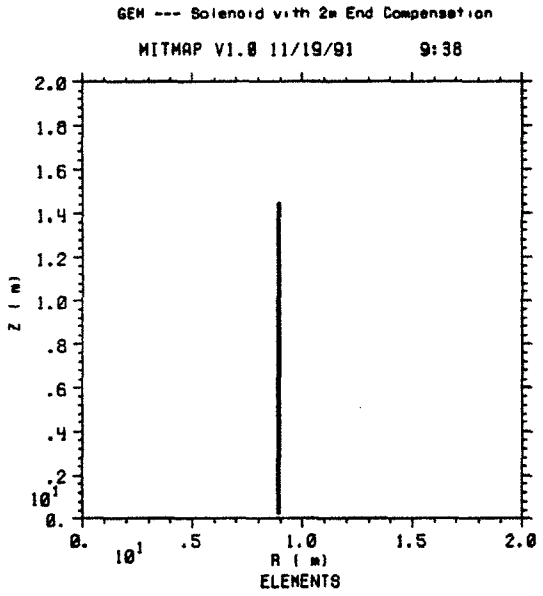

Figure 139: Side view of a superconducting solenoid without iron pole pieces and with the current doubled in the last 2 m. Note that the beam axis (the z axis) is vertical on the page and the transverse (radial) axis is horizontal.

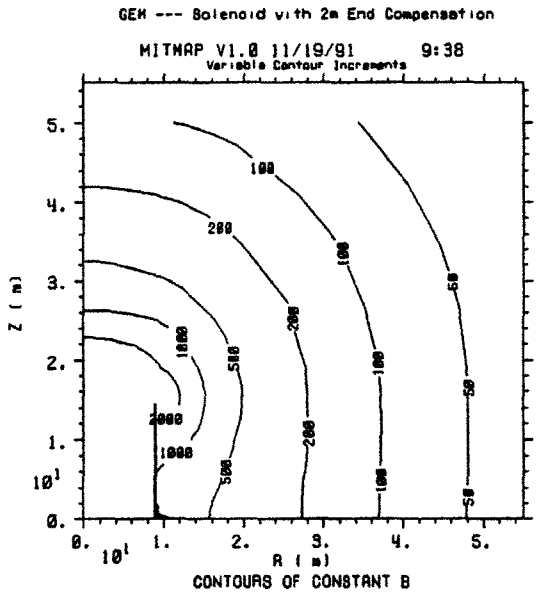

Figure 140: Contours of constant $|\vec{B}|$ superposed on a side view of the magnet; isopleths are labeled in gauss.

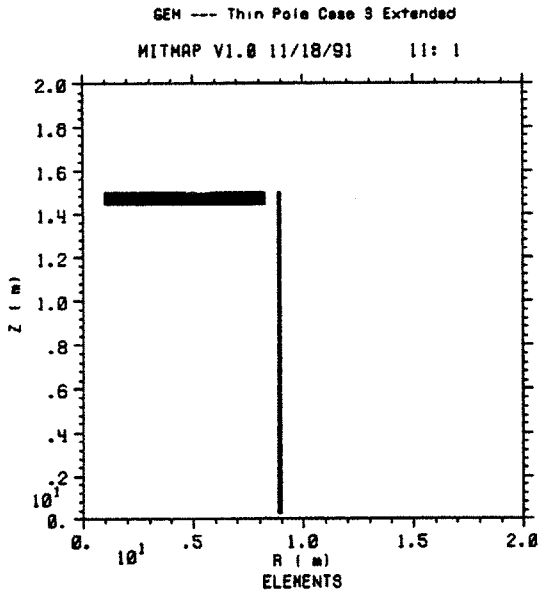

Figure 149: Side view of a superconducting solenoid with the conductor extended over the pole piece. Note that the beam axis (the z axis) is vertical on the page and the transverse (radial) axis is horizontal.

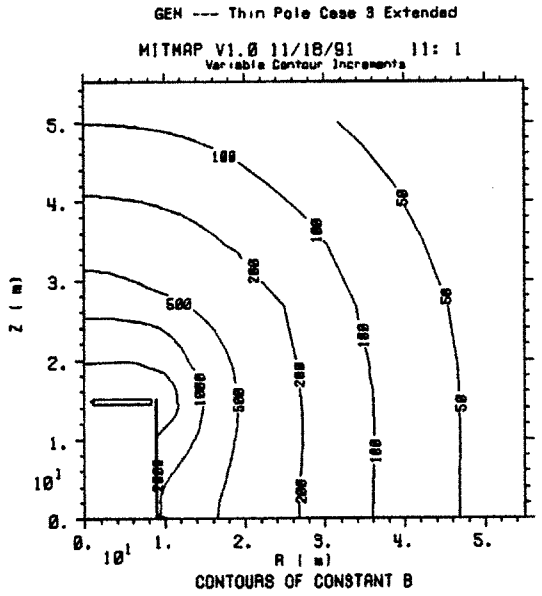

Figure 150: Contours of constant $|\vec{B}|$ superposed on a side view of the magnet; isopleths are labeled in gauss.

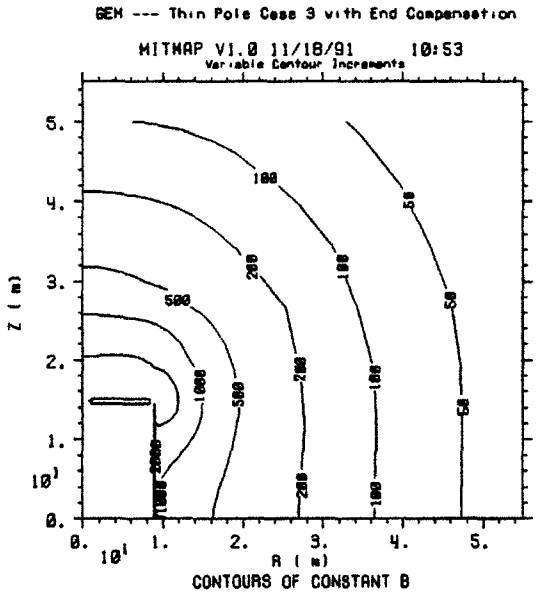

Figure 120: Contours of constant $|\vec{B}|$ superposed on a side view of the magnet; isopleths are labeled in gauss.

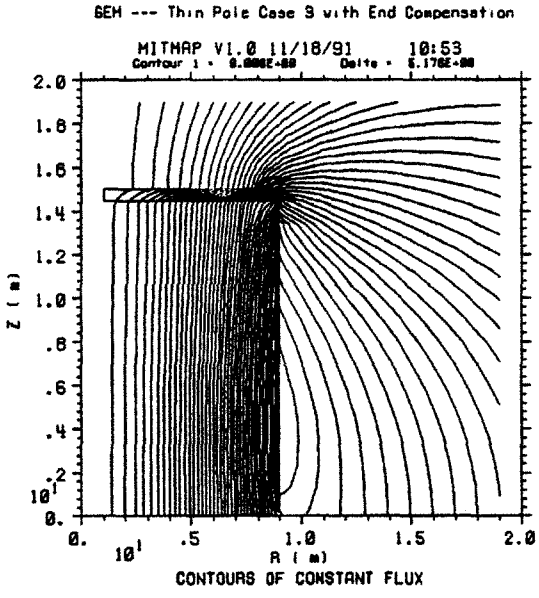

Figure 121: Flux lines superposed on a side view of the magnet design.

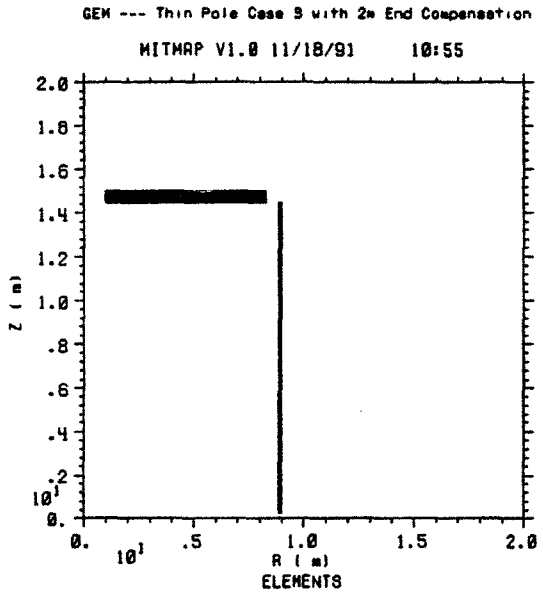

Figure 129: Side view of a superconducting solenoid with the current doubled in the last 2 m. Note that the beam axis (the z axis) is vertical on the page and the transverse (radial) axis is horizontal.

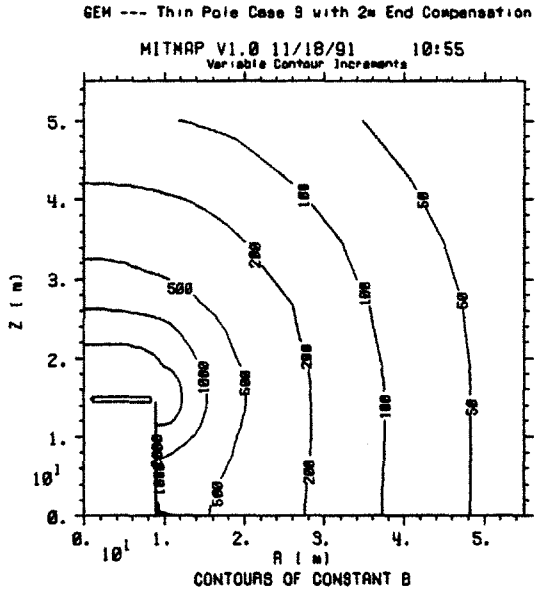

Figure 130: Contours of constant $|\vec{B}|$ superposed on a side view of the magnet; isopleths are labeled in gauss.

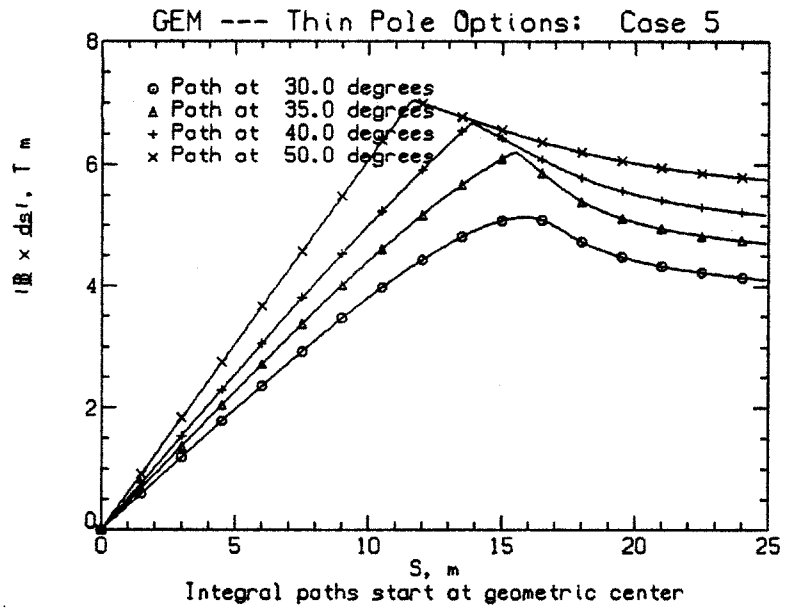

Figure 103: Plot of $|\vec{\mathcal{I}}|$ for the LoI baseline magnet versus path length from the interaction point for tracks at 30, 35, 40, and 50° (from the beam line).

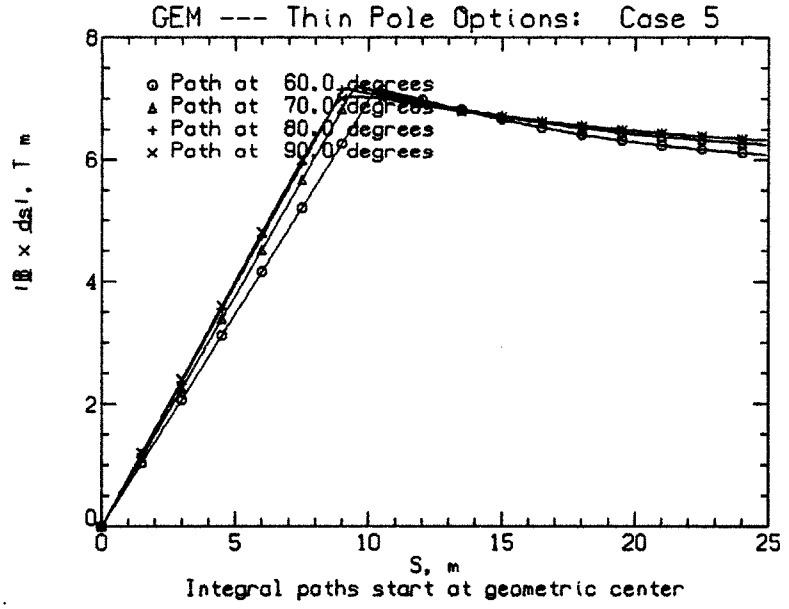

Figure 104: Plot of $|\vec{\mathcal{I}}|$ for the LoI baseline magnet versus path length from the interaction point for tracks at 60, 70, 80, and 90° (from the beam line).

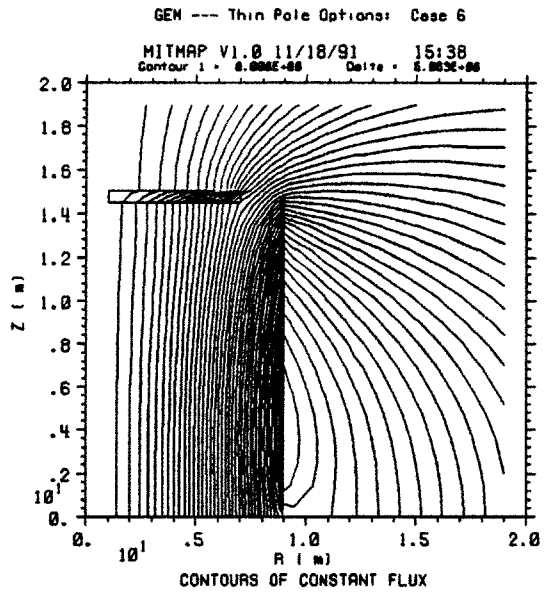

Figure 112: Flux lines superposed on a side view of the magnet design.

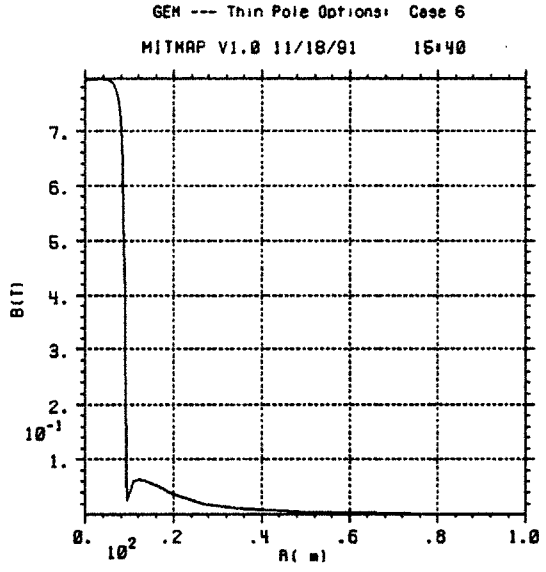

Figure 113: $|\vec{B}|$ versus radius in the hall.

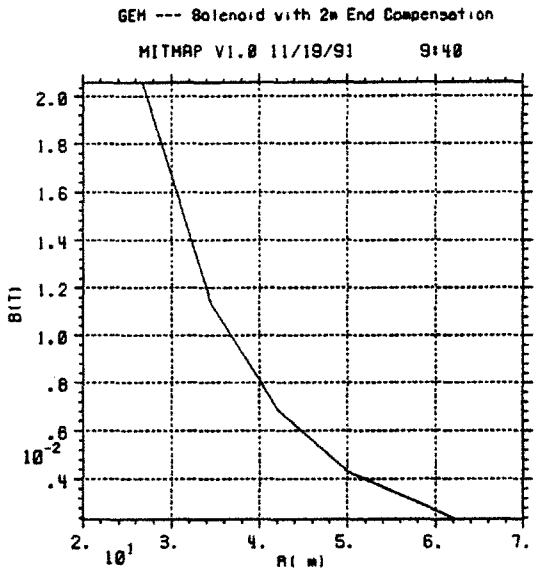

Figure 143: $|\vec{B}|$ versus radius near the surface.

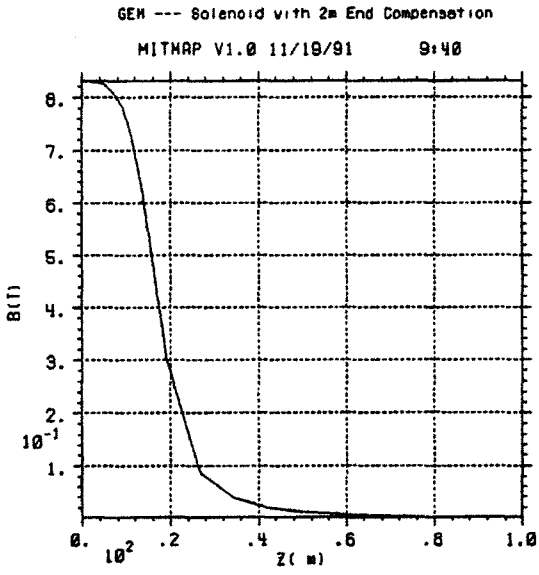

Figure 144: $|\vec{B}|$ versus z on axis in the hall.

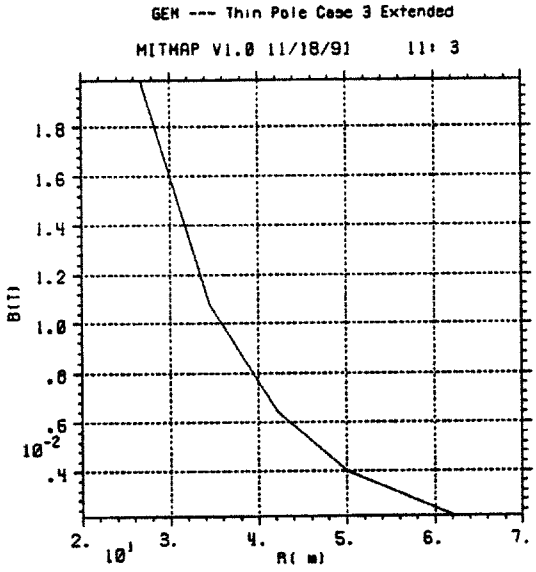

Figure 153: $|\vec{B}|$ versus radius near the surface.

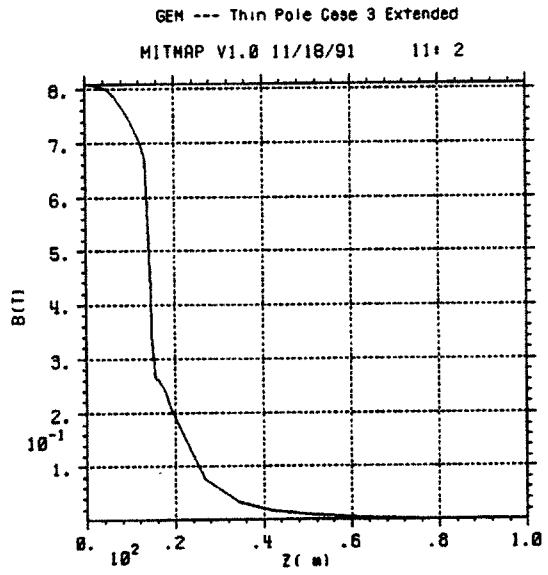

Figure 154: $|\vec{B}|$ versus z on axis in the hall.

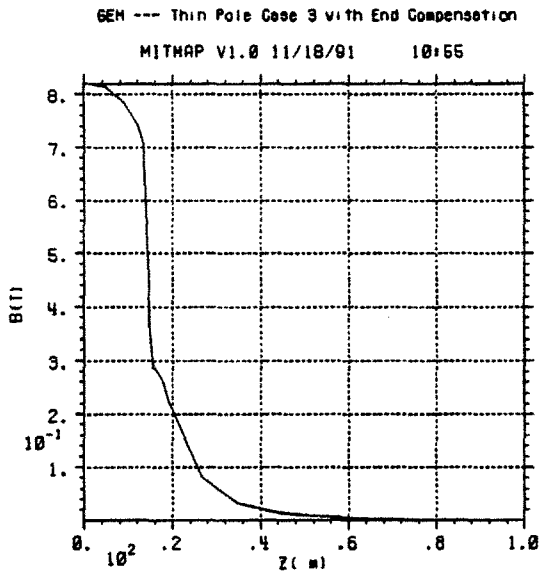

Figure 124: $|\vec{B}|$ versus z on axis in the hall.

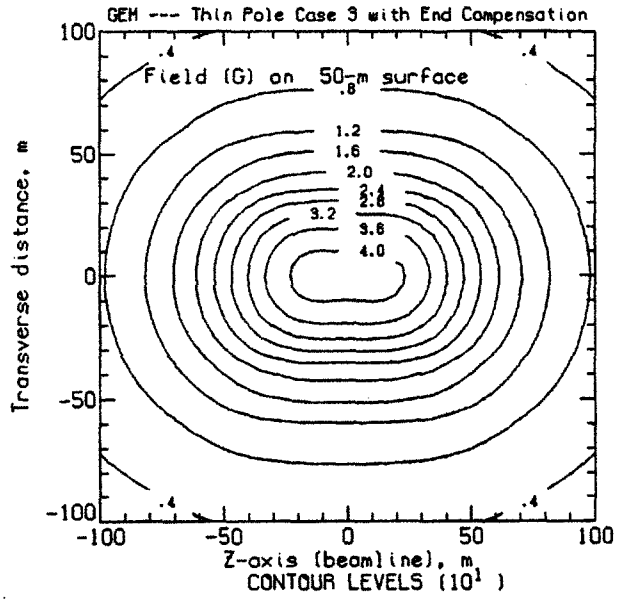

Figure 125: Isogauss contours of the field on a surface at a nominal elevation of 50 m above the beamline (centerline).

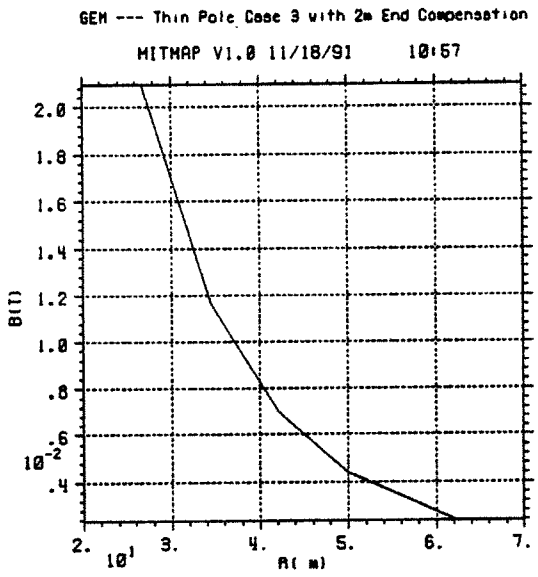

Figure 133: $|\vec{B}|$ versus radius near the surface.

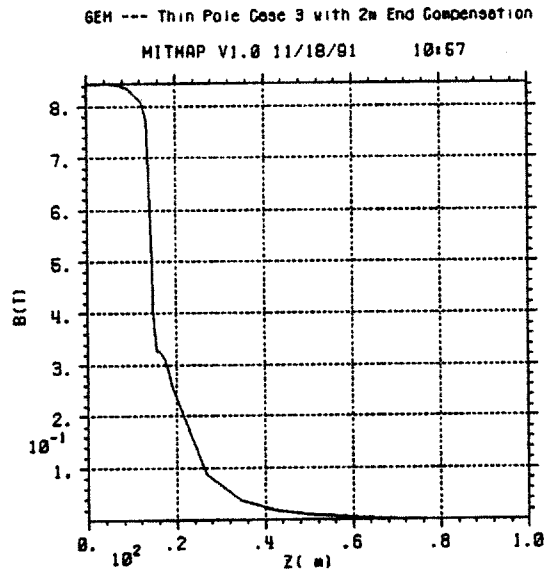

Figure 134: $|\vec{B}|$ versus z on axis in the hall.

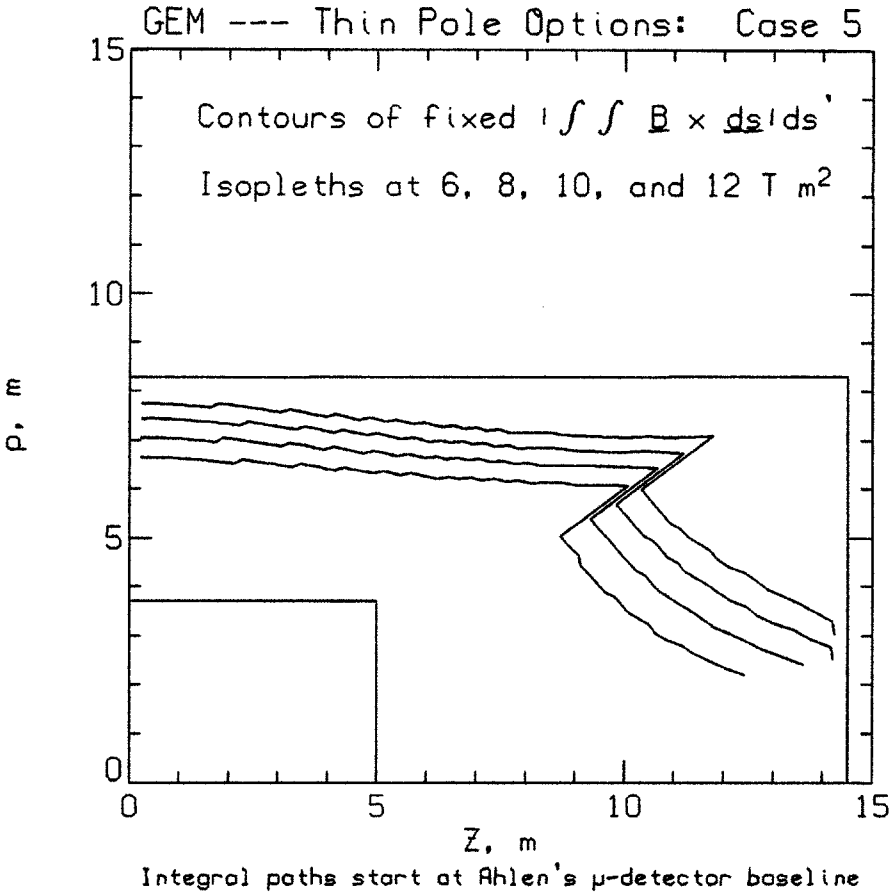

Figure 107: Isopleths of constant $\mathcal{BL}^2$ superposed on a sketch of the GEM concept; isopleths increase with distance from the origin.

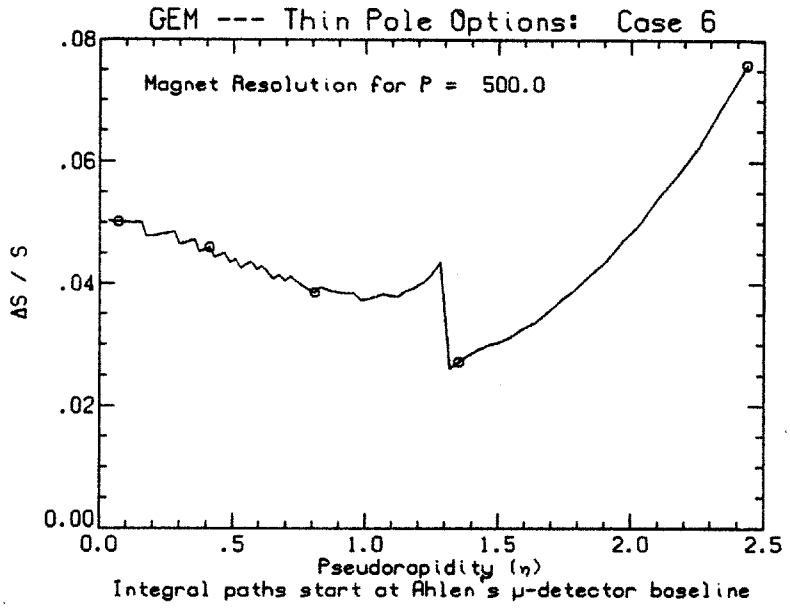

Figure 116: Resolution for constant P as a function of η.

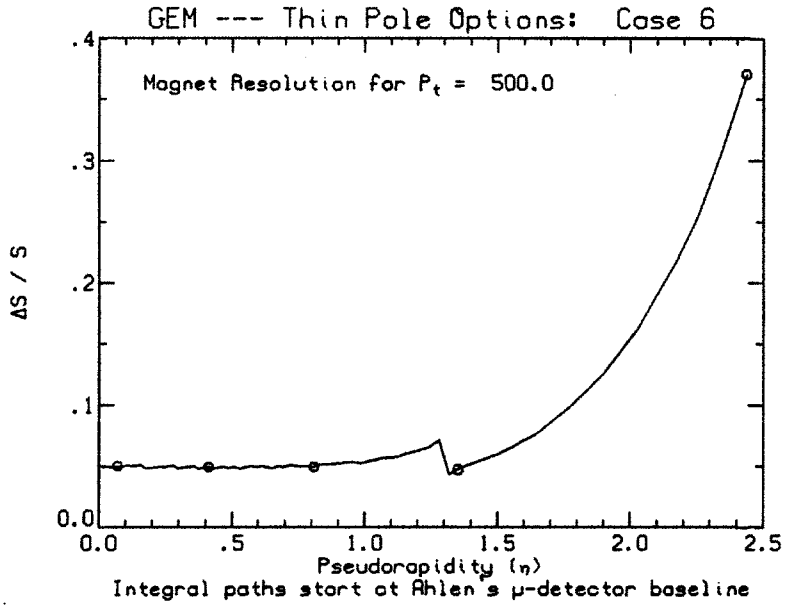

Figure 117: Resolution for constant P_t as a function of η.

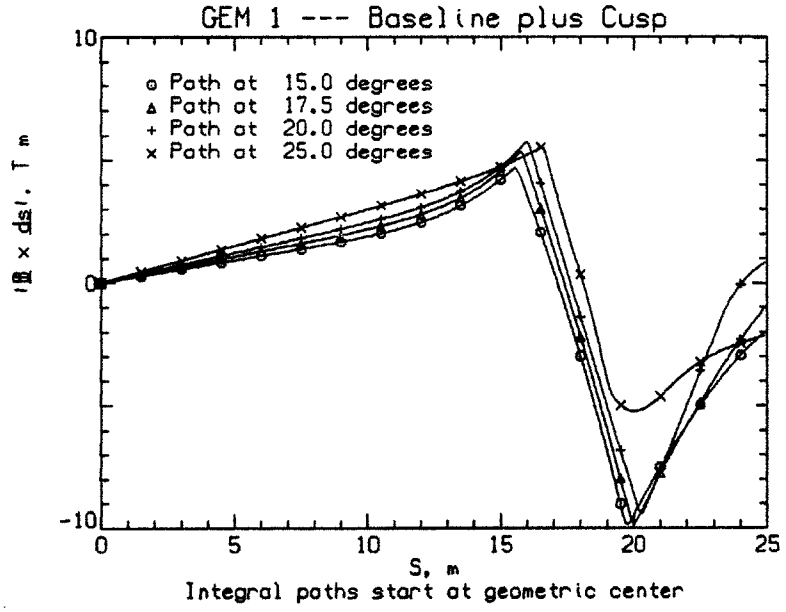

Figure 238: Plot of $|\vec{\mathcal{I}}|$ versus path length from the interaction point for tracks at 15, 17.5, 20, and 25° (from the beam line).

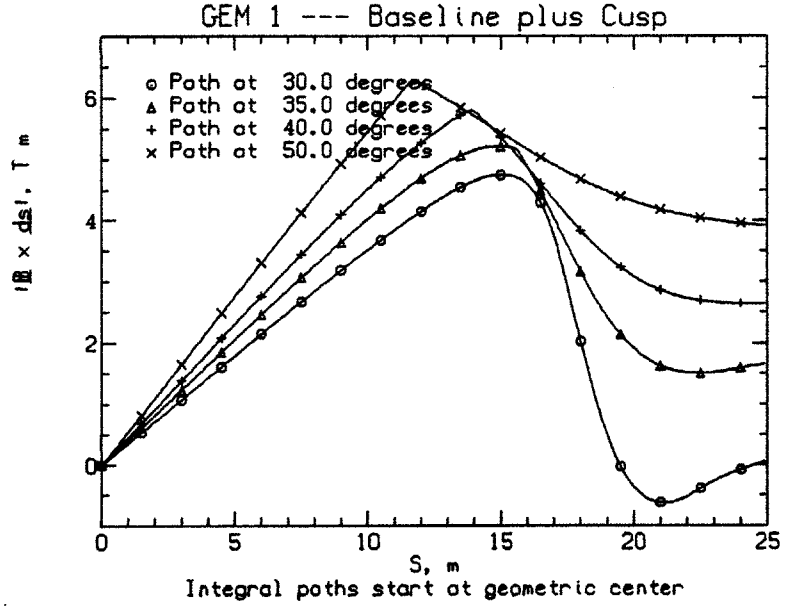

Figure 239: Plot of $|\vec{\mathcal{I}}|$ versus path length from the interaction point for tracks at 30, 35, 40, and 50° (from the beam line).

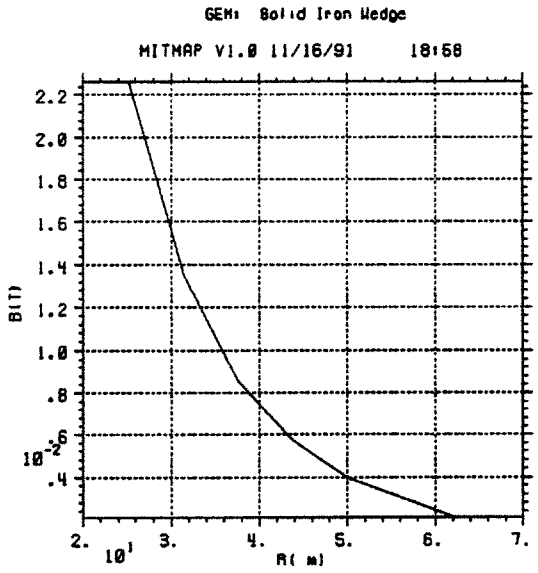

Figure 248: $|\vec{B}|$ versus radius near the surface.

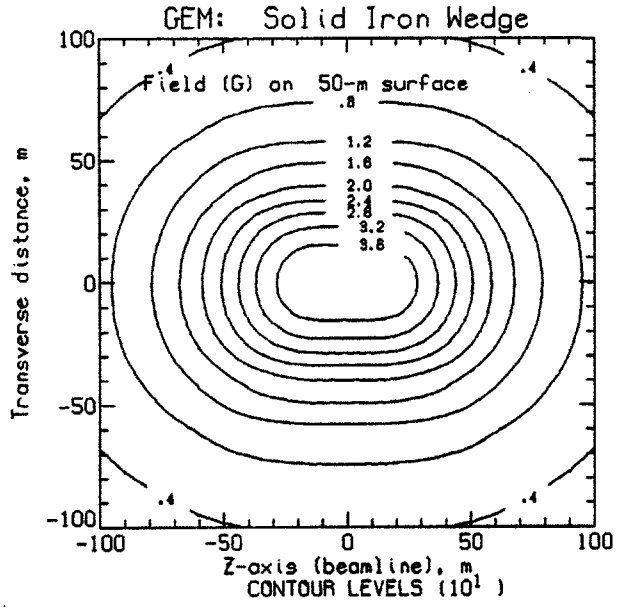

Figure 249: Isogauss contours of the field on a surface at a nominal elevation of 50 m above the beamline (centerline).

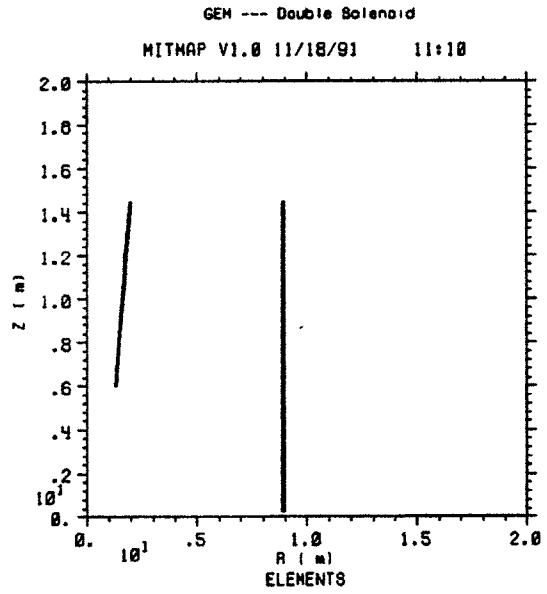

Figure 217: Side view of a superconducting solenoid without an iron end pole but with a separate superconducting "wing" coil to model an iron cone (cf. Figures 244–252). Note that the beam, z, axis is vertical on the page and the transverse axis is horizontal.

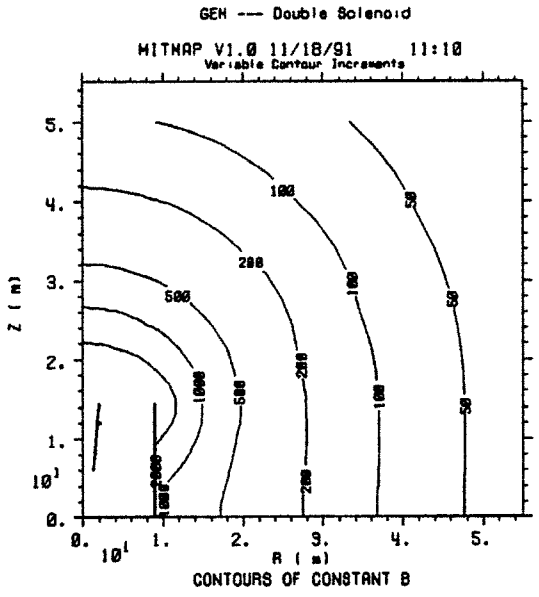

Figure 218: Contours of constant $|\vec{B}|$ superposed on a side view of the magnet; isopleths are labeled in gauss.

A.2.4 Miscellaneous

Figures 227–229 are from an early attempt to both cancel the field and shape it; the central field is $\times 2$ too large in this example (i.e., 1.6 T). Figures 230–243 tried to simultaneously satisfy the far (surface) field requirement and improve small angle response by replacing the end poles with superconducting cusp coils (cf. Appendix A.4.2); thus the far field is no longer dipolar (or at least the dipole moment is reduced.)

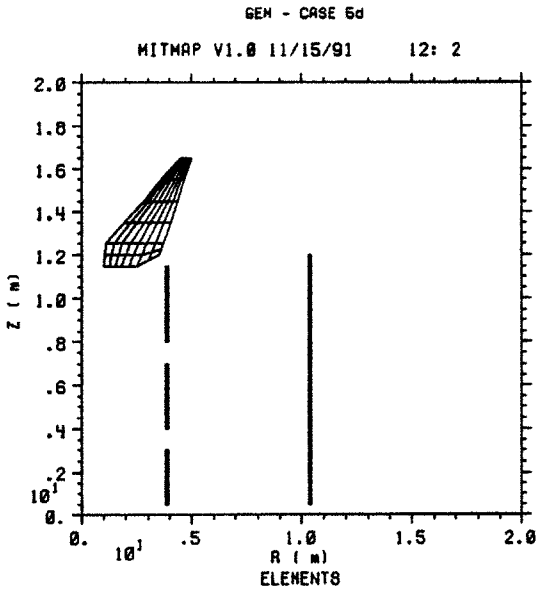

Figure 227: Side view of a superconducting solenoid with a superconducting return and an iron wedge. Note that the beam axis (the z axis) is vertical on the page and the transverse (radial) axis is horizontal.

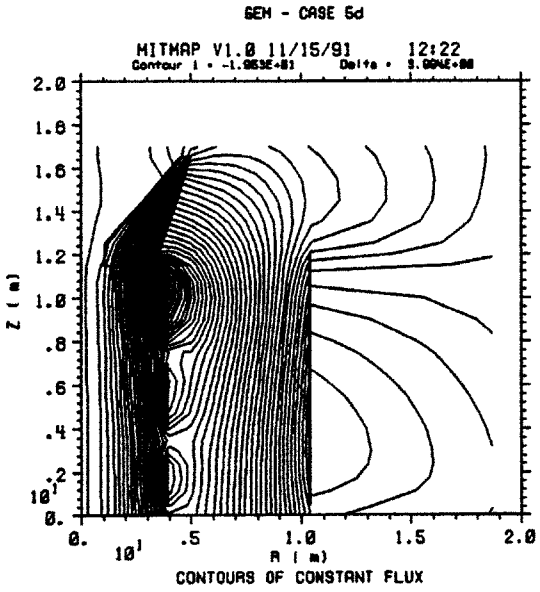

Figure 228: Flux lines superposed on a side view of the magnet design.

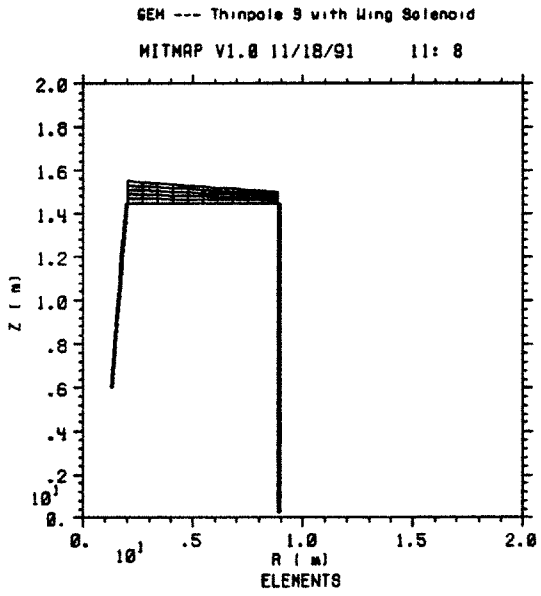

Figure 197: Side view of a superconducting solenoid with an iron pole and with a separate superconducting "wing" coil to model an iron flux shaping wedge. (cf. Figures 262–270). Note that the beam, z, axis is vertical on the page and the transverse axis is horizontal.

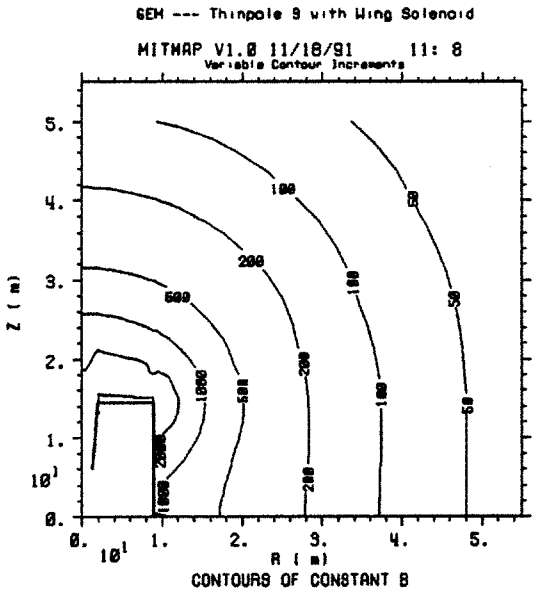

Figure 198: Contours of constant $|\vec{B}|$ superposed on a side view of the magnet; isopleths are labeled in gauss.

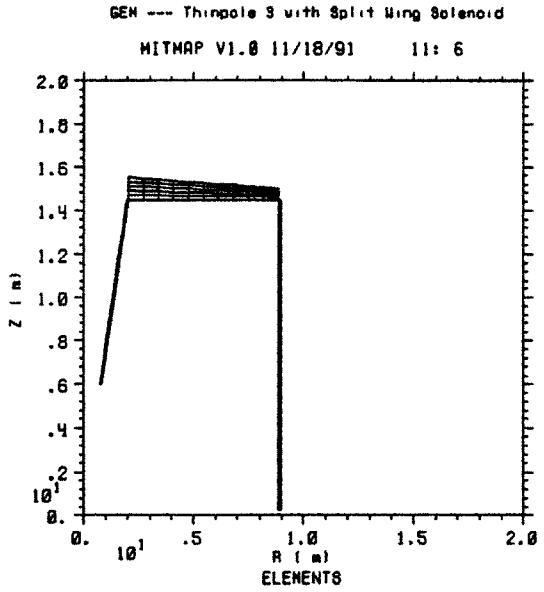

Figure 207: Side view of a superconducting solenoid with an iron end pole and with a separate split superconducting "wing" coil to model a 50% iron calorimeter and an additional iron cone. (cf. Figures 271–279). Note that the beam, z, axis is vertical on the page and the transverse axis is horizontal.

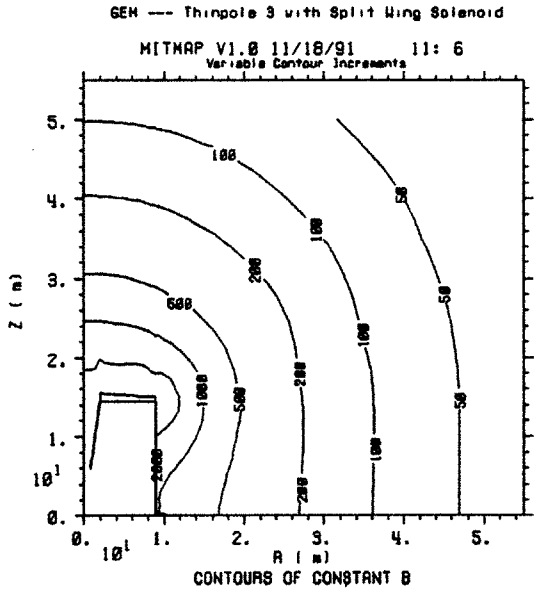

Figure 208: Contours of constant $|\vec{B}|$ superposed on a side view of the magnet; isopleths are labeled in gauss.

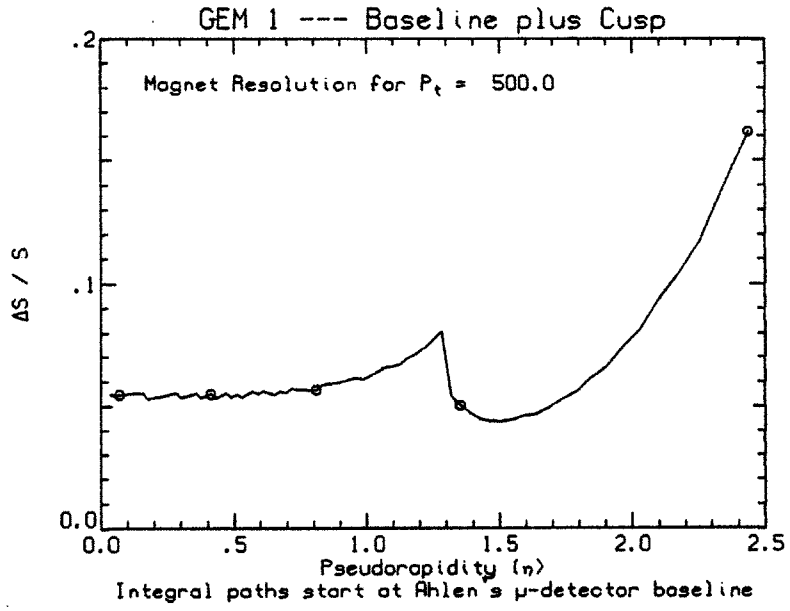

Figure 242: Resolution for constant P_t as a function of η.

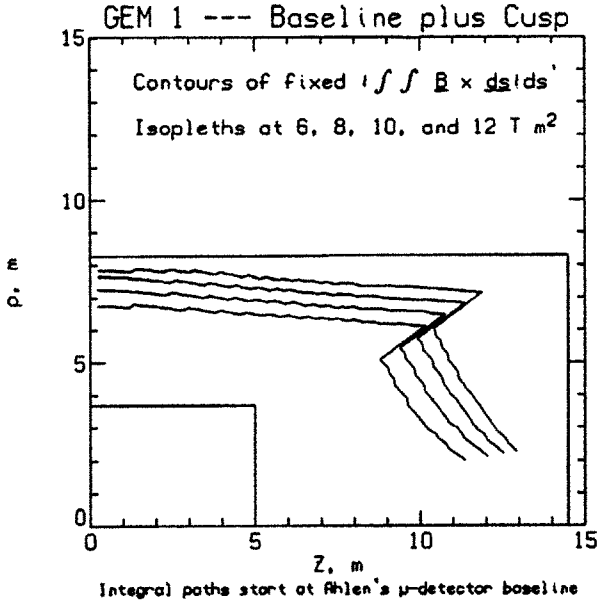

Figure 243: Isopleths of constant $\mathcal{BL}^2$ superposed on a sketch of the GEM concept; isopleths increase with distance from the origin.

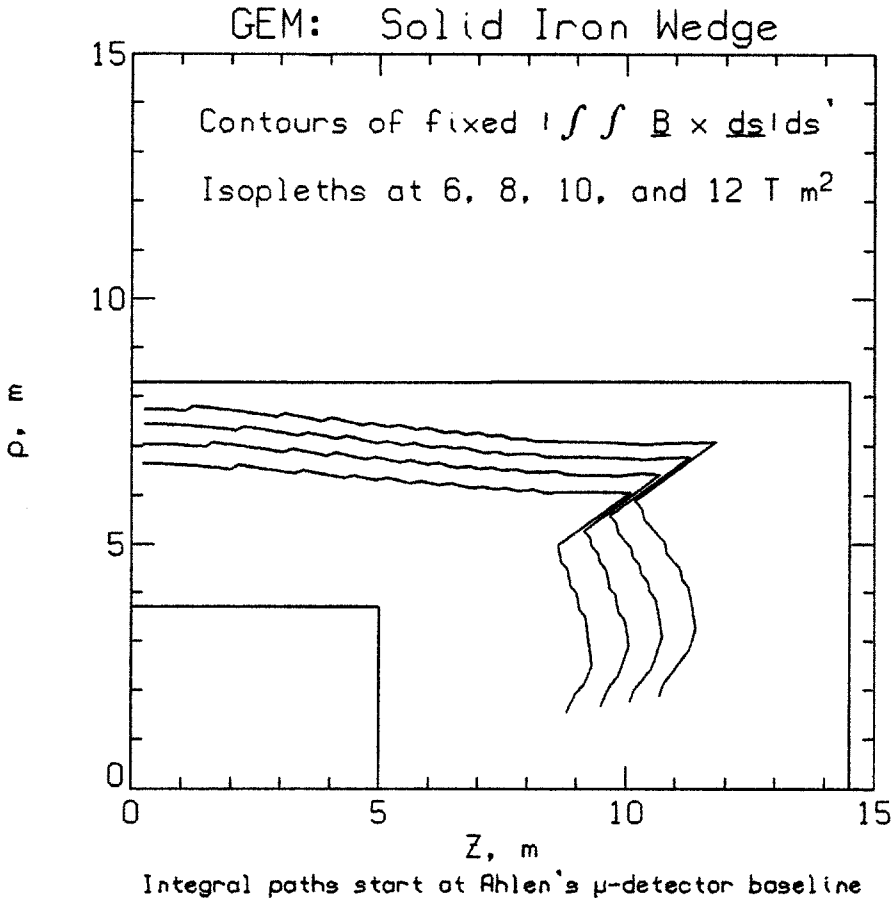

Figure 252: Isopleths of constant $\mathcal{BL}^2$ superposed on a sketch of the GEM concept; isopleths increase with distance from the origin.

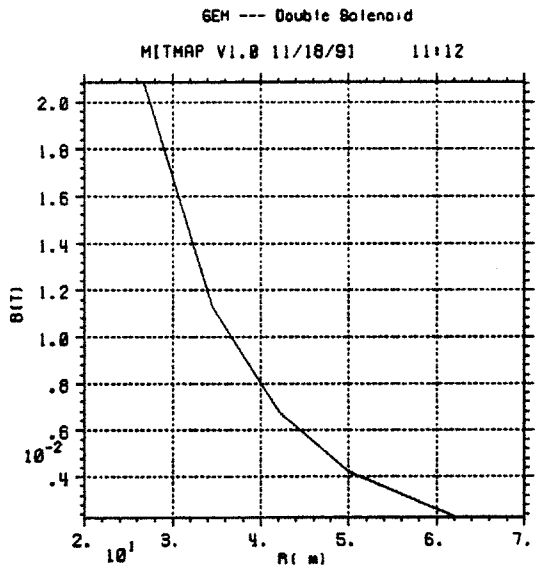

Figure 221: $|\vec{B}|$ versus radius near the surface.

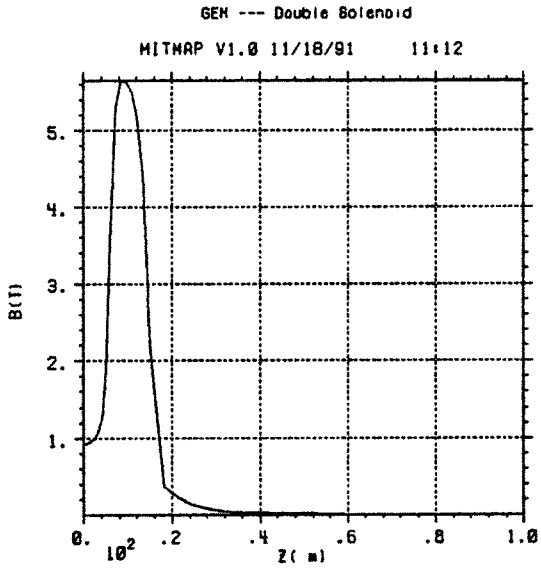

Figure 222: $|\vec{B}|$ versus z on axis in the hall.

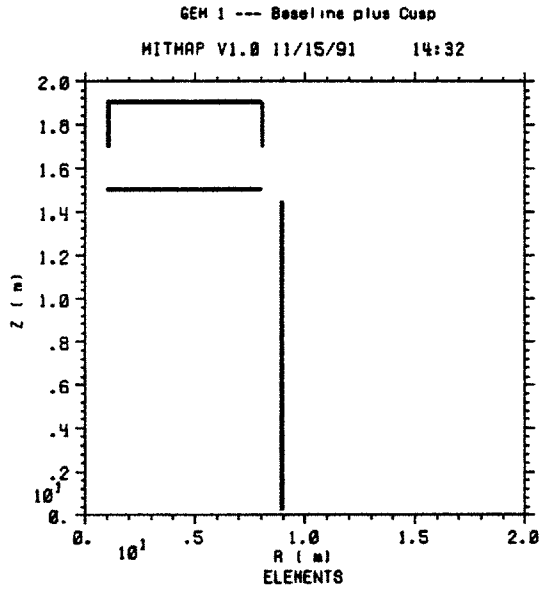

Figure 230: Side view of a superconducting solenoid with the end poles replaced with superconducting cusps. Note that the beam axis (the z axis) is vertical on the page and the transverse (radial) axis is horizontal.

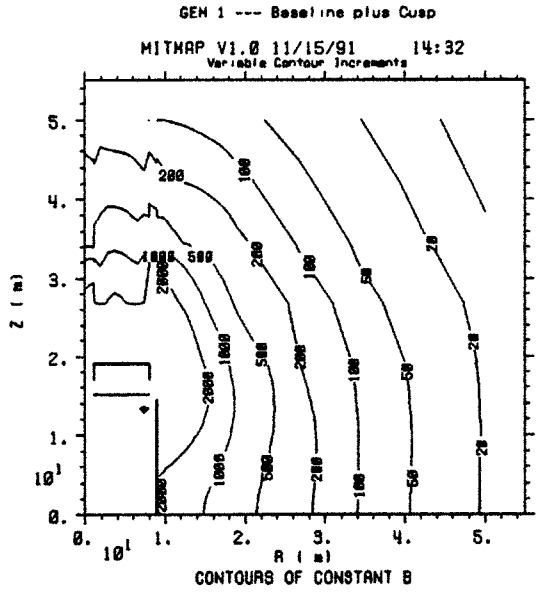

Figure 231: Contours of constant $|\vec{B}|$ superposed on a side view of the magnet; isopleths are labeled in gauss.

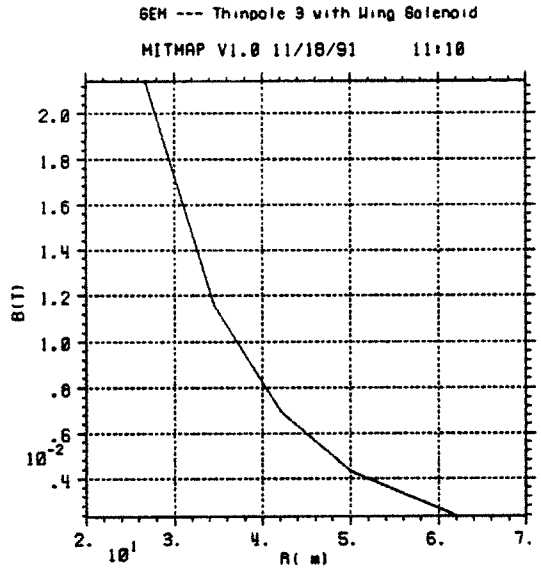

Figure 201: $|\vec{B}|$ versus radius near the surface.

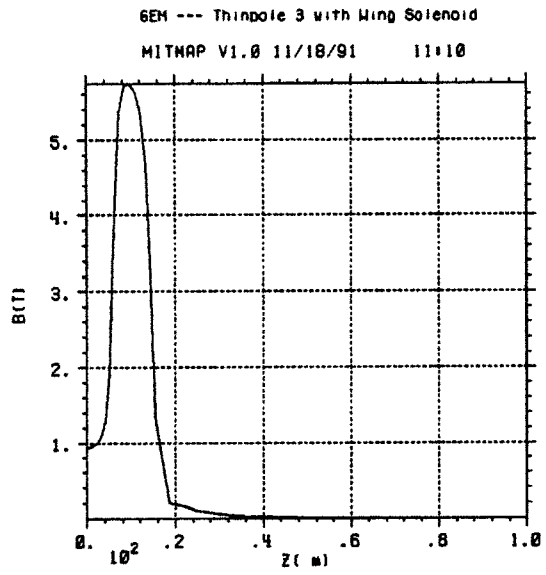

Figure 202: $|\vec{B}|$ versus z on axis in the hall.

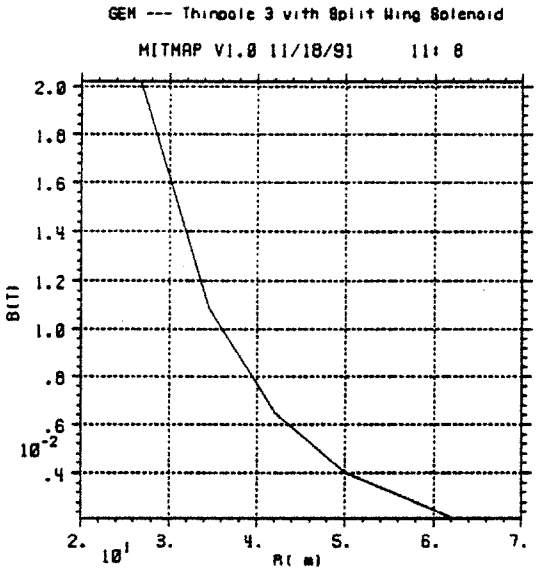

Figure 211: $|\vec{B}|$ versus radius near the surface.

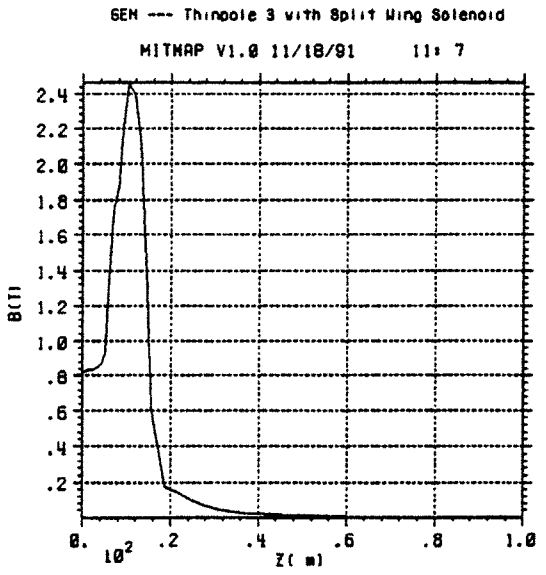

Figure 212: $|\vec{B}|$ versus z on axis in the hall.

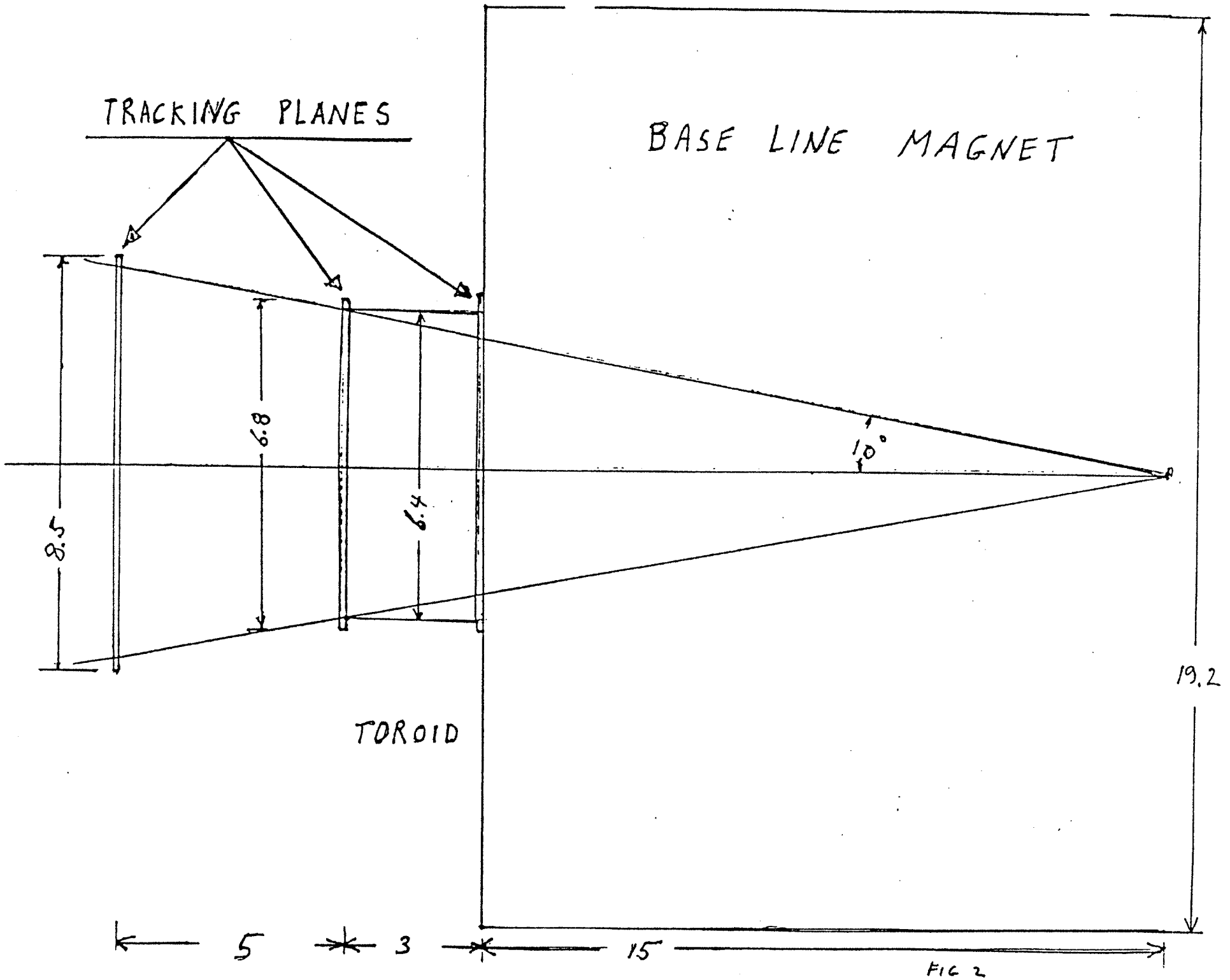

FIG 2

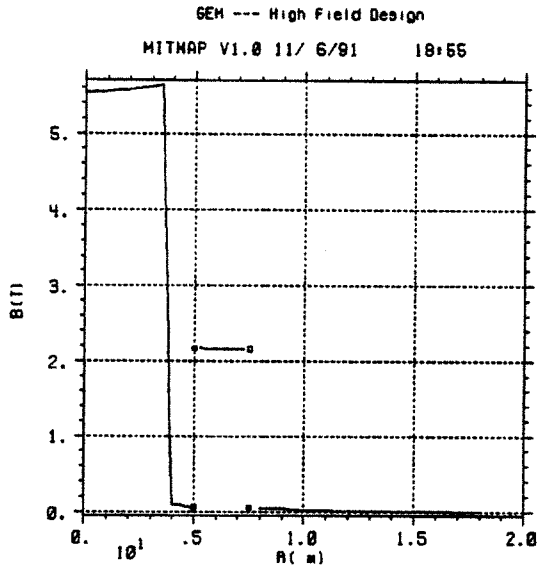

Figure 310: $|\vec{B}|$ versus radius in the hall for the "Ko" option.

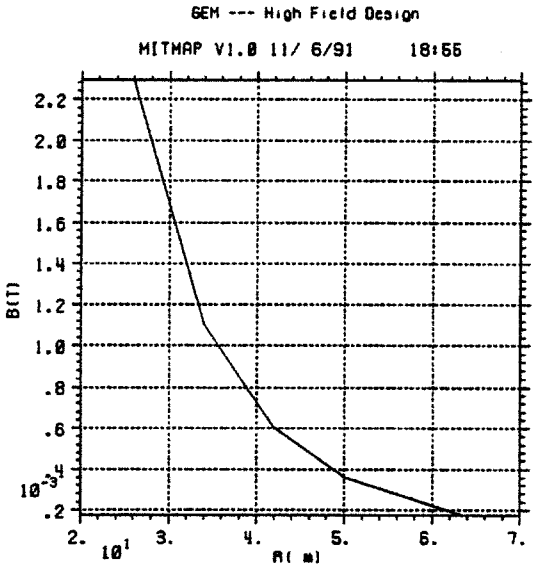

Figure 311: $|\vec{B}|$ versus radius near the surface for the "Ko" option.

B Pless's Analysis

Stimulated by the following analysis, preliminary designs and cost estimates have been run for various toroids at small angles. A separate report on these options is in preparation.

A.4 Shielding

A.4.1 Full iron return frames

See Figures 13–18 in Section 5; also see Appendix A.5 where iron return frames are used for much higher fields (5 T).

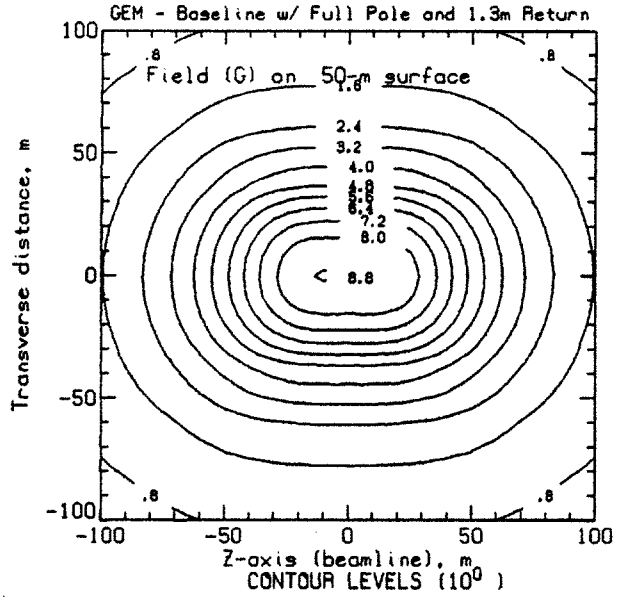

Figure 293: Isogauss contours of the field (1.3 m return frame) on a surface at a nominal elevation of 50 m above the beamline (centerline). Note that the peak field is less than 10 G.

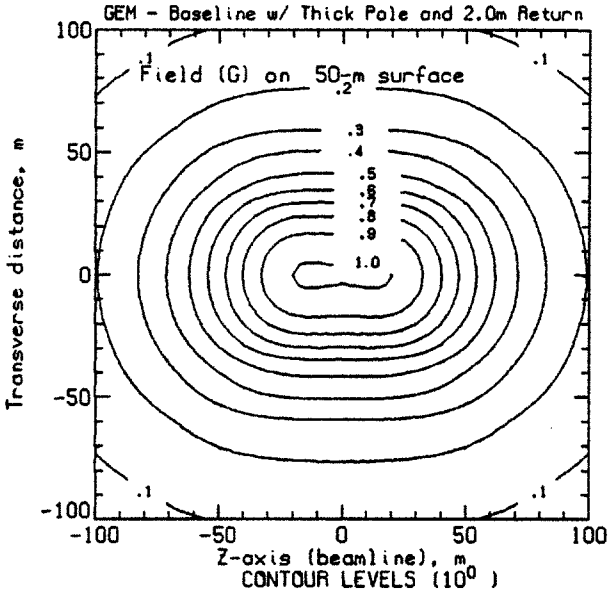

Figure 294: Isogauss contours of the field (2.0 m return frame) on a surface at a nominal elevation of 50 m above the beamline (centerline). Note that the peak field is ~ 1 G.

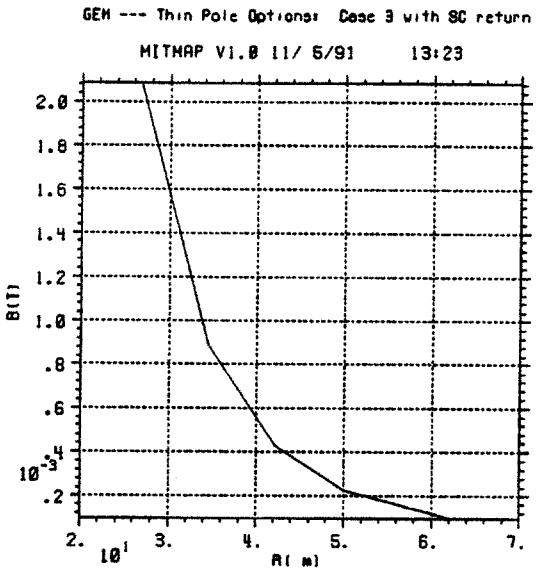

Figure 302: $|\vec{B}|$ versus radius near the surface.

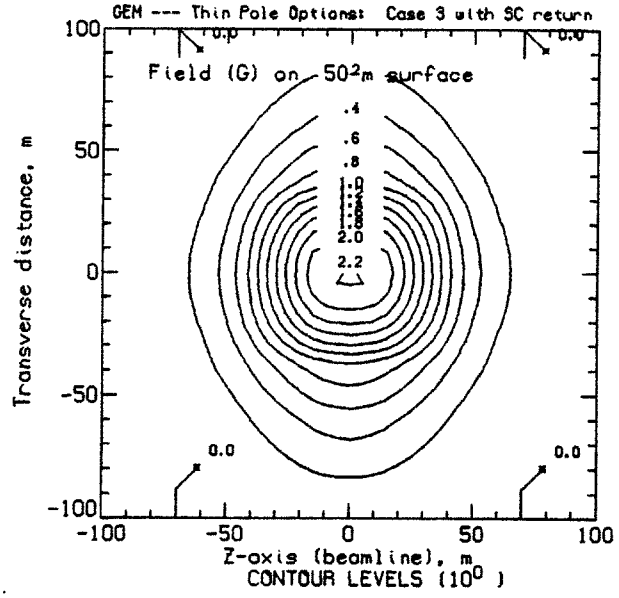

Figure 303: Isogauss contours of the field on a surface at a nominal elevation of 50 m above the beamline (centerline).

We can look at the stored energy of the toroid compared to the solenoid.

stored energy of toroid / stored energy of solenoid =

$$(\text{diameter (T)} / \text{diameter (S)})^2 \cdot \text{length (T)} / \text{length (T)} / \text{length (S)} \cdot$$

$$(B\ (T) / B\ (S))^2$$

$$= (6.4 / 19.2)^2 \cdot 3 / 30 \cdot (1 / .8)^2 = .017$$

Hence the toroid has about 1.7% the stored energy of the solenoid. The cost of this toroid should be of the order of $ 1 x 10^6 or less.

The three tracking planes are in air and can be of conventional construction. They are not large by current standards.

The addition of the toroid system allows a resolution of 500 GeV tracks from 10° to 2° of about 2.5%. This is a very useful region for the study of asymmetries of muon production.

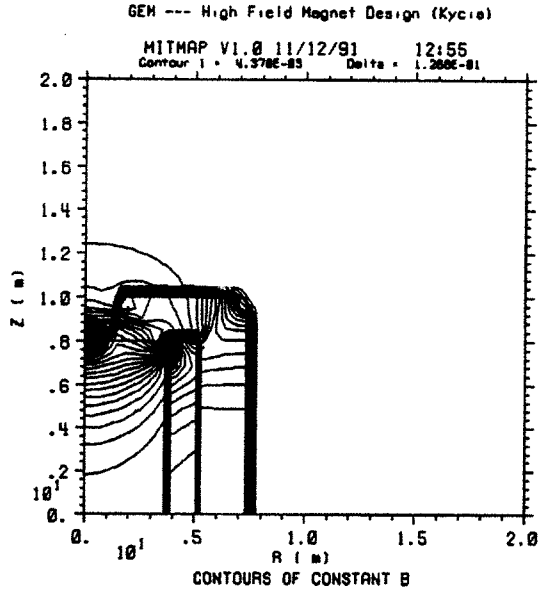

Figure 314: Contours of constant $|\vec{B}|$ superposed on a side view of the "Kycia" option.

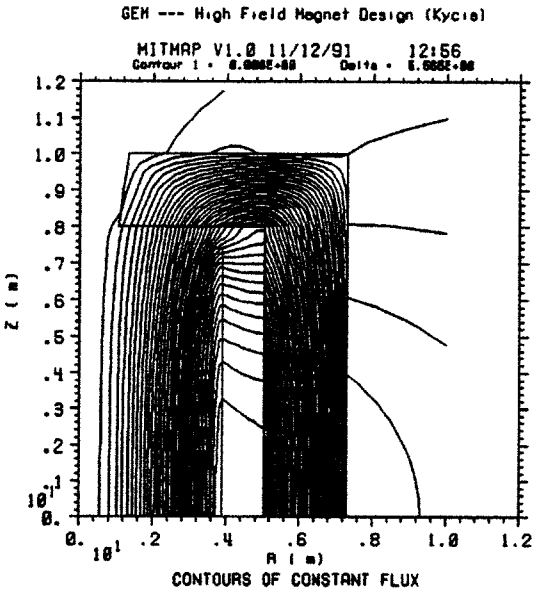

Figure 315: Flux lines superposed on a side view of the "Kycia" option.

accuracy, that the complete trajectory of the track is contained in the osculating plane.

For simplicity, we will discuss a uniform solenoidal magnetic field parallel to the beam of the SSC. There are three important parameters for this magnet.

1. $|B|$ = The magnitude of the field.
2. R = Radius of the magnet.
3. L = The length of the magnet.

The philosophy of the New Detector Collaboration (NDC) design is to have all measuring components inside the magnetic field.

In this case the momentum is measured by using the Sagitta technique. Again, for simplicity, assume the charged particle leaves the interaction region at 90°, along a radius of the solenoid. Figure 1 shows the trajectory and the relevant variables. Note the SSC beam (and magnetic field) is coming out of the plane of the drawing.

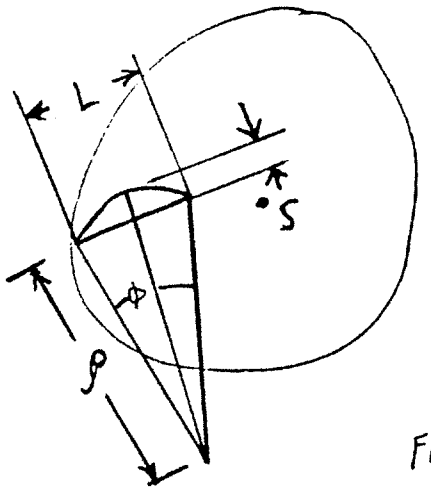

FIG 1

We will show that for this case:

$$S = (.3 / (8P)) (B) L^2 \qquad (2)$$

For this case $B = B\perp$.

This leads to considering $B\perp L^2$ as the resolution parameter since for large $B\perp L^2$ one has large S.

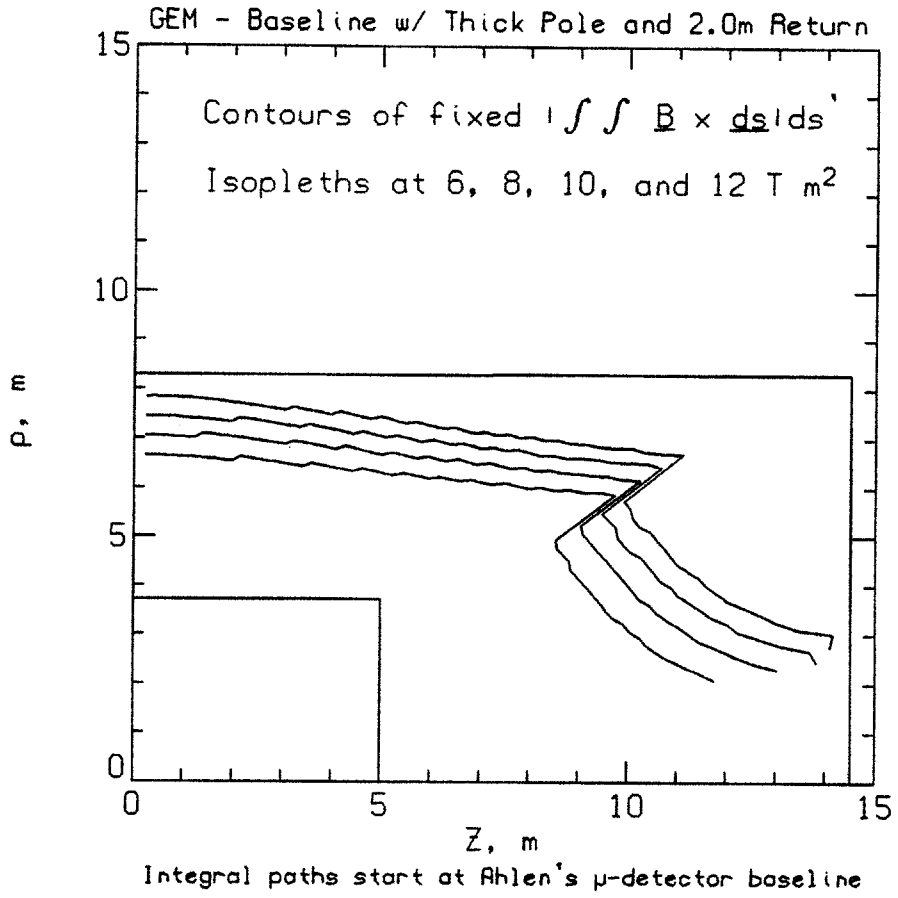

Figure 297: Isopleths of constant BL^2 superposed on a sketch of the magnet concept.

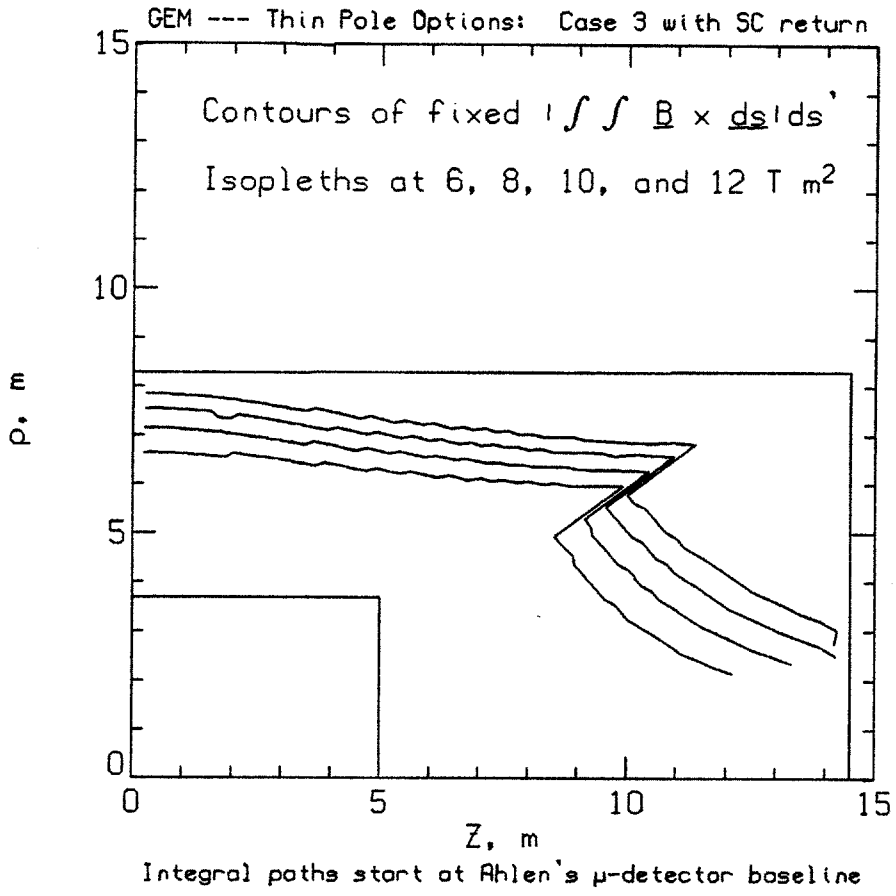

Figure 306: Isopleths of constant $\mathcal{BL}^2$ superposed on a sketch of the GEM concept; isopleths increase with distance from the origin.